Pulsed Plasma Thrusters for Small Satellites

Peter Vallis Shaw

Submitted for the Degree of
Doctor of Philosophy
from the
University of Surrey

Surrey Space Centre
Faculty of Engineering & Physical Sciences
University of Surrey
Guildford, Surrey GU2 7XH, UK

June 2011

Abstract

Since the Russian launch of the Zond-2 satellite in 1964 there have been over fifty years of research dedicated to the understanding of the first electric propulsion device to be flown in space, the Pulsed Plasma Thruster. The Pulsed Plasma Thruster originates from the evolution of the vacuum arc switch, but due to its microsecond operation time, the internal dynamics and nature of operation have remained unclear. The Pulsed Plasma Thruster is generally cheap to manufacture and to operate, which keeps it a popular device to research within institutes worldwide and has contributed to its longevity.

As a satellite propulsion device it has unique capabilities that other propulsion systems cannot provide. The thruster operates by accelerating plasma formed in the accelerating electrodes (or nozzle) in short discrete packets of thrust or impulse. The pulsed nature of the thruster means that between pulses energy can be stored in capacitors, ready for the next discharge. The storage of energy over time means the power draw is variable and is only dependant on the frequency that the system is pulsed at. This property of the thruster makes the Pulsed Plasma Thruster extremely versatile, allowing the thruster to perform both velocity correction and control manoeuvres and attitude control manoeuvres. The Pulsed Plasma Thruster is mechanically scalable but the performance of the thruster has been shown to depend linearly on the energy storage ability of the thruster's capacitor.

The work presented here covers two areas. Firstly is the critical analysis of the physical mechanisms that occur within a Pulsed Plasma Thruster through a review of literature, experimentation and the development of a high current plasma flow model. The second area is the design, development, manufacture and evaluation of the Pulsed Plasma Thruster for use on a nanosatellite platform known as the CubeSat.

Several novel observations and contributions were made during the critical analysis of the physical mechanisms of the Pulsed Plasma Thruster. The most significant was realising how the erosion of the metal electrodes affected the overall discharge process. It is postulated that the expulsion of material from emission sites (or cathode spots), the ionisation of that material and the resulting freed electrons, create a pinched plasma column between the electrodes. It is postulated that the interaction of the electrode sheath region and the intersecting plasma column cause the current flow to become limited. This was then shown to affect the efficiency with which the stored energy of the capacitor was converted to energy to accelerate the plasma. Understanding this issue is key in improving future designs of the Pulsed Plasma Thruster.

The observations and conclusions made during this work were put into practice to create an eight μPPT propulsion module for a 3U CubeSat. Initial results show that a μPPT with a specific impulse of 321s, an impulse bit of 0.56μNs and a mass bit of 0.17μg has been developed. The thruster was developed for two technology demonstration CubeSats. STRaND-1 is a joint collaboration between Surrey Space Centre and Surrey Satellite Technology Limited and UKUBE-1 is a joint collaboration between Surrey Space Centre and the UK Space Agency. Both CubeSats are scheduled for launch late 2011, early 2012. The propulsion module for the STRaND-1 CubeSat will be the first to provide full axis control and the first to provide electric propulsion on this class of satellite, showing the advantages of the Pulsed Plasma Thruster for Small Satellites.

Contents

List of Figures

List of Tables

Nomenclature

Attitude Determination and Control System

Air Force Research Laboratory

Austrian Research Centre

Ablative Z-pinch Pulsed Plasma Thruster

Computer Aided Design

Components off the Shelf

Discharge Initiator

Extremely Low Frequency

Electromotive Force

Earth Observation 1

End of Life

Electric Propulsion and Plasma Dynamics Lab

European Space Agency

Equivalent Series Resistance

Geostationary orbit

Gas Fed Pulsed Plasma Thruster

Hot Air Solder Level

High Voltage

Intensified Charged Couple Device

Illinois Observing Nanosatellite

Infra Red

Information Technology

Institute of Terrestrial Magnetism Ionosphere and Radio Wave Propagation of the Russian Academy of Science

Inductance Capacitance Resistance

Low Earth Orbit

Lincoln Experimental Satellite

Liquid Propellant Pulsed Plasma Thruster

Late Time Ablation

Microelectromechanical Systems

Magneto-Hydro-Dynamic

Micro Propulsion Attitude Control System

National Aeronautics and Space Administration

National Instruments Data Acquisition

ordinary differential equation

Printed Circuit Board

Pulsed Plasma Thruster

Pulsed Power Unit

Retarding Field Energy Analyser

Research Institute of Applied Mechanics and Electrodynamics

Rocket Propulsion Establishment

Synchronous Meteorological Satellite

Simulation Program with Integrated Circuit Emphasis

Surrey Space Centre

Surrey Satellite Technology Limited

Surrey Training, Research and Nanosatellite Demonstrator

	Thermocouple
	Transit Improvement Program
	Tokyo Metropolitan Institute of Technology
	Time of Flight
	University of Illinois Urbana-Champaign
	Vacuum Arc Thrusters
	delayed differential equation
e	Elimentary charge, C
e_0	Vacuum permittivity of free space, Fm^{-1}
g_0	Gravitational constant, ms^{-2}
k_B	Boltzmann constant, JK^{-1}
μ_0	Magnetic permeability of free space, NA^{-2}
μ_{Earth}	Standard gravitational parameter, m^3s^{-2}
α_i	Ion current normalised by arc current, %
$\kappa_{Ballistic}$	Ballistic coefficient, kgm^{-2}
ϵ	Electromotive force, V
ϵ	Permittivity, $\text{Fm}^{-}1$
ρ	Mass density, kgm^{-3}
ϕ_B	Magnetic flux, Vs
Φ_{wall}	Potential of the wall, V
Ω	Magnetic gyration frequency, Hz
ω_p	Plasma frequency of particle species, Hz
ω_{pulse}	Frequency of pulse discharge, Hz
σ_{sub}	Sub conductor conductivity, $\Omega^{-1}\text{m}^{-1}$
σ	Electrical conductivity, $\Omega^{-1}\text{m}^{-1}$
τ	Characteristic time of the pulse discharge, s

τ_L	Characteristic ion particle time of flight across inter-electrode gap, s
τ_S	Characteristic time of relaxation of ion charge states from cathode spot to quasi steady state value, s
υ	Velocity of the object relative to the fluid, ms^{-1}
υ_{ie}	Electron ion collision frequency, Hz
Γ_i	Ion erosion rate, kgC^{-1}
A	Area of the conductor plate, m^2
A_{Sat}	Satellite cross-sectional area, m^2
B	Magnetic field, T
C	Capacitance of the PPT capacitor, F
C_D	Drag coefficient
C_n	Accumulated ion fraction distribution at freezing zone of the $\sum \mathrm{n}^{th}$ levels
D_0	Electric displacement field, Cm^{-2}
D_0	Electric field strength, Vm^{-1}
d	Distance between the capacitor conductors/plates, m
$d_{ij,mn}$	Distance between central axes of two sub conductors given by the position vectors i, j, n and m, m
d_{sheath}	Sheath thickness, m
E	Energy of the PPT discharge, J
F_{Drag}	Drag force, N
F_{PPT}	Force produced by the PPT, N
f_n	Charge state fraction along the axis from the cathode of the n^{th} level
f_n^0	Charge state fraction distribution at the freezing zone of the n^{th} level
h	Separation distance between electrodes, m
I	Circuit loop current, A
I_{arc}	Arc current flowing through the circuit loop, A

I_{bit}	Impulse generated per discharge, Ns
$I_{i,n}$	Ionisation energy to take an ion from the $n-1$ state to the n charge state
I_{sp}	Specific impulse, s
I_{spot}	Current associated with each cathode spot, A
I_x	Moment of inertia in x axis, kgm^2
I_y	Moment of inertia in y axis, kgm^2
I_z	Moment of inertia in z axis, kgm^2
J	Current density, Am^{-2}
k_n	Ionisation coefficient of the nth charge state level
L	Impulse, Ns
$L_{circuit}$	Inductance of the circuit, H
L'	Inductance per unit length, Hm^{-1}
L_{sub}	Self inductance of sub conductor, H
l_{sub}	Sub conductor length, m
M	Mach number
M_{bit}	Mass eroded per discharge, kg
$M_{ij,mn}$	Mutual inductance between two sub conductors given by the position vectors i, j, n and m, H
$M_{Propellant}$	Propellant mass, kg
M_{Sat}	Satellite mass, kg
m	Total mass contained within the ‘plasma flow’, kg
m_e	Electron mass, kg
m_j	Particle mass of species j, kg
N_e	Electron density, m^{-3}
N_j	Electron density of particle species j, m^{-3}
N_{Pulses}	Total pulse number provided by the PPT

P	Plasma pressure, Nm^{-2}
Q	Charge on the Capacitor conductors/plates, C
Q_{ei}	Electron energy losses under elastic and inelastic electron-ion collisions, J
$\overline{Q_0}$	Initial ion charge state number in plasma jet
$\overline{Q}$	Mean ion charge state number in plasma flow
Q_n	Ion charge state at the nth ionisation level
R	Radius of the plasma flow where the plasma pressure equals the constraining magnetic pressure, m
$R_{circuit}$	Resistance of the circuit, Ω
R_{sub}	Sub conductor resistance, Ω
r_{Orbit}	Orbit radius, m
r_0	Initial orbit radius, m
S	Lever arm, m
S_g	Gravitational lever arm of satellite, m
S_0	Surface area of the initial plasma flow near the mixing region, m^2
S_{spot}	Surface area of the cathode spot near the mixing region, m^2
T_{cr}	Critical electron temperature in the plasma flow, K
T_e	Electron temperature, K
T_g	Maximum gravity torque, Nm
T_m	Maximum electron temperature in the plasma jet, K
t	Time, s
t_{min}	Minimum thruster firing time, s
t_{sub}	Sub conductor thickness, m
u_e	Exhaust speed, ms^{-1}
V	Bulk plasma velocity, ms^{-1}
V	Voltage applied across the Capacitor, V

V_e	Electron velocity, ms^{-1}
w	Electrode width, m
w_{sub}	Sub conductor width, m
z	Distance from the cathode along the axis that joins the cathode to the anode, m
z_0	Distance above cathode that the plasma mixing region is located, m

Acknowledgements

Almost six years have been dedicated to this work and I hope I will do it justice. In this time of discovery I have seen the best and worst of my capabilities. I have been pushed to utter despair and raised to euphoria on the roller-coaster ride that has been my PhD, my journey. Like a rollercoaster ride you are never quite the same person you were when you first got on. I have changed and hopefully for the better!

This journey has not been a lone effort and my first acknowledgement is to all those people, places and experiences that shaped the person I am today. When I look back on my life I have no regrets, none at all!

Mum and Dad, I think all I need to say is ‘I love you’, this PhD is dedicated to you both. As anyone understands, parents make great sacrifices for their children and my parents have been no exception. You have been my pillars of support, fountain of advice and always willing to give me a swift kick in the derrire when required. Whenever I was at my lowest your tender loving care gave me strength. To my sister I say simply ‘I love you’ but I have never forgiven you for conning my pound coin pocket money for 2 penny pieces with the excuse that ‘They’re bigger so they’re better!’. To the rest of my family, both from England and Austria I send a big hug. I know I have been rubbish at not keeping in touch but my thoughts are with you. To Opa, although I found it hard to communicate with you, I’d just like to say ‘You were my inspiration and a lot of my drive to obtain this PhD was because of the successes you achieved in your lifetime’.

To Julia simply from the heart, ‘You mean the world to me and you always will. I Love you’.

Family is important but so are friends and I’d like to say that my friends have been great! Special thanks goes to a few groups of friends, first of all the guys from home who I grew up with and will be life long mates: Russ, Ad, John, Jules, Ed, Kerry and Roy. The Mountaineering Club here at the University, so many good times, so, so many! You guys and girls are just plain amazing! The lot from the Territorial Army, thanks for all those good memories out on exercise. Those from the Space Centre, you lot go through the same trials and tribulations and for that I have the upmost respect for you all. The lunch group girls: Jess, Emily and Kate, thanks for keeping me entertained and giving me a curious insight into the mind of a young lady! The LARPers, as crazy as the hobby is, you lot are the salt of the earth and your friendships mean a lot to me.

In amongst my groups of friends there are a few individuals who need special thanks: First of all is Nic elf, you've been an awesome mate, always up for a laugh and never backing down from a challenge, the best years at Uni were the ones where we were up to no good! Torr you're mad, but you're still a very 'special' mate, don't change! Vicky and Al, you guys cared for me during the hard times, time and time again. I'm fortunate to have mates like you. Andy and Fluff, simply put, thanks guys, you've been good friends. Kirstyne, thanks for the advice and inspiration. The words you once spoke to me, 'That's why not everyone can call themselves a Doctor - It's a whole other level of dedication!', those words would always get me motivated through tough times.

Of all my friends special thanks though goes to my close friend Ollie. You have gone beyond the call of duty as a mate, it will never be forgotten, you truly are a Hero, 'Stay black!'

Whatever you all do in your lives remember my advice to you all, plain and simple 'Have fun!'

Now to those that actually helped me complete my PhD. Thank you goes to the funding provided by EPRSC DTG Fund for all but the first year of funding and my parents who believed in me and provided the first year of funding with the help of the Wingate scholarship fund.

A big thank you goes to my supervisor, Dr. Vaios Lappas for putting up with me and supporting my work. You have constantly tried to improve the facilities here at SSC and the ever expanding electric propulsion group. The success of this group is a sign of your dedication to the electric propulsion cause. Thanks goes to those who have helped me learn in both the scientific field and the spacecraft applications field, in particular; Dr. Craig U., Rod B., Ian C., Dave G., Mick, Shaun, and George. The technical staff at the University who made the research possible: Dave F., Eric, Charles, Richard, Bill, Bob, Phil U., Richard, Chris, Dave C., Judith, Adrian, Mike R. and Duncan. The administration staff: Karen C., Karen K. and Noelle. Lastly thanks to the guys and girls at the learning support centre for diagnosing my dyslexia, ironically though in my last year of education!

'If you stop dreaming you will wake up in a desolate nightmare!'

Chapter 1

Introduction

1.1 Motivation for Research

Exploration of the celestial sphere is the next evolutionary step that mankind must make. It is this core principle that the research in this thesis is presented. Although the modest and unassuming grandfather of electric propulsion might not be the device used to take man beyond the Earth-Moon system, it will and can be used as a stepping stone to aid in mankind's exploration. The Pulsed Plasma Thruster (PPT) first experienced space travel in 1964 on the Zond-2 Russian spacecraft. Since then it has been the subject of intense scrutiny, gaining favour in recent years as the development of smaller satellites continues. The demand for efficient, low mass, low voltage, low cost propulsion systems for the next generation of satellites has meant that a fresh look has been taken on the underlying physics and principles of the PPT. This, in turn, has led to some interesting observations that have spearheaded the direction and development of a miniaturised PPT to be used on a small satellite known as a CubeSat. This thesis covers the modelling, design, development, evaluation and iteration of a series of PPTs at the University of Surrey. The research is an end to end account of the science and engineering developments made, which have contributed to the field, from initial circuit analysis through to complex modelling of electrode erosion phenomena and development of breadboard systems to flight hardware.

The PPT remains a popular device with researchers, but often it is underestimated due to its simplicity and relatively low cost to manufacture. Low energy conversion efficiency ratings from electrical to kinetic energy and the yet to be ascertained goal to increase this value above 20% in conventional designs has meant that the PPT is not a popular device within industry. Current research is focussed on a number of aspects surrounding the PPT, including the modelling of the plasma plume, novel propellant feeding mechanisms, electrode geometry and creating whole systems for dedicated missions. The internal dynamics of the plasma production and the electrode erosion are less understood and it is only recently, with advances in measuring equipment and high speed cameras, that this area is being looked into. The main reason though for a lack of advancement is funding in this field. Although simple and cost effective to produce, the PPT has complex underlying physical principles and research groups can fall into the honey trap of building these devices without having the supporting equipment to probe these devices in detail. It was only by chance that the research in this thesis was conducted as its original goal was to study Teflon^{TM} erosion. It was only when a piece of Teflon^{TM} got dislodged and fell from its holder and the device still operated nominally that this new direction was investigated. This allowed the link to be made with the film deposition research field, which is well funded and relatively well understood, and that insight was gained on the internal plasma dynamics of the PPT within the discharge chamber.

The research focuses on two key areas: simulation of the electromagnetic contribution of the plasma discharge and experimentation to compare simulations with measured results. The simulations were based on previous models found within literature and expanded upon with novel contributions from the film deposition research field. This was conducted in tandem with an experimental programme, which looked at procuring, refurbishing, developing and commissioning equipment, facilities and prototypes of the PPT and its supporting facilities. Once experimental data was collected, this database formed the basis of a validated engineering model that was used to create improved prototypes of the PPT. The model and prototypes were evaluated several times over a four year period.

The PPT operates by discharging stored energy into some form of propellant located between two electrodes. The initial input of energy by an external device ionises propellant, forming a low resistance plasma which electrically connects the capacitor to the electrodes, allowing it to discharge. High currents induced by low resistance create strong magnetic fields within the electrodes. Energy released by the capacitor is used to ionise further propellant, creating additional plasma. The cross product between the current density flowing through the plasma and the magnetic fields create a force (i.e. the Lorentz force) that accelerates the plasma bulk along the axis of thrust. The coupled LCR system creates a multi pulse plasma discharge in the order of tens of microseconds. The complete process is repeated on a regular basis, leading over a period of time to create exploitable thrust by a satellite propulsion module.

The kinematic modelling used in this work for the PPT is based on a lumped circuit analysis model in which certain elements of the model are expanded upon by further complex sub models. The lumped circuit analysis model assigns each component a resistance, inductance or capacitance as appropriate. The lumped circuit analysis is then coupled with Newtonian mechanics to obtain a model that describes the full PPT discharge process. After initial experimental prototyping this established model was further expanded upon by developing a model for the plasma mass and resistance as a function of the eroded electrode material due to the process of cathode spot emission. The model was coded, validated and evaluated through several iterations that were used to build a number of thruster prototypes over the course of this research, which went from classic designs based on literature, to the stripped down bare essentials to overcome experimental shortcomings, to eventually an effective compact design for a CubeSat propulsion system.

1.2 Outline of Chapters

1.2.1 Literature Review

This chapter reviews the available literature and is split into three sections. The first looks into the history of flown PPTs from the first flight on Zond-2 to the more recent NASA EO-1 satellite. It reports on some of the successes and failures of the thruster aboard satellites in recent history. The review then reports on the experimental observations that have been made over the years with emphasis on experiments that bring insight into the plasma processes. The final section draws upon elements of the literature to describe the current state of understanding of the processes that occur within the PPT.

1.2.2 CubeSat Mission Design & Analysis

One of the new types of satellite platforms emerging is the CubeSat, which is a sub 5kg satellite made from modular segments. A review of the CubeSat is conducted with an analysis of all the current propulsion systems that have previously been developed for this class of satellite. A review of propulsion systems biased towards electric propulsion was undertaken to assess if any candidates could be developed for this class of satellite. The PPT is chosen on its merits and a PPT based on postulated performance from the literature explains the advantages the PPT brings to the CubeSat platform.

1.2.3 PPT Experiments

To further understand the PPT, test facilities were developed and experiments were conducted. After three and a half years of facility development and several iterations of thruster testbeds a set of PPT experiments were conducted. The experiments focused on several aspects: The electrical and geometric properties of the sparkplug were looked into. A study on the effect of the Teflon^{TM} propellant width on the propellant mass errosion was undertaken. The effect of the electrode geometry and discharge gap distance on the current and voltage profile was looked at. Finally, a study was conducted on the discharge properties when Teflon^{TM} was and was not present between the electrodes.

1.2.4 PPT Modelling

Based on observations made during the literature review and the experimental phase, this chapter describes the development of a PPT model. The model is based on a lumped circuit analysis model with sub models to describe various time dependant processes. Sub models describe the skin effect within the electrodes, the mass errosion from the electrodes, the magnetic field setup around the electrodes and a simplified quasi state Magnetohydrodynamic flow model to describe the properties of the plasma flow between the cathode and anode. The model is validated with experimental data and then it is used to analyse the plasma properties of the PPT plasma. Finally the model is used to predict performance trends within a PPT so that an optimised thruster can be developed.

1.2.5 Developing a μPPT for CubeSat Applications

The PPT model and observations from the experimental phase are used to develop a μPPT propulsion module for a 3U CubeSat. An initial design is proposed, built and evaluated. This leads to the design and build of a qualification module and flight hardware for a launch on a CubeSat known as STRaND-1 which will launch in November of 2011.

1.3 Novelty and Research Achievements

Within the course of this work, the following novel contributions have been made to the current state of the art, for the Pulsed Plasma Thruster field:

- From critical analysis of the literature review and with observations during experimentation that a PPT, without Teflon^{TM} propellant, produces plasma from the errosion of the electrode surface.
- It is postulated that in most PPTs, with or without standard Teflon^{TM} propellant, the plasma originates from the errosion of the electrode surface.
- It has been highlighted with circumstantial evidence from the literature review that within the PPT, the process of cathode spots is the cause of electrode errosion.
- It has been shown through experimentation that the current discharge profile in the circuit loop of the PPT is a function of the stored energy but is not a function of the eroded Teflon^{TM} mass.
- It is postulated with experimental evidence that the presence of Teflon^{TM} acts as an arc bridge. When the discharge is initiated this bridge acts as a 'path of least resistance' in which the initiated discharge tracks across. The presence of the bridge allows for larger currents to flow and stronger magnetic fields to form which enhance and elongate the LCR ringing effect of the discharging circuit.
- It has been highlighted with analytic evidence from the literature review that each pulse of the ringing discharge relates to a new plasma formation. It is also highlighted that beyond the first pulse the location of each new plasma formation coincides with the location of the neutral particle sheet (if present).

- Based on models from the literature a simplified MHD plasma flow model that originates from the production of plasma from cathode spots has been formed. This model, which takes cathode spot data from the plasma coating field and a flow model from research into short pulse high current cathodic plasmas, is implemented to explain the internal dynamics of the PPT. The simplified MHD plasma flow model coupled with a lumped circuit analysis model, a Lorentz force model, an electrode skin effect model and a plasma errosion model make the completed novel PPT model. The PPT model, within the confinements of quasi steady state is able to accurately predict the current profile of a discharging PPT. The PPT model also predicts, within reasonable magnitudes, values of plasma parameters that are seen within literature, including the mean ion charge state and the electron density. The PPT model predicts temperature distributions in the early stages of the plasma formation that coincide with the observed back flux of carbons seen on Teflon^{TM} samples. Lastly the PPT model, in the early stages of the plasma formation, predicts similar shapes of the plasma flow to that seen in current density distribution data.

- It is postulated from observations made using the developed PPT model, that within the plasma flow 'choke' points form due to instabilities within the plasma flow. These lead to localised areas of high ion mean charge states, high electron temperatures and high electron number densities. I also postulate that the main limiting factor of arc current within the plasma flow is due to the charge-space limitation of the anode sheath. I postulate that until this limitation is reduced by careful manipulation of the plasma flow near the anode sheath the efficiency of PPTs to convert electrical energy to kinetic energy will remain low.

- The developed model was used to design a novel type of PPT electrodes that were based on a blade like configuration. This configuration was chosen as it would hopefully promote cathode spot formation in a single area along the blade edge.

- A novel propulsion module for a sub 5kg satellite platform has been developed with eight μPPTs that will provide two axis with pitch, roll and yaw attitude control. The μPPT boasts several novelties including a contact trigger discharge initiator, low circuit inductances and resistances using a custom pulse capacitor and no Teflon^{TM} propellant. All these innovations have meant that four μPPT can be mounted on a single PC104 board.

Chapter 2

Literature Review

2.1 Introduction

The enigma of the PPT has been its unusual longevity as a concept for research. Since 1964, with the launch of the first PPT (and first electric propulsive device in space) it has remained on the research agenda. Its physical simplicity and relative low cost has made the PPT accessible, enticing researchers to integrate it on a satellite program (i.e. FalconSat, Dawgstar) or in a research project. However, with so much keen interest over the past five decades it is interesting to note that there has been little improvement in the thruster's performance since its early conception. The fact that there has been a lack of progress has shown that underneath the simplicity and accessible exterior lies a more complex operating mechanism.

It is of benefit to ask the question, 'What defines a Pulsed Plasma Thruster?' The traditional view of the Pulsed Plasma Thruster is that it is made up of several constituent parts; Teflon^{TM} that acts as the propellant, a capacitor that stores energy, a power unit to supply the capacitor with energy, electrodes which accelerate the forming plasma and then finally a sparkplug to initiate the discharge, see Figure 2.1.

The outsider would consider this to be the definition of a Pulsed Plasma Thruster, but this would be an inadequate representation of the field. For instance, the propellant has not always been Teflon^{TM}. Several research institutions have used water [8], methanol and ethanol [9] as propellant alternatives. The energy storage device does not need to be a capacitor, an inductor could also be theoretically used. Other faults can also be seen in this traditional view of the Pulsed Plasma Thruster.

So as the understanding of the Pulsed Plasma Thruster is developing, it is important to offer a redefinition of what a Pulsed Plasma Thruster is, to ensure that thrusters that are being developed are known for what they are and not how they have been previously labelled. For this work we will redefine the traditional view of the Pulsed Plasma Thruster to:

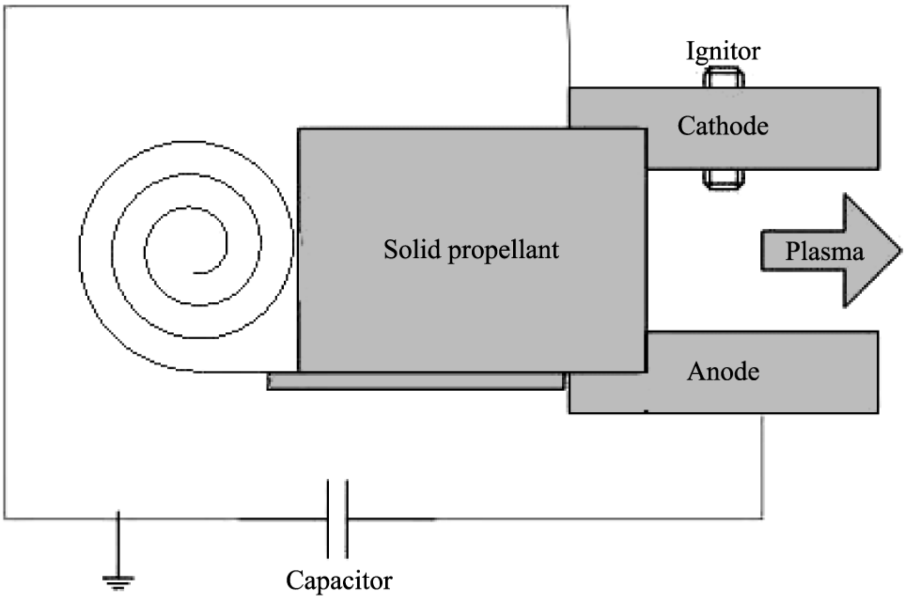

Figure 2.1: The traditional view of the Pulsed Plasma Thruster in its constituent parts

A rapidly discharging finite electrical energy source that transfers energy to a self created magnetic field around an induced current flow, in which part of the current flow is through a self generated plasma. In which exploitable thrust is created from the Lorentz force which is produced by the interaction of the magnetic field with the flowing current through the plasma.

This definition focuses on the accelerating principle mechanism as a form of definition rather than on how the thruster is designed. The literature review begins with the history of flown PPTs and then looks at the reseach within the PPT field. The research comes under two broad groups. The first is research and development in the terms of practical application to a satellite mission. The second group is the research of the underlying principles and mechanisms of a pulsed plasma thruster. The literature review then ends with a summary of the current theory that describes the discharge process of the Pulsed Plasma Thruster.

2.2 History of Flight of Pulsed Plasma Thrusters

Early experimentation in electric propulsion can be dated to Russian experiments from 1934 however the first electric propulsive device flown in space was developed by Antropov and Khrabrov between 1962 and 1964 and was the Pulsed Plasma Thruster. Its maiden voyage was on the Mars bound satellite Zond 2, which was launched from Baikonur, but after several months communications was lost. The PPT was continued to be developed in the United States at the Fairchild Republic company and the Massachusetts Institute of Technology Lincoln laboratory. On 26^{th} September 1968 the first US developed PPT was used for attitude control on the Lincoln Experimental Satellite (LES-6) and provided 10 years of operation.

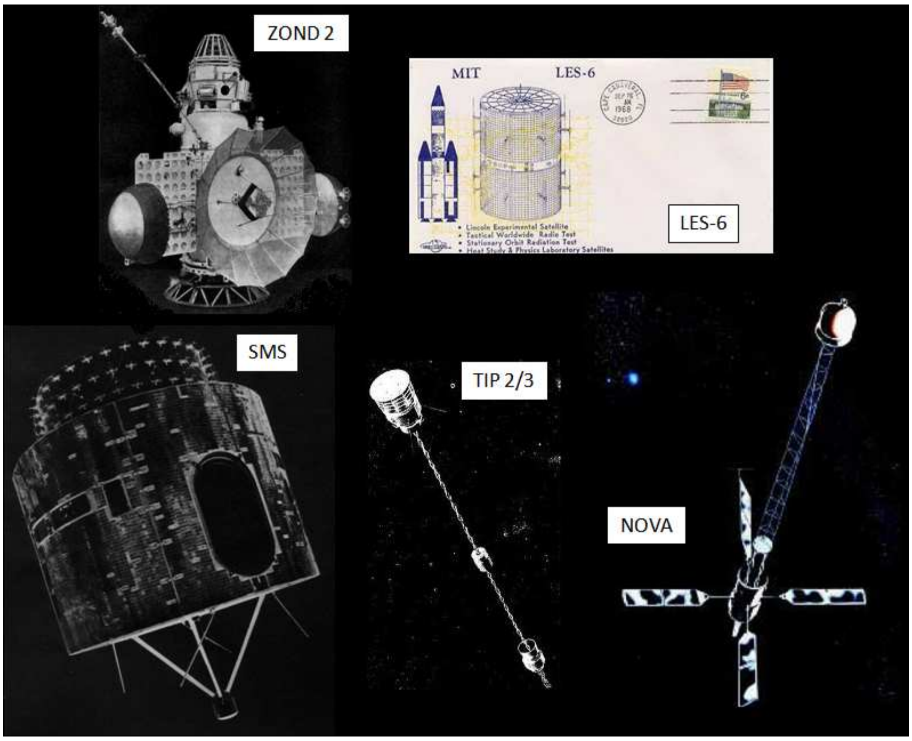

Figure 2.2: Satellites from 1964 to 2000 that have flown a Pulsed Plasma Thruster

In 1974 a PPT flew on the Synchronous Meteorological Satellite (SMS). The PPT had variable thrust capability and was used for spin axis precession control [40].

Transit was the world's first radio navigation satellite system built for the US Navy and began in 1959. After 10 years of success the TIP (Transit Improvement Program) was initiated with the objective to provide a radiation-hardened satellite. Triad-2 (TIP-2) and Triad-3 (TIP-3) satellites were each equipped with a redundant PPT system used for drag compensation. The 1kg Teflon^{TM} propellant, used for both thrusters, provided a fuel supply for 10 years. The Transit program was expanded with three more NOVA spacecraft, nearly identical to the TIP series design. The NOVA satellites used the PPT system of the TIP series satellites to compensate for drag. The NOVA satellites had operational lifetimes of 8 to 9 years. Between the TIP and NOVA PPTs for the TRANSIT program, over 50 million pulses and over 20 years of operation provided reliable impulse bits which enabled the satellites to provide very accurate ephemeris data and could correct for disturbances down to 10^{-11}g [41].

The trend in developed hardware parted from previous decades in the new millennium to provide attitude control for non-spin axis stabilised satellites and to become the primary propulsion system on ever decreasing volume and mass bound satellites. Recent history though has been plagued with cutbacks and failed missions. Since the turn of the millennium several flight PPTs have been developed, but only two PPTs in the past decade have flown successfully.

As part of the New Millennium program in 2000, NASA launched the Earth Observation 1 satellite which had a PPT experiment on board based on the design heritage of previous missions (LES 6, LES

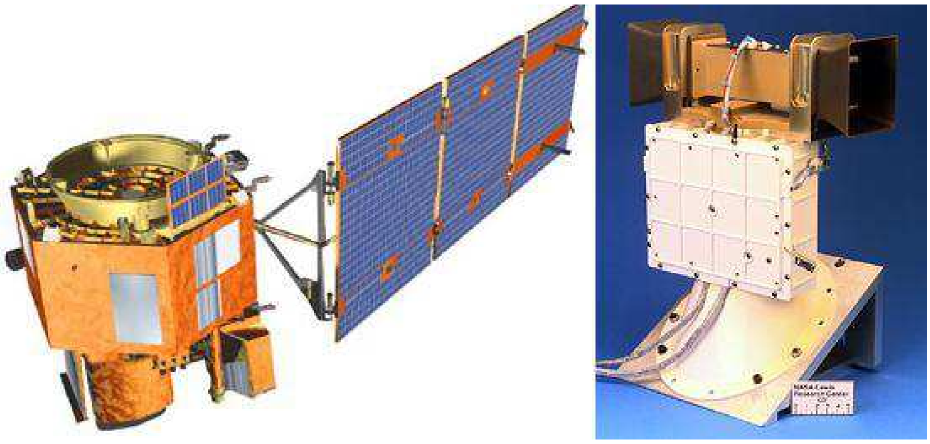

Figure 2.3: Left: Earth Observation 1 satellite, Right: EO-1 PPT experiment

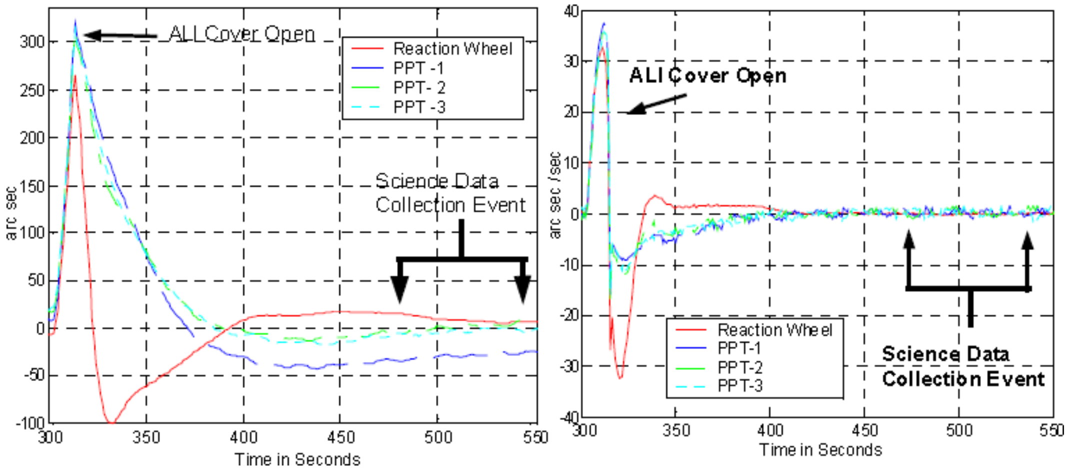

Figure 2.4: EO-1 in orbit data of a manoeuvre performed four times (optics cover opening), once with a reaction wheel and three times with a PPT. The left graph shows the pitch attitude error comparison between the reaction wheels and the PPT and the right graph shows the pitch rate error comparison [1]

8/9, SMS and TIP/NOVA), see Figure 2.3.

The PPT was thought to be a high risk experiment that could affect other systems, but after initial tests, lasting 26 hours and 96,000 pulses, the thruster performed nominally and there was no detrimental effects observed with other systems or instruments. The EO-1 PPT experiment successfully demonstrated the ability of the PPT to provide comparable pointing performance compared to reaction wheels. The pitch of the satellite was controlled with a reaction wheel assembly and then compared with a repeated manoeuvre using PPTs, see Figure 2.4. The experiment showed that although the PPT had a lower torque authority, the lack of internal momentum accumulation and the precision impulse capability enabled excellent pointing performance [42].

Since the initial experiments, the PPT has remained in a powered down state, until such a time when the EO-1 mission comes to the end of life (EOL), this should happen sometime between 2012 and 2014. During this period high risk experiments will be conducted with the onboard PPT experiment [1].

The Electric Propulsion and Plasma Dynamics Lab (EPPDyL) at Princeton University began collab-

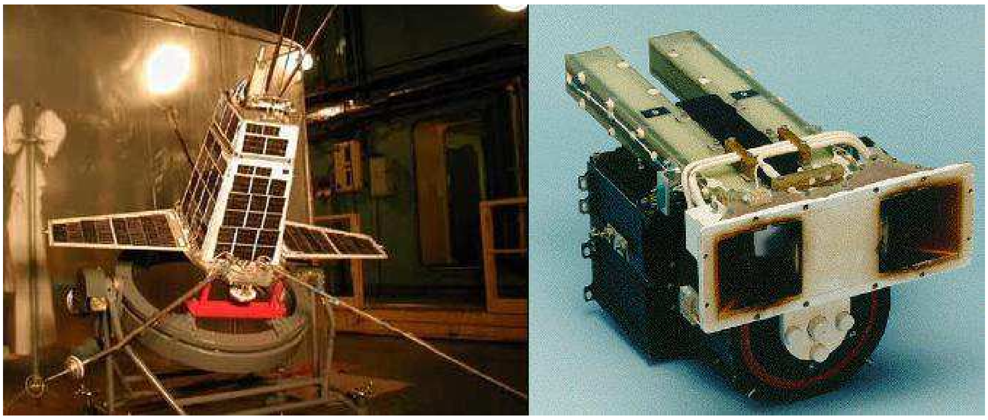

Figure 2.5: Left: COMPASS-2 satellite, Right: LES 8/9 PPT, a similar design was flown on COMPASS [2]

oration in 1996 with the Institute of Terrestrial Magnetism Ionosphere and Radio Wave Propagation of the Russian Academy of Science (IZMIRAN) on the COMPASS P^{3}OINT mission. The Russians wished to use the Lincoln Experimental Satellite (LES 8/9) PPT module that had been developed to flight-ready status twenty years previously, but never flown, on the COMPASS satellite [2]. It is unclear if this collaboration was successful but on 10th December 2001 the Zenit-2 rocket launched the remote-sensing satellite from Baikonur cosmodrome's site 45. COMPASS soon failed after launch delivering no useful data.

Despite the 2001 setback, the Russian lead COMPASS project was not scrapped and on the 26th of May 2006 at 22:50 Moscow Summer Time, the Shtil converted ballistic missile blasted off from a submerged K-84 Ekaterinburg submarine in the Barents Sea. The rocket carried an 86-kilogram COMPASS-2 science satellite designed to study physical phenomena associated with earthquakes, see Figure 2.5. After launch there were conflicting reports about the status of the satellite but it was clear that it was either severely tumbling or the solar panels had failed to deploy. IZMIRAN announced that due to insufficient power supply the activation of the scientific payload onboard COMPASS-2 was impossible. The satellite was considered to be dead, until in late November of 2006, the satellite was revived and commissioned. One of the payloads was a Russian built Teflon^{TM} propellant PPT.

The Dawgstar PPT was developed in partnership with Primex Aerospace and University of Washington (Cornell University). The Dawgstar Satellite was one of three microsatellites that made up the Ionospheric Observation Nanosatellite Formation (ION-F), see Figure 2.6, part of the AFRL University satellite program. The mission was a precursor to TechSat21 and was designed to show that a PPT can enable formation flying, station keeping and attitude and orbit control. The three satellites built by students were originally planned to be launched on the US Space Shuttle as a 'get away special'. This was pushed back due to the Columbia shuttle accident in 2003 and the program was eventually cancelled [43] [44].

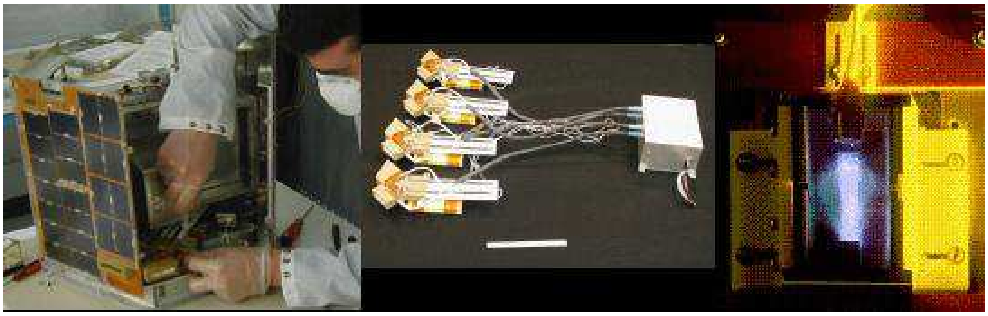

Figure 2.6: Left: PPT being integrated into the ION-F satellite, Middle: Complete Dawgstar PPT module and Right: Breadboard Dawgstar module firing

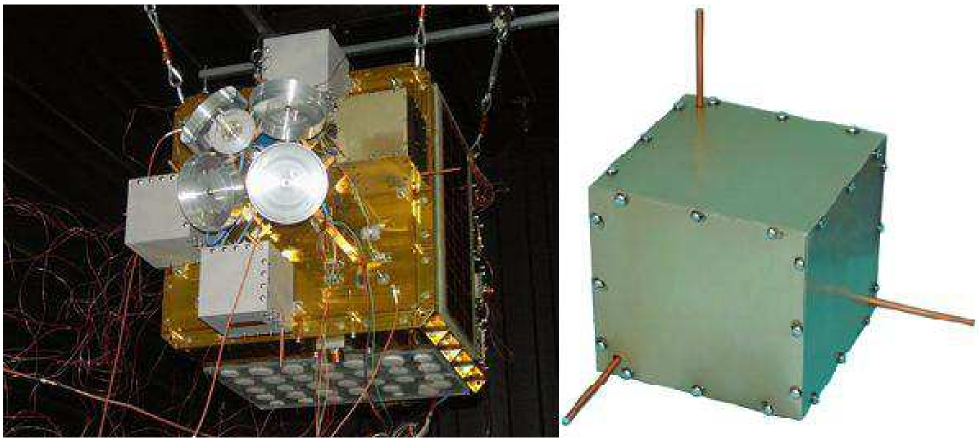

Figure 2.7: Left: FalconSat3 Satellite Right:AFRL coaxial PPT developed by Busek

The US Air Force Research Laboratory (AFRL) has been developing a μPPT since 2001. The original concept was to build a PPT for TechSat21 in a very innovative manner for two reasons. First of all the coaxial PPT was of a very small size and relied on this to cause a breakdown in the PTFE propellant between the inner and outer electrode, this circumnavigated the need for an external discharge initiator. The second reason was that the electrodes themselves were going to form part of the satellite structure, after launch these electrodes would then be eroded away with the PTFE creating thrust. TechSat 21 was cancelled in 2003 but the research and developments of the μPPT were continued and in partnership with Busek developed into the Micro Propulsion Attitude Control System (MPACS) of which four of these modules were flown on FalconSAT 3 in 2007, see Figure 2.7. FalconSAT 3 used a gradient boom, but during commissioning the boom was released before the satellite had stabilised, the satellite began to spin uncontrollably and communications became intermittent. Even 3 years after launch AFRL are still working to regain control of the satellite [45].

Table 2.1 summarises the history and performance of the flown PPTs. Despite the lack of successful outcomes in the past decade, PPTs are still being researched and developed with an eye on CubeSat propulsion where low mass, volume and power constraints make the PPT an ideal solution [46].

Table 2.1: Previous flown PPTs and their respective performances, with the addition of the Dawgstar flight hardware ready PPT.

Year	**Mission**	**Impulsebit, μNs**	**Specific Impulse, s**	**Energy, J**	**Notes**	**Reference**
1964	Zond 2	5000	410	50	Mars mission, Satellite failed	[40]
1968	LES 6	27	312	1.85	E-W Stationkeeping	[40] [41]
1974	SMS	111	505	8.4	Attitude Control	[40] [41]
1970s	LES 8/9	300	1000	20	Attitude Control	[41]
1981	TIP/NOVA	400	543	20	Orbit Insertion, Drag maintainance	[40] [41]
2000	EO-1	860	1400	56	Experiment	[1] [42]
2001	COMPASS P^3OINT	285	836	18	Based on LES 8/9 PPT, Failed on launch	[2]
2002	Dawgstar	66	266	4.9	Program cancelled	[43] [47] [48]
2006	COMPASS II	-	-	-	Satellite lost but later revived	-
2007	FalconSAT 3	-	-	-	Satellite failed	[45]

2.3 Review of Pulsed Plasma Thruster Research

The 35 year review of research conducted by Burton et al. [40] has become a commonly referenced paper that informs and influences research that has manifested over the past ten years since it was written. This review separates the research into two broad envelopes; Hardware development and fundamental science development.

2.3.1 Hardware Development

The Pulsed Plasma Thruster can be considered to be compromised of several hardware components which can be generalised as:

- The Power Unit - The function of this unit is to take the power from the spacecraft bus and convert it into a high voltage line.
- The Energy Storage Device - The function of this device is to provide energy to the plasma discharge.
- Discharge Chamber - The chamber functions to allow energy to flow from the storage device into the plasma. The chamber in its geometry may also affect the acceleration properties of the plasma.
- Discharge Initiator - This device will initiate the discharge by introducing electrons that ‘short’ the isolated terminals of the energy storage device to create a conducting path.
- Propellant - The propellant provides the mass to the plasma which is accelerated in the discharge chamber.

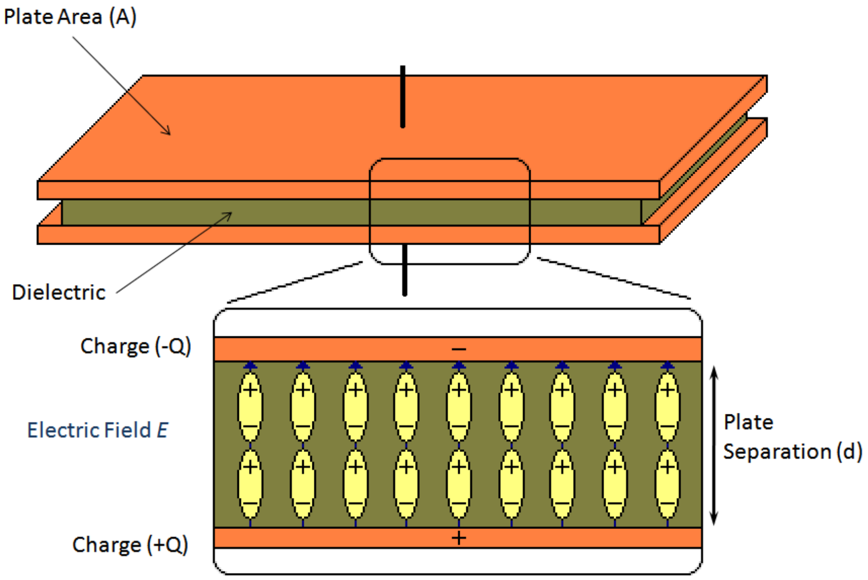

Figure 2.8: The basic principles of a capacitor

The literature for each of these broad categories is summarised below except for the power unit as this subject is more connected with the advancement of power electronics than the development of the thruster itself.

Energy Storage Device Development

The energy storage device in a PPT is commonly a high voltage pulse capacitor and is unequivocally the most significant component within the PPT, its properties affect the whole of the thruster and as such will be explained from first principles.

A capacitor consists of a pair of conductors separated by a dielectric material, when work is done by an external influence to move charge between the conductors (i.e. a voltage is applied to the plates) an electric field is established that stores energy within it. If the charge is allowed to return to its equilibrium position the energy will be released. In this way energy can be stored over an extended period of time but released in a short burst providing the PPT with enough energy to create a short duration plasma.

The ratio between the charge held on the conductors to the voltage applied across those conductors is called the capacitance and in an ideal system this would be fixed. In reality a small current will pass through the dielectric from one conductor to the other and so each capacitor has with it an Equivalent Series Resistance (ESR). Assuming a uniform electric field and that the width of the plates is much greater than the separation, the capacitance can be expressed as a function of the geometric properties of the capacitor and the permittivity of the dielectric material, see Figure 2.8 and Equation 2.1. To increase the capacitance a larger surface area of the conductors is required, the separation between the conductors must be decreased or the permittivity of the dielectric material must be increased.

$$C = \frac{Q}{V} = \frac{\epsilon A}{d} \tag{2.1}$$

The amount of energy that can be stored within a capacitor is limited by its breakdown voltage, above this voltage the electric field is greater than the dielectric strength and the dielectric becomes conductive. The high fields within the dielectric rip electrons from the atoms in the dielectric material and creates a path of conduction. Research into new high dielectric strength materials for PPT capacitors led to a small business innovation research program funded by NASA. Vanderbilt University and Aerojet developed a diamond dielectric film capacitor using chemical vapour deposition. It was expected to decrease the discharge time, decrease internal heating within the dielectric and increase the lifetime, however after manufacture it was found to be comparable to other commercially available capacitors [49].

Capacitors deviate from the ideal capacitor Equation 2.1 in several ways: the permittivity of the dielectric can be affected by a number of factors including temperature, pressure, humidity and discharge frequency. Also imperfections with the dielectric substrate will cause the capacitor to have a small leakage current effectively giving the capacitor an ESR. The ESR can be modelled as a linear effect however the frequency dependence of the dielectric is more complicated. The permittivity of a dielectric can be represented by a complex function. The response of a normal material to external fields generally depends on the frequency of the field. This frequency dependence reflects the fact that a material's polarisation does not respond instantaneously to an applied field. The definition of the complex permittivity $\hat{\epsilon}(\omega)$ therefore becomes;

$$D_0 e^{-i\omega t} = \hat{\epsilon}(\omega) E_0 e^{-i\omega t} \tag{2.2}$$

where

$$\hat{\epsilon}(\omega) = \epsilon'(\omega) + \epsilon''(\omega) \tag{2.3}$$

$\epsilon'(\omega)$ is the real part of the permittivity, which is related to the stored energy within the dielectric and $\epsilon''(\omega)$ is the imaginary part of the permittivity, which is related to the dissipation (or loss) of energy within the medium. Figure 2.9 is a representation on how the complex permittivity is affected by the frequency of the alternating electric field. The discharge frequency of the PPT is in the range of 10^5 to 10^6Hz. The plot shows that in this frequency range, dissipation and hence energy losses in the displacement field, come from ionic polarisation effects.

The ESR and dissipation losses in the dielectric affect the total energy that is transferred to the plasma discharge of the PPT and is lost in several ways, the most noticeable is in the form of joule heating. Testing completed at University of Illinois Urbana-Champaign in 2002 recorded the temperature rise of there UIUC PPT-7, see Figure 2.10. It shows that over a period of 16 minutes the temperature of the

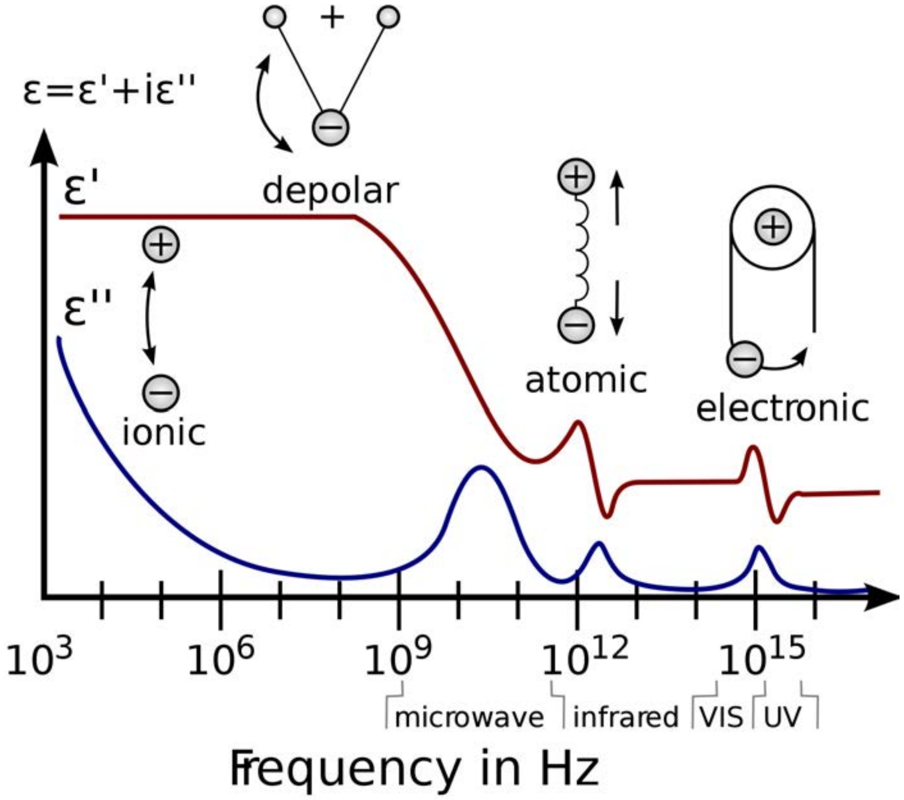

Figure 2.9: The dielectric permittivity spectrum over a wide range of frequencies. Various processes are labelled on the image: ionic and dipolar relaxation, and atomic and electronic resonances at higher energies

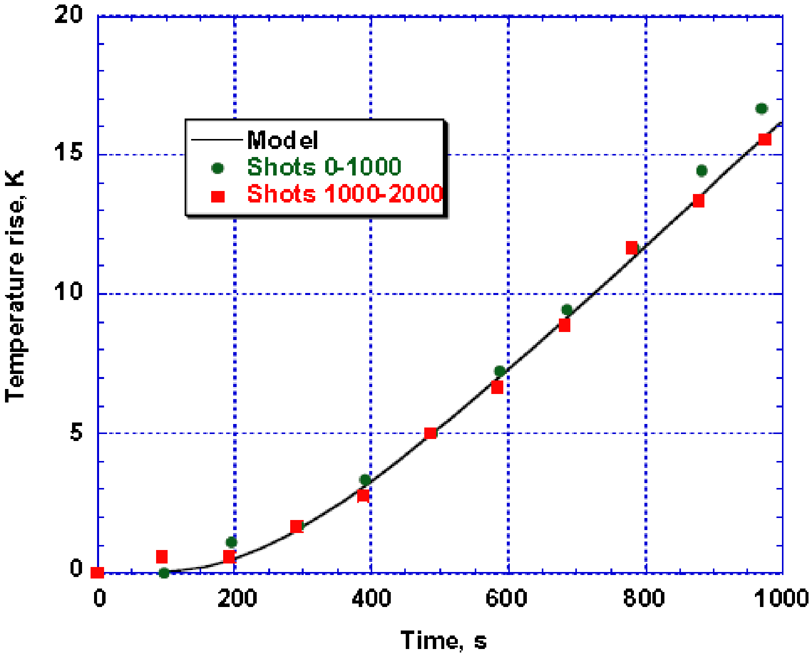

Figure 2.10: Temperature rise of the UIUC PPT-7 during two tests with their developed model fit

capacitor rose by 16K. Comparing this result to a model the University developed, it showed that 14% of the energy stored in the capacitor to begin with was lost as heat to the capacitor, instead of being transferred to the plasma [50] [51].

The Research Institute of Applied Mechanics and Electrodynamics (RIAME) studied the heating affect caused by the internal resistance of a capacitor for a 50J PPT discharging with a firing rate of 1 Hz. Temperature increases were shown to be up to 30K over a 2 hour period. Reducing the internal resistance of the capacitor decreased the rate at which the temperature increased, allowing the temperature of the capacitor to attain thermal equilibrium more quickly [52].

Research has been conducted into the development of ceramic capacitors, which have been an attractive choice for PPTs providing good energy storage to mass/volume as they do not require hermetic packaging and are highly resistant to radiation in space [53]. However the physical stresses on the dielectric when pulsed can cause mechanical fatigue causing cracks in the ceramic leading to early failure. Newly developed ceramics like the CR09 ceramic from Calramic Technologies LLC report being able to be pulsed for greater than 1 million pulses. These would be suitable for short to medium term missions.

Micropulsing research conducted by NASA was another method to reduce the mass and volume of the PPT capacitor. The idea was to use smaller capacitors that would store less energy but to increase the frequency of firing to maintain similar thrust levels. Testing at NASA Glenn Research Centre in 2004 showed that micropulsing was possible. The reduced capacitance and voltage rating of the smaller capacitors led to a reduction in the specific impulse and efficiency of the PPT. The PPT would then require more propelant, to provide equivalent total impulse for a similar mission, negating the mass savings made in reduceing the size and mass of the capacitor to begin with [54].

Discharge Chamber Development

The discharge chamber of the PPT can be considered as the volume and components that are involved with the acceleration of the plasma that is created within it. Issues involved with the discharge chamber include its geometry, material it is made from, the gradual erosion of that material and external devices that interact and alter the acceleration dynamics. The electrode geometry and the volume/shape of the discharge chamber are closely linked. Usually the electrodes themselves become the physical boundary of the discharge chamber i.e. the coaxial electrode PPT. Studies over the past 50 years have proposed new shapes and designs from the traditional parallel plate or coaxial electrodes which include double coaxial electrodes, double parallel electrodes, flared electrodes and coaxial designs to exploit Z-pinch acceleration effects.

The different proposed shapes have all had a variety of reasons as to why they were developed. Initially it was thought that the parallel plate electrodes maximised electromagnetic acceleration effects and that coaxial electrodes maximised electro thermal acceleration effects, but studies by Keidar et al. showed that even in coaxial electrode configuration the primary acceleration mechanism was electromagnetic acceleration [55].

Double coaxial electrodes were developed to remove the need for a discharge initiator, the inner coaxial electrodes were at a very close distance to each other and so the dielectric between them would break down at a relatively low voltage. The small plasma produced would then be used to connect the circuit loop with the outer electrode. This design was eventually developed into the AFRL FalconSat 3 Busek MPAC thruster, see Figure 2.7.

In 2007 the University of Southampton used double parallel plate electrodes which were initially developed to accelerate late time eroded material, see Figure 2.11. After the electromagnetic acceleration stage of the initial wave of charged ions, neutrally charged atoms or large (and hence relatively slow) macroparticles were ejected from the discharge chamber at a slower velocity. The second set of electrodes which were downstream from the first set were designed to accelerate the slower particles by injecting them with a burst of energy from a second capacitor. The results presented showed interesting trends, although the second electrodes are at a much lower voltage (3.75V to 300V) than the first set of electrodes (1kV to 2kV), significant current signals were recorded running through the second electrodes. This would suggest that as the late time eroded material traverses through the secondary electrodes it creates a current path for the second capacitor to discharge through. It is unclear though whether this secondary discharge accelerates the late time eroded material or if once the current begins to flow another effect comes into play (i.e. the high current passing through the electrodes, erodes and ejects new mass that is formed into a plasma and is accelerated) [3].

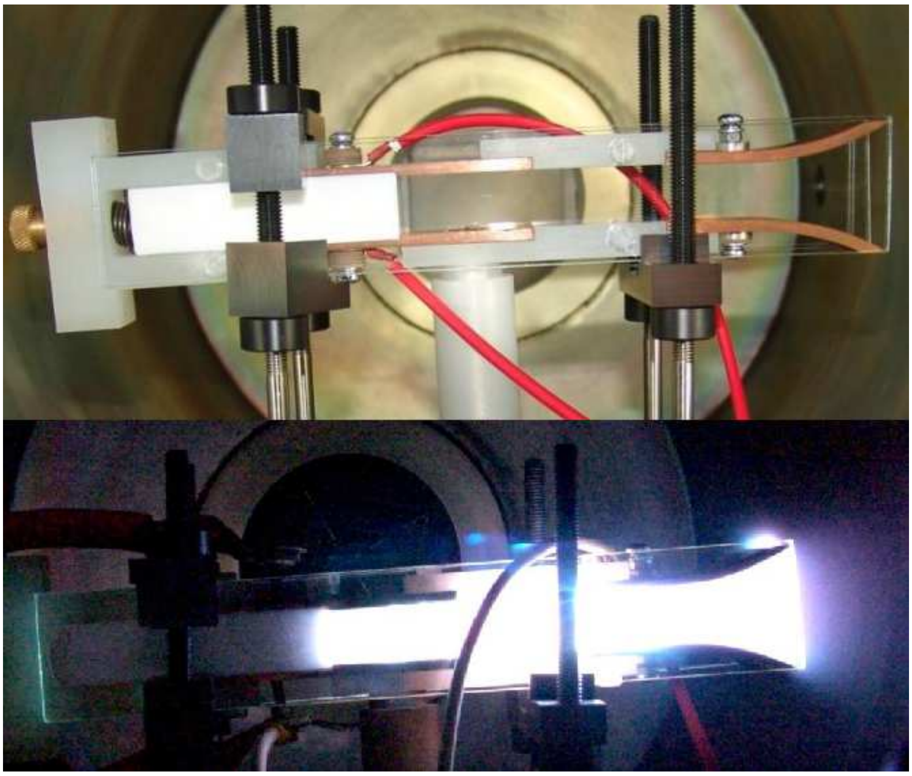

Figure 2.11: The double parallel plate electrode setup [3]

The inclusion of additional electrodes has shown peripheral benefits but it is the shape and dimensions of the electrodes in respect to each other which has yielded benefits to the performance of the thruster. In 2000 Princeton University and University of Michigan worked on a Z-pinch PPT, see Figure 2.12, instead of using the Lorentz force directly to accelerate the plasma sheet, plasma is directed into the central core of the thruster and pinched. The orifice in the cathode allows for plasma to be ejected axially and comparable speeds to the initial pinching speed are obtained. The design lead to thruster performance characteristics comparable with conventional PPTs [4].

NASA Glenn research centre performed a matrix study in 2002 of a parallel plate electrode PPT changing several variables including the capacitance, discharge energy, electrode separation and propellant composition. The preliminary study showed trends indicating that the geometry of the electrodes had a significant impact on the impulse bit. Maximising the ratio between the electrode separation distance to the electrode width had the highest impact [25]. Research continued at NASA Glenn, in 2005, with experiments looking at high energy PPTs that would discharge between 50J to 700J. The PPTs tested in this regime obtained a maximum thrust efficiency of 36.4% and a maximum specific impulse of 3940s. A reduction of the transmission line inductance by a factor of six did not increase the efficiency of the system significantly and the biggest change in performance was when the width of the electrodes was reduced [56].

In 2007 the Institut für Raumfahrtsysteme at the University of Stuttgart varied several aspects of

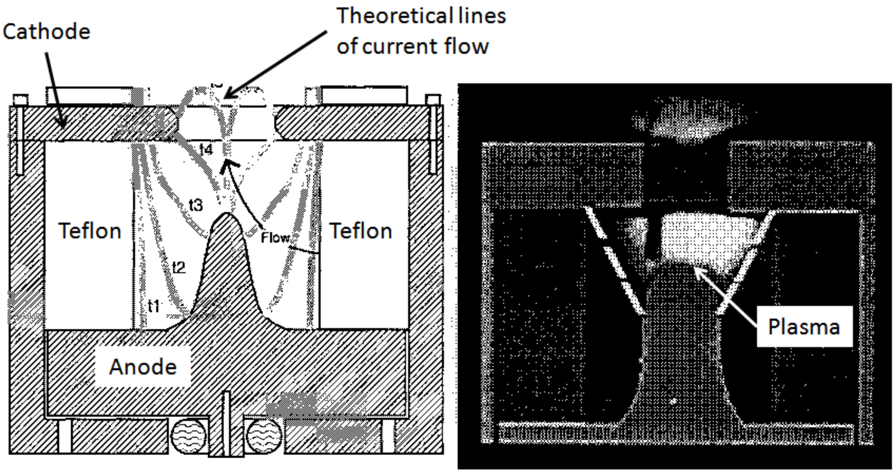

Figure 2.12: Left: Schematic for the AZPPT2 thruster, Right: High speed photography of the discharge with a 590nm filter [4]

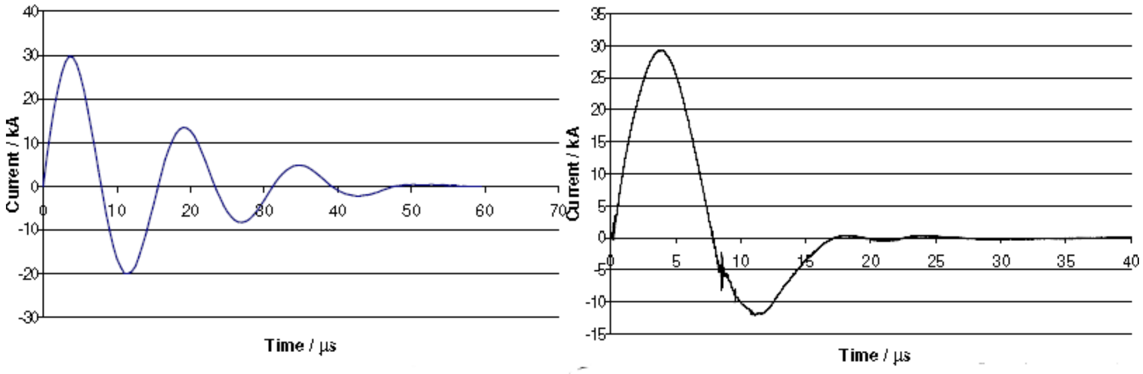

Figure 2.13: Current discharge profiles of the SIMP-LEX PPT with an electrode width of, Left: 50mm and Right: 40mm [5]

the PPT including the capacitor voltage, the electrode width, the electrode separation and the shape of the electrodes. The PPT was compared by measuring the mass lost from the Teflon^{TM} per discharge, the impulsebit and the exhaust velocity. It was found that as the electrode separation increased the mass bit and the impulsebit increased but the exhaust velocity decreased. When decreasing the width of the electrodes an optimum was found and by using flared electrodes it had the effect of increasing the impulsebit and the exhaust velocity [57]. Figure 2.13 shows an example of how the discharging current profile changed when the electrode width was reduced by 10 mm for the SIMP-LEX PPT.

The Austrian Research Centre (ARC) in 2008 developed a miniaturised parallel plate PPT with a 31μF capacitor discharging at 8J. Experiments undertaken altered the electrode width between 7.5-10mm and the electrode separation between 5-15mm. It was shown that there was a correlation between the aspect ratio and impulse bit, see Figure 2.14. The results showed that as the aspect ratio was increased from 0.6 to 2.1 the impulse bit increased linearly from 30μNs to 70 μNs. It was also shown that increasing the aspect ratio by decreasing the width at high energies (8J) had a negative impact but at lower energies (4.7J) had a slightly positive impact, whilst at all energies increasing the aspect ratio by increasing the

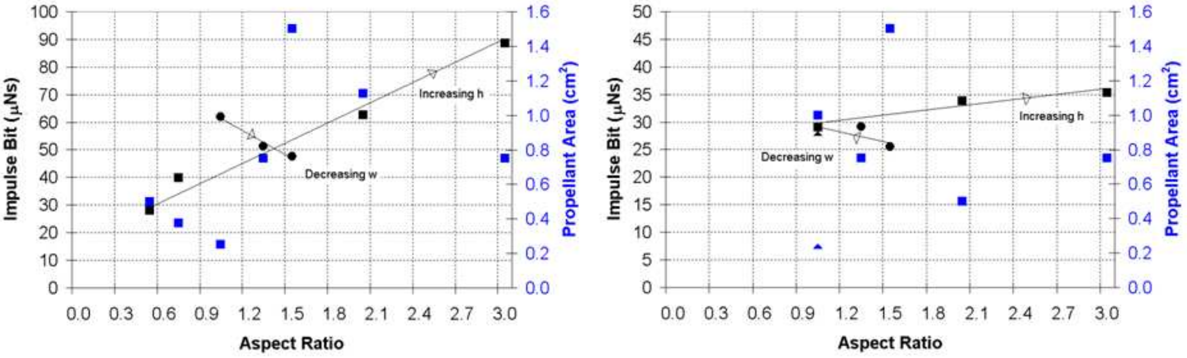

Figure 2.14: The dependence of the impulse bit on the aspect ratio of the electrodes for a Left: 8J discharge and Right: 4.7J discharge. Note the directions of the arrow on the trend line which shows how the decreasing/increasing of the specific dimension has affected the results [6]

Table 2.2: Results of the electrode erosion material study performed by Fairchild Industries. Cathode material is copper [35]

Anode Material	**Anode Erosion per discharge μg**	**Cathode Erosion per discharge μg**
Copper	11.99	4.36
Graphite	4.59	3.17
Thoriated Tungsten	40.25	4.10
Tantalum	27.72	1.76
Tungsten coated copper	15.16	1.55
Molybdenium	16.93	3.48
25% Copper 75% Tungsten	27.81	3.86
Platinum	22.79	1.18

electrode separation had a positive impact on increasing the impulse bit. The conclusion drawn was that the inductance gradient of the electrodes had a significant role in optimising the impulse bit [6].

Another area of the discharge chamber that was studied was the erosion rate of the electrode materials. Fairchild Industries in 1979 studied the erosion rate of electrodes in detail after performing endurance tests on their millipound PPT and finding that the sparkplug ignitor and the process of electrode erosion were life limiting factors of the thruster. A study was performed were a selection of materials were used for the anode but the cathode remained as copper. The PPT was discharged for around 100,000 pulses and the total electrode mass loss was measured and than averaged to give a mass loss per discharge. The most significant result was that the mass loss per discharge varied dependent on the anode material, see Table 2.2 [35].

Fairchild Industries also conducted a configuration study and noticed that as the length of the parallel plate electrodes was increased the overall electrode erosion per discharge decreased, see Table 2.3. It was noted that at the longest length (17.3 cm) no particulate or crater formation was observed on the electrode surface under an electron scanning microscope [35].

In developing a PPT for μLabSat II in 2002 the Tokyo Metropolitan Institute of Technology, the

Table 2.3: Results of the electrode erosion configuration study performed by Fairchild Industries. Cathode material is copper [35]

Electrode Length cm	**Erosion per discharge μg**
7.0	12.00
14.7	1.90
17.3	0.76

Table 2.4: Lifetime tests for the μLabSat 2 PPT after 500,000 pulses [36]

	Molybdenum	**Brass**	
Energy,J	3.59	3.59	2.37
Specific Impulse, s	1127	1149	927
Impulse Bit, μNs	29.6	28.04	16.5
Teflon^{TM} Erosion, μg per shot	2.6	2.49	1.78
Cathode Erosion, μg per shot	0.029	0.252	0.155
Anode Erosion, μg per shot	0.149	0.195	0.112

Astro Research Corporation and the National Space Development Agency of Japan did lifetime tests for a low power parallel plate PPT with an electrode separation on the order of 10mm. A total of 500,000 pulses were discharged through a 1μF capacitor at 2.37J and 3.59J for Brass and Molybdenum electrodes. Table 2.4 shows that at the same discharge energy the performance with the two different electrode materials is comparable. The results for the brass electrodes also show that the performance and errosion also scale proportionally with total energy. A point to stress is that in the low energy regime when Teflon^{TM} is present, material selection for the electrodes does not affect the performance of the PPT [36].

The University of Illinois at Urban-Champaign in 2003, developed a coaxial PPT in which they studied the anode electrode material and geometry. The geometry of the anode tip was shown to have an impact on the anode mass loss as it varied between 0.042 - 0.261 μgJ^{-1}. The optimal design was a truncated cone. Truncated tip anodes made from Elkonite (90% W and 10% Cu), Pure Tungsten and Glidcop (98.9% Cu 0.6% Al with trace Fe and Pb) were experimented on. It was shown that Elkonite had the highest erosion rate 0.41 μgJ^{-1} and that Tungsten had the lowest 0.12 μgJ^{-1} [58].

The discharge chamber has been shown to be affected by external devices. In 1978 research at the University of Tokyo was conducted by applying an external magnetic field to the parallel plate PPT by using a solenoid which could achieve a maximum magnetic field of 0.6 Tesla. The research showed that if the applied magnetic field was in the same axis as the self created magnetic field around the electrodes and when the magnetic field was increased, the maximum impulse bit also increased but eventually plateaued. The increase in impulse bit due to the applied magnetic field was significant and was shown to double for a magnetic field of 0.6T [59].

Discharge Initiator Development

The discharge initiator is the device that causes in some fashion the introduction of charged particles into the discharge chamber. This acts to augment the electric field to an extent that a breakdown between the electrodes occur. Commonly this role has been fullfilled by a sparkplug in a PPT, however other forms of discharge initiation have been developed for the thruster. Early plasma film deposition machines used contact trigger electrodes, a cathode and high voltage anode which would mechanically be brought together. The current would flow through the connection. When the electrodes were parted current would try to continue to flow causing a spark to be generated. The spark introduced a burst of charged particles which would ignite a gaseous propellant and initiate the plasma. Issues involving cold welding and mechanical fatigue meant that this option for a PPT was not developed [24].

The mass and volume for the power unit of a PPT only becomes significant when the satellite is less than 100kg. All flown PPTs have been on satellites above this mass limit. This has led to the more convenient option of using a sparkpulg to initiate the plasma discharge as it was fairly compact and a well established proven COTS component within the automotive industry. The lifelimiting factor of the sparkplug was studied at NASA in 2004. Using a breadboard PPT developed for the EO-1 PPT the sparkplug accumulated a total of 38 million pulses. Although the PPU and energy storage unit (mica foil capacitor) performed satisfactorily, the sparkplug used failed consistently between 1-4 million pulses. This was due to fluorocarbons (soot) from the Teflon^{TM} forming on the surface of the sparkplug and so it would need to be regularly cleaned. The cleaning process also showed that the outer nickel electrode was being significantly eroded away and so developments into electrodes with both inner and outer electrodes made from iridium were researched and developed [49].

Laboratory PPTs have shown possible alternative methods to initiate a discharge. In 2002, the Electric Propulsion and Plasma Dynamics Lab (EPPDyL) experimented with an Infra Red (IR) laser pulse system to promote thermionic emission from the electrode surface. Results from their initial tests showed that initiation using this laser was caused not by thermionic emission but by water desorption from the electrode surfaces [60]. In 2003 an improved setup with a Nd:YAG laser with a fundamental wavelength of 1064mm using a Gas Fed Pulsed Plasma Thruster (GFPPT) with Argon propellant at 2torr was used. Tungsten foil was inset onto the copper cathode and heated by the laser that had a 1cm spot diameter and pulsed at 10Hz with energies up to 200mJ. The heated Tungsten was thought to emit thermionic electrons and cause a Townsend avalanche within the Argon gas and initiate a discharge. At the conditions used it was shown by experiment and theory that the current density required to initiate a discharge was 10^{-7} to 10^{-8} Am^{-2}. It was suggested that electrons injected at the cathode, drift towards the anode, creating a wake of ions. The electrons then exit the discharge gap and leave the ions behind. The resulting space charge augments the electric field already present and makes ionisation more likely, to the point where a breakdown occurs. However it was not concluded whether the electrons came from

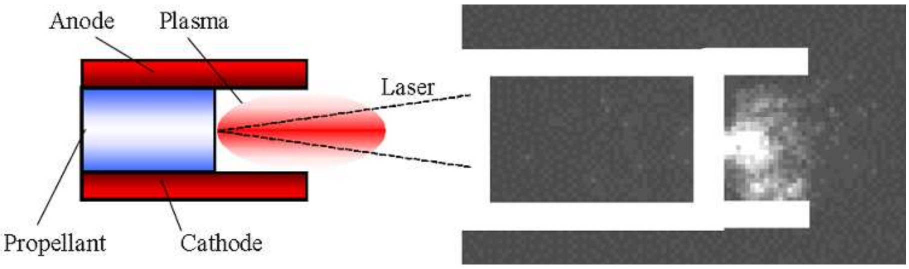

Figure 2.15: Laser initiated discharge with a pulse energy of 220mJ. Left: Experimental schematic Right: A 10ns exposure ICCD image taken at 500ns after the laser is pulsed, showing the PPT about to breakdown and initiate [7]

a thermionic emmision or some other effect (i.e. field effect electron emission) [61].

In 2003 the Tokai University also performed PPT initiation tests with a Nd:YAG laser with a fundamental wavelength of 1064mm with a fixed pulse energy of 220mJ per pulse and with a pulse width of 10ns, see Figure 2.15. Low discharge voltages between 20V to 100V were successfully discharged with comparable peak currents of up to 80A for a rectangular parallel plate PPT with an electrode separation of 3mm with an alumina propellant (rather than the standard Teflon^{TM}) [7].

Propellant Development

Due to the close nature between the propellant and the plasma discharge this part of the review has been split into two parts. Research involved with understanding how the mass is utilised in the plasma discharge phase is reviewed in the next section. Research involved with the development of the propellant or after discharge issues are reviewed here.

The plasma produced in the discharge requires mass. This has been percieved to be attributed to the propellant that is introduced into the discharge chamber. All flown PPTs have used Teflon^{TM} as a source of propellant, this has been due to both tradition and that Teflon^{TM} is an inert substance that has little outgassing properties in a vacuum. As the PPT discharges the Teflon^{TM} is eroded away in a non-uniform fashion which creates a sterotypical indentation of the Teflon^{TM} surface, see Figure 2.16. This in turn is due to the distribution of the plasma bulk which is non uniformly distributed across the entire discharge chamber. The bulk of the plasma is found closer to the cathode and coincides in the location where the greatest errosion of the Teflon^{TM} occurs.

In 2002 a laboratory PPT at the Ohio State University was developed to overcome this non-uniform mass errosion issue. A hybrid liquid/solid system was constructed with the idea that water would uniformly diffuse through the propellant, see Figure 2.17. It was theorised that the energy and current flowed through the Teflon^{TM} during the initial stages of the discharge and due to some form of propellant interaction more energy was ‘dumped’ in the initial stages of this process and so more erosion was seen at the cathode. The introduction of water was to provide a path of lesser resistance and so the energy could be distributed over the whole propellant surface. Water was held in a resevoir behind the Teflon^{TM}

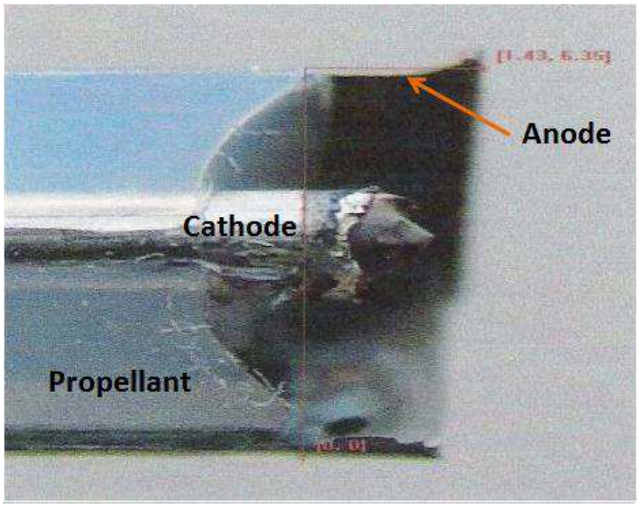

Figure 2.16: The errosion seen on the AFRL coaxial PPT after being repitively discharged at 6J.

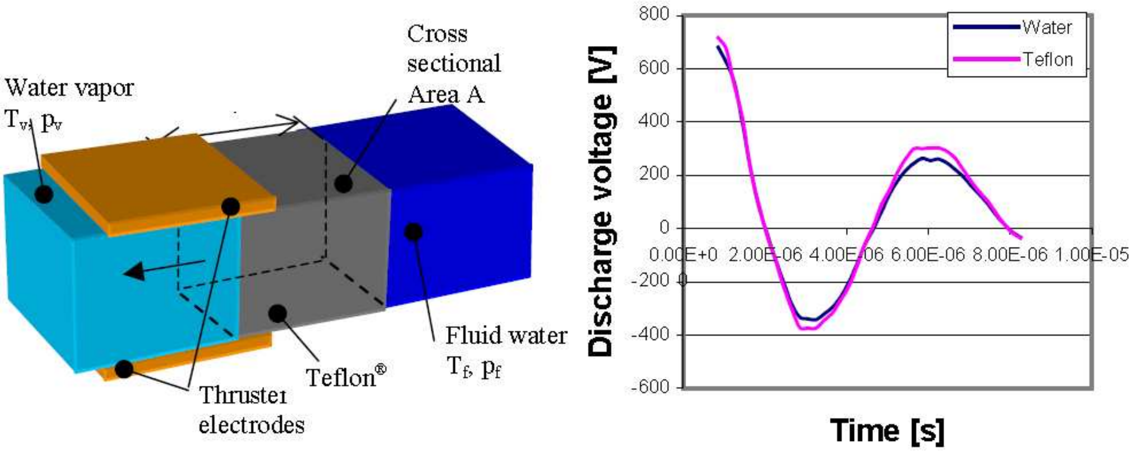

Figure 2.17: The hybrid Liquid/Teflon^{TM} PPT. Right: Concept schematic, Left: Voltage discarge profiles comparing a discharge with the hybrid experiment and a discharge with just Teflon^{TM} present [8]

and was allowed to diffuse through the material. The rate of diffusion was controlled by the contact area between the water in the resevoir held at 1 atm pressure and the surface of the Teflon^{TM}. It was found that the flow rate of water through the Teflon^{TM} was 65 pgμs^{-1}. Long duration tests showed that the water was having an impact as stereotypical depressions in the Teflon^{TM} surface were missing, however when comparing the discharge voltage profile between a pure Teflon^{TM} and Teflon^{TM}/water hybrid propellant profile there was not a significant difference [8].

This research was followed by other labratory Liquid Propellant PPTs (LPPPT), but using liquid as the main propellant removing the traditional Teflon^{TM} altogether. In 2006 John Hoskins University Applied Physics Labratory developed a novel mini LPPPT that measured 25mm x 25mm x 13mm powered with a a 1.0μF at 700V capacitor and produced an impulse of 0.4 - 0.6 μNs [62].

The University of Tokyo, during 2003 - 2005, investigated a PPT with a liquid propellant system to overcome issues of 'carbon tracking'. Solid Teflon^{TM} is made from long carbon polymer chains and when

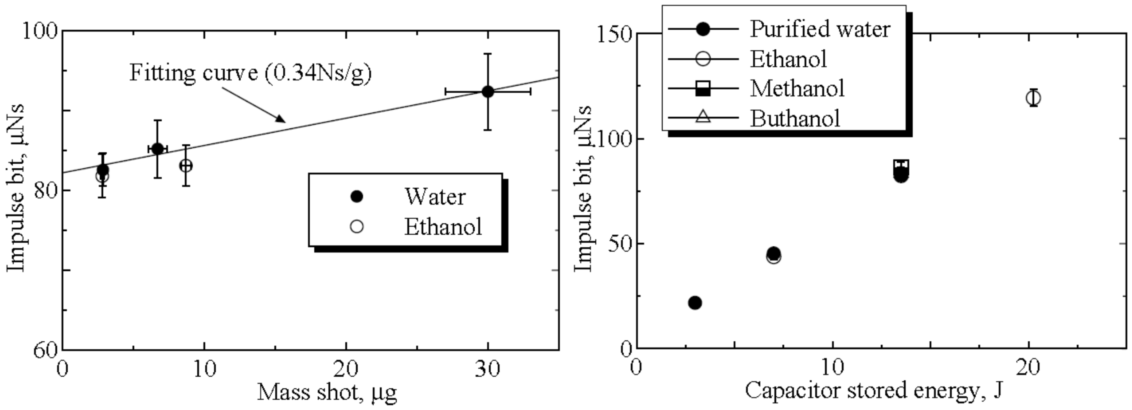

Figure 2.18: The University of Tokoyo LPPPT experimental results. Left: Impulse bit comparison with mass shot size of the water and ethanol propellant at a discharge energy of 14J. Right: Impulse bit comparison with discharge energy with a 3g mass shot of liquid propellant [9]

broken down in the discharge the carbon locked in these chains would coat the thruster housing. If the carbon built up it would create an electrical path between the electrodes which would cause tracking that would lead to the thruster failing (as the capacitor would fail to charge up between discharges). By using low carbon propellants (including purified water, methanol, ethanol and butanol) the idea was to extend the operating time of the thruster.

Despite the different compositions of the propellants used, all four liquids showed a linear relationship that all followed the same curve when investigating how the impulse bit varied with energy, see Figure 2.18. A similar trend was also shown with mass bit measurements. Inkjet technology was used to introduce fine mass bits of liquid (10μg) into the discharge chamber. The data shows that for this specific setup as the mass bit of the injected liquid was increased from 4 to 26μg the impulse bit of the system increases from 82 to 90μNs. Intrestingly the data shows a non-zero origin, so as the introduced mass is reduced to zero the impulse bit is around 82μNs. This non zero nature suggests an additional plasma production mechanism not related to the introduced mass bit is present. When the energy of the discharge is altered the impulse bit is also linerarly altered, see Figure 2.18. The results imply that the impulse bit generated from the discharge energy is independant of the composition of the propellant. This could be seen as contary to tests conducted with solid Teflon^{TM} which showed a linear dependance of mass errosion with discharge energy [9] [18] [63] [64].

The geometry of the Teflon^{TM} bar was studied in 1997 at NASA Lewis Research Centre where a simplified matrix study was undertaken. It was shown that there was relatively no difference in performance of the PPT between a nominal flat propellant bar and a notched propellant bar that had a greater surface area. Taken into context with the above Tokoyo research this would suggest that the exposed Teflon^{TM} surface area has little impact on the performance of the PPT [65].

Returning to solid propellant PPT's in 2003 AFRL, University of Michigan and the University of Illinois at Urbana-Champaign looked at carbon effects which occured on the AFRL coaxial μPPT.

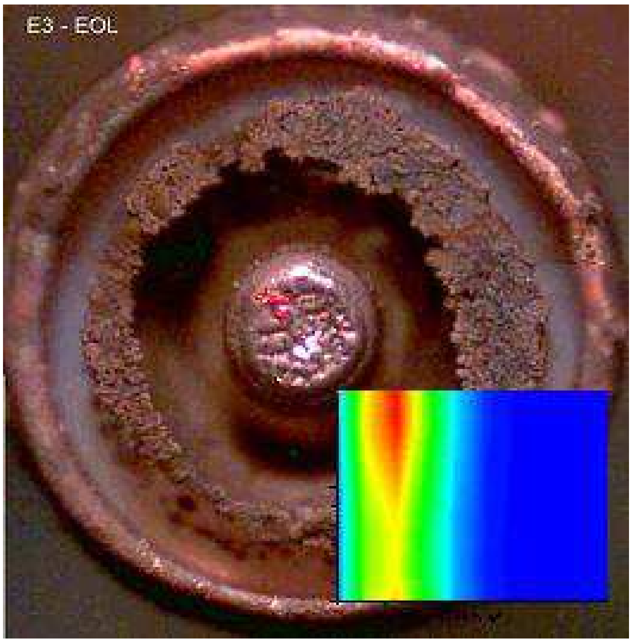

Figure 2.19: Teflon^{TM} surface photo and the Teflon^{TM} surface temperature field and the ablation rate in the case of a 3.6mm diameter micro-PPT [10]

Using an X-ray energy dispersive spectroscopy technique it was found that the charred areas contained mostly carbon deposits but had a significant portion of copper, flourine and silicone. The silicone was proposed to have come from the diffusion pump oil of the vacuum pump. The evidence suggested that the charred areas was due to the backflux of carbon particles returning from the plasma and impinging on the Teflon^{TM} surface. Comparing the observed electron microscope imagery with samples from the carbon deposition industry using DC electric arcs, the composition was very similar. This meant that the charred areas were not from incomplete decomposition of the Teflon^{TM} surface during the discarge but from the backflux of particles from the plasma. Two dimensional modelling also showed that there was a significant backflux of particles (around 10kms^{-1}) onto the surface during the discharge process and that there were areas of the Teflon^{TM} surface which had low surface tempertures. These areas also had low erosion rates and were also the areas which corresponded in the photography to the areas with the most charring, see Figure 2.19 [10] [66].

Temperature experiments of the propellant surface confirmed the modelled temperatures at AFRL. Drawing on heritage from the dynamic crack propogation community which used photovoltaic IR detectors, a HgCdTe detector was used to measure the temperature rise in a material in the microsecond timescale. The emmisitivity of the Teflon^{TM} was measured during a discharge and related to the surface temperature. It showed that the surface temperature oscillated between between 700K and 1000K as the current in the discharge oscillated. When the current reversed (i.e. crossed the zero axis) the surface temperature was 700K and as the current reached its maximum, the surface temperature reached 1000K [67].

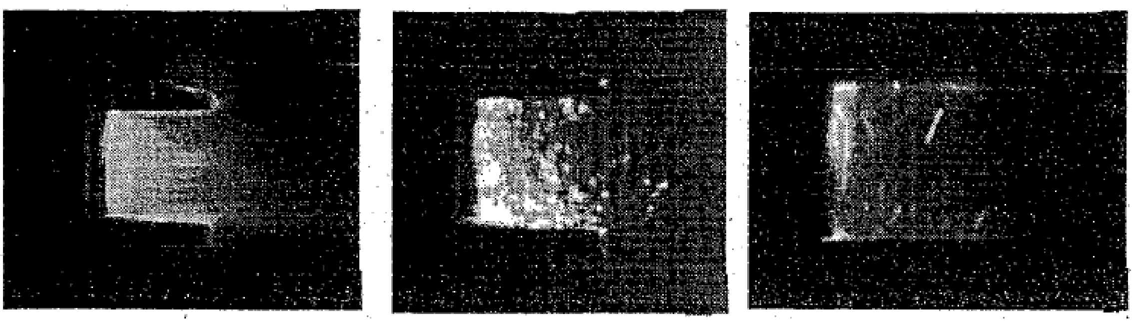

Figure 2.20: Broadband emission from the PPT exhaust, Left: 10μs shutter during the discharge, Middle: 10μs shutter initiated 100μs after the discharge, Right: 100μs initiated shutter 100μs after the discharge [11]

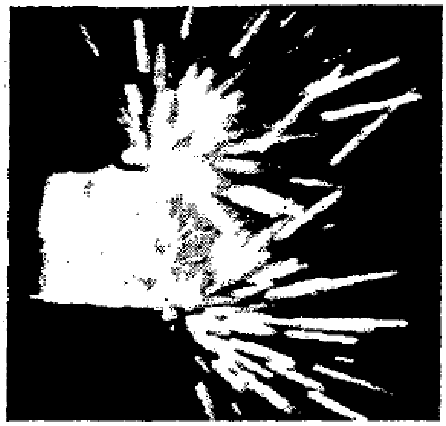

Figure 2.21: Emission at 200μs with a 100μs exposure time showing streaks indicative of particles with velocities of approximately 300 ms^{-1} [12]

During the discharge the propellant is heated. After the plasma discharge has been accelerated out of the discharge chamber, the excess heat is thought to breakdown and thermally expell neutral particles and large macro-particulates in a process reffered to as 'Late Time Ablation' (LTA). Hughes STX Corporation in partnership with the Air Force Phillips Laboratory in 1997 studied the interaction effects of macro-particulates associated with the LTA effect within a parallel plate PPT. Broadband light emission using a high-speed frame camera was used, however it was only able to take single frame images. The images showed, see Figure 2.20, that no particulates formed in the first 10μs. At 100μs after the initiation the image showed that a significant amount of macroparticles were formed. Streak photography, see Figure 2.21, inferred that the velocity of the macroparticles was approximately 300ms^{-1} and that they originated from the electrodes, prominantly at the end of the electrodes at the edge. Scanning electrode microscope images, taken of a target aluminium plate placed to capture particulates in the plume, show impact craters with large carbon deposits and a multitude of other deposits which is assumed to be particulates made from the erosion of the electrodes [11].

The University of Michigan in 2001 studied the interaction effects of macro-particulates. It was shown that particulates with a size less than 10μm decomposed in less than 10μs for a plasma with a density

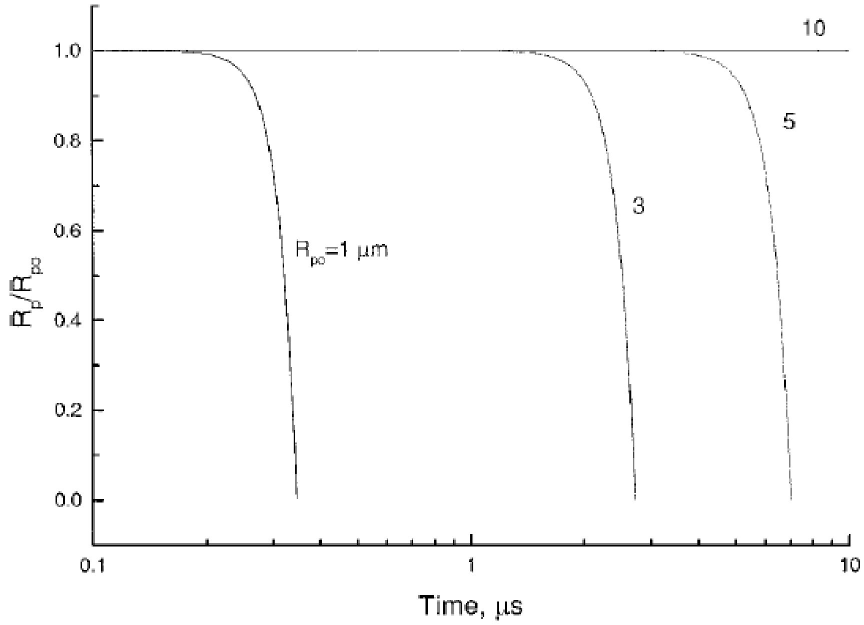

Figure 2.22: Macroparticulate radius vs time with the initial particulate radius as a parameter, T_e = 1.5 eV and $N_e = 10^{23}m^{-3}$ [13]

of $10^{23}m^{-3}$ and an electron temperature of 1.5eV, see Figure 2.22. This showed that the particulate mass distribution at the start of the discharge would differ to the mass distribution at the end of the discharge (i.e. the experimentally observed distribution of particulates will be different than those created in the initial discharge). It was calculated that for the plasma conditions described above that a 1μm particulate would have a velocity of around 230ms^{-1}. The forces acting on the particulates is a mixture of a drag force with neutral atoms and ions and an electric force due to the presence of an electric field in the current carrying plasma. Finally it was shown that only particulates with a dimension of less than 0.1μm in the above plasma conditions could be entrained in the plasma bulk whilst larger particulates are generally slower and flow substantially behind the plasma bulk [13].

An interesting observation made by the Propulsion Directorate OL-AC Phillips Labratory was when they used interferometery to measure the neutral and plasma density of the XPPT-1, see Figure 2.23. When the neutral and plasma densities were compared as a function of discharge energy for three seperate capacitances, it showed that at greater capacitances the densities of the two species became more comparable to each other and did not significantly diverge off from each other with increasing energy [12]. This would indicate an interesting link between the capacitance size and the production method of neutral particles created in the discharge.

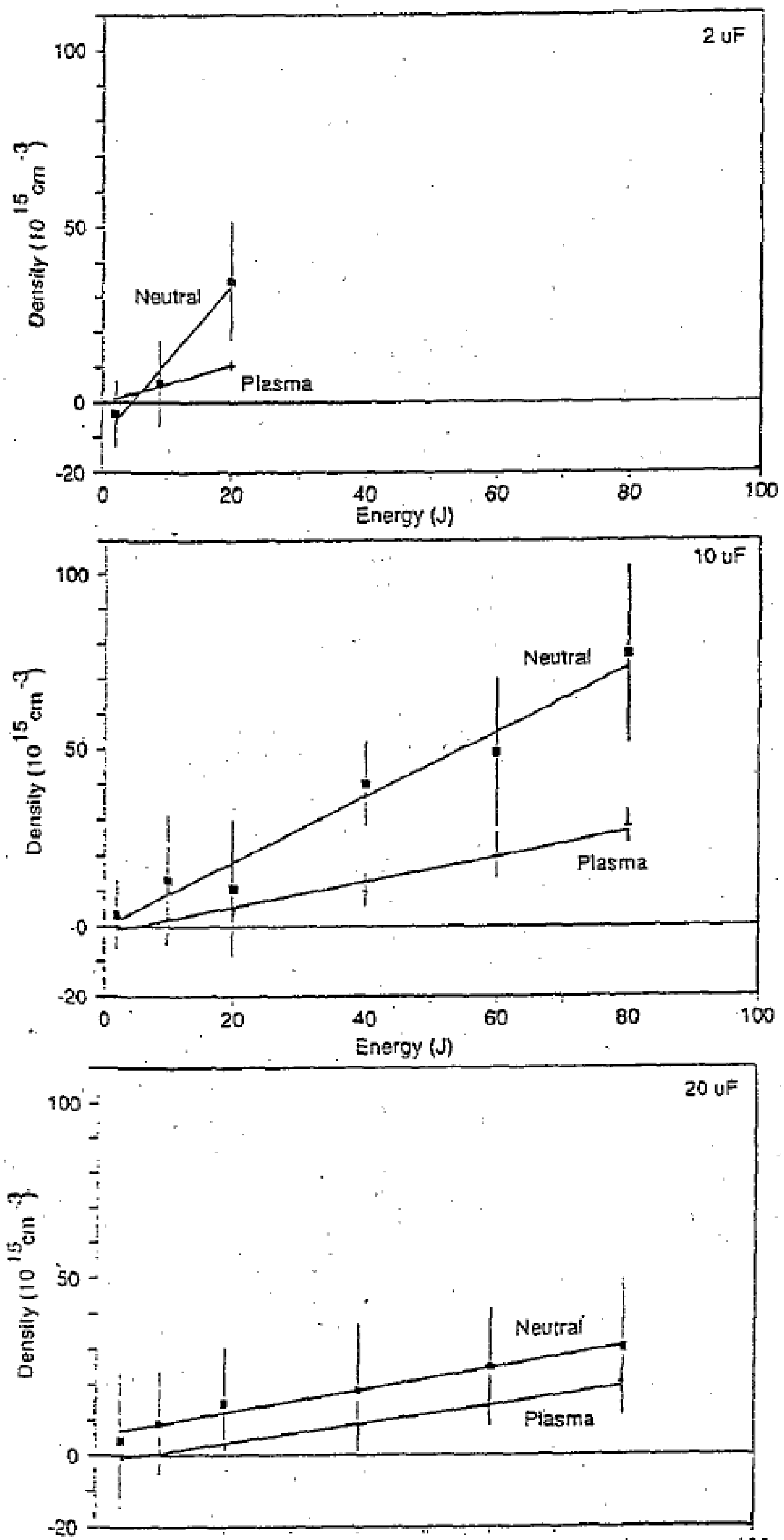

Figure 2.23: Neutral particle and plasma particle density dependance on energy, Top: 2μF, Middle: 10μF, Bottom: 20μF [12]

2.3.2 Fundamental Science Development

The simplicity in constructing a PPT is in contrast to the complexity in understanding the discharge process. The total discharge process occurs on the microsecond timescale but certain effects and formations occur on the nanosecond timescale. There are two periods to the discharge process: the first is when the plasma is in the discharge chamber and is being created and accelerated. The second is when the plasma is expelled from the chamber and forms a plasma plume.

In the first period intrusive measurements into the discharge chamber (i.e. Langmuir probes) can affect the discharge process itself and so a number of non-intrusive measurement techniques have been used to study this period. These include the rogowski coil, which is located around one of the capacitor terminals to measure the amount of current flowing between the discharge electrodes. Voltage probe data measure the potential difference between the capacitor terminals as it discharges. Magnetic field probes measure how the current sheet evolves with time. Laser interferometery measurements measure the electron density. Spectroscopic emission measurements study the light emissions from the plasma mass constituent parts and high speed photography to image the discharge process on the nanosecond time scale. High speed cameras with a 10ns gate time with a 10ns exposure time can cost up to 250 thousand pounds. High speed cameras have only been used for PPT research development since 1996 in a number of limited cases.

In the second period once the plasma has been expelled from the discharge chamber more intrusive measurement processes are used. The Retarding Field Energy Analyser (RFEA) uses a number of charged grids that can be used to detail the ion composition of the plasma plume. Triple and current-mode quadruple Langmuir probes measure the electron temperature, electron density and the ratio of ion speed to most probable thermal speed in the plasma plume. The RFEA and Langmuir probes can also act as a Time of Flight (ToF) probe measuring the speed of the fastest ions from the discharge chamber to the probe heads.

Using the aforementioned measurement techniques a number of interesting observations have been presented in the literature.

Within the Discharge Chamber

The Kurchatov institute in 2004 reported that ultraviolet radiation measurements (with wavelengths of approximately 160nm) showed that there was no time delay between the discharge current flowing between the electrodes via the discharge chamber and the appearance of ultraviolet radiation from the plasma near the propellant surface [14]. It has been thought that during the discharge the current flows through the Teflon^{TM} surface heating it up and subliming it into a gas. However this process would have some form of characteristic time delay between the current flowing, the Teflon^{TM} heating up and then the plasma forming, which is contrary to the results presented, see Figure 2.24.

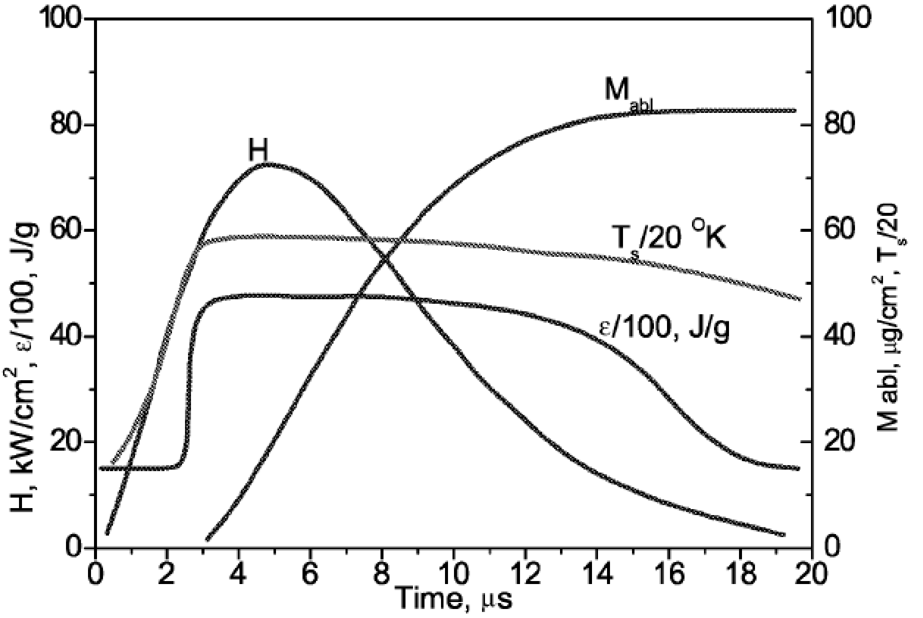

Figure 2.24: Time dependencies on the radiation flux density, H, maximum surface temperature of the Teflon^{TM}, T$_s$, eroded Teflon^{TM} mass, M$_{abl}$ and specific energy, ϵ, of the Kurchatov experimental 300J PPT [14]

Research at the Edwards Air Force Base using spectroscopic emission measurements of a discharging Teflon^{TM} propellant PPT (XPPT-1) showed that the intensity of the emissions for the species of C$_2$, C+, F and F+ spectra directly correlated to the intensity of the current discharging through the formed plasma, see Figure 2.25 [15]. This shows a direct correlation between the properties and characteristics of the forming plasma with the intensity of the current flowing through it.

The plasma propagation was investigated with an Argon GFPTT at Princeton University in 2003. Using a magnetic field probe sensor, measurements were taken at 432 different spatial locations around the discharge chamber. The results from the magnetic probes were manipulated to show the time evolving current sheet density of the first half period of the capacitor discharging (1-5 μs), see Figure 2.26. The structure of the current sheet shows a large canted bulk from the cathode towards the anode with the anode leading edge in front of the cathode leading edge with an area of increased current density attached to the cathode (seen most clearly at 2-3μs) [16]. This shows that the current density distribution within the leading plasma edge was not uniform both physically or in composition and that the current density when the discharge current was at its peak forms around the cathode structure.

Electron density measurements have also shown that processes occur around the cathode. In 2002 the Kurchatov Institute made measurements using laser interferometery on a 100J parallel plate PPT. A number of measurements were taken that plotted the maximum electron density in both spatial and time domains. It showed that for a current pulse that was underdamped but with almost no ringing (i.e. one wavelength when the amplitude of the first peak is much greater than the amplitude of the second peak) the maximum electron densities were located close to the Teflon^{TM} surface and interestingly at the end

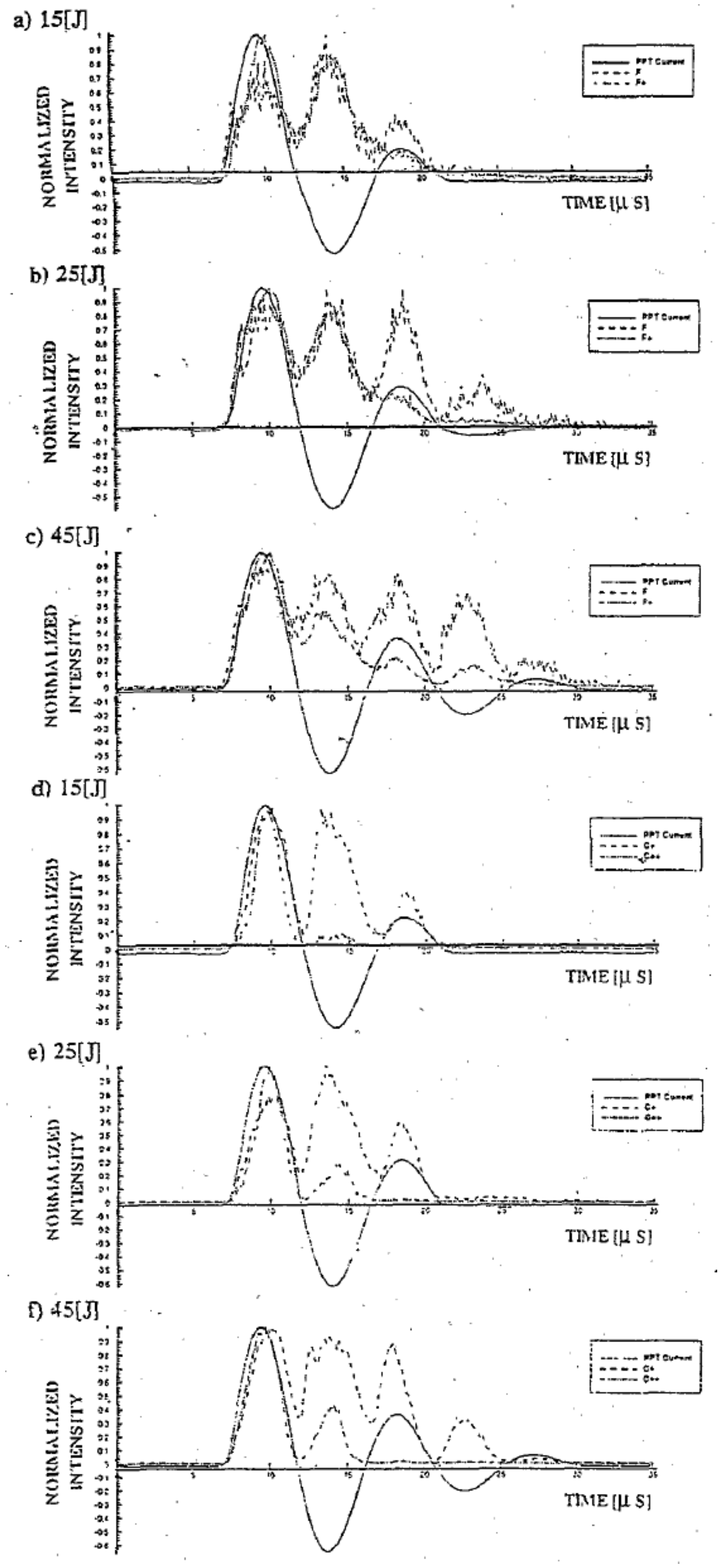

Figure 2.25: Normalised intensity of carbon and flourine atoms and ions compared to the discharging current profile with respect to time [15]

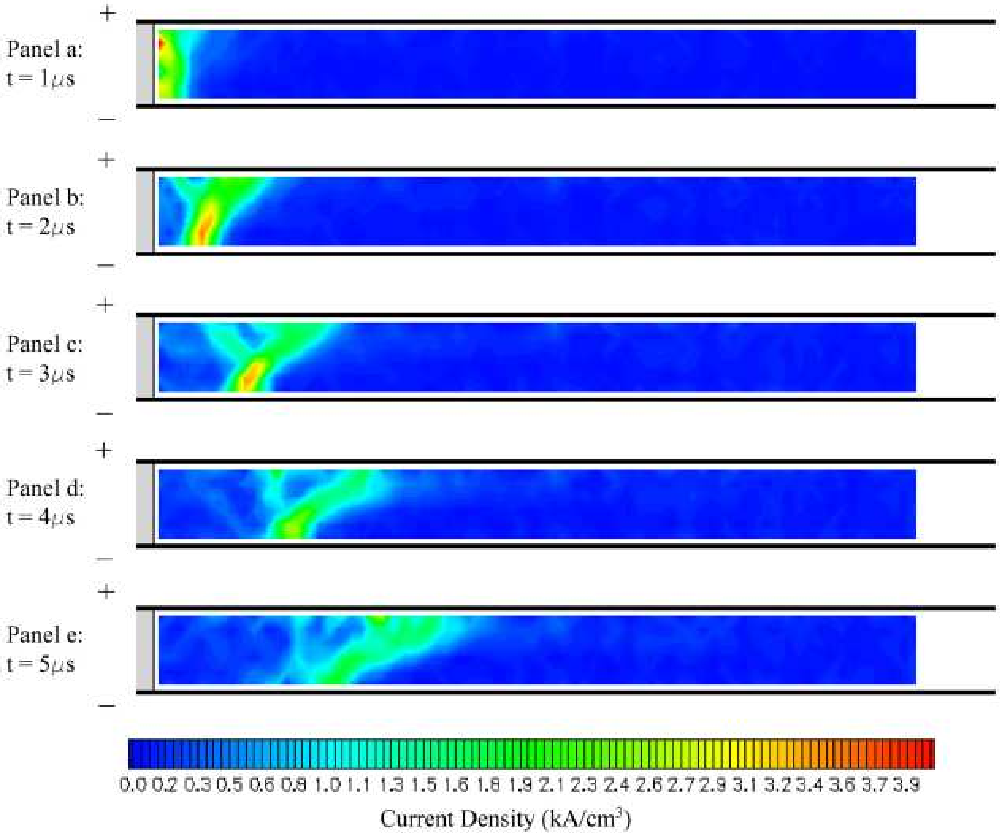

Figure 2.26: The current density profile mapping of the first half cycle of a PPT discharging [16]

of the PPT electrodes (where typical electrode charring formations are seen after long pulse duration tests), see Figure 2.27. The maximum electron density was non-uniform throughout the chamber in the x-axis spatial domain. This suggests that the mean ion charge (due to displaced electrons) is greater at the end of the electrodes and across the Teflon^{TM} surface than any other place in the PPT.

The y-axis spatial domain measurements in the plume of the PPT at a distance of 5cm from the end of the electrodes, see Figure 2.28, show that there is a maximum electron density in the centre of the PPT. The electron density is greater towards the cathode than it is towards the anode supporting the evidence that there is a process occurring near the cathode. Measurements performed in close proximity to the anode and cathode reaffirm this and it was reported that the maximum electron density at the cathode is twice as high as the maximum electron density at the anode [17].

Another observation was the occurrence of bright spots located on the electrodes when the PPT discharges. The Ohio State University in 2000 experimented on an inverse pinch coaxial pulsed plasma thruster. Using a Princeton Instruments (576S/RBE) ICCD camera detector with a 50ns minimum gating an image was taken to coincide with the peak current and it can be seen that the majority of the luminescence and bright spots are located on the central electrode and at the edge of the rim on the outer electrode where electric field gradients are at their highest, see Figure 2.29 [18].

In 2002 the Tokyo Metropolitan Institute of Technology studied the TMIT-PPT for the μ-Lab Sat II.

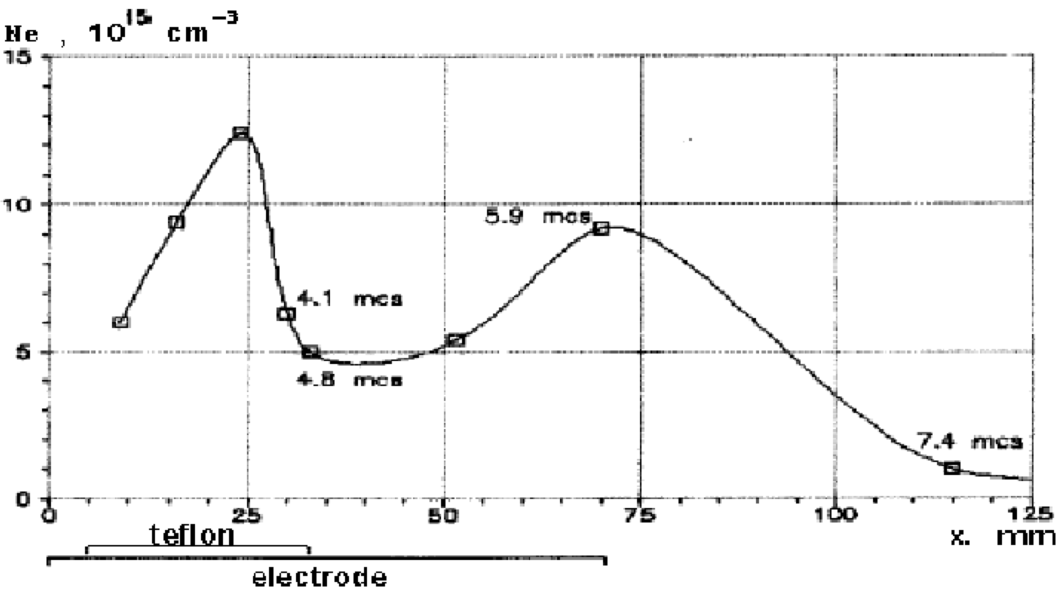

Figure 2.27: At a given distance the maximum electron density was found during the discharge process. This maximum electron density was than plotted against the dimensions of the discharge chamber [17]

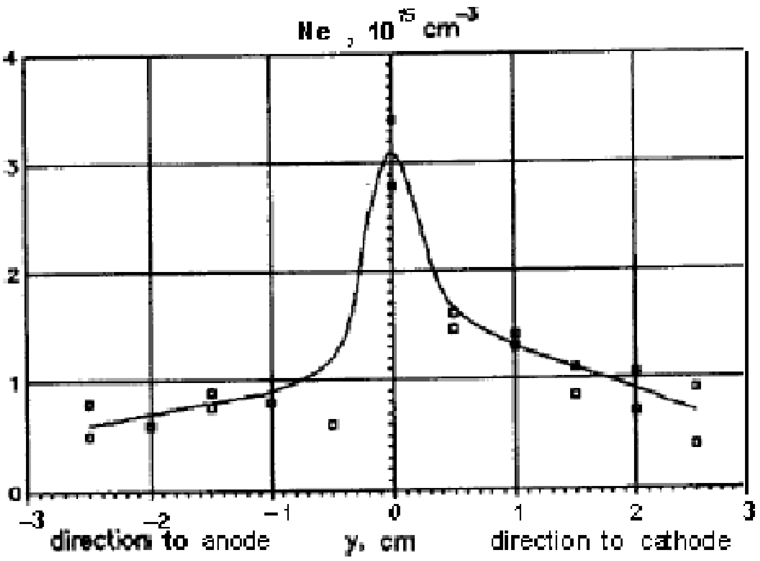

Figure 2.28: Distribution of maximum electron density across the plasma at a distance of 5cm from the PPT nozzle exit plane [17]

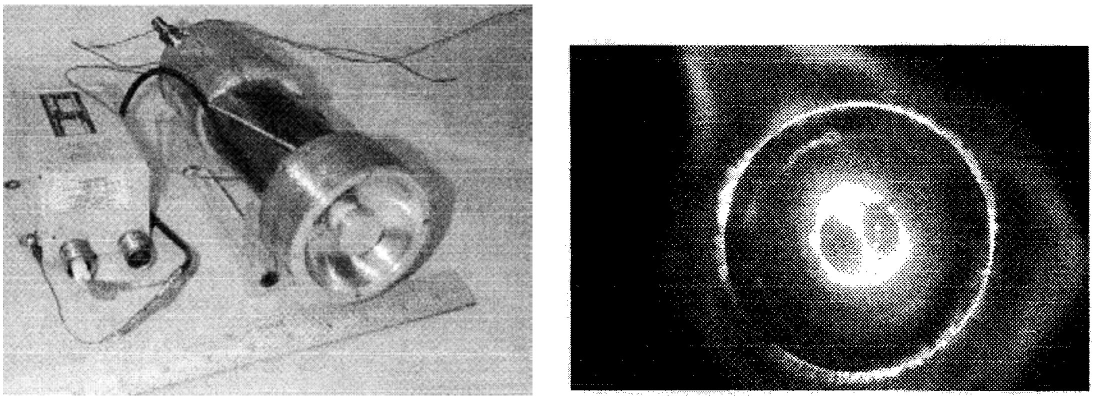

Figure 2.29: Right: Inverse pinch coaxial PPT, Left: Discharge image at peak current [18]

Part of the studies used an ULTRA 8 high speed camera from NAC Technology Inc that had a spectral response of 380nm-850nm and could take 8 images at 20ns intervals. The composite image is from two successive discharges with the first eight frames being from one discharge and the latter eight from the successive discharge. The broadband spectral images show several interesting features, see Figure 2.30. The images can be compared to the current discharge profile. Image 5 is when the current begins to flow, image 9 is at the peak of the first half cycle of the current discharge and image 14 is when the current is at zero and the polarity of the electrodes change. The images show that initially the current flows across the surface of the Teflon^{TM} (image 5) but by image 9 three distinct formations are present: a formation across the surface of the Teflon^{TM}, an arcing formation that forms on the cathode separate from the Teflon^{TM} and an arcing formation that originates from the point where the Teflon^{TM} and anode meet and travel diagonally to intersect with the cathode plasma stream. It is interesting to note that from images 9 to 13 one can see that where the two arcing formations meet and then intersect with the cathode, a formation of bright spots occur on the cathode on the far right. The luminosity of these formations is proportional to the current that flows through the plasma. The second half cycle of the current (aka the re-ignition) does not form on the surface of the Teflon^{TM}, instead the original plasma formation which originated on the Teflon^{TM} (in image 5) has continuously travelled almost in parallel to the Teflon^{TM} surface at a consistent rate. When the current reverses (note this also swaps the polarity of the electrodes) the new plasma formation occurs on the cathode (now bottom) and intersects where the original plasma formation is currently [19].

In 2007 the University of Stuttgart used a DiCam-2 highspeed camera with a shutter speed of 20ns that could detect wavelengths between 380nm to 900nm. The results from these photos were surprising, see Figure 2.31. The plasma is travelling right to left. The discharge showed two plasma sheets being accelerated out of the chamber. The first is between 3000 to 7900ns and the second is between 8200ns and 12700ns. The sheets had the characteristic canting and were located on the cathode (note that although the second sheet forms on the other electrode it is still the cathode as the voltage across the capacitor has reversed polarity at this point). The average plasma sheet velocity of these sheets were calculated and found to be between 20km^{-1} to 28km^{-1}. The trends found that as the electrode separation was increased the average plasma velocity decreased and that as the energy of the capacitor was decreased so did the average plasma velocity.

The images show in detail two structures: first, close examination of the photos show that bright spots occur on the electrode surface and that from these bright spots it appears that small but intense jets are formed, seen most clearly on the top electrode at 4800ns and 5100ns. Secondly the photos showed that although there was a bulk movement of plasma mass, over time it showed that the bulk plasma was not a defined structure and the fine patterns of light intensity would rapidly change from frame to frame. These images indicate that the plasma bulk is not steady and that rapid changes occur on the

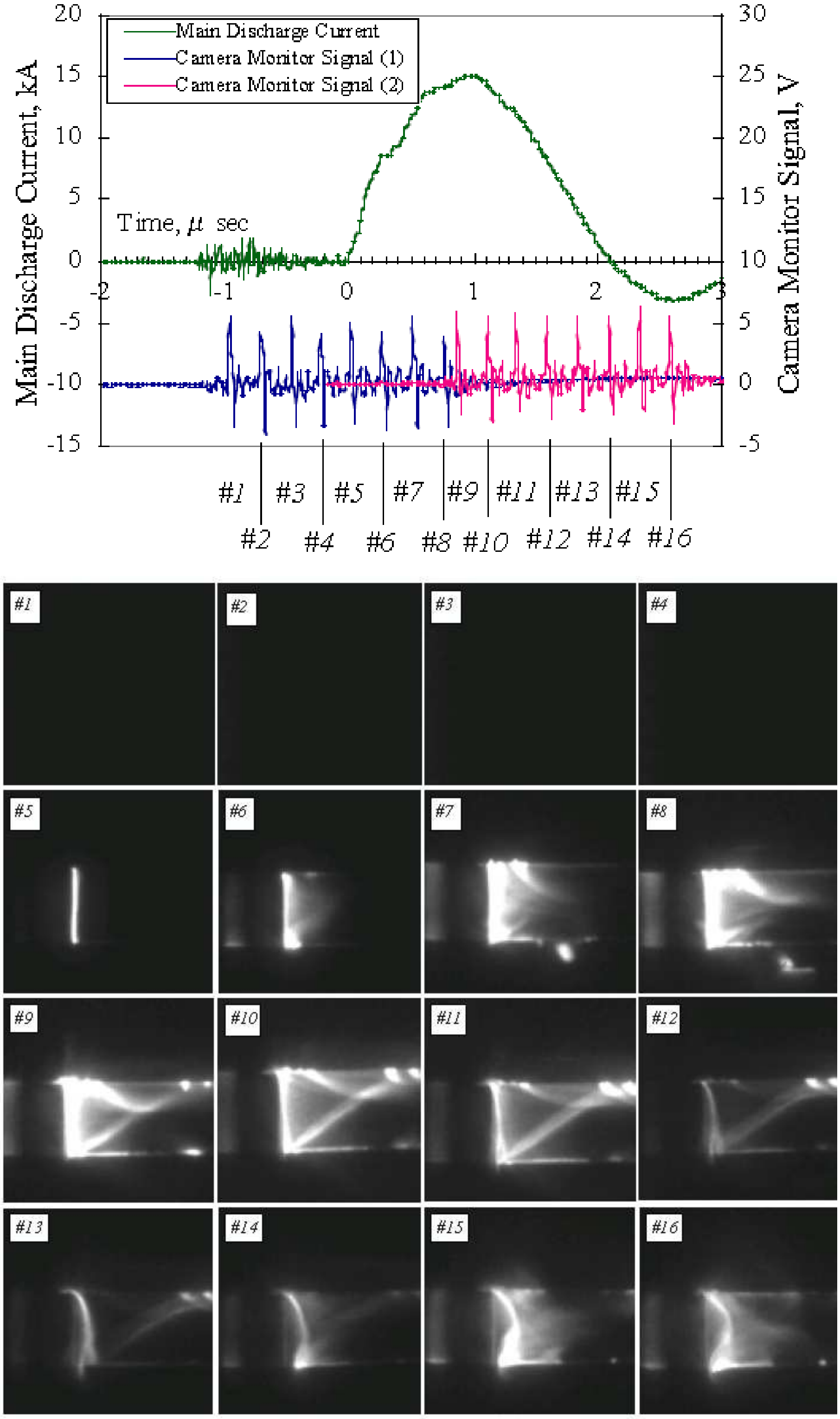

Figure 2.30: (Top:) The timing of the taken images in relation to the current discharge profile. (Bottom:) Broadband highspeed spectral imagery. The top electrode is initially the cathode [19]

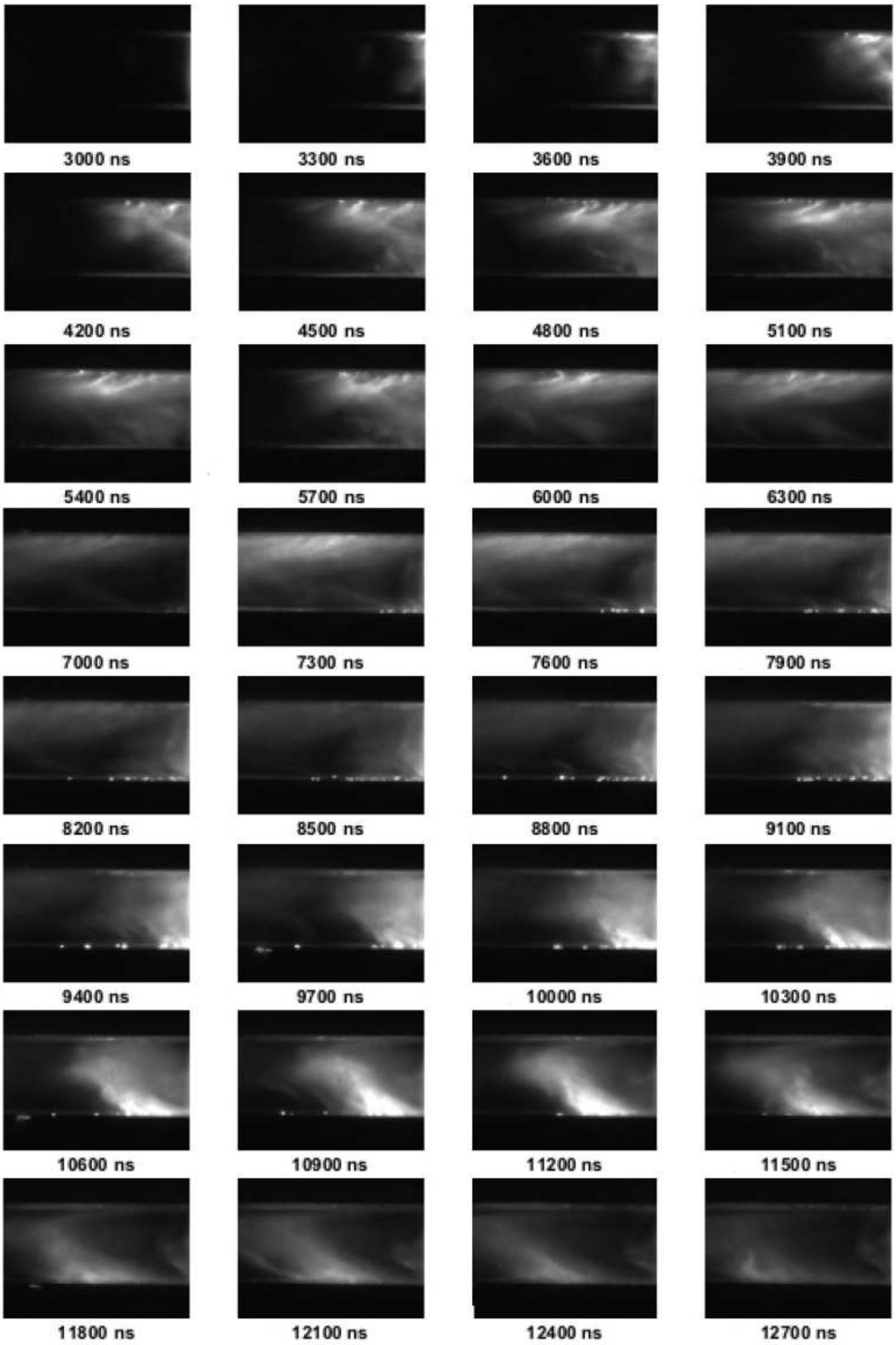

3000 ns
3300 ns
3600 ns
3900 ns
4200 ns
4500 ns
4800 ns
5100 ns
5400 ns
5700 ns
6000 ns
6300 ns
7000 ns
7300 ns
7600 ns
7900 ns
8200 ns
8500 ns
8800 ns
9100 ns
9400 ns
9700 ns
10000 ns
10300 ns
10600 ns
10900 ns
11200 ns
11500 ns
11800 ns
12100 ns
12400 ns
12700 ns

Figure 2.31: Plasma movement during the first current half cycle (3000-6300ns) and the second current half cycle (7000-12700ns) with an electrode separation distance of 36mm [20]

short scale (less than 20ns) [20].

In 2007 the Japanese Aerospace Exploration Agency and the University of Tokoyo performed filtered high speed photography at 514.5nm and 426.8nm which correspond to C_2 (neutrals) and C^+ (ions) emission lines. In parallel they also performed magnetic field profile mapping. Figure 2.32 is the evolution of the neutral particles and ions. From the images the neutral particle sheet was calculated to be moving at 1.8kms^{-1} and the ion particle sheet at a speed between 10-20kms^{-1}. The calculated speeds were consistent with other literature and similar to experiments. The real interesting point to note is the correlation between the second and third reignitions at 1.58μs and 3.15μs. The point of reignition looking at the ion filtered photographs corresponds with the location of the neutral particle sheet at 1.58μs and 3.15μs on the cathode electrode, noting that the electrodes switch polarity as the capacitor 'rings'. This indicates that the reignition process is affected by the propagating neutral particle layer. When the discharge reignites the neutral layer either acts as the path of least resistance for the new current path and in turn ionises some of the gas neutrals in that sheet or the gas neutral layer promotes some form of process at that location on the cathode surface that creates a new plasma sheet [21].

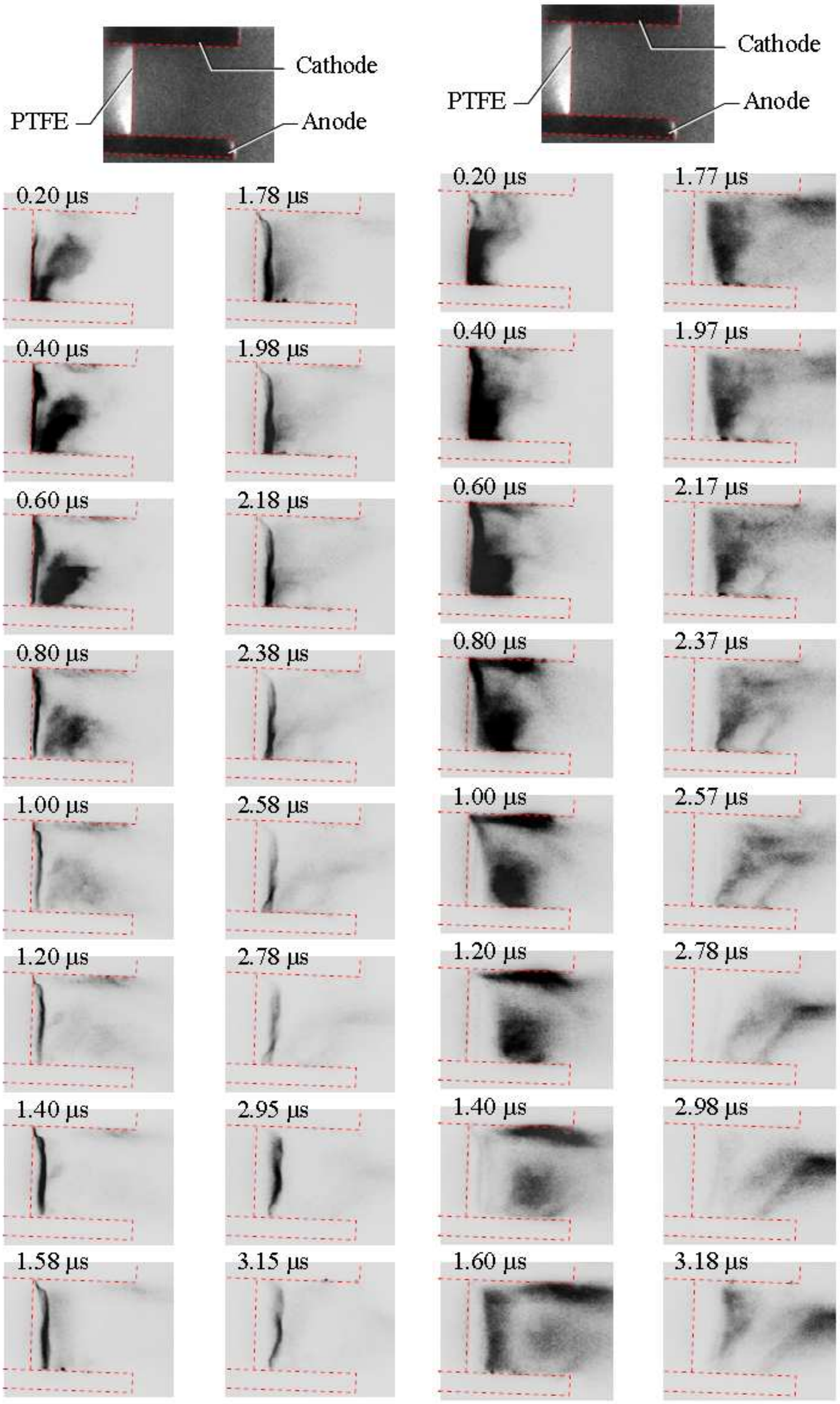

Figure 2.32: Successive images of the PPT firing with a Left: 514.5 nm filter corresponding to C_2, Right: 426.8 nm filter corresponding to C^+ [21]

Within the Plasma Plume

In 2000 NASA with Worcester Polytechnic Institute developed a triple Langmuir probe to measure the electron temperature, electron density and the ratio of ion speed to most probable thermal speed in the PPT plume. The results were plagued by serious noise contamination and so a smoothing routine was implemented to analyse the data. It is unclear how this affected the accuracy of the results [68]. Experiments showed that the electron temperature decreased the further downstream from the thruster and propellant face that the measurements were taken. However the results did show that there is a region of maximum temperature located towards the cathode side of the PPT [69].

Collaboration continued in 2002 with the development of a current-mode quadruple Langmuir probe. The experiments used a PPT based on the design of the EO-1 PPT, except that it used a capacitor with a 33μF capacitance. The current mode operation based on Laframboise current collection theory and thin sheath theory did not require voltage measurements within the noisy and fluctuating PPT plume, increasing the accuracy of the collected data. Peaks were observed in the electron temperature that had a characteristic delay due to time of flight effects but coincided with the current ringing of the discharging capacitor. The electron density of the plume sharply rose to a maximum of 10^{20-21}m^{-3} and decayed over the discharge period to 10^{19-20}m^{-3}. The electron temperatures ranged in excess of 10eV during the rise of the current pulse, but were typically less than 5eV for the rest of the pulse, see Figure 2.33 [22] [49].

In 2007 the University of Stuttgart and the University of Hamburg used triple current Langmuir probes to measure the electron density and temperature of a PPT plasma plume as the electrode separation distance was varied (21mm, 36mm and 46mm). The intrusive measurements were taken inside the main discharge channel at three locations along the horizontal axis. It was shown that as the electrode separation distance increased the electron temperature decreased but the electron density increased, see Figure 2.34. Using the same measurement points, Time of Flight (ToF) probes showed that the plasma velocity decreased as the electrode separation was increased [20].

A gridded RFEA can be used to distinguish the ion composition of the plasma plume and as a ToF probe to measure the speed of the fastest accelerated ions. The time between the discharge of the PPT and the probe detecting a signal can be used to determine the speed of the fastest ions to reach the probe. Studies on the Dawgstar PPT showed ion velocities between 55kms^{-1} to 105kms^{-1}. The RFEA also showed that high energy ions were being produced in the plasma plume. Figure 2.35 shows the current observed as the repelling grid voltage is increased. At 140V there is still a small amount of recorded current. It was reported that at even higher voltages (199V) there was still current being measured. This means that ions with a large mean ion charge state are being produced within the PPT discharge [23].

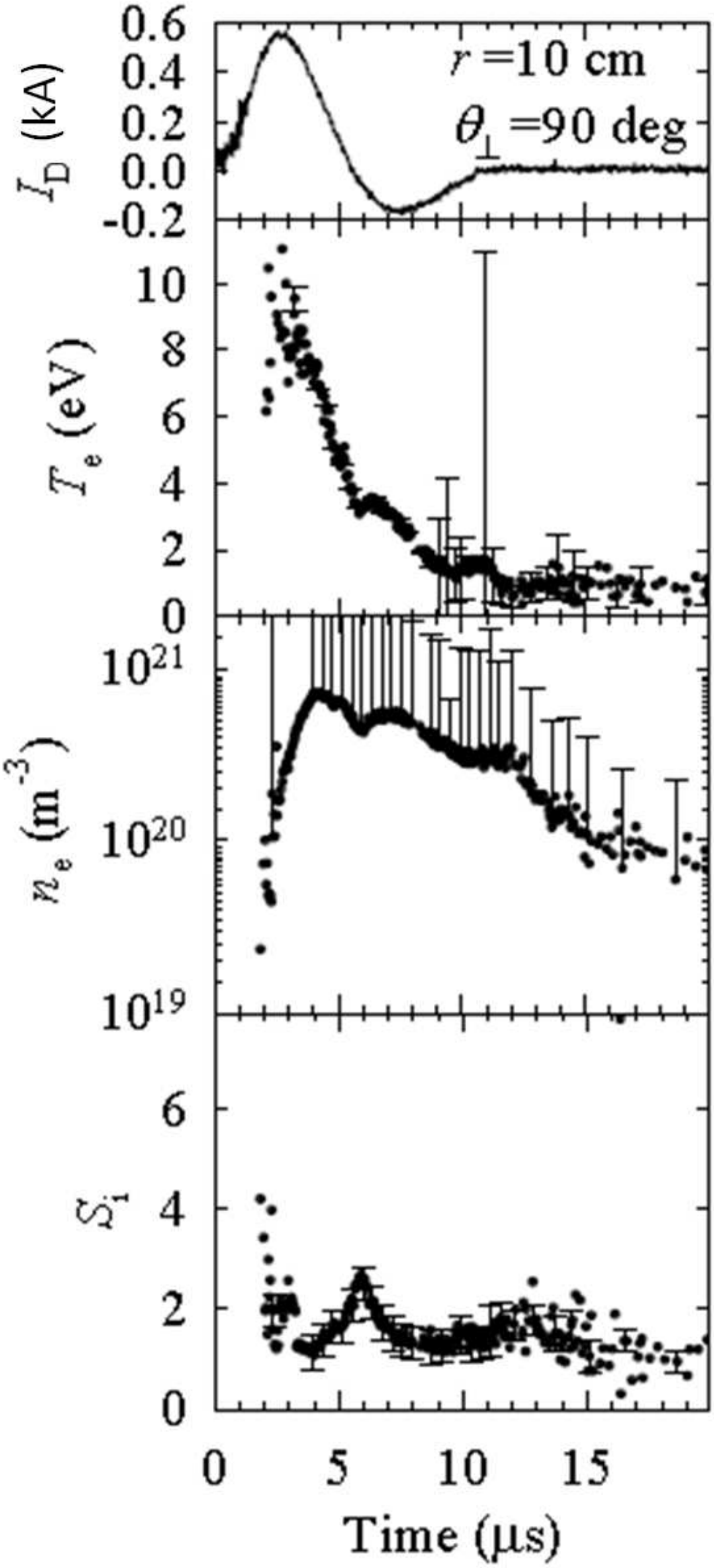

Figure 2.33: Discharge current, electron temperature, electron density and ion speed ratio from quadruple probe measurements taken on the perpendicular plane of a 20-J laboratory PPT plume at a distance of 10cm [22]

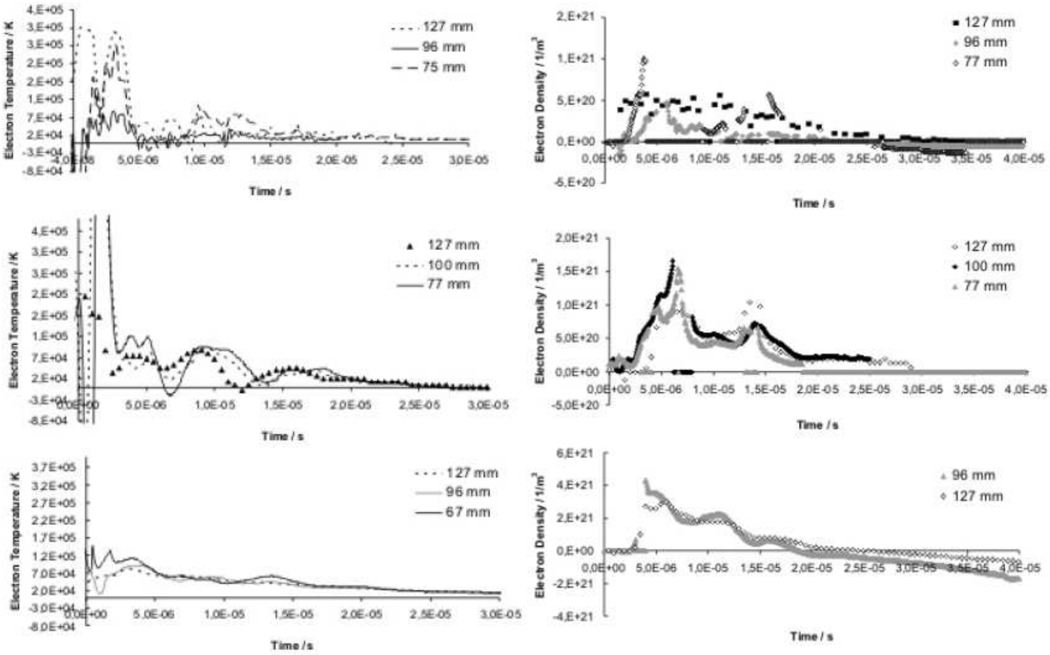

Figure 2.34: SIMP-LEX PPT triple probe results. Left: Electron temperature vs. time Right: Electron density vs. time. For 21mm, 36mm and 46mm electrode distance from top to bottom respectively [20]

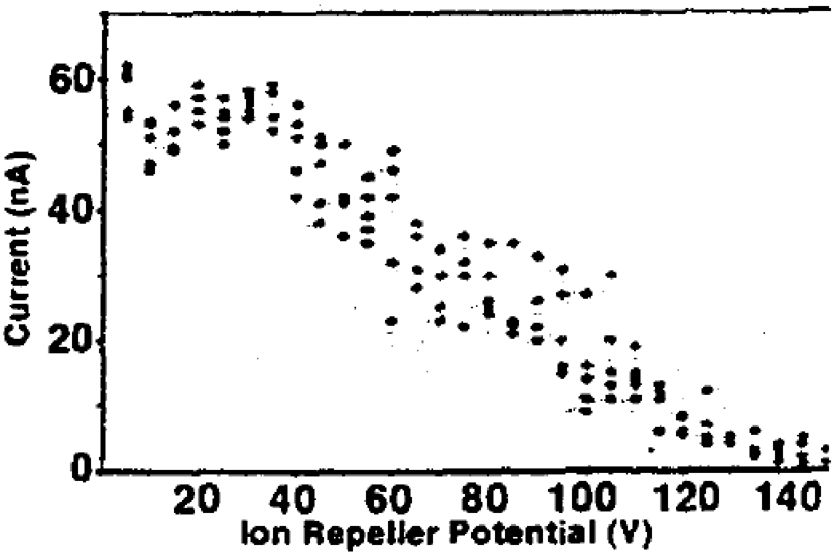

Figure 2.35: RFEA collection plate current as a function of the ion repelling grid voltage for an experimental PPT discharge [23]

2.4 The Pulsed Plasma Discharge Process

In summary we can draw upon the literature review to evaluate the current theory and processes that occur during a PPT discharge. The process is explained in terms of a nominal PPT with a capacitor as an energy storage device, the electrodes are in a parallel plate configuration where the electrode separation is larger than the electrode width, the electrodes have a Teflon^{TM} propellant bar in between them and that the discharge initiator is a sparkplug, see Figure 2.1. The process described below is for a single pulse of the total PPT discharge.

2.4.1 Pre-ignition

The process starts with a power unit supplying electrical energy to the capacitor. The capacitor is charged up over time until it saturates (which is a function of the capacitance and potential difference across the capacitor plates). The energy supplied to the capacitor over time (or power) dictates the speed that the capacitor charges up at and hence the frequency that the PPT can be discharged at. It does not, as long as the potential difference across the capacitor terminals before the discharge remain constant, affect the discharge properties (i.e. ISP, Impulse bit) of the PPT. The capacitor has a dielectric medium between its plates and as it is charged the dielectric molecules realign to the applied electric field which augments the capacitors surface charge. Once the plates are saturated the PPT is now ready to be discharged.

2.4.2 Ignition

A sparkplug is used to initiate a discharge between the main parallel electrodes. Exactly how this is achieved is under review. Two possible theories are plausible: the first is that current passes through the inner electrode of the sparkplug to the outer electrode of the sparkplug over (or through) the sparkplug ceramic material when it breaks down. The conducting path erodes the electrode and insulating ceramic material into a small formation of plasma. The plasma is introduced into the discharge chamber and augments the electric field creating a conducting path, into which the main discharge then occurs.

The second theory involves field emission. The energy required to release an electron from a metal surface is known as the work function, ϕ, and is the energy required to remove an electron from the Fermi level of an atom into the energy level of free electrons outside of the solid. When no electric fields are present the free electron energy level is constant and electrons require the energy equivalent to the work function to escape the solid. However in the presence of strong electric fields a potential barrier forms at the surface of the solid, see Figure 2.36.

If the electric field is strong enough and the potential barrier suitably thin then electrons can tunnel quantum mechanically through the barrier and escape into the vacuum. The electrons being emitted

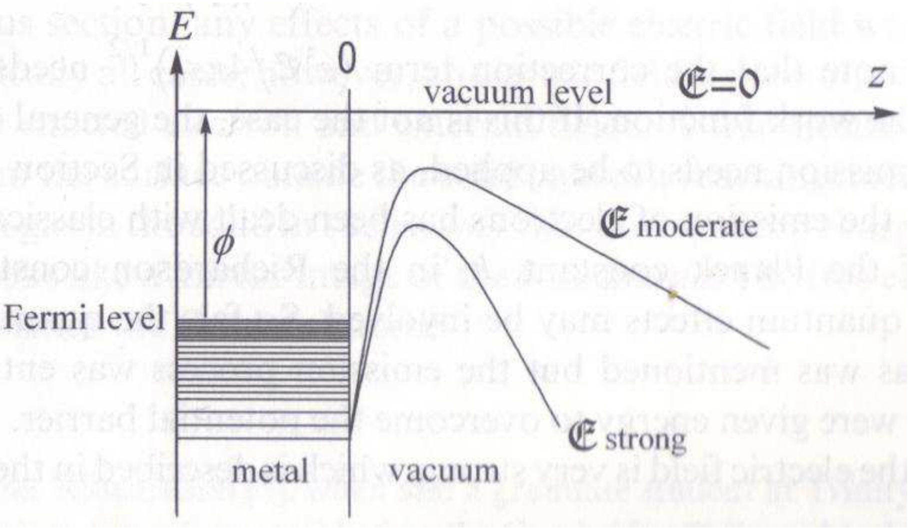

Figure 2.36: The effect of strong electric fields on the free electron energy level (labled here vacuum level) near the surface of a metal [24]

would then augment the electric field creating a conductive path, into which the main discharge then occurs.

High speed photography taken by the Tokyo Metropolitan Institute of Technology, see Figure 2.30 (image 5) shows that initially the conductive path occurs across the surface of the Teflon^{TM} via an unconfirmed mechanism but most likely some form of electron avalanche through the surface layers.

2.4.3 The LCR Discharge

After the discharge is initiated a conductive path between the charged plates of the capacitor via the discharge chamber electrodes through the plasma is established. This is known as the current loop. As current begins to flow through the system, energy from the capacitor is stored within the magnetic field around the electrodes. The resistance within the conducting loop is small ($\leq 1\Omega$) which gives rise to large discharge currents in the kilo ampere range and strong magnetic fields form around the electrodes.

As the energy of the capacitor is transferred to the magnetic field around the electrodes the voltage across the capacitor drops and eventually all the charge on the capacitor will diminish and the potential difference across the capacitor plates will be zero. However the current will continue to flow because the electrodes act like an inductor which tries to resist change in the flow of current. The energy used to keep the current flowing is extracted from the magnetic field, which will then begin to diminish. The current will charge the capacitor with a voltage of opposite polarity to its original charge. When the magnetic field is completely diminished the current will stop and the charge will again be stored in the capacitor, with the opposite polarity as before. Then the cycle will begin again, with the current flowing in the opposite direction through the electrodes. The charge flows back and forth between the plates of the capacitor through the discharge electrodes and the plasma. The energy oscillates back and forth between the capacitor and the magnetic field until resistances within the plasma, capacitor and electrodes make the oscillations die out. A typical example of this can be seen in the SIMP-LEX PPT discharge current profile, see Figure 2.13.

The electrode shape and size has been shown to have an impact on the performance of the PPT, see Figure 2.14. This is because the geometry of the electrodes, both the individual geometry and the combined geometry of the two electrodes, has an impact on the self and mutual inductance of the electrodes and the distribution of the magnetic field.

2.4.4 Mass Production

The description above assumes a conductive path is maintained during the discharge process and for this to occur in the discharge chamber plasma needs to be created and maintained. The mechanism of plasma production is under development with advanced models being presented to explain the Teflon^{TM} propellant-plasma interaction [70]. However in this section the descriptions are limited to experimental observations. This is because in models, assumptions are made that may be contradicted by experimental observation. In the instance of the model presented by Keidar et al. it is assumed that there is a plasma-Teflon^{TM} interaction each time the capacitor reverses polarity, but high speed photography, see Figure 2.32, shows this is only the case for the first half cycle of the discharge.

The plasma itself has been shown to contain species of carbon and fluorine of various ion charge states. Collected RFEA data from the University of Washington observed that probe current production was still occurring on its collector grid when a repelling grid had a 199V potential difference put across it. This would indicate that the maximum ion charge state being produced could be C^{4+}, F^{6+} or Cu^{9+} as they fall equal to or under 199V [23].

Electron density measurements taken in the spatial domain within the plasma discharge (i.e. all the measurements taken at the same time but at different positions) showed that there was a significant build up of electrons near the surface of the propellant and close to the end of the electrodes, see Figure 2.27. This is also observed in the images taken by the Tokyo Metropolitan Institute of Technology, see Figure 2.30 (image 9 - 13), where there is bright luminescence originating near the Teflon^{TM} and near the end of the cathode. The images suggest that the plasma filaments originating from the Teflon^{TM} surface converge downstream and promote some form of activity here at the electrode end.

The high electron densities are supported by the observation of high ion charge states and caution should be taken that the plasma in some regions may not be able to be considered as 'quasi-neutral' (i.e. over suitably short distances the electron and ion number density populations are equal).

The distribution of current across the discharge gap has been shown to be non linear and mapping of the current sheet has shown that the maximum current density is found close to the cathode, see Figure 2.26 (at 2-3 μs). The images, see Figures 2.29, 2.30 and 2.31 also show that bright spots can be seen on

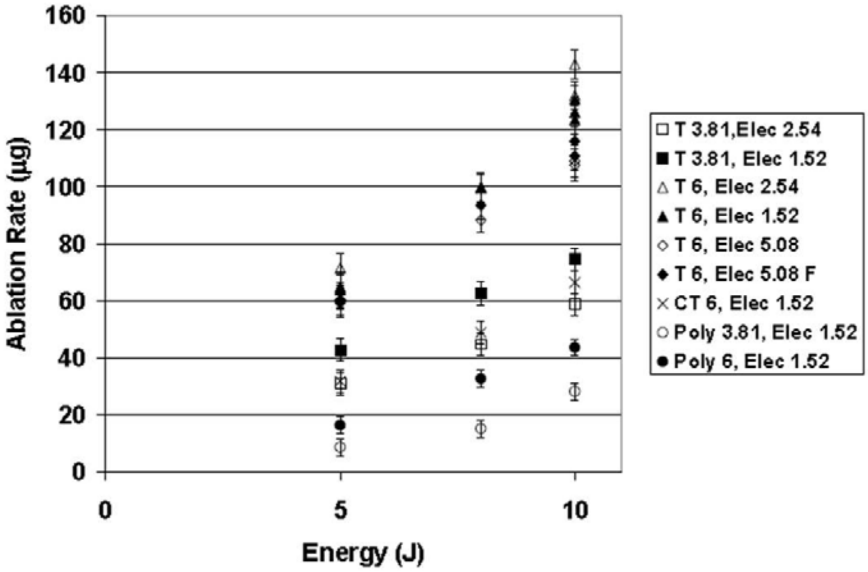

Figure 2.37: Mass erosion (ablation) rates for a variety of PPT configurations conducted at NASA Glenn Research Centre. T = Teflon^{TM}, CT = 2% Carbon impregnated Teflon^{TM}, Poly = High density polystyrene and the numbers indicate the electrode separation distance in cm [25]

the surface of the electrodes (predominantly the cathode) with plasma filaments or jets originating from them which are bent (or canted) in the direction of the plasma flow.

The surface temperature of the plasma increases with the flux density of the radiation from the plasma, see Figure 2.24. These processes occur at the same time and by doing so suggest that the two processes happen in parallel rather than sequentially. The significance of this means that if the Teflon^{TM} was the source of the plasma through resistive heating (via conduction of current through the surface layers of the Teflon^{TM}) then there would be a finite time delay between the Teflon^{TM} surface heating up and the production of radiation from the plasma. The results show that this is not the case and that the heating of the Teflon^{TM} is a product of the plasma being present. This is strengthened by the University of Tokoyo LPPPT results, see Figure 2.18. The results show a non-zero trend line when comparing the introduced liquid mass bit to the produced impulse bit of the PPT as it discharges. The trend line suggests an impulse bit of 82μNs when ‘no mass’ is introduced into the system.

These results suggest that the initial production of plasma and mass within the PPT is not from the Teflon^{TM} but from another source. This other source would then produce plasma and the interaction with this plasma would cause erosion from the Teflon^{TM} surface. The more energetic this plasma is would suggest the more Teflon^{TM} that would be eroded. This has been shown to be the case in many experiments where the Teflon^{TM} mass erosion was in direct relationship with the applied discharge energy, see Figure 2.37 [25].

Mass erosion has been identified in experiments as coming from the Teflon^{TM} surface, see Figure 2.16 but also from the electrodes, see Table 2.2. The exact nature on how the electrode erosion occurs is not understood but by understanding this process better an improved model for the discharge process can be created. Being able to model the properties of the plasma (in particular the plasma resistance) will lead to better understanding on the coupling effects between the plasma resistance and the LCR circuit. Knowing how the energy is lost from the transfer of energy from the magnetic field to the capacitor due to the plasma resistance will help to explain how that consumed energy is being used and in what processes (e.g. plasma joule heating, particle acceleration etc).

2.4.5 Plasma Propagation and Acceleration

The plasma bulk that creates a conductive path is created in the vicinity of the propellant surface and the cathode electrode. As current flows through the electrodes, magnetic fields are established. The current will flow from the positive charged plate to the negative charged plate of the capacitor. As the current passes through the anode the magnetic field, in accordance to Ampères law, will have a given direction vector. As the flow of current in the cathode is opposite to the flow in the anode the magnetic field vector, in accordance to Ampères law, is in the same direction in the cathode as it is in the anode. This combination of magnetic fields coupled with strong currents creates significant magnetic fields in the discharge chamber.

The strong current densities flowing through the plasma interact with the strong magnetic fields and a force is produced, otherwise known as the Lorentz force. The Lorentz force vector is perpendicular to the magnetic field and the current flow. As the current discharge rings and the polarity of the electrodes oscillate the coincidental nature of operation dictates that this force vector will always remain pointing in the same direction. The force pushes and accelerates the plasma particles along the force vector and when seen on the larger scale this is seen as the entire plasma bulk being accelerated along and out of the discharge chamber.

However in preparation for the Earth Observation 1 (EO-1) PPT experiment NASA Glenn Research Centre investigated multi axis thrust measurements and found that there was a significant off-axis thrust component in the direction of the anode. For a 54J discharge the thrust in the Lorentz force axis was 890μN, 67μN in the axis that goes from the cathode to the anode and 19μN in the axis perpendicular to these. A thorough analysis of these results showed that this effect was caused by internal plasma mechanics within the EO-1 PPT [71].

High speed photography, see Figures 2.30 and 2.31, which are unfiltered images show significant extremes of the plasma bulk being bent (canted) from the cathode towards the anode in the direction of the Lorentz force vector. In filtered imagery, see Figure 2.32, there is no bending or canting to be seen from neutral carbon charge carriers, which we would expect as these particles would not carry current and so would not be effected by the Lorentz force. The propagation of the neutral particles is parallel to the Teflon^{TM} surface. The propagation of the carbon ions is not as clear but the images suggest that to begin with the carbon ions propagate equally perpendicular to the Teflon^{TM} propellant but as time elapses the current and magnetic fields become stronger. By 2.37μs canting can be observed in the carbon ion population.

These observations suggest there are several processes occurring simultaneously. Particles being introduced into the chamber by the eroded Teflon^{TM} move perpendicular to the propellant surface, coincidently in the same axis as the Lorentz force vector. Another process is occurring which provides a force originating from the cathode and directed towards the anode. This force combined with the Lorentz force may be what causes and instigates the bending (or canting) of the plasma bulk. If plasma particles were introduced into the chamber from the cathode heading to the anode and were subjected to the Lorentz force this would give the particles a combined vectored force and on the large scale would appear as the bent (canted) plasma bulk.

To complicate the situation the inductance and resistance of the electrodes is continually changing as the plasma bulk propagates down the discharge chamber. The current loop will try to follow the path of least resistance and so as time elapses the current path follows the ever expanding propagation of the ion sheet until the ion sheet leaves the chamber. As this current loop expands the effective volume of the inductor increases. This alters the overall inductance and resistance of the circuit due to the current having to physically pass through more material.

Figure 2.32 shows that neutral particles are produced in the discharge. The neutral particle sheet remains constant as it propagates with a leading edge that is parallel with the Teflon^{TM} surface. The neutral particle sheet is not accelerated by electromagnetic forces and so moves down the chamber at a constant but reduced speed compared to the ion sheet. As the magnetic field around the electrodes begins to collapse, current in the system becomes reduced and the ion production is decreased. By the time the capacitor plates have been recharged (at an opposite polarity to the initial state), ion production is at its lowest (but non zero) as current ceases to flow, see Figure 2.25. If able to, a secondary discharge occurs and is referred to as a re-ignition. The re-ignition however does not occur across the Teflon^{TM} surface (as the initial discharge did) but occurs at the point where the neutral particle sheet coincides with the new cathode, see image 14 of Figure 2.30. Either the neutral particle sheet acts as a path of least resistance and breaks down or the sheet promotes some form of activity on the cathode. Either way a current loop is established and the plasma creation and acceleration process begins anew. The re-ignition process reoccurs several times depending on the discharge characteristics of the LCR circuit.

2.4.6 After Effects

Once the discharge process has been completed and the energy of the capacitor has been depleted additional processes occur. Only a small proportion of the total discharged energy was used to accelerate the ion particles. Some energy was locked in the depolarisation rotation effect of the capacitor and some was lost to radiation and heat during the discharge.

The energy lost to heating effects is deposited in the discharge chamber walls and propellant surface. If sufficient, the energy causes a transition change and either melts or sublimes the chamber walls and Teflon^{TM} surface respectively, creating small and large particulates. These particulates are accelerated by gaseous pressure forces out of the discharge chamber at a speed of 200-300 ms^{-1}. This process happens for a few hundred microseconds.

2.5 Summary

There has been over five decades of research into the Pulsed Plasma Thruster which has left a rich legacy of literature. This review began with a focus on PPTs that have been flight qualified or flown. Up until the turn of the millennium the PPT was nominally used on spin axis stabilised satellites. The PPTs on the TIP and NOVA satellites operated for a total of 20 years and fired over 50 million pulses. As technology improved the mass and volume of a satellite began to decrease. The PPT was then designed and qualified to give three axis attitude control but with a number of satellite launch failures and delays there has only been two successfully flown PPTs since 2000.

A comprehensive review of experiments in the areas of hardware development and fundamental science was undertaken. The pertinent points of the experiments were distilled and presented allowing parallels to be drawn with other works within the PPT field. The review finished off with a description on the PPT discharge process which gave an account on the current theories of what processes occur and also highlighted areas in which there is currently a lack of understanding. These areas are listed below;

- Off axis thrust production - A significant component to the thrust vector is in the cathode-anode axis originating from the cathode and directed towards the anode. Currently this force producing mechanism is not understood.

- Plasma production from the electrodes - The mass erosion mechanism from the electrodes is not fully understood.

- Role of the neutral particle sheet in the re-ignition process - The neutral particle sheet seems to dictate the position in the discharge chamber where a re-ignition event takes place. But it is not known whether the re-ignition is caused because the neutral particle layer breaks down or if the presence of the neutral particle sheet promotes some other process or mechanism.

- Magnetic Field - The magnitude and distribution of the magnetic field that is produced around the inductors (electrodes) has a direct impact on the acceleration process of the particles. To increase the coupling between the magnetic field and the plasma it is important to understand how the topology of the magnetic field changes with time during the discharge.

This thesis will be dedicated to investigating the first three areas as there is synergy between them and a possibility that they are all linked by a common process.

Chapter 3

CubeSat Mission Design & Analysis

3.1 Introduction

The nanosatellite revolution has been gradually growing over the years. Standardisation and development of modular subsystems have fuelled the popularity and accessibility in the 10cm × 10cm × 10cm CubeSat concept. The CubeSat standard alone allows companies and research institutes to focus on developing single modules, knowing that these modules if kept to that standard can be marketed, sold and used in a number of CubeSat satellites. This has led to the plug and play attitude of the CubeSat community which has driven down the costs of making a nanosatellite to an accessible level, allowing other institutes to join and contribute to the community. Although the CubeSat platform is less customisable, the philosophy developed is 'What mission can be done with this platform?' instead of the more expensive, traditional philosophy of 'What platform is required to conduct this mission?' held by the few large scale independent satellite producers. So the question is what mission can be done with the CubeSat platform and how does developing a micro propulsion system for a CubeSat platform influence the CubeSat mission portfolio?

3.2 CubeSats

The CubeSat standard was initially developed and written in 1999 by California Polytechnic State University and Stanford University as a way to help academia institutes to develop nanosatellites for space science and exploration. The standard details the requirements that developed modules must adhere to, to allow for successful integration with other 'plug and play' modules. The CubeSat standard is based on existing industry standards within the IT field and requires each module to adhere to the PC104 layout and specifications, see Figure 3.1. The CubeSat standard also dictates the maximum dimensions of the CubeSat to allow for the integration of the satellite with a standard CubeSat deployer

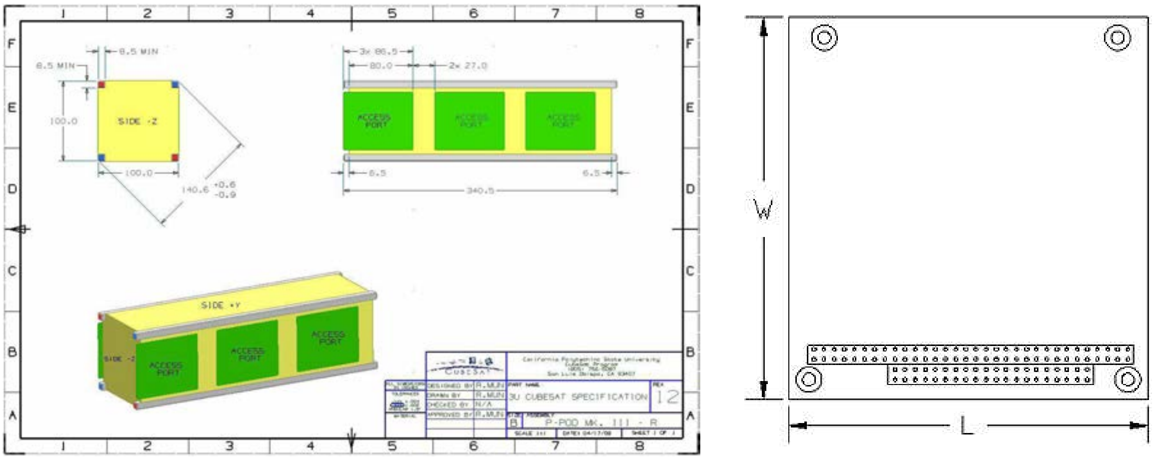

Figure 3.1: CubeSat standard physical dimensions for a 3U CubeSat and a PC104 module W = 95mm and L = 90mm

commonly known as a P-POD, see Figure 3.2.

A CubeSat is a 10cm × 10cm × 10cm satellite and is referred to as a ‘1 Unit’ CubeSat or ‘1U’. A CubeSat can be any number of units i.e. 2U, 3U, 4U etc. These units are stacked on top of each other and so a 2U satellite would be a 10cm × 10cm × 20cm satellite. The P-POD deployer can only handle up to 3 units worth of CubeSats but can handle any combination and number of CubeSats that make up the 3U i.e. 1U + 2U, 1U × 3 or one 3U.

The hardware costs for a CubeSat are relatively cheap compared to a commercial 100kg satellite. A 1U to 3U CubeSat will have a total hardware cost in the order of £50-60k, with an additional £50-60K per kilogram of the total satellite mass in launch costs. This cost is feasibly within a dedicated academic budget. In comparison a 100kg satellite will cost in the order of £5-10 million. The cost effective nature of the CubeSat is a driving force which pushes new (possibly ‘risky’) technologies on to the PC104 module. These new technologies can then be flown and used with a low cost and reduced risk approach that larger satellites cannot afford to commit to. This is another method in which a technology can be given flight heritage at a reduced risk and so can be incorporated into larger more expensive satellites in the near term future. This practice was conducted by Aerospace Corporation, a large USA satellite manufacturer, which than went to make the public comment:

‘In these projects, the corporation’s usual role of contractor oversight was turned around by 180 degrees. Such an exercise powerfully illustrates the reasons for, and the psychological responses to, the standard space systems development process.’ and ‘Since 1998, Aerospace Corporation has built 11 picosatellites and nanosatellites. Eight have been tethered pairs, and three were individual CubeSats. One overriding goal of these efforts has been to demonstrate that miniature satellites, launched as secondary payloads, can do a great deal to mitigate risk on much larger programs.’

Another advantage of the CubeSat platform is the short development time of CubeSat missions. The plug and play ability of the CubeSat standard usually means that a well planned program can build a

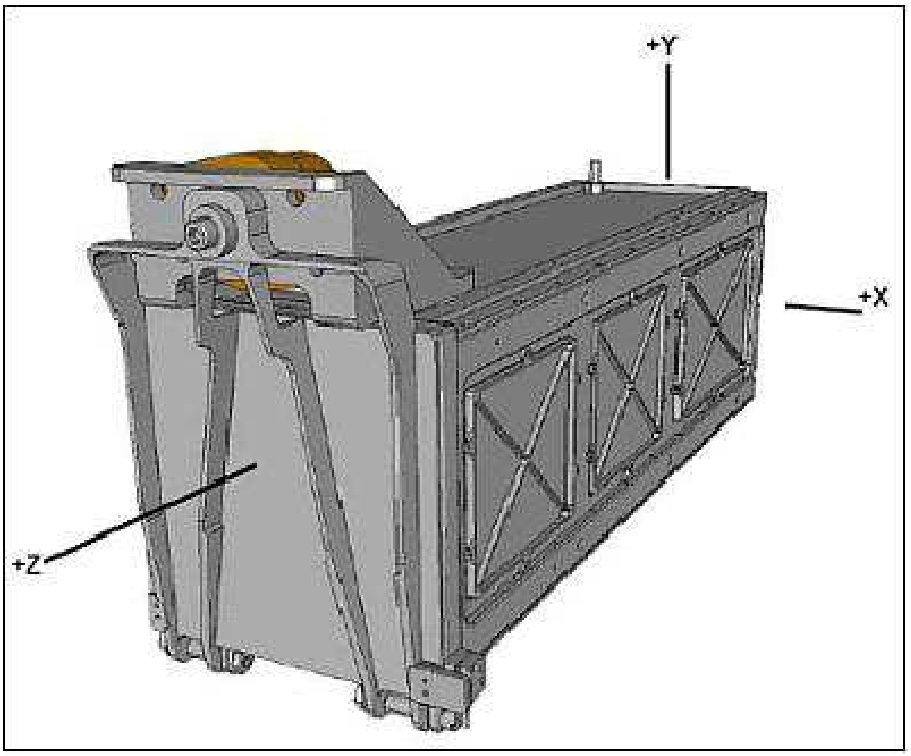

Figure 3.2: A P-POD CubeSat launch deployment system

CubeSat with COTS components within three months. However mission programs are usually extended due to the time it takes to develop custom modules for the specific mission. In comparison a 100kg satellite will often take 18 months and large GEO satellites can take up to five years to manufacture.

The biggest hurdle to a rapid deployment is the availability of launches. For a CubeSat as they are a secondary payload they are subject to the schedule of the primary payload. If the primary payload is delayed, which is not uncommon, any CubeSats on that mission will also have their schedules delayed. This could mean that some CubeSats have been waiting on shelves in storage for durations longer than it took to develop the satellite in the first place!

3.3 CubeSat Missions

The following CubeSats are picked from a rich list of successful missions that have flown since the first launch of the first six CubeSats on the Russian Eurockot LV rocket on 30^{th} June 2003 from Plesetsk. On the first launch was QuakeSat by Stanford University, see Figure 3.3. QuakeSat was one of three satellites from the initial batch that successfully operated past their initial proposed lifetime. Designed for a six month mission it operated flawlessly for 11 months and its beacon was picked up in October 2007, which was four years after its launch. QuakeSat was a 3U CubeSat that was designed to pick up Extremely Low Frequency (ELF) magnetic signal data to detect and/or predict the presence of earthquakes of magnitude 6.0 or higher. The method of detection was based on deflected ELF signals from the Earths Ionosphere

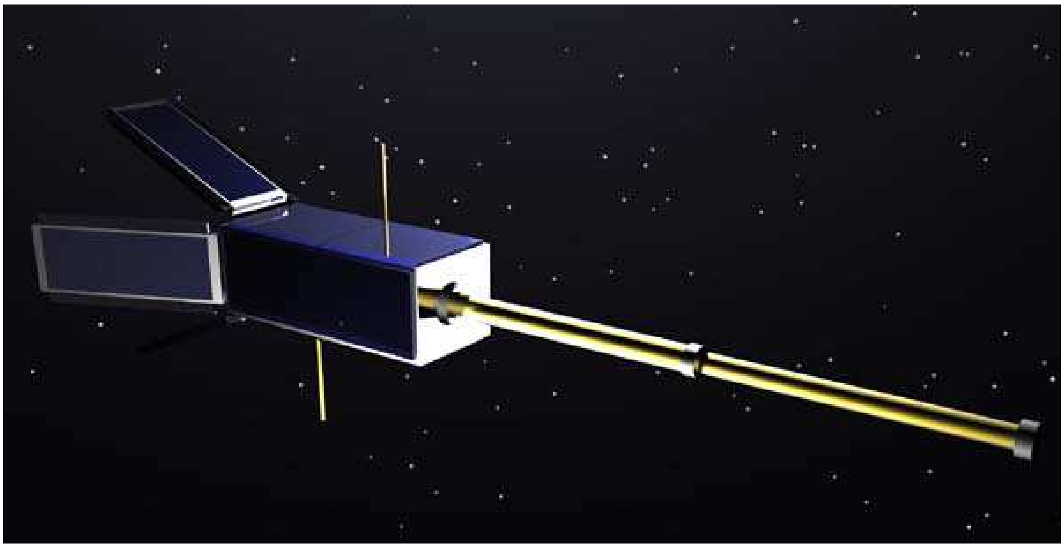

Figure 3.3: QuakeSat in its deployed configuration [26]

that was detected by a magnetometer housed in a 0.7m deployable boom that extended from QuakeSats main chassis. QuakeSat was predominantly made from COTS components but due to it being one of the six pioneering CubeSats there was a fair cost in development and overheads which put the build and launch of the satellite around one million dollars and a monthly running cost of 170,000 dollars [26].

The CubeSat success has been spearheaded by the academic community and there has been a significant scientific element to many of the CubeSats that have flown. These have even included advanced payloads such as tether and biological experiments [72] [27]. On the 16^{th} December 2006, NASA launched GeneSat-1 on a Minotaur launch vehicle from NASA Wallops Flight Facility. GeneSat-1 was developed by the Centre for Robotic Exploration and Space Technologies. The satellite was a 3U CubeSat and performed experiments on E. Coli bacteria in space, see Figure 3.4. The 96 hour experiment was successfully completed six days after launch but GeneSat-1 continued to send telemetry till April 2008 [27].

The focus by academia on novel but cost effective scientific experiments on CubeSats is galvanising support in both the public and private sectors. One such example of private interest was a series of CubeSats that were developed by the Aerospace Corporation (USA). Although AeroCube-1 was destroyed in July 2006 due to the Russian DNEPR LV launch vehicle disintegrating during launch, they developed AeroCube-2 which was successfully launched nine months later and AeroCube-3 which was launched in May 2009, see Figure 3.5. AeroCube-2 demonstrated a potential use of CubeSats to perform fly-by inspection missions. On release from the P-POD deployer AeroCube-2 took an image of Cal Poly CubeSat CP-4 launch, see Figure 3.6 the first and only picture taken of one CubeSat by another in space. During the time of the AeroCube development program the return-to-flight status of the space shuttle was still unknown (due to the Columbia shuttle accident). It was important to routinely fly satellites to keep program office customers interested and so the AeroCube program was established. The goal was to test company developed hardware in a cost effective manner to give new technologies (tethers and

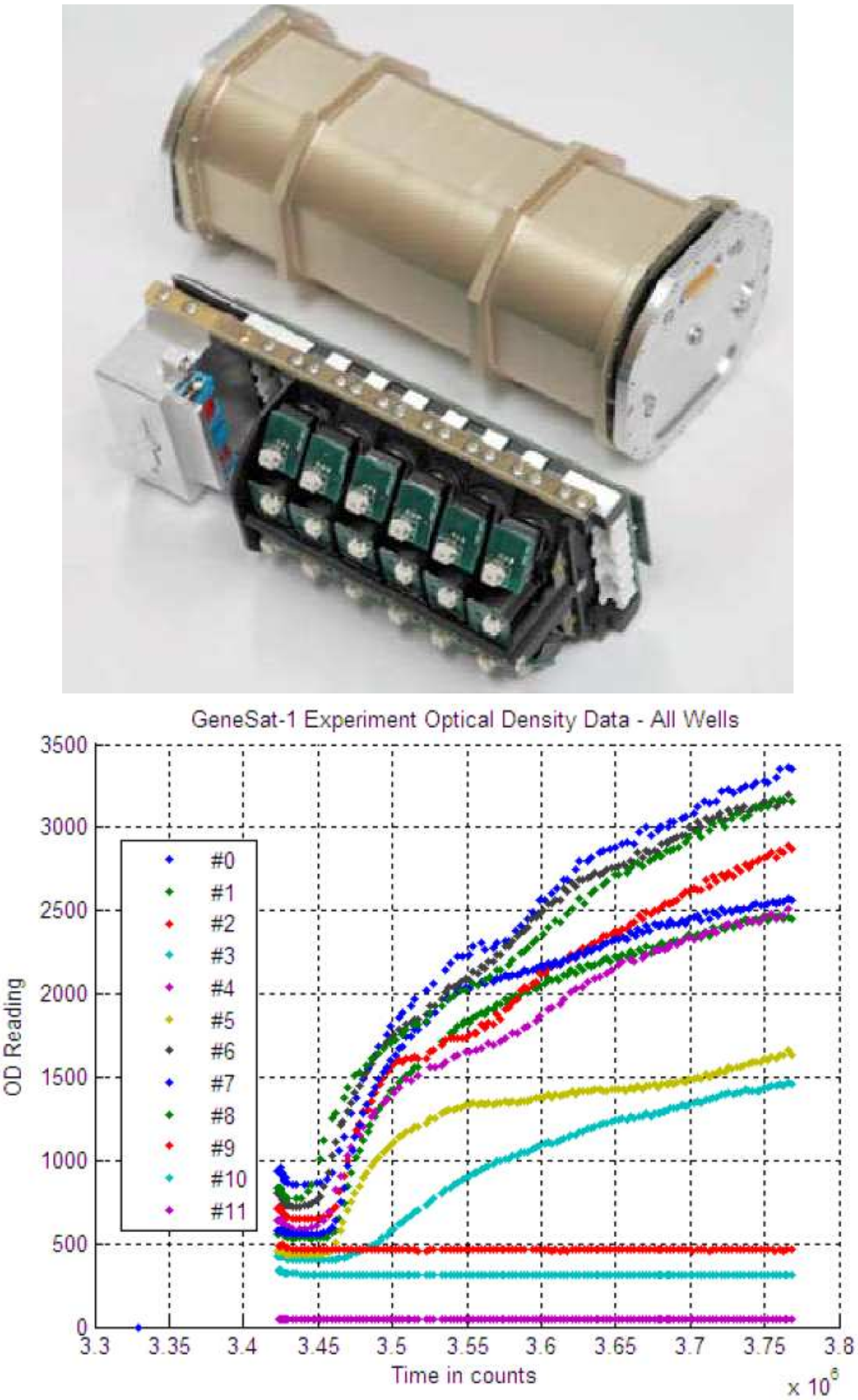

Figure 3.4: The GeneSat payload and resulting data from a biological experiment conducted in a 3U CubeSat [27]

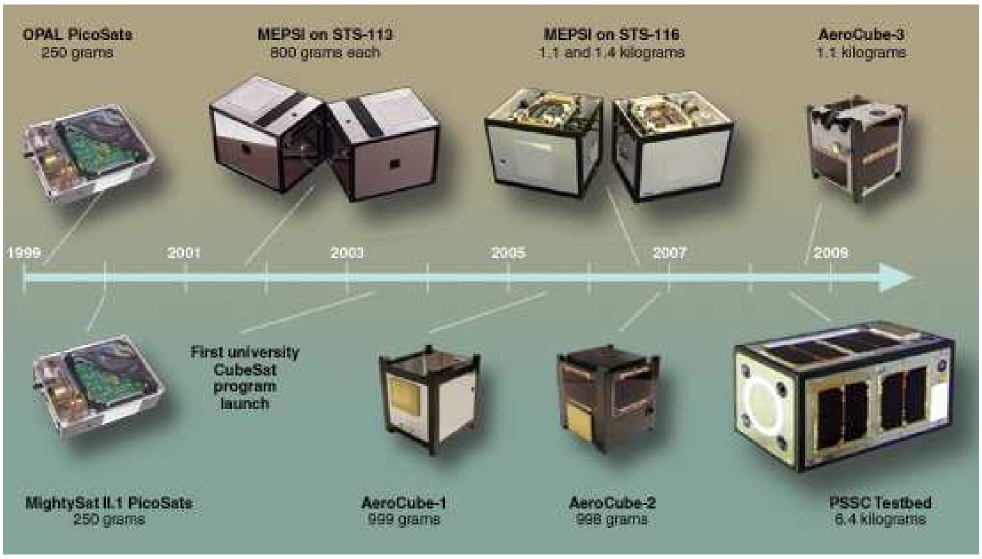

Figure 3.5: The evolution of the Aerospace Co. nanosatellite program

rapid de-orbit devices) flight heritage. In this manner high risk technologies could be tested for future larger satellites in a way that brought down future programmatic and technical risks.

Propulsion research for CubeSats is currently an active topic, with several Universities developing some form of CubeSat orbit manoeuvring capability. The methods proposed even include exotic propulsion techniques like solar sails and tethers [72] [73]. CubeSats are limited in there mass, volume and power. They are also usually secondary payloads onboard a launch vehicle and so to reduce potential risks to the launch vehicle or primary payload, launch regulators typically forbid the use of highly pressurized tanks and pyrotechnics, which limit propulsion options for CubeSats. In a survey of micro propulsion conducted by NASA Jet Propulsion Laboratory only three technologies of existing or nearly off-the-shelf propulsion technologies were identified as candidates for CubeSats. These were; low pressure butane systems, μPPTs and Vacuum Arc Thrusters (VAT) [74].

To date only one CubeSat has sucessfully flown with propulsion on board. In April 2008 the University of Toronto launched CanX-2 CubeSat on the Indian Polar Satellite Launch Vehicle. The 3U satellite was equipped with a liquid-fuelled cold gas propulsion system using sulphur hexafluoride as the propellant (SF_6), see Figure 3.7. The propulsion unit consisted of a single thruster head that was situated off axis and was used for spin axis experiments to characterise its performance. The satellite angular rates achieved by the propulsion system were measured using the on-board attitude determination subsystem. Maximum thrust was estimated to be 35mN, the minimum impulse bit was 70μNs at 75psi and 150μNs at 255 psi and the average specific impulse was 46.7s. Currently additional tests are being conducted on the long-term leakage rates of the sulphur hexafluoride storage tank [28].

The Illinois Observing Nanosatellite (ION) was potentially going to be the first CubeSat with an electric propulsion device but in 2006, 86 seconds after lift-off the Russian DNEPR launch vehicle it was

Figure 3.6: An image of the Cal Poly CubeSat CP-4 taken from the AeroCube-2 CubeSat

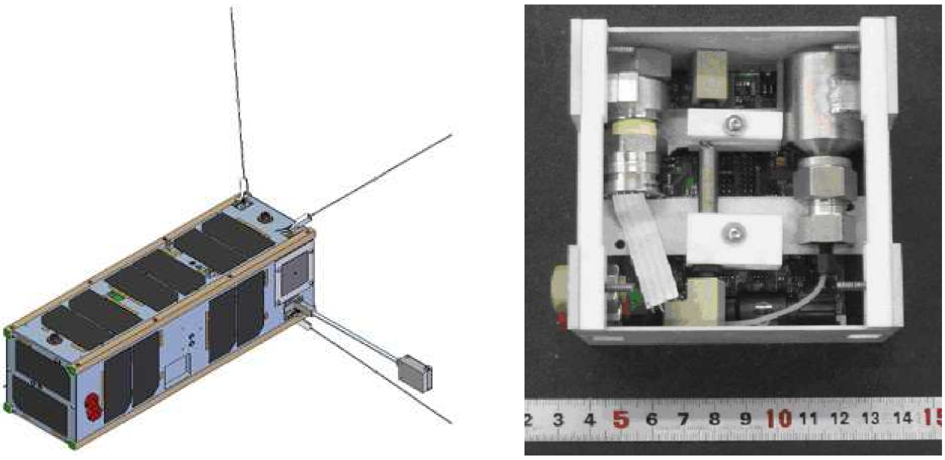

Figure 3.7: The CanX-2 CubeSat and propulsion module [28]

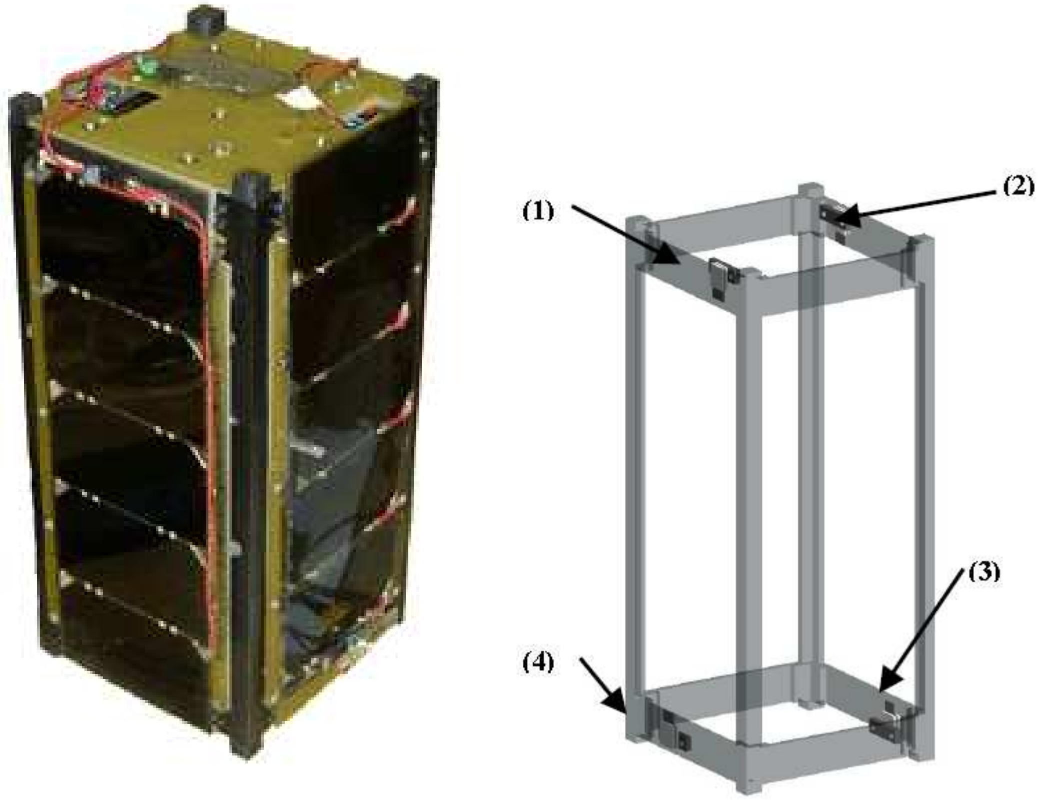

Figure 3.8: The ION CubeSat and placement indication of the four μVATs [29]

Table 3.1: Propulsion performance characteristics onboard CanX-2 and ION [37]

CubeSat	**Type**	**Min. Impulse bit, μNs**	**Specific Impulse, s**	**Thrust, mN**
ION	VAT	10^{-3} - 30	-	60×10^{-3}
CanX-2	Cold Gas	70 - 150	46.7	35

carried on disintegrated along with 11 other CubeSats. ION was a 2U CubeSat that included four μVATs allowing for two-axis rotation, see Figure 3.8 [29]. The mission was to observe airglow phenomenon in the earth's upper atmosphere using a photomultiplier tube.

The propulsion performance characteristics of the CanX-2 and ION CubeSats are listed in Table 3.1.

3.4 CubeSat Propulsion Requirements

Basic CubeSat propulsion requirements were published by ESA, see Table 3.2 [38]. These were a first draft of what a CubeSat propulsion system should aim to achieve. The requirements focus on the constraints of the CubeSat envelope and standard, however as previously mentioned due to CubeSats being a secondary payload the launch vehicle operators will often insist that no high pressure or propulsion system using pyrotechnics are used.

Currently most CubeSats are launched with a passive Attitude Determination and Control System

Table 3.2: Cubesat performance requirements set out by ESA [38]

Description	**ESA CubeSat requirements**
Micro-thruster module dry mass budget, kg	0.150 - 1.0
Number of micro thrusters per CubeSat	1 - 6
Power required by full assembly, W	1 - 10
Bus voltage, V	5 - 8
Volume required by full assembly, m^3	0.0001 - 0.0125
Thrust range, μN	1 - 1000
Minimum impulse bit, μNs	5
Specific impulse, s	60 - 1000
ΔV, ms^{-1}	1 - 60

(ADCS). Magnotorquers are the most common form of ADCS but momentum wheels, gradient booms and permanent magnets have also flown. However, none of these devices can actively change the orbit of the CubeSat and so the CubeSat is constrained to the orbit in which it was inserted in to by the launch vehicle. This is becoming a serious concern due to new legislation that is becoming common place. It will soon be required that satellite operators/providers will need to ensure their satellite de-orbits or is placed into a 'graveyard' orbit within a 25 year period of the mission end of life, to reduce the total amount of space debris.

CubeSats are rarely primary payloads on launches and often they are injected into their orbit once the primary payload has been successfully deployed, so risk of collisions with the primary are mitigated. Coupled with the 25 year legislation this can put the nanosatellite platform at a disadvantage. It is important to establish the limits of the CubeSat platform in Low Earth Orbit (LEO). Atmospheric drag will naturally cause a satellites orbit to decay. The size, mass and volume of the satellite will determine the time it will take. Atmospheric drag can be calculated from the drag equation used in fluid dynamics;

$$F_{Drag} = \frac{1}{2}\rho v^2 C_D A_{Sat} \tag{3.1}$$

This equation can be applied to atmospheric drag if the velocity of the satellite and the relative density of the atmosphere is known. The coefficient of drag, C_D, is taken to be 2.2 for most satellites [75]. If the satellite propagates in a circular orbit the velocity, v_{Sat}, can be expressed as a function of the orbit radius;

$$v_{Sat} = \sqrt{\frac{\mu_{Earth}}{r_{Orbit}}} \tag{3.2}$$

The atmospheric density can be found as a function of the satellite's altitude by using standard look up tables [76] [75]. Atmospheric drag removes energy from an orbit causing the orbit to get smaller. As the orbit gets smaller (i.e. decreases altitude) the denser the atmosphere becomes which increases the atmospheric drag. This leads to an exponential like decline in the satellites orbit altitude over time. The

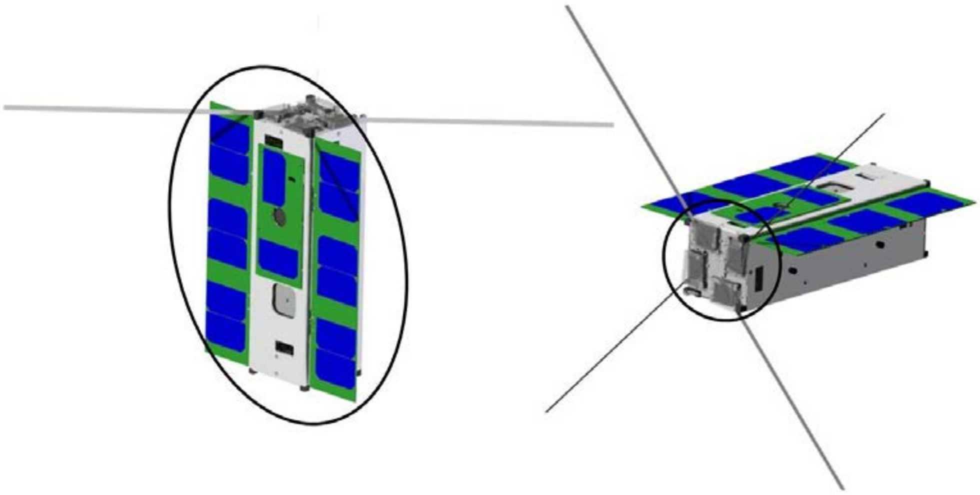

Figure 3.9: Exposed surface areas of a CubeSat that will be subject to atmospheric drag depending on its orientation

Table 3.3: Estimated Cubesat platform properties

Property	**1U CubeSat**	**3U CubeSat**
Mass, kg	1.3	4.5
Exposed surface area to atmospheric drag, m^2	0.01	0.01 or 0.09
Moment of Inertia of S/C - x axis, kgm^2	0.017	0.155
Moment of Inertia of S/C - y axis, kgm^2	0.332	0.155
Moment of Inertia of S/C - z axis, kgm^2	0.330	0.011
Lever arm - x axis, m	0.05	0.15
Lever arm - y axis, m	0.05	0.15
Lever arm - z axis, m	0.05	0.05

constant but low force effect that results in a spiralling decaying orbit can be modelled using the Ward spiral equation;

$$r_{Orbit} = \frac{r_0}{\left(1 + \frac{F_{Drag}}{M_{Sat}}\sqrt{\frac{r_0}{\mu_{Earth}}}t\right)^2} \tag{3.3}$$

Three scenarios using two CubeSat platforms are considered. The first scenario is a 1.3kg 1U CubeSat. The second and third scenarios use a 4.5kg 3U CubeSat with deployable solar panels. However, the difference between the two is the orientation of the satellite and exposed surface area, with respect to the drag force, see Figure 3.9.

Table 3.3 summarises the properties of the two CubeSat platforms. The moments of inertia were taken from computational modelling done in Solidedge^{TM} and the lever arms were taken as the maximum lengths in their respective axis from the geometric centre point.

Using these platform properties in the atmospheric drag calculations, see Figure 3.10, the maximum altitude a CubeSat can be at the end of its mission to meet the 25 year limit is: 588km for the 1U CubeSat, 513km for the 3U CubeSat with the minimum area exposed to atmospheric drag and 651km

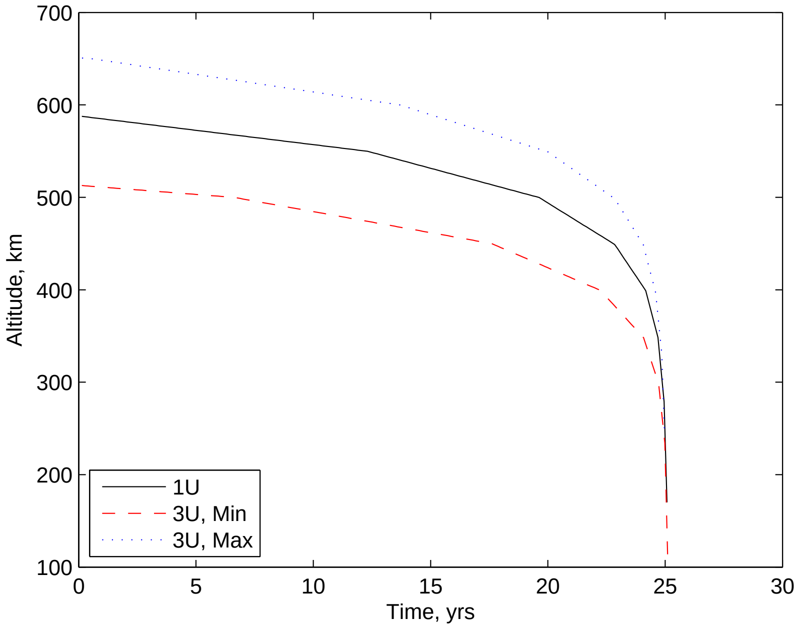

Figure 3.10: Maximum altitude a CubeSat can be at end of life to meet the 25 year deorbit legislation

for the 3U CubeSat with the maximum area exposed to atmospheric drag. Due to these limits and legislation the number of launch opportunities for CubeSats to be launched on is restricted as they require insertion orbits of the primary satellite to be less than the scenario limit. Using a constant low thrust spiral transfer orbit, the ΔV required to move a satellite from 820km to 513km is 164ms^{-1} and from 700km to 651km is 24ms^{-1}. Developing a propulsion system to deliver enough ΔV to overcome this issue will increase the number of potential launch opportunities for future CubeSats.

As well as meeting end of life altitude requirements a propulsion system could be used to perform both ‘Velocity correction and control’ and ‘Attitude control’ manoeuvres. The ‘Velocity correction and control’ manoeuvres in LEO include: transfer burns, drag compensation, rephasing, plane change and satellite disposal. The ‘Attitude control’ manoeuvres in LEO include: spin-up, spin-down, cancelling aerodynamic torque, cancelling gravity gradient torque, cancelling magnetic field torque, cancelling solar radiation torque, attitude manoeuvring in the three axes and maintaining pointing in the three axes.

The mission scenario will determine which of the above manoeuvres are considered and the total ΔV that is required from the propulsion system. In the mission scenario used for this work the following assumptions are made:

- The launch injection orbit, mission orbit and disposal orbit are the same. The altitude is set to the relevant orbit where the 25 year de-orbit requirement is met.
- The launch injection inclination, mission inclination and disposal inclination are the same.
- The satellite orbit does not need rephasing.

- The satellite does not require to do spin-up or spin-down procedures.
- The satellite is not spin stabilised.
- The centre of gravity coincides with the centre of solar radiation pressure and the centre of aerodynamic pressure.
- There is no residual magnetic dipole to interact with the Earths magnetic field.

Based on the above assumptions further consideration is given to drag compensation during the operation of the mission, cancelling gravity gradient torque, attitude manoeuvring and maintaining pointing in a specific direction. Similar to the previous discussion, compensating for drag is required to maintain a satellite at a specific altitude. For each circular orbit this can be estimated as:

$$\Delta V_{Orbit} = \pi \frac{C_D A_{Sat}}{M_{Sat}} \rho r_{Orbit} v_{Sat} \tag{3.4}$$

For the 1U CubeSat at a mission altitude of 588km the yearly ΔV for drag compensation is 4.39ms^{-1}. For the 3U CubeSat with the minimum exposed surface area at a mission altitude of 513km the yearly ΔV for drag compensation is 2.18ms^{-1}. For the 3U CubeSat with the maximum exposed surface area at a mission altitude of 651km the yearly ΔV for drag compensation is 2.03ms^{-1}.

The Earths gravity decreases according to the inverse-square law, so the part of the satellite closest to the Earth will be affected more than the part furthest away. The discrepancy between the two will cause a torque which will cause the satellite axis with the smallest moment of inertia to align with the gravity gradient. The worst case torque can be estimated by [75]:

$$T_g = \frac{3\mu_{Earth}}{2r^3_{Orbit}} \left| I_z - I_y \right| sin\left(2\theta\right) \tag{3.5}$$

θ is the maximum deviation of the z-axis from local vertical and can be assumed to be equal to the pointing accuracy. The required propellant mass to compensate for this torque can be found for the entire duration of the mission from [75]:

$$M_{propellant} = \frac{L}{g_0 I_{sp} S} = \frac{\int T_g dt}{g_0 I_{sp} S_g} \tag{3.6}$$

The equivalent ΔV of this mass can be found from using the standard Tsiolkovsky rocket equation. For attitude manoeuvres the impulse required for a manoeuvre can be found by [75]:

$$L = I_{x,y,z}\omega \tag{3.7}$$

where ω is the angular rate of the particular manoeuvre, note that impulse will be required to decrease the angular rate after the manoeuvre is complete. Maintaining a specific pointing accuracy is achieved by assigning a deadzone angle. As the satellite moves, this angle represents the allowed angle to which the satellites pointing can drift. Once this limit is reached the satellite propulsion system is fired in a direction to counteract this drift, resulting in a 'back and forth' drift through the deadzone angle. The impulse needed to maintain a specific deadzone angle, θ_d, or pointing accuracy is [75]:

$$L = \frac{TS{t_{min}}^2}{4\theta_d I_{x,y,z}} t \tag{3.8}$$

where t is the mission duration in seconds and T is the thrust of the propulsion system. The ΔV per year to compensate for gravity gradient disturbances, attitude maintenance and attitude pointing depends heavily on the thruster that is used to perform the specific manoeuvre.

3.5 CubeSat Propulsion Trade-off

The constraints placed on a CubeSat propulsion system limits the selection of avaliable propulsion devices. Low power requirements exclude many conventional electric propulsion devices. Mass and volume requirements limit the total propellant tank size in coldgas and chemical thrusters. To miniaturise a conventional propulsion system (be it electrical or chemical) generally requires advancement in Microelectromechanical Systems (MEMS).

Using a propulsion system that has flown on a larger platform and miniaturising this technology leads to a system that has reduced risk, in comparison to flying a completely new concept. When funding is limited this approach is usually desirable. As such this trade-off is focused on flown technology that can be miniaturised.

A cold gas thruster is probably the simplest propulsion system that has flown. It consists of a propellant tank with pressurised propellant, a valve that separates the tank from the nozzle and a nozzle that released gas expands through to create thrust. The resistor jet is similar to the cold gas thruster and has an additional stage between the nozzle and valve which heats up the propellant to produce higher levels of thrust. The simplicity of the thruster reduces the risk of this system. The main issue in miniaturisation is the manufacturing of a micro valve that can withstand the pressurised propellant tank pressures.

A solid propellant thruster is the simplest form of chemical propulsion. It has no valves, tanks or propellant feed system. However it is a one use only solution because once the propellant is ignited it is not possible to stop or control the thrust. These systems are commonly used to provide a single high impulse manoeuvre. The issue here is the lack of repeat firings.

A monopropellant thruster feeds liquid propellant through a catalyst bed which causes the propellant to decompose into hot exhaust gases, which are then expanded through a nozzle. The issue in miniaturising this system is similar to the cold gas thruster and resistorjet and in creating a micro feed system that can deliver the liquid propellant to the catalyst bed.

The Hall thruster uses charged plates and magnetic fields in an annular formation to produce thrust. Neutral gas is introduced into an annular chamber that has a radial magnetic field within it. Electrons trapped in this radial field ionise the gas propellant. The ions are then accelerated due to a potential difference within the chamber. High specific impulses can be achieved but at low thrust level. The system requires many features of a cold gas thruster (i.e. propellant tank, valves etc) and also draws significant power, requires significant voltages and overall is relatively complex.

The gridded ion engine electrostatically accelerates charged particles through a system of grids held at high potentials like the Hall thruster. The system requires many features of a cold gas thruster including a power unit for the generation of high voltages. The issue with the gridded ion thruster is the sputtering and erosion of the ion grids due to impact of charged particles.

The VAT and PPT have similar architecture. Both systems require a power unit that can supply energy via a pulsed discharge. The VAT differs from the PPT in that between the electrodes (connected to a HV capacitor) is an insulator with a metallised film layer upon it and the PPT (in a traditional configuration) has Teflon propellant between it. The VAT thruster uses a high voltage breakdown across the metallised film to initiate a discharge when a PPT uses an external device (i.e. sparkplug) to initiate a discharge. In both cases a high voltage breakdown occurs. High currents pass through the electrodes eroding them and both produce a plasma, which is then accelerated to create thrust. This simple design has proven to be reliable, but the issues here are the miniaturisation of the propellant feed system, HV capacitor and the electronics of the power unit.

Table 3.4 provides examples of miniature propulsion systems based on flown larger concepts. Although it is a non-exhaustive list it does provide a good synopsis of the current state of the art.

A technology demonstration mission was proposed by industry. Surrey Satellite Technology Limited was looking for new technologies to be flown on a CubeSat platform. The PPT was an ideal payload because unlike other EP systems its power draw was a function of its discharge frequency. This meant it could easily be scaled up or down in power draw from the satellite bus dependant on the requirements and resources.

The thrust from the PPT although relatively small, compared with cold gas systems, is provided over an extended period in a discrete train of pulses. This gives the PPT multifunctionality. The PPT can be used in a number of ways; it can compensate for orbit perturbations (i.e. atmospheric drag), the small minimum impulse bit of the train of pulses can provide accurate pointing and over extended periods of operation it can be used for orbit raising and lowering. Other benefits provided by the PPT are a quick 'warm-up time' (less than 10 seconds) and the use of solid inert propellant. Figure 3.11 shows the trend lines comparing a number of PPTs as a function of energy. In the massbit trend, two lines are produced. These are due to the configuration of the PPT, the lower one indicates a breech fed PPT, whilst the

Table 3.4: Examples of miniature propulsion systems

Type	**Example**	**Thrust, μN**	**Specific Impulse, s**	**Mass, g**	**Max. Power, W**
Cold gas (Nitrogen)	58X125A (Moog)	4400	65	9	10
Cold gas (Butane)	μVACCO	25,000	70	30	1
Monopropellant (Hydrazine)	HmNT	129,000	150	40	8.25
Monopropellant (Hydrogen Peroxide)	Kuan et al.	221,000	125	5.8	15
Solid propellant	ATK (STAR 4G)	257,000,000	269.4	1500	-
Hall effect	MIT	1800	865	-	126
Ion engine	MiX1 (Xenon)	10	3200	200	13
PPT	AFRL μPPT	30	-	500	1
VAT	Bizmuth	40	1000	150	1

upper indicates a side fed PPT.

The nominal minimum thruster firing time, or pulse length, for a PPT is between 5 to 30μs. Figure 3.11 shows the minimum impulse bit is dependant on the energy of the discharge. The specific impulse for the PPT can range between 250 - 5000s dependant on the speed that the ions are accelerated out of the thruster. The massbit of the discharge determines the total pulse count, N_{Pulses}, that the PPT can provide;

$$N_{Pulses} = \frac{M_{Propellant}}{M_{bit}} \tag{3.9}$$

The total thrust of the PPT can be calculated by the impulse bit and the discharge frequency, noting that an increase in discharge frequency affects the power draw of the thruster;

$$F_{PPT} = f_{discharge} I_{bit} \tag{3.10}$$

$$Power = f_{discharge} E_{discharge} \tag{3.11}$$

The energy of the discharge neglecting losses can be estimated to be equal to the energy stored in the capacitor.

$$E = \frac{1}{2} C V^2 \tag{3.12}$$

A μPPT with a pulse length of 30μs, an impulse bit of 20μNs, a discharge frequency of 0.1Hz (therefore

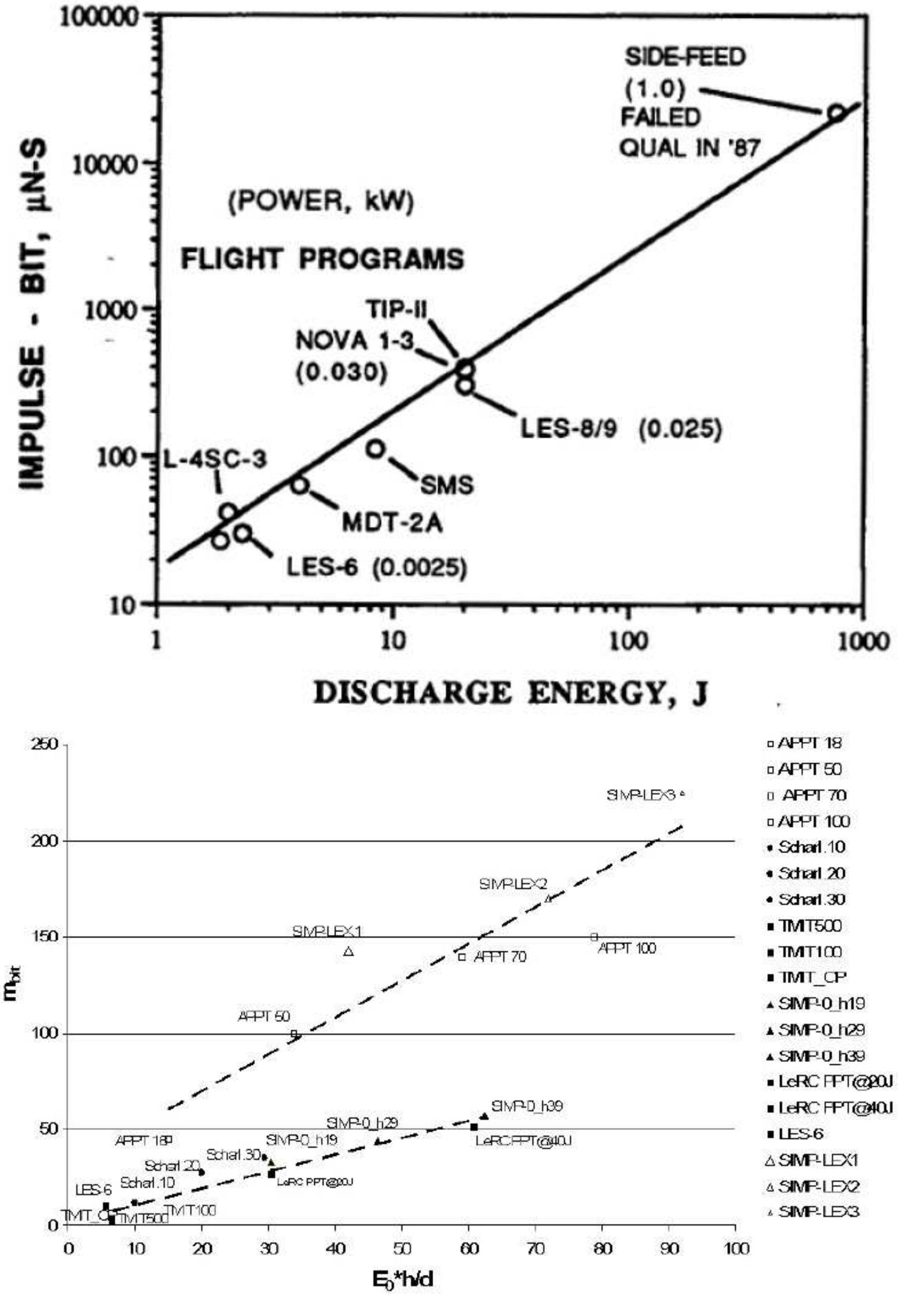

Figure 3.11: Trend lines in the impulse bit and mass bit as a function of energy for a number of developed PPTs [30] [20]

Table 3.5: Yearly ΔV requirements for the CubeSat platforms

Parameter	**1U CubeSat**	**3U CubeSat Min.**	**3U CubeSat Max.**
Stipulated 1J μPPT			
Mission altitude, km	588	513	651
Drag compensation, ms^{-1}	4.390	2.180	2.030
Gravity gradient disturbance, ms^{-1}	0.004	0.056	0.053
Attitude pointing in all axes, ms^{-1}	Neg.	Neg.	Neg.
PPT total ΔV per year, ms^{-1}	4.394	2.236	2.083
58X125A Moog Cold Gas Thruster			
Mission altitude, km	588	513	651
Drag compensation, ms^{-1}	4.390	2.180	2.030
Gravity gradient disturbance, ms^{-1}	0.004	0.056	0.053
Attitude pointing in all axes, ms^{-1}	1.236	0.548	0.548
58X125A total ΔV per year, ms^{-1}	5.630	2.784	2.631

a thrust of 2μNs) and a specific impulse of 250s was compared to the 58X125A Moog cold gas thruster. The cold gas thruster is assumed to have a minimum thruster firing time of 10ms. The comparison used the previously stated three scenarios with the 1U and 3U CubeSat configurations, see Table 3.5. In the comparison the ΔV per year for drag compensation, cancelling gravity gradient torque and maintaining pointing in a specific direction is calculated. These calculations assume a pointing accuracy of 0.2^o is required from the CubeSat platform.

Table 3.5 shows that in all three scenarios where accurate pointing of the satellite is required a CubeSat with a PPT uses less propellant. The negligible amount of propellant used by the μPPT for pointing is attributed to the extremely small pulse length and impulse bit.

3.6 Summary

The CubeSat standard has led to a growth of nanosatellite development since it was first introduced to the academic field in 1999. The past ten years of development have focussed on providing heritage to COTS components for future use and novel scientific research. The modular format of the CubeSat standard has allowed the research community to expand, where individual members can either provide a whole CubeSat or parts there of to the rest of the community.

Based on trends within literature the performance of a μPPT was postulated and a CubeSat mission analysis was conducted. A limiting factor of the CubeSat platform is the 25 year deorbit limit legislation and the situation that CubeSats are nominally secondary payloads on launch vehicles. The legislation means that a CubeSat (dependant on its size and mass) needs to be placed in an orbit between 513km to 651km. As these satellites are secondary payloads, they may be inserted into orbits greater than these, up to 820km for the Soyuz launch vehicle. A propulsion system delivering ΔV between 24ms^{-1} to 164ms^{-1} would ensure that CubeSats achieve the limits set out by the 25 year legislation whilst not being limited to the launch they are placed on.

A CubeSat with propulsion could also counter orbital disturbances i.e. atmospheric drag, solar radiation pressure, gravitational effects from other bodies etc. Dependant on the platform, the incorporated thruster and the orbit the yearly ΔV requirement is estimated to be approximately 2ms^{-1} to 6ms^{-1}.

The μPPT provides additional benefits; it is low cost to manufactuer, the propellant is inert and not pressurised (which is a safety concern from launch providers where secondary payloads are concerned), it has a discreet small repeatable impulse bit allowing the CubeSat to have precise pointing accuracy and it can be used to dump accumulated momentum from reaction wheels.

There is now a need to study the PPT in detail to overcome issues in miniaturisation, in particular condensing the propellant, the propellant feed mechanism and the discharge initiator, whilst maintaining good performance. This will be done in several stages. A large scale PPT will be constructed and experimented upon. A performance model will be created that compares real data to modelled data. The understanding and learning from these processes will then aid in the construction of a μPPT that will be flown on a 3U CubeSat.

Chapter 4

PPT Experiments

4.1 Introduction

The experimental work of this research was split in to two phases. The development of the facilities and the actual experiments. Due to limited funds experimental facilities were not present from the beginning of the research and had to be procured over a period of time. The initial lack of experience using some of the procured facilities and/or equipment meant that unforeseen delays and errors occurred that affected the overall research schedule. In all, these delays extended the project by two and a half years. The first part of this chapter reviews this period in which several iterations of facilities and PPT breadboard models were constructed and evaluated.

Once the facilities and equipment were in a state to complete useful research, experiments were performed to study the erosion effect of the Teflon^{TM} and how certain geometrical and electrical parameters of the thruster module affected the erosion rate and carbon deposition back on to the Teflon^{TM} surface. The erosion of the Teflon^{TM} and the carbon deposition that coats the Teflon^{TM} surface after each discharge has a significant impact on the lifetime of the thruster and would be a major life limiting factor in a μPPT. It was during this time that an accident in the laboratory occurred when the Teflon^{TM} became dislodged and fell from its holder, however the thruster still operated nominally. From this event it was decided to look closer at the electrode erosion effect and to study how this process affects the overall discharge within the PPT. A vast majority of the experiments were conducted without Teflon^{TM} to create a database of current and voltage signals of the discharging capacitor in a variety of electrode configurations. This database would then become the validation tool to future computational modelling. The second part of this chapter reviews and comments on the results of the conducted experiments.

During this work, many designs and PPT concepts have been proposed for a number of proposals and conference submissions, see Figure 4.1. The next section is dedicated to the concepts that were further developed into experimental testbeds.

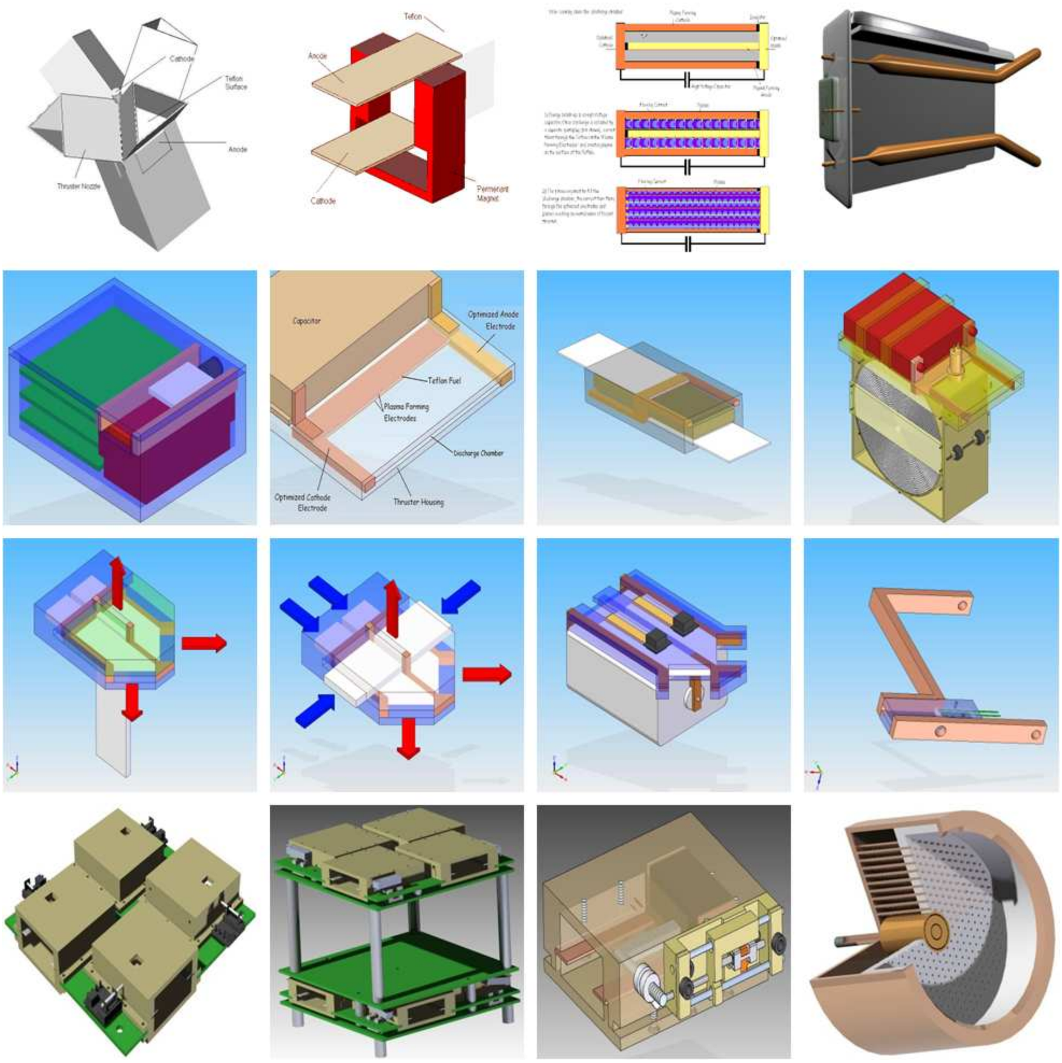

Figure 4.1: A montage of design work on various PPT concepts undertaken during this work

4.2 Part 1: Evolution of Facilities and Breadboard PPTs

A goal for this research was the development of facilities and equipment for electric propulsion work. Initial funding was restrictive, which dictated the direction and growth of the research. The Surrey Space Centre indicated that it wished to perform an experimental program within the electric propulsion field focusing on the goal of creating a thruster for small satellites. With minimal funds and no facilities key components were identified that would need to be built or developed. Limited funds also affected the reach and scope of the initial research to experiments that could be conducted with cost effective facilities. The key facilities and components that were identified prior to experimentation were as follows:

- Breadboard PPT: A Breadboard PPT is needed where parts of the design can be altered to measure various parameters. Parameters of study include Teflon^{TM} surface area exposed to plasma, separation distance between electrodes and electrical parameters of the PPT capacitor.

- A Vacuum Chamber: Although a PPT can be discharged at atmosphere (if the charge voltage overcomes the atmospheric dielectric strength), the plasma mass created would originate from the ionisation of air molecules. To ensure operation at vacuum conditions experiments need to operate at around 10^{-6}mbar. Pressures higher than this will cause the breakdown of the discharge through residual gas molecules within the vacuum chamber, rather than the desired propellant.

- High Voltage Power Supplies: The PPT works by storing energy in a high voltage pulse capacitor and discharging this energy initiated by a discharge initiator. Two power supplies are required: one to charge the PPT capacitor and the other to initiate the discharge via a sparkplug. The PPT capacitor will need to be charged up to 5kV and the sparkplug would need up to 30kV to initiate a spark within the vacuum environment.
- Measurement Collection Equipment: To collect meaningful data that could be compared with modelled results a high bandwidth oscilloscope with sensitive probes is required. The oscilloscope will be required to record data on the sub microsecond scale accurately; data collection above 100MHz will be adequate. A short rise time high current rated rogowski coil situated around one of the electrodes insulated against high voltage will be used to collect discharge current data. A high voltage oscilloscope probe will be required to collect voltage data.
- Scales: Mass loss data from the propellant is required to calculate the mass flow or mass bit per discharge. Each discharge will erode around 1-30μg of propellant so a sensitive balance is required to measure the mass loss over a given experimentation time. The sensitivity of the balance will affect the duration of each experiment conducted.
- Impulse Balance: An impulse balance is required to calculate the actual performance of the thruster. Although the impulse can be calculated with around a 10% error from manipulating the current signal (which does not take into account post process effects like macro particle ejection), a sensitive impulse balance is essential in gathering actual data on thruster performance characteristics.

4.2.1 Breadboard PPT: Attempt One

The budget put aside for this PPT research was very restrictive and there was limited budget for buying equipment. All the facilities were procured for free, borrowed or built from scratch. The experiments were tailored to goals that could be achieved with limited resources. Early effort focussed on constructing a PPT testbed and the necessary facilities. Experimental goals focused on investigating the relationship between the surface area of the Teflon^{TM} exposed to the plasma and the resulting mass erosion from the Teflon^{TM}, meaning only a sensitive set of scales was required to measure the mass loss of the propellant bar before and after experimentation that kept facility costs to a minimum.

The first testbed developed is shown in Figure 4.2. The acrylic thruster housing was designed so that the aluminium plate electrodes could be adjusted to various separation distances, which ranged between

2mm to 102mm, however the nominal distance the electrodes were set at was 35mm. The electrodes were 3mm thick, had a width of 60mm and a total length of 120mm. The Teflon^{TM} propellant bar could be various widths and heights but for nominal testing was kept at 35mm in height and 20mm in width. The electrodes were connected to a 0.25μF capacitor (rated at 4kV) by multi strand threaded copper wires that were bolted into place. The discharge initiator was made from two tungsten wires located in close proximity and embedded into a block of Teflon^{TM} to insulate the Tungsten wires from the aluminium cathode of the testbed.

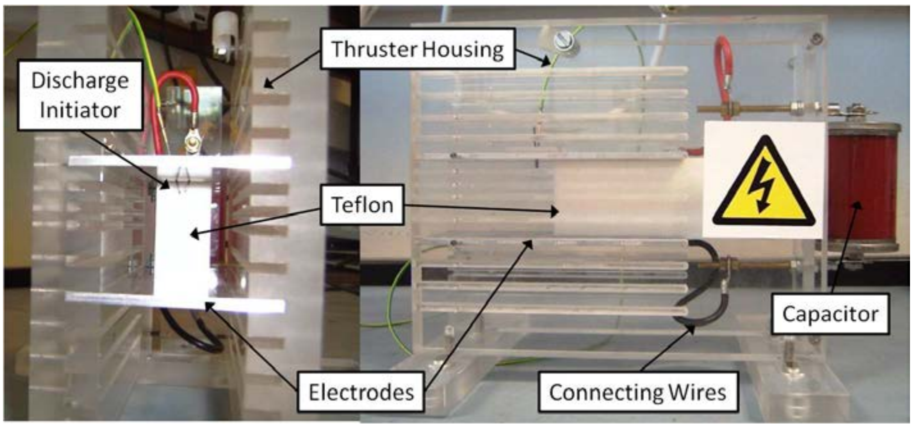

Figure 4.2: The first PPT testbed

The testbed capacitor was charged by a power unit designed and constructed by one of the University technicians, see Figure 4.3. The power supply provided a High Voltage (HV) signal at 3.6kV and operated by switching a high frequency transistor that was linked in series with a step-up transformer. The high voltage peak that was created by the switching of the fly back convertor transferred 0.4mJ every 20μs at 3.6 kV to a set of four HV capacitors which were used to charge up the main testbed capacitor.

The Tungsten wires were connected to a spark generator which was in the form of a transformer, capacitor and transistor mechanism, see Figure 4.5. A standard automotive ignition coil was used as a transformer as these devices where inexpensive COTS that were especially designed to handle repetitive high voltage spark generation. 250V D.C. was supplied to a set of five parallel 0.22μF capacitors that in turn were connected in series to the ignition coil. A high voltage transistor was inserted between the ignition coil and ground. Switching the transistor allowed the capacitors to discharge through the transformer (100:1). The voltage was stepped-up to around 20kV which was thought to be enough to overcome the dielectric strength of the Teflon^{TM} propellant and initiate a discharge. The transistor was connected to an analogue automated trigger and counting circuit that controlled the total number of discharges.

To conduct the PPT experiments it was required to procure a vacuum chamber. The University had no suitable chambers and buying one given the limited budget was out of the question. The Westcott vacuum chamber, see Figure 4.6, was salvaged from a once secret establishment known as the 'Rocket

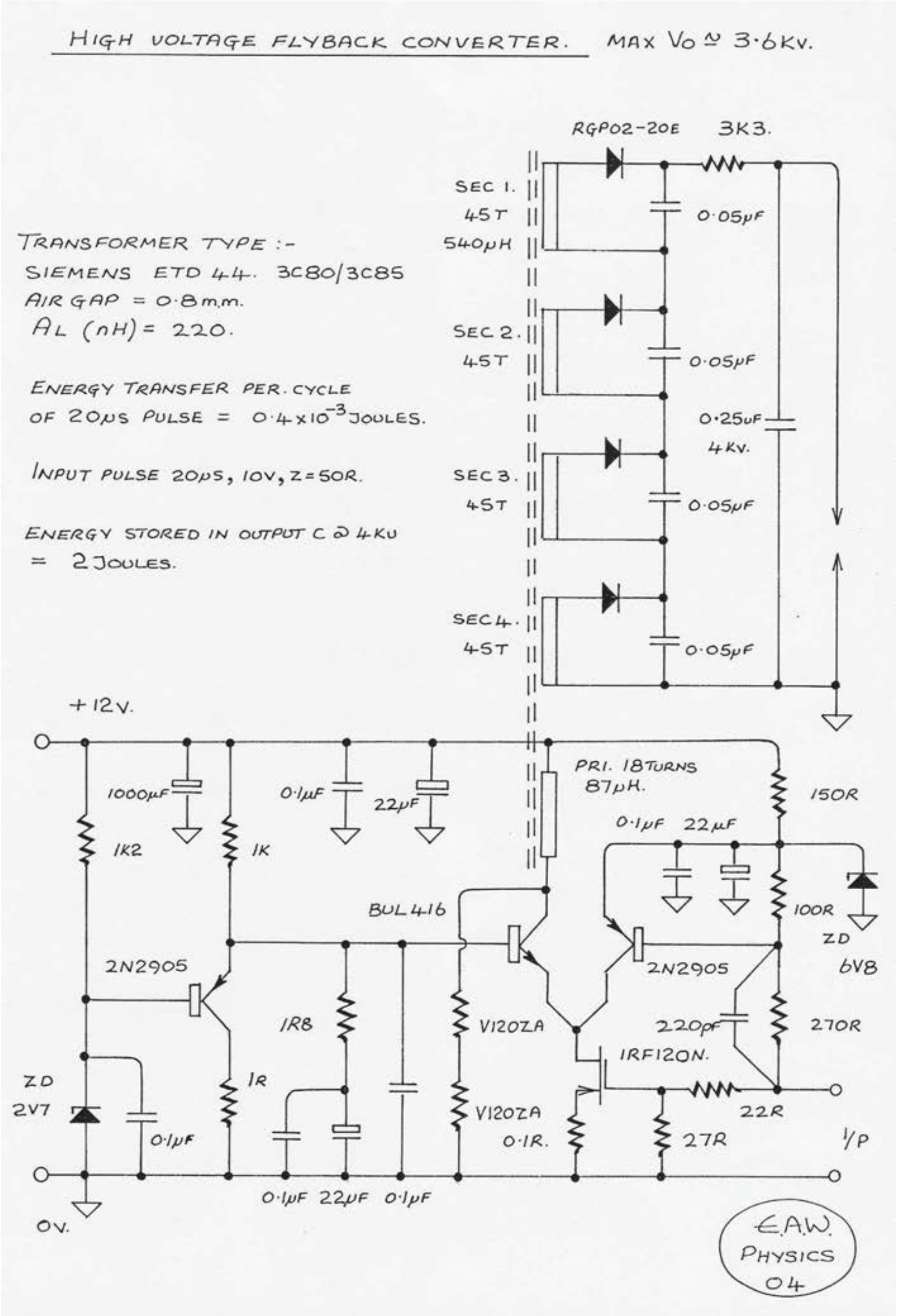

Figure 4.3: Circuit schematic for a 3.6kV high voltage fly back convertor

Propulsion Establishment (RPE)' located in Westcott. The RPE developed military ballistic missiles, including the Blue Streak rocket engine during the 1950's and 60's. The chamber is a diffusion pump based vacuum system with its main cylindrical chamber being 100cm in length and 30cm in width.

The diffusion pump, see Figure 4.7, operates by momentum transfer and can achieve ultimate pressures of 10^{-10}mbar in modern systems, however it has a tendency to back stream its oil into the main vacuum chamber contaminating surfaces if operated incorrectly. Oil is heated in the central part of the base of the diffusion pump turning it into vapour that rises through a jet assembly. The vapour which rises in a laminar flow regime is converted into a molecular and supersonic flow regime through the jet

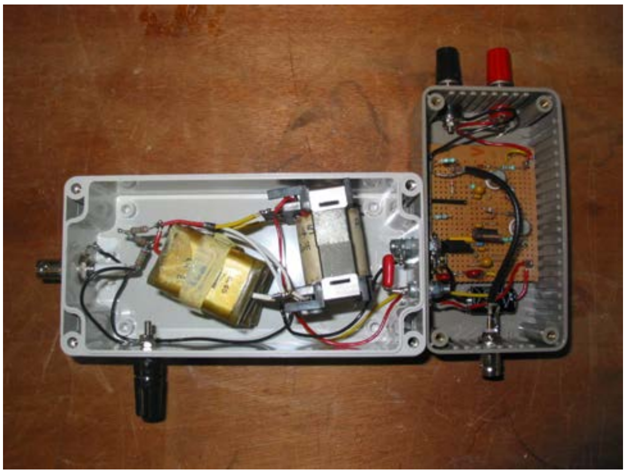

Figure 4.4: The completed 3.6kV high voltage power supply

Figure 4.5: The completed 20kV spark generator

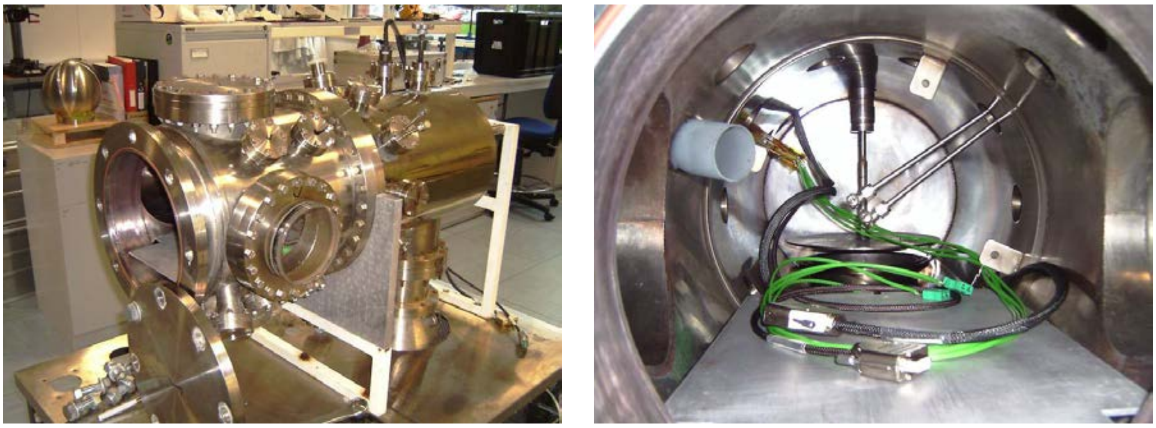

Figure 4.6: The external and internal view of the Westcott small vacuum chamber facility

assembly. The jets are then directed out of the central column to the side chamber of the diffusion pump walls where the oil is rapidly cooled by an external cooler and the oil, via gravity, returns back into the base oil well. Whilst in the supersonic molecular phase travelling from the central column to the outer walls, the individual oil molecules collide with other molecules within the vacuum environment partially transferring momentum. The directed streams ensure that the momentum and flow of particles is to the bottom of the pump where a connected roughing pump will extract the accumulated particles.

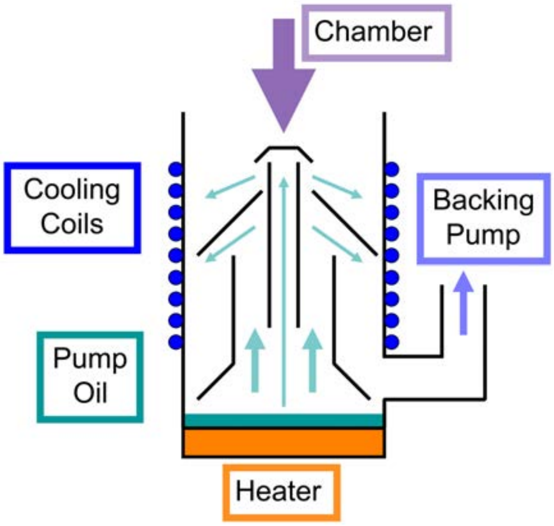

Figure 4.7: The internal dynamics and operation of a diffusion pump

Table 4.1: Westcott vacuum chamber statistics

Parameter	**Value**
Pump type	Diffusion pump
Volume	$0.07m^3$
Ultimate pressure	$10^{-4} - 10^{-5}mbar$
Pumping time	40 min

After refurbishment the chamber was able to obtain the following performance, see Table 4.1. The pressure gauges for the chamber were pirani gauges that were limited to an operational pressure of $5e^{-5}$mbar. It was not possible due to budget constraints to obtain gauges to measure beyond this pressure and so the ultimate pressure was unknown.

After refurbishment and solving several other minor issues the first testbed PPT showed a discharge within the vacuum chamber and some form of plasma creation, see Figure 4.8. This was taken as proof of concept of the thruster. It was only after prolonged testing of around 10,000 pulses per experiment that it became clear that the discharges that were taking place were not via the Teflon^{TM} propellant as no erosion was taking place. The conclusion was that the discharges were occurring through residual atmosphere in the chamber.

All in all the design, procurement, re-commission, development, evaluation and initial testing involved with all of the above took around 12 months. Two options presented themselves at this time, due to being able to show a ‘proof of concept’. Funds were made available for either the procurement of a larger second hand chamber from the space and defence company Astrium or the refurbishment of the Westcott chamber. To advance the goals and facilities overall at the Surrey Space Centre it was decided to invest in the larger chamber from Astrium. Due to imminent renovation works at the company the

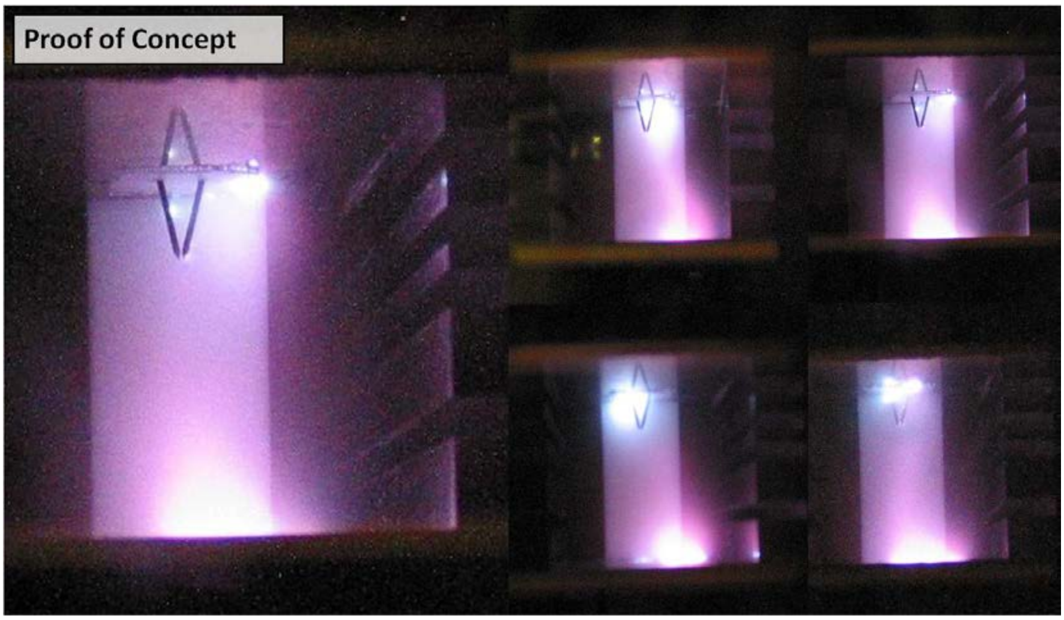

Figure 4.8: Proof of concept of a pulsed plasma thruster discharging in the Westcott small vacuum chamber facility

chamber was originally destined for the scrap heap until a chance meeting occurred that saw agreement from Astrium and the University of Surrey for the transferral of the chamber to the Surrey Space Centre, see Figure 4.9.

Figure 4.9: Left: Moving of the large vacuum chamber from Astrium to the Surrey Space Centre. Right: The chamber in its original configuration

4.2.2 Breadboard PPT: Attempt Two

During the time it took to resolve the procurement and refurbishment of the larger vacuum facility a second testbed PPT was constructed. By the time the larger vacuum chamber was complete there was a pressing need to obtain results. By designing a PPT based on lessons learnt from previous experiments and that had similar features to those found in literature it was thought that this would be the quickest way to get a testbed operational.

The second testbed developed is shown in Figure 4.10. The testbed was designed in parallel with initial modelling efforts that had been conducted, which suggested that the dimensions of the plasma within the discharge chamber were significant. In an effort to constrict the plasma with a physical barrier, a testbed with adjustable side walls was designed. The electrode separation distance was non-adjustable and set to 30mm (a common distance found in literature; LES8/9[41], E0-1[42] and Dawgstar[43] all had similar dimensions). The electrodes were made from aluminium had a thickness of 3mm, a width of 60mm and a total length of 120mm. The main housing was made from acrylic, but the constricting side walls were made from Ultem^{TM}, which had a relatively high dielectric strength and melting temperature. The capacitor was also changed in several ways; the capacitance was increased to 4μF and the connections between the capacitor terminals and the electrode plates were directly bolted together (in an effort to decrease the overall inductance of the system). The discharge initiator was also brought more in line with conventional PPTs by using an automotive sparkplug set into the cathode electrode.

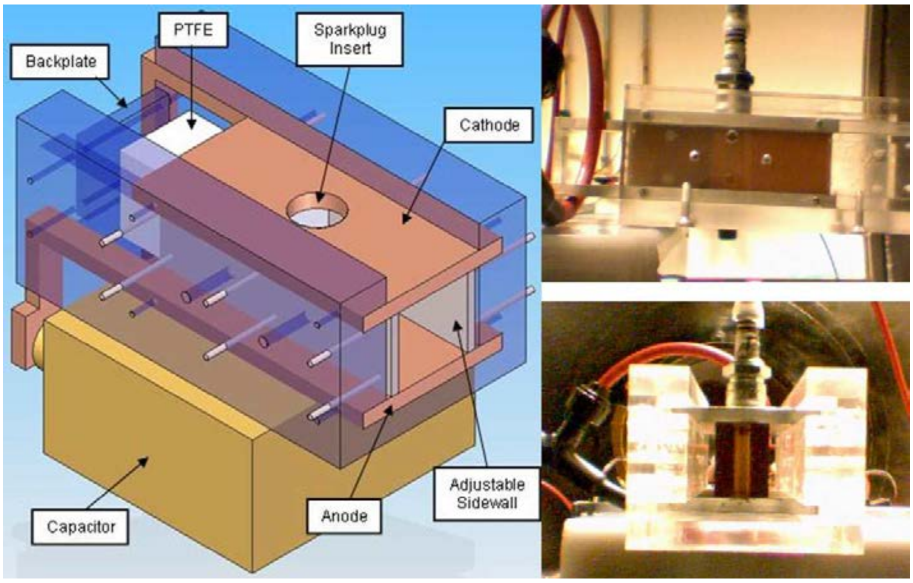

Figure 4.10: The second PPT testbed

With an increase in funds, updated equipment and facilities could be procured. A Stanford Research System Inc. PS350 rated at 5kV and 25W power supply was acquired to replace the custom built single output 3.6kV power supply. A Testec 40kV voltage probe and a Power Electronic Measurements Ltd. CWT rogowski coil were procured to measure the voltage drop across the main PPT capacitor terminals and the current that flowed from one terminal to the other, see Figure 4.11.

Initially the discharge initiator and current limiting circuitry between the PS350 power supply and the capacitor were housed inside the vacuum chamber, as this provided an electrically safe working environment (with the vacuum chamber acting as a faraday cage). It became apparent that this was not adequate as the power dissipation through the resistors of the current limiter began to melt in the vacuum environment (due to poor heat conduction). Several attempts were made to rectify this by

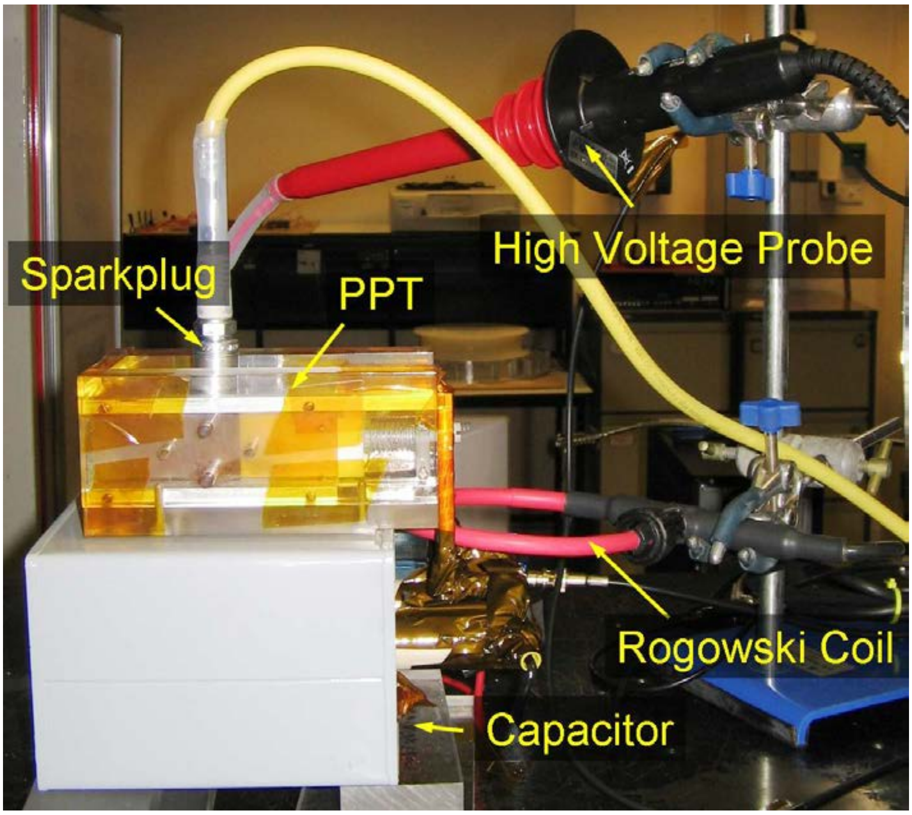

Figure 4.11: The in situ CWT rogowski coil and the Testec 40kV voltage probe

adding large heat sinks but eventually it was decided to remove the circuitry from within the chamber and place it outside where normal convection with air kept the resistors cool. This meant that additional high voltage feedthroughs were required.

The upgraded large vacuum chamber, named Pegasus, is a turbo molecular pump vacuum system with a main cylindrical chamber that is approximately 1.2m in diameter and 1.5m in length. The vacuum chamber in its lifetime at the Surrey Space Centre has been refurbished twice, once when it first arrived and then again after the control stack failed to operate.

The turbo molecular pump, see Figure 4.12, operates by momentum transfer and can achieve ultimate pressures of 10^{-8}mbar. The pump operates using multiple layers of rotating blades and fixed stators. The angled rotating blades collide with the gas molecules and transfer their mechanical momentum into them, directing and 'pushing' the molecules in a downwards direction. The fixed angled stators inbetween the rotating layers limit the back flow of molecules. The mechanism and physical limitations of the high speed rotational pump can only compress the molecules to a pressure of around 10^{-3}mbar. If higher pressures exist at the outlet of the pump it will stall, so a roughing pump is required to maintain a low backing pressure at the pumps' outlet.

The Pegasus chamber was donated to Surrey Space Centre by Astrium and after initial renovation the chamber was successfully operated. The original setup had various issues which were born out of its 25 years of service and, prior to its transferral, minimal maintenance. The ultimate pressure was unknown

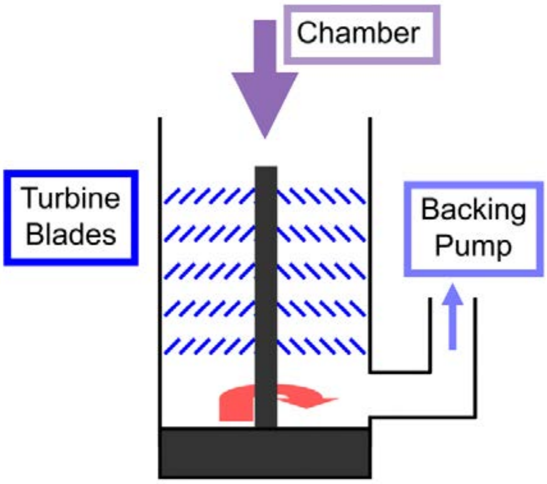

Figure 4.12: The internal dynamics and operation of a turbo molecular pump

due to a faulty ion gauge controller that was assumed to be giving the correct readout and so for a long period the chamber was thought to be in a good condition. After the turbo pump failed and was replaced at a significant cost, a new ion gauge was added with a separate controller. It was shown that the ultimate pressure was only 10^{-4}mbar, indicating significant leaks. Substantial funding was secured and the chamber went through an extensive period of refurbishment, replacing many components and controls. The Pegasus chamber, once refurbished, had the following statistics, see Table 4.2.

Table 4.2: Pegasus vacuum chamber statistics

Parameter	**Value**
Pump type	Turbo molecular pump
Volume	$1.5m^3$
Ultimate pressure	$10^{-7}mbar$
Pumping time	2 hrs

During the time of refurbishment the second testbed was also upgraded. The 4μF discharge capacitor (which was an old metal casing oil/paper capacitor) began to fail during development of this testbed, so a 5kV PPR50RD-405 custom purpose built capacitor from Hivolt Capacitors Limited which could handle repeated pulse discharges was acquired (which had a six month lead time).

Once the testbed was upgraded and the Pegasus chamber had been through substantial refurbishment, significant testing occurred. An issue that occurred immediately in the vacuum at 10^{-7}mbar was that the discharge of the PPT testbed was not being initiated consistently and only operated for the ten or so discharges after the experiment was pulled down to vacuum conditions. The solution to this problem was not immediately obvious and it was initially thought to be a problem with the sparkplug and the distance between the sparkplug electrodes. However after extensive tests and reading in available literature the sparkplug electrode distance in the vacuum, at the 1±0.5mm scale should not have been an issue. Literature suggested though that the sparkplug electrode surface conditions did have an effect.

Trying different surface conditions (polished and filed) did not improve anything.

Focus changed to the discharge initiator and specifically the ignition coil, see Figure 4.5. It was realised that although ignition coils created significant voltages it did not provide enough current to the initation of the discharge. A new discharge initiator was built using a 60kV power supply, a current limiter (to provide surge protection to the power supply) and a single 10nF (rated at 30kV) capacitor put in parallel with the sparkplug. This system to initiate a discharge worked and was consistent which allowed for extended testing.

However new issues occured which involved inadequate grounding of experimental facilities and erroneous discharges. The inadequate grounding caused floating potentials to be observed and the destruction of two power supplies and the rogowski coil electronic integrator. Initially the problem was thought to be wear and tear, but once identified the solution was to have a single point common ground for the PPT and vacuum chamber that was connected to a three phase earth line. A second single point common ground that was filtered through an isolation transformer was then used for the experimental devices.

The final straw for the second testbed was the inability to suppress substantial erroneous discharges. Kapton tape was used to try to insulate high voltage breakdowns in certain areas but to no success. The second testbed had an unfortunate flaw in its design in which sharp edges near the rear of the testbed PPT promoted locational discharges in that area. The only solution was to redesign the testbed.

4.2.3 Breadboard PPT: Attempt Three

The third attempt of designing the testbed, produced a PPT which looked very abstract, see Figure 4.13. The testbed focussed on stripping the PPT to its bare essentials in an attempt to design out any possible areas that could lead to erroneous discharges or breakdown via unwanted surfaces. The electrode material was changed from aluminium to copper, a more common metal for PPT electrodes to be made from. The sidewalls that contained and constricted the plasma were made from Ultem^{TM} and were directly bolted to the Teflon^{TM} propellant, via plastic screws, see Figure 4.14.

The focus of experiments at this time had evolved to investigate the erosion of the Teflon^{TM} as a function of the surface area that the discharge plasma covered and how this also affected the back flux of carbon atoms on to the Teflon^{TM} surface.

To investigate the carbon back flux experiments it was important to obtain the heat gradient of the Teflon^{TM}propellant bar. K type thermocouples were mounted within the Teflon^{TM} bar at a distance of 1mm behind the surface of the propellant, which was exposed to the generated plasma. Drilled inserts from the rear were used to locate the thermocouples as close to the surface as possible, see Figure 4.14. Thermocouples were then passed through the vacuum chamber wall and attached to a National Instruments data acquisition card which interfaced with a LabVIEW controller.

The data received from the thermocouples was inconclusive, the thermocouples and NIDAQ card did

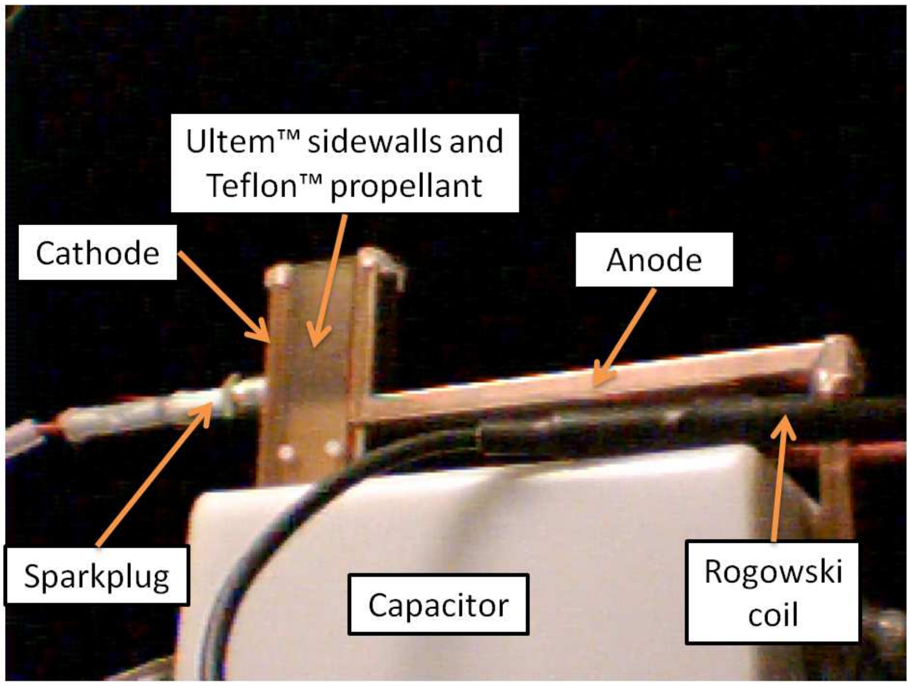

Figure 4.13: The third PPT testbed

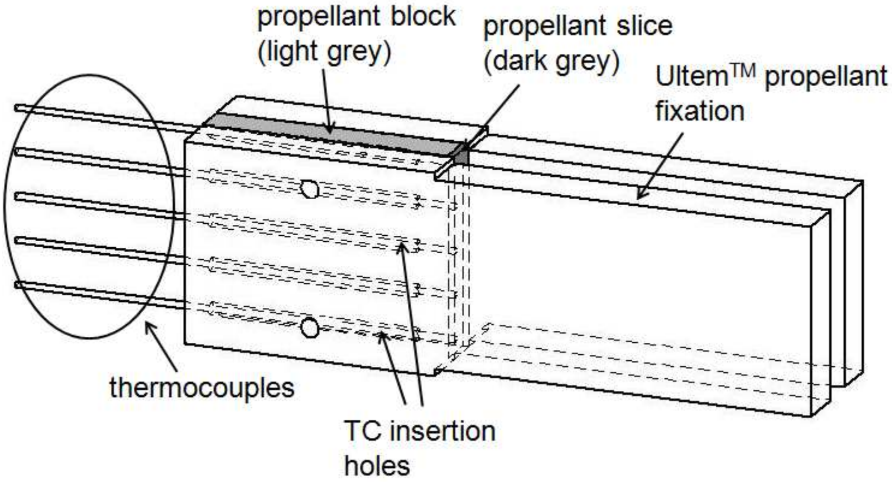

Figure 4.14: Five thermocouples (TC) mounted within the Teflon^{TM} block, that was bolted to the Ultem^{TM} sidewalls of the thruster housing

not differentiate any changes in temperature within the propellant bar on the microsecond timescale, see Figure 4.15. The achievable bandwidth, the sample rate of the NIDAQ card and the sensitivity of the thermocouples were the main issues. Procuring a large bandwidth NIDAQ card was not within the project budget. Repeated long duration tests were not conducted as this was not seen as a main priority. Due to time constraints the investigation using thermocouple data was dropped from the experimental phase.

A sensitive mass balance was required to investigate the erosion of the Teflon^{TM}. The mass before and after a set number of discharges was compared and the average mass loss per discharge was recorded.

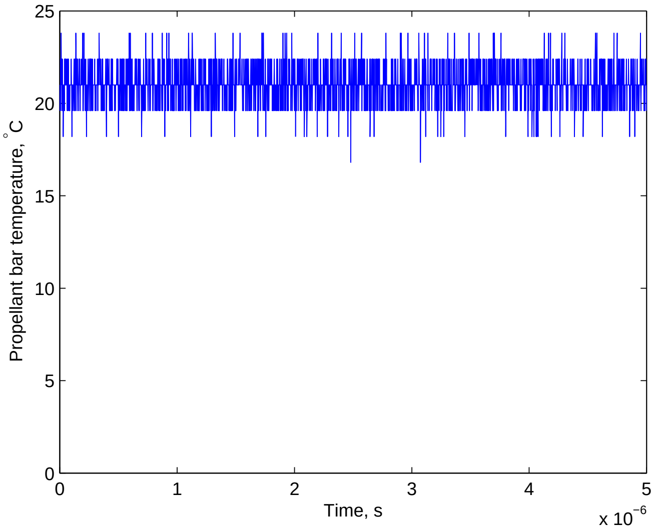

Figure 4.15: A typical example of the acquired thermocouple data for a single discharge

The mass balance used was a Sartorius MC5 that was limited to a total sample mass of 5.1g and was accurate to 1μg. This required that the Teflon^{TM} used in the experiments was a thin slice placed and clamped into position on the surface of a Teflon^{TM} block, see Figure 4.14. The absolute sensitivity of the balance $\pm 1\mu$g was in the range of the desired measurements (1-20μg) and so it was necessary to perform a statistically large number of discharges per experiment to minimise the inaccuracy that this would create. Further difficulties arose in using the sensitive measurement balance due to static charging of the Teflon^{TM} samples, the static charge would interfere with the internal measurement sensors within the balance. Averaged repeat measurements and anti static precautions were implemented when using the sensitive balance to minimise the effect of this inaccuracy on the results.

Due to the need to run the experiment over a long duration (hundreds to thousands of pulses), it was important to automate the discharge process. To do this the National Instruments LabVIEW software was integrated into the experiment. The LabVIEW program controlled nearly all the experimental devices, the block diagram of the program is shown in Figure 4.16.

The Testec 40kV voltage probe was designed to be attached to a multimeter to give analogue measurements to within 10% accuracy. When the signal from this probe was inputted into the LabVIEW program via the NIDAQ card (as with the thermocouples) it was found to be unusable for measuring the pulsed voltage information over the 30μs pulse discharge. A Tectronics TDS2024 oscilloscope with 2.4GHz bandwidth with an Agilent Technologies high-voltage oscilloscope probe was used to measure the voltage profile of the discharging capacitor. The limitation of the oscilloscope probe was that it was only rated to 4kV, which would put a limiting factor on the maximum capacitor charge voltage that could be applied to the testbed.

During the long duration tests significant deposits of carbon were building up on the Ultem^{TM}

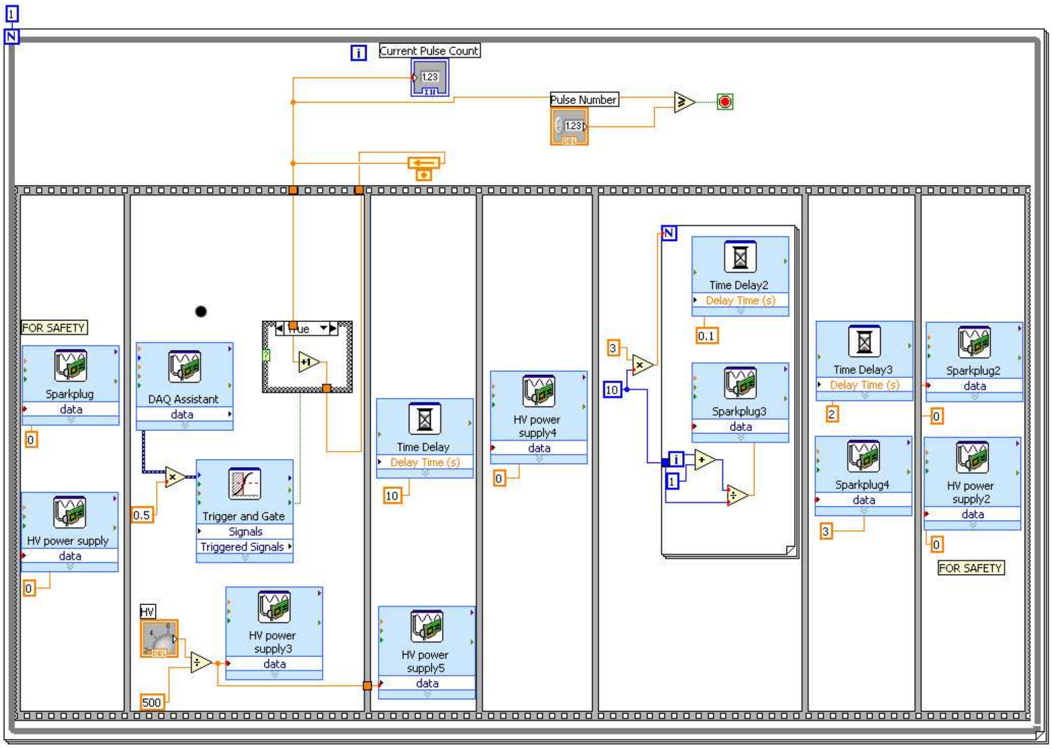

Figure 4.16: Block diagram of the LabVIEW program that controlled the PPT experiment

Figure 4.17: Carbon build up on the Teflon^{TM} surface

sidewalls and Teflon^{TM} propellant, especially for discharges above 3kV, see Figure 4.17. The carbon deposits built up enough over a single testing regime to provide a conductive layer and alternative route for the capacitor to be discharged through, acting like a bleed resistor between the two capacitor terminals. During these experiments as the PPT discharged, the maximum charging voltage the capacitor could attain decreased. This was because with each discharge the effective bleed resistance of the carbon conductive layer was decreasing. In an effort to overcome this issue the Ultem^{TM} sidewalls were removed and the experiments were limited to 3.1kV, see Figure 4.18.

During testing without the Ultem^{TM} sidewalls, two important observations were made. The first

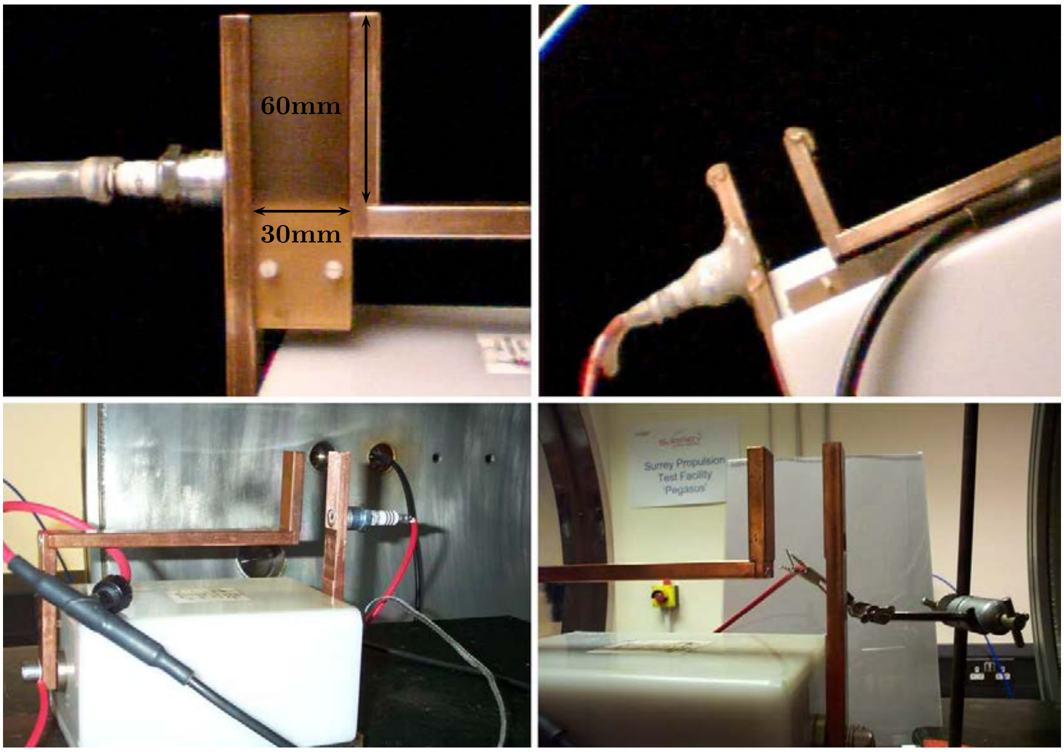

Figure 4.18: Final modifications made during experimental testing. Top Left: PPT testbed with Ultem^{TM} sidewalls and Teflon^{TM} propellant. Top Right: PPT testbed without sidewalls but with Teflon^{TM} propellant. Bottom Left: PPT testbed without sidewalls and Teflon^{TM} propellant. Bottom Right: Changing the sparkplug to a single Tungsten electrode

was that the dimensions of the Teflon^{TM} propellant were having little effect on the current signal of the discharge. Several differing widths of Teflon^{TM} were placed between the copper electrodes and at the same discharge voltage they had similar current discharge profiles. The second observation was that during one of the tests the Teflon^{TM} slipped from its holder, yet it still discharged with no Teflon^{TM} inbetween the electrodes, see Figure 4.19.

These two observations changed two assumptions that had been made throughout the work to date. The first assumption was that the surface area of the Teflon^{TM} 'roughly' defined the dimensions of the plasma bulk. This assumption was changed to say that the dimensions of the electrodes 'roughly' defined the dimensions of the plasma bulk. The second assumption was that the plasma formed on the Teflon^{TM} surface first and then accelerated through the discharge chamber. However the measurements suggested that the plasma can form without the need for the Teflon^{TM} propellant bar to be present.

To get to this stage three and a half years had passed. These measurements were intriguing and it was decided that the rest of the short period left to conduct experiments should be dedicated to gaining data of discharges without Teflon^{TM}. It was decided to conduct experiments with different electrode separation distances and then create a model which would be validated against these results. The tests went relatively smoothly because there was no carbon to build up on sparkplug electrodes or on other surfaces to form an alternative conducting path. However due to the mass of the electrodes it was

Figure 4.19: A still image of the plasma forming during a PPT discharge without Teflon^{TM} propellant

impractical to measure the relative masses before and after tests. It was therefore important to find an accurate mass model to predict the mass loss from the electrode surfaces during the discharge.

Another issue that arose during these tests was the modes of discharge that occurred using a sparkplug, see Figure 4.20. The top profile is a discharge initiated by thermionic electron emission. When current flowed through the ceramic material of the sparkplug into the embedded cathode an orange glow would form on the ceramic. The heated metals and ceramic would then promote electron emission and a discharge would occur. The bottom profile is a discharge initiated by thermo-field emission[24]. Brady noted two similar 'modes' of discharge using a sparkplug as a discharge initiator in a PPT[77].

The sparkplug was swapped for a single Tungsten filament, see Figure 4.18. The filament was held at a distance of 10mm from the cathode surface and was charged to a negative 15kV with a 10nF (rated at 30kV) capacitor placed in parallel with it. This method of discharge focussed on using thermo-field emission to initiate a discharge and performed flawlessly throughout the rest of the experimentation.

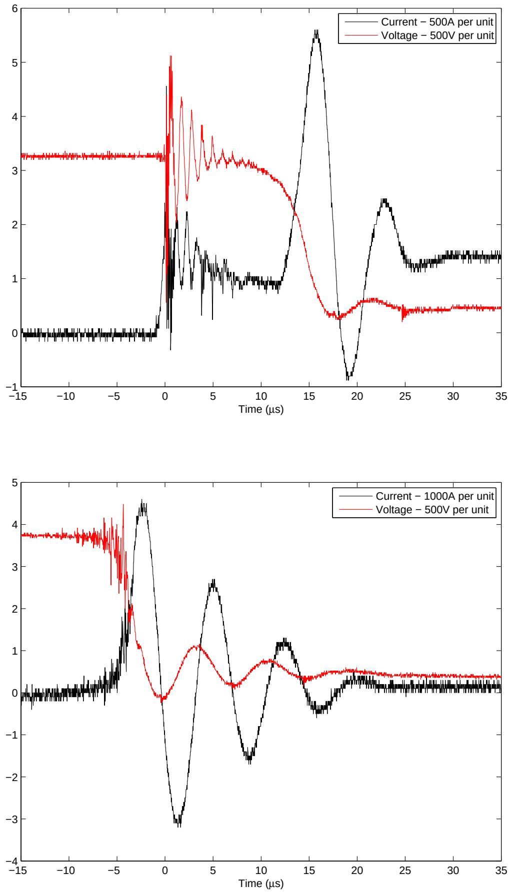

Figure 4.20: Current and voltage profiles showing two types of discharge. Top: Thermionic emission. Bottom: Thermo-field emission. The voltage is measured across the capacitor and the current measured by the Rogowski coil around the anode

4.3 Part 2: Experimental Results

4.3.1 Formation of the Data Sets

This section relates to the formation of the data sets as presented in Appendix B that were collected using the final iterations of the PPT testbed. The plots within Appendix B are the mean current and voltage signal profiles. These profiles are averaged over a number of samples. The current data is recorded by a CWT rogowski coil that was located around the anode, see Figure 4.21. The voltage data was recorded by an Agilent Technologies 4kV voltage probe that was indirectly connected to the anode terminal of the PPT discharge capacitor and to ground. Although the ground connection of the PPT discharge capacitor and the ground connection of the voltage probe was common, the two connections to this ground were not localised in the same area. This may have caused noise within the observed signal. The 4kV Agilent Technologies voltage probe was connected to the power line outside of the vacuum chamber which fed to the anode terminal of the PPT discharge capacitor. This power line had two locations where it was exposed (not shielded) within the vacuum chamber, so this may be another source of noise within the signal data.

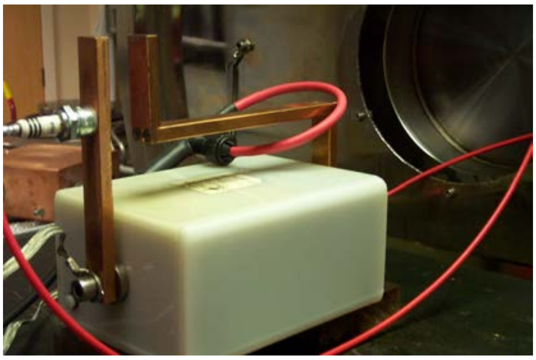

Figure 4.21: Location of the red CWT rogowski coil around the PPT anode

The two signals were processed through a TDS 2024 oscilloscope, which saved the data as comma separated value files. Once a number of samples were collected for each set of experimental variables they were then processed in the MATLAB environment. Data was adjusted to take into account the multiplication factors of the two probes. It was than smoothed to remove transient effects due to noise, using the internal MATLAB 'Savitzky-Golay Filtering' function, see Figure 4.22.

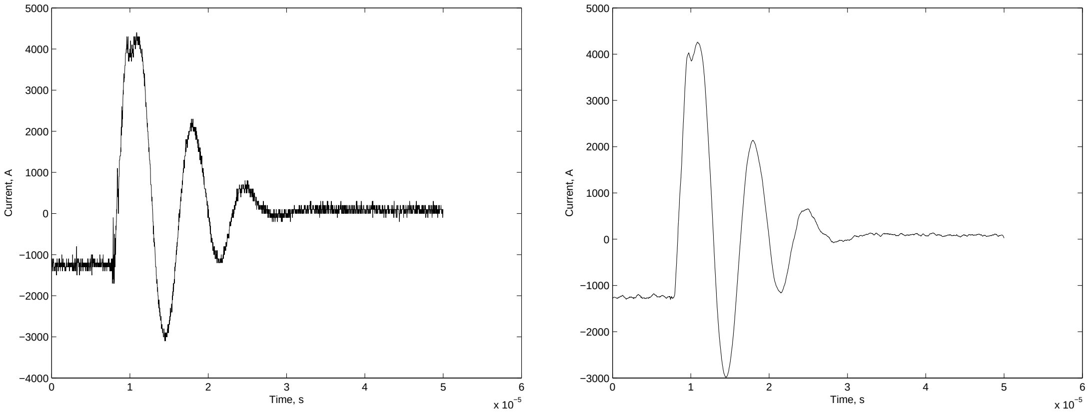

Figure 4.22: Smoothing the signal data using the MATLAB 'Savitzky-Golay Filtering' function. Left: Before filtering, Right: After filtering

A significant issue with the data manipulation was that the signals although common in size and amplitude, did not share common origins. To average these signals it was required to align them in the most effective manner, see Figure 4.23. The top profile shows the distribution of the unaligned samples. The first step was to identify two common points within all the signal data which would aid in aligning the data with each other. The first common point chosen was in the current axis and was the area in which the signal stopped ringing. In theory this is the point where no current flows through the electrodes. Taking a signal average of this area and subtracting it from the original signal aligned all the data samples in the current axis, see the middle profile of Figure 4.23. The signal than needed to be aligned in the time axis and this was done by aligning all the data samples so that the maximum of the first peak in the current profile was aligned with each other. The time stamps for when this occurred were than transferred to the voltage signal so these could than be appropriately aligned as well, see the bottom profile of Figure 4.23.

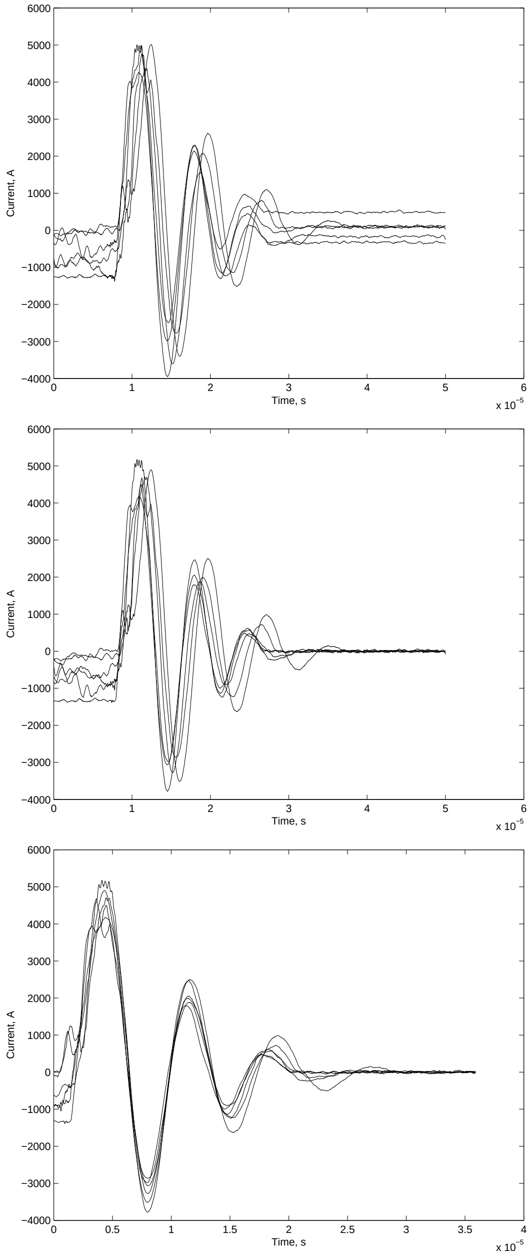

Figure 4.23: Top: Unaligned signals. Middle: Aligned data in the current axis. Bottom: Aligned data in the current and time axis

Once aligned the average signal for the current and voltage were calculated. Error bars are formed from the standard deviation from this average signal. The impulse bit I_{bit} of the discharge can be estimated using the following relationship;

$$I_{bit} = L' \int I^2 dt = \frac{1}{2}\mu_0 \frac{h}{w} \int I^2 dt \qquad (4.1)$$

It has been reported that Equation 4.1 has a tendancy to over predict the impulse bit. A number

Table 4.3: Standard configuration for the PPT testbed

PPT Parameter	**Experimental PPT**
High Voltage Capacitor	
Capacitance	4.06μF
Inductance	$\approx$325nH
Charging voltage	Variable
Discharge Initiator (DI)	
Type of sparkplug	NGK
Charging voltage	30kV
DI Capacitance	10nF
Electrodes	
Material	Copper
Width	20mm
Thickness	10mm
Discharge channel length	60mm
Separation	30mm
Teflon^{TM} (if present)	
Width	Variable
Height	30mm

of emperical alternatives have been reported for the inductance per unit length, L' [78]. However in all cases the inductance per unit length is thought to be a constant and the time varying significant factor is the current. So although the specific value of the impulse bit in the following plots may be inaccurate the trends that are seen are still significant.

Equation 4.1 only finds the electromagnetic contribution of the impulse and not that generated from neutral vapour gas dynamic acceleration or macro particle ejection that may be measured by using an impulse balance. The data for these signal sets is presented in Appendix B such that the current signal data is on the left hand side of the page and the voltage data is on the right hand side of the page. Each page shows up to four of these data sets. In the Figure label the graphs are sequentially referenced from one to four, one being the top pair of signals and four being the bottom pair of signals. The labels of each of the pair of signals show any alterations from the standard configuration as shown in Table 4.3.

The plots from Appendix B are used in this chapter to show how for a given set of variables the impulse bit varies with discharge energy, as calculated from Equations 4.1 and 3.12 respectively. The error bars for the impulse bit data is found by using the minimum and maximum current signal profiles with respect to the standard deviation from the average signal. These maximum and minimum profiles are then integrated in Equation 4.1 to provide the limits of the maximum and minimum impulse bit.

4.3.2 Discharge Initiation Experiments

Initial experiments focused on the Discharge Initiator (DI) to observe how the initiation of the thruster affected the overall performance. Literature indicated the significance of the initiation so it was important to establish how altering the DI had an effect on the overall performance of the PPT. Some researchers have theorised that the DI circuit creates a small injection of plasma that initiates the discharge. It was thought that by altering the energy used to create this initial plasma the overall thruster conditions would be altered. The standard DI configuration used a NGK sparkplug charged to 30kV with a 10nF capacitor in parallel.

The DI sparkplug voltage was increased from 15kV to 30kV to show how the increase in DI energy affected the overall discharge. At 15kV the DI energy would have been 1.13J and at 30kV this would have risen to 4.5J which was significant in relation to the ≈8J energy stored in the PPT discharge capacitor during these experiments. Figure B.1 shows the results of these experiments and it can clearly be seen that the energy of the DI has not had any effect on the signal profiles of the current or voltage signals. An additional capacitor was placed in parallel with the standard 10nF capacitor and again there was no effect on the signals of the overall discharge, see Figure B.2. The additional capacitor was removed and a 100M resistor was placed in series with the sparkplug in an effort to limit the flow of current and extend the period in which the DI capacitor discharged. Figure B.2 shows that this had no effect.

The capacitor was removed from the DI meaning that the 15kV power line was connected directly to the sparkplug. Yet again the PPT discharged and had similar properties to the previous experiments. At this point it was realised that the method of initiation was to do with the properties of the electric field around the sparkplug electrode rather than any mechanism that introduced a plasma into the discharge chamber. As an additional confirmation the sparkplug was replaced with a single Tungsten filament located in close proximity to the anode, see Figure B.2, which shows similar results to the previous signal profiles. The Tungsten filament was located in several different positions which had no effect on the overall signal profile properties of the discharging PPT.

In conclusion to these experiments it was shown that it was important to create an arc breakdown through the vacuum to initiate a discharge but the properties of this initial arc from the DI do not appear to be of significance to the discharging capacitor of the PPT.

4.3.3 Mass Errosion Experiments

Mass erosion experiments were conducted to measure the mass loss of the Teflon^{TM} propellant per pulse discharge. Another goal of the experiment was to see if there was any change in this mass loss per discharge as a function of total number of pulses discharged. The theory was that as the total pulse number increased than there would be additional carbon deposits upon the Teflon^{TM} surface and this would cause a decrease in performance and affect the mass loss per pulse discharge rate. The total number of pulses measured was 100, 301, 501 and 887 pulses. The Teflon^{TM} samples were measured on the Sartorius MC5 scales before and after exposure to the set number of discharges. The PPT was configured to the standard configuration. The width of the Teflon^{TM} investigated was 3.00mm. Figure 4.24 shows how the mass loss of the Teflon^{TM} per pulse discharge changed with the total number of pulses.

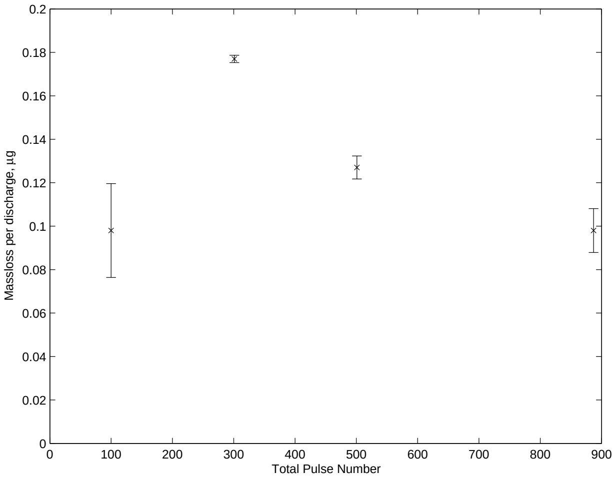

Figure 4.24: Comparing the mass loss per pulse discharge for a set number of pulses

There is a significant variation in the mass loss per pulse discharge of the samples which varies between 0.1-0.18μg. This variation can be explained if the datasets are examined, see Figure B.3. The variation observed in the mass loss per pulse discharge varies with the average discharge energy supplied to the PPT during the experiment. Although there are not enough samples to draw clear conclusions this does initially point to a correlation between the discharge energy and the mass loss per pulse discharge.

Figure 4.25 compares the carbon build up as a function of total pulse count. It can be seen that as the total pulse count increases the visible amount of carbon deposition also increases. However from visual inspection there is not a significant difference in carbon colourisation between the 501 pulse count and 887 pulse count sample, possibly indicating some form of steady state.

Figure 4.25: Carbon build up on the Teflon^{TM} samples as a function of total number of pulses

A PPT with sidewalls was also experimented on to see the effects of having a confined plasma has on the total mass loss. The PPT was set up in the standard configuration with a 3mm width piece of Teflon^{TM} between the electrodes. The PPT was then enclosed with Ultem^{TM} sidewalls that had a separation width equal to the Teflon^{TM} width, see Figure 4.18. The PPT in this configuration was pulsed for 178 discharges and an average mass loss per pulse discharge of 0.594μg±9.4ng was observed. Although this caused a triple fold increase in the mass loss per pulse compared to experiments without sidewalls the impulse bit of the discharge was similar to those from the previous experiments, see Figures B.3 and B.4. This suggests that the additional mass lost due to the sidewalls confining the plasma did not impact the performance of the thruster.

To summarise, the first set of experiments indicated that variations in the supplied discharge energy affected the total mass erosion of the Teflon^{TM}. The experiment with the sidewalls suggests that the manipulation of the mass erosion (by plasma confinement) does not affect the current and voltage properties of the pulse discharge. These results suggest that the eroded mass of the Teflon^{TM} is not intrinsically linked to the properties of the pulse discharge and the eroded mass is rather a by-product of the plasma being present. These results help to support the view that Teflon^{TM}mass erosion comes from the presence of a pre-existing plasma, rather than the other possibility that eroded Teflon^{TM} forms the basis of the evolving plasma.

It was during these experiments that a major leak in the vacuum chamber that had not been observed before was finally detected (due to a faulty ion gauge). Instead of being 10^{-6}mbar the pressure was actually 10^{-4}mbar. The results for these experiments may have been contaminated by this leak and should be taken with caution, however at 10^{-4}mbar-mm the discharge can still be considered as a vacuum breakdown.

4.3.4 Teflon^{TM} Width Experiments

Once the vacuum chamber leak had been resolved the next set of experiments were to confirm the results from the previous experiments and to see if the conclusions were valid over a larger set of variables. The PPT was configured to the standard configuration, see Table 4.3. The width of Teflon^{TM} between the electrodes that were investigated were 3.00mm, 3.53mm, 4.00mm, 5.00mm, 6.00mm and 7.50mm. The PPT discharge energy that each Teflon^{TM} was subjected to can be summarised in Figure 4.26. Following the same procedure as previous experiments a comparison was made between the mass loss per pulse discharge and PPT discharge energy. A second comparison was made between the impulse bit of the pulse discharge and PPT discharge energy. Figure 4.27 shows both comparisons. The average voltage and current profile data sets for these measurements can be found from Figure B.5 to B.8.

Comparing the impulse bit to energy for this set of experiments shows a clear trend. The linear relationship suggests a strong correlation between the impulse of the pulse and the energy supplied by the capacitor. The variation in Teflon^{TM} widths has not had an impact on the impulse bit of the PPT pulse.

Comparing the mass loss per pulse discharge to the discharge energy reveals some interesting results. First of all the width of the Teflon^{TM} does not seem to be a significant variable in these experiments. At low energies (below one joule) their is a large scatter in the mass loss per pulse discharge, with some values being negative. This represents the Teflon^{TM} sample gaining mass. This gain in mass could either be explained by electrostatic interference when using the micro mass balance (but repeated measurements tried to overcome this), contamination of the samples by alien objects (but the samples

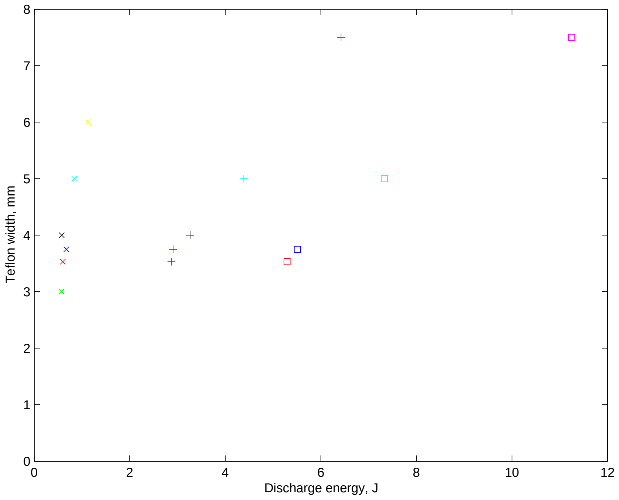

Figure 4.26: Matrix showing the conditions for the proceeding experiments

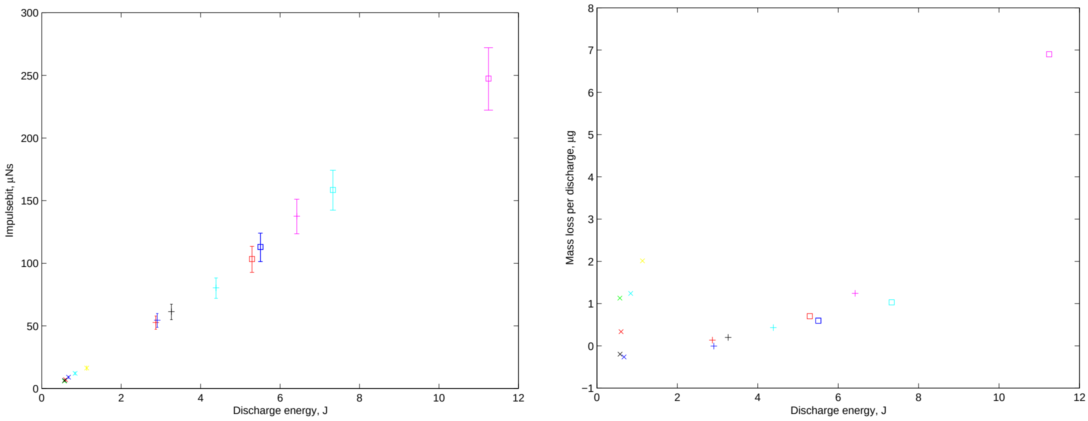

Figure 4.27: Left: Comparison between the impulse bit and PPT discharge energy, Right: Comparison between the mass loss per discharge and PPT discharge energy

were cleaned before each measurement), the temperature of the mass balance (but it was in a semi-controlled environment) or the carbon build up upon the Teflon^{TM} surface.

The large scatter may be an artefact of these measurement errors but at higher energies between 3-8J the scatter of measurements falls close to a trend line, where the mass loss per pulse increases with energy linearly. This would suggest that the procedural process is adequate and that the results below one joule are indicative of a process that is happening in this regime. The results suggest that at low energies the Teflon^{TM} mass loss per pulse is greater than it would be at energies between 3-8J.

The reason for this higher mass loss per pulse at low energies (less than one joule) could be for a number of reasons. There could be some form of resonant interaction that means more energy is absorbed into the Teflon^{TM} and so when this energy is converted to heat, more Teflon^{TM} macro particles are eroded. A second reason could be that at low energies the peak currents are significantly less, meaning that the magnetic fields produced by the flowing currents through the electrodes are also not as strong. This would lead to lower confinement of the plasma by the magnetic fields. If more plasma is distributed evenly throughout the discharge chamber and not confined close to the electrodes then there is more probability for the plasma to interact with the Teflon^{TM} and create larger erosion rates.

Figure 4.28 compares the carbon build up as a function of sample width and PPT discharge energy. Upon visual inspection there does not seem to be any trends when comparing the distribution of carbon build-up to the width of the sample. Below one joule (top line) there is minimal discolouration to the carbon samples despite the relatively large mass loss per pulse that can be seen from Figure 4.27. This suggests that the eroded mass is being efficiently accelerated away from the Teflon^{TM} surface without significant levels of carbon atoms returning to the Teflon^{TM} surface.

As the energy of the PPT discharge increases from ≈2J to ≈7J (middle line) several features develop. The first is an accumulation of scorched marks at the bottom edge of the Teflon^{TM} sample, indicating some form of high temperature process occurs here. This would coincide with the bright spots and their location as seen in images 7-11 in Figure 2.30. Also in this energy regime on each sample there is a deposition of carbon which evenly spreads itself over two thirds of the sample and peters out towards the top of each sample. As the energy is further increased from ≈5J to ≈11J (bottom line) another feature appears. This is a bare patch of Teflon^{TM} that is void of carbon deposition.

The void area suggests that carbon back flux is limited in these areas, this may be for a number of reasons. The magnetic field in this area may be stronger than in other areas ensuring that the flow of carbon cannot back flow onto the Teflon^{TM} surface. Another possibility is that the plasma temperature may be higher in this localised area, allowing for complete decomposition of the Teflon surface, while in other areas, the surface only partially decomposes leaving a visible carbon layer. This localised temperature would be similar to the plasma formations seen in the high speed photography, see Figure 2.32 between 0.6μs and 1.77μs (426.8nm filter) and Figure 2.31 between 4200ns and 7900ns.

It should be pointed out that not all the samples in this experiment were discharged with equal total pulse counts. As the carbon built up upon the Teflon^{TM} sample surface it became conductive acting as a bleed resistor between the electrodes. As the carbon built up the effective resistance would lower and the ultimate potential that the PPT capacitor could be charged to was limited. Experiments were cut short when the desired potential could no longer be attained.

In summary despite the higher erosion rates for the discharge energies below one joule, the mass loss per pulse does not directly affect the current and voltage signal of the PPT pulse (otherwise at energies below one joule the impulse bit gradient would have been different to the impulse bit gradient between 3-8J). This conclusion strengthens the argument that Teflon^{TM}erosion is independent from the voltage and current signal of the PPT pulse. It also strengthens the argument that plasma forms before the Teflon^{TM} erosion occurs and that the mass eroded from the Teflon^{TM} does not impact the electromagnetic contribution of the impulse bit of the PPT. This conclusion then suggests that if the plasma forms before the Teflon^{TM}erosion occurs then the PPT could operate without the presence of

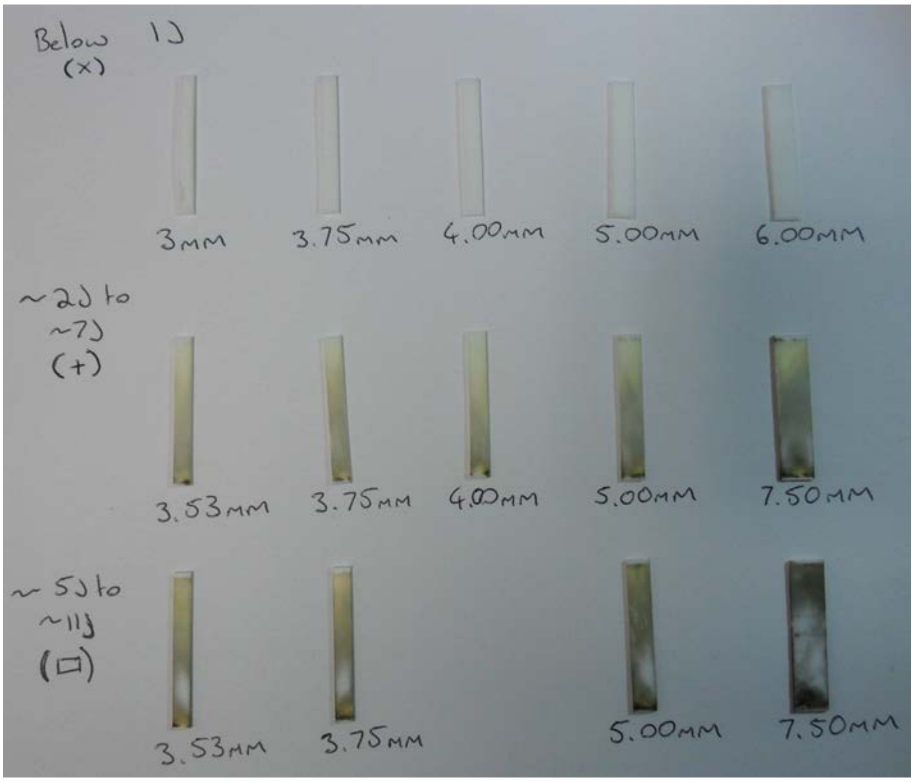

Figure 4.28: Carbon build up on the Teflon^{TM} samples as a function of PPT discharge energy. The symbols in brackets relate to the symbols in Figure 4.26 and 4.27

Teflon^{TM}.

4.3.5 Discharge Energy Experiments without Teflon^{TM}

The next set of experiments were conducted to see how the stored energy within the PPT discharge capacitor affected the overall properties of the PPT when the Teflon^{TM} sample between the electrodes was removed. The PPT was configured to the standard configuration, see Table 4.3. At each set voltage the experiment was repeated a number of times at different DI potentials (15kV, 20kV, 25kV and 30kV). This was done for two reasons: first, to reassess previous results but at various PPT discharge potentials to see if there is an effect at low or high energies. The second is to see if, without Teflon^{TM}, the properties of the discharge initiator had an effect on the overall discharge. The data sets for these experiments are shown in Figures B.9 to B.13. Comparing the impulse bit to energy for this set of experiments a clear trend is observed, see Figure 4.29. The linear relationship suggests a strong correlation between the impulse of the pulse and the energy supplied by the capacitor.

Figure 4.29 shows that as with previous tests the DI potential has no impact on the properties of the PPT pulse. More importantly it shows that when Teflon^{TM} is not present between the electrodes, plasma is still being formed, high currents are still flowing through the system and the PPT capacitor is still discharging.

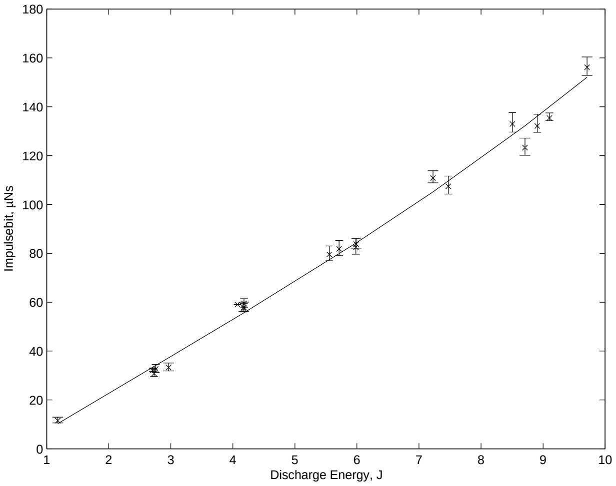

Figure 4.29: Impulse bit to PPT discharge energy comparison for the standard configuration with no Teflon^{TM}

As an aside, during these tests, it was noticed how just after the discharge was initiated, that over a period of a few seconds, the vacuum pressure of the chamber would increase. Crude measurements were taken visually from the gauge and recorded the maximum pressure rise as a function of the PPT discharge energy, see Figure 4.30. After a few seconds the pressure would return to around 10^{-6}mbar. The fact that this rise happened over a few seconds and was not just an artefact of electromagnetic interference as the pulse discharged suggests that the pressure rise was due to a release of material, most likely mass erosion from the electrodes. Although not further explored within this work the linear trend seen here could be used in further work to estimate the total mass eroded per discharge.

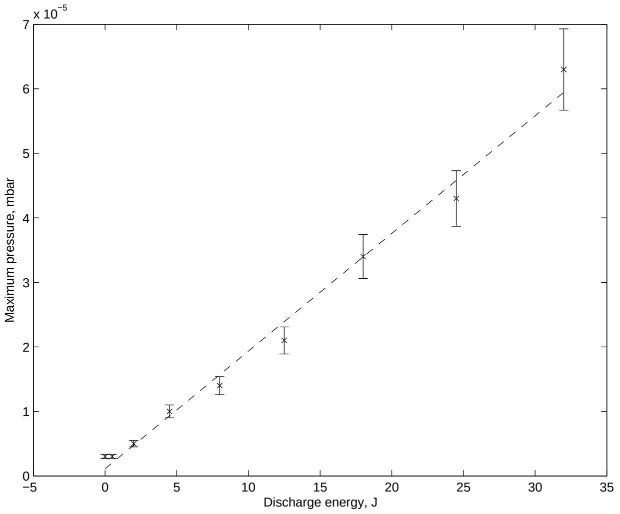

Figure 4.30: Maximum pressure rise within vacuum chamber as a function of PPT discharge energy

4.3.6 Electrode Separation Experiments

The separation distance between the parallel bar electrodes was then investigated. This was to observe how the physical dimensions of the area between the electrodes had an effect on the PPT pulse discharge. The PPT was configured to the standard configuration, see Table 4.3. The separation distances investigated were 10mm, 30mm, 50mm, 70mm, 80mm and 90mm. The data sets for these experiments are shown in Figures B.14 to B.44.

Several observations can be made from these data sets. As the energy stored in the PPT capacitor increases, the period of capacitor ringing also increases. This means that for each additional half cycle of the current signal, an additional plasma discharge occurs within the discharge chamber i.e. the overall discharge of the PPT is actually an amalgamation of several discharges (as the capacitor rings). The number of ringing periods and the magnitude of these current peaks increase as the impulse bit increases.

The separation distance has a direct influence on these variables. First of all as the separation distance is increased the number of ringing periods that are observed decrease. At 10mm and 5.2J (profile 2 of Figure B.16), the number of ringing periods was approximately nine with a peak mean current of ≈7kA but at 90mm and 4.9J (profile 2 of Figure B.42) the number of ringing periods was approximately three with a peak mean current of ≈2.2kA. Another observation was that at 90mm separation the peaks in the mean current after the primary pulse decrease with some form of exponential component whilst at 10mm this decrease appears to be less pronounced.

These observations show that as the separation distance increases the plasma resistance also increases (indicated by the lowering in peak current) and the rate of rise in plasma resistance between each individual discharge within the overall pulse increases (indicated by the exponential growth in decay of the current peaks). As this plasma resistance increases it also reduces the ability of the plasma to form new discharges (indicated by the lowered current ringing).

The data sets become less stable as the electrode separation distance increases. This meant that during tests the deviation from the mean pulse signal diverged significantly, suggesting that as the electrode distance increased, the plasma became less consistent between individual discharges. The exception to this observation is at an electrode separation of 10mm. At this distance an additional currently unexplainable phenomena occurs during the first current peak (but sometimes also observed in the second current peak), see Figure B.42. An additional peak on top of the primary peak occurs indicating that for a small period of time during the primary discharge the plasma resistance becomes even lower. The additional peak is not especially stable and so induces an error when the signals are averaged. This explains the exception to the trend that error in the average signal increases with separation distance.

Another observation is found in the fine detail of the current and voltage signal. As the voltage initially decreases fluxuations can clearly be observed. In some cases the fluxuations between voltage and current are clearly linked, see profiles 1-3 in Figure B.33. However in others the link is not so clear, see profile 3 in Figure B.19. As the capacitor initially discharges there is a sharp change in the gradient of the decreasing voltage signal. It is around this time that the rate of flow of current begins to decrease. This fluxuation indicates the time at which the rate of energy stored within the magnetic field begins to slow down.

Comparing the impulse bit to energy for these sets of experiments several other observations are made, see Figure 4.31.

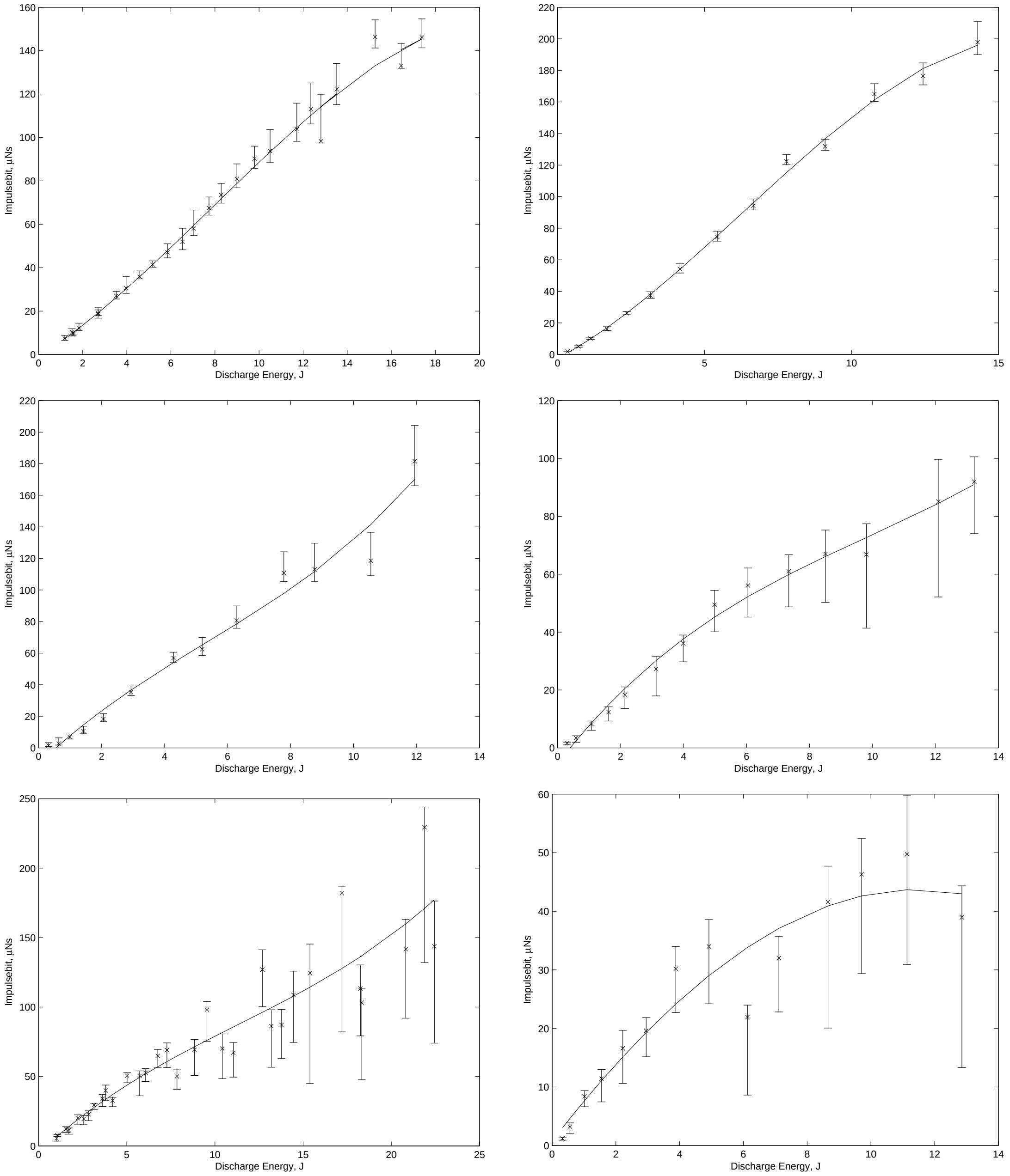

Figure 4.31: Numbered from left to right and from top to bottom, 1: Electrode Separation = 10mm, 2: Electrode Separation = 30mm, 3: Electrode Separation = 50mm, 4: Electrode Separation = 70mm, 5: Electrode Separation = 80mm, 6: Electrode Separation = 90mm

The deviation from the mean impulse bit increases as the separation distance increases; this is because the created plasma behaves less consistently. However for each experiment the lower energy experiments showed less deviation than at higher energies suggesting that the low energy plasmas were more consistent. To analyse the data in Figure 4.31 further data points around the 1.6J, 4J, 5J 8J, 9.5J and 12J were extracted. The impulse bit was compared to the electrode separation distance at these energies and the results can be seen in Figure 4.32.

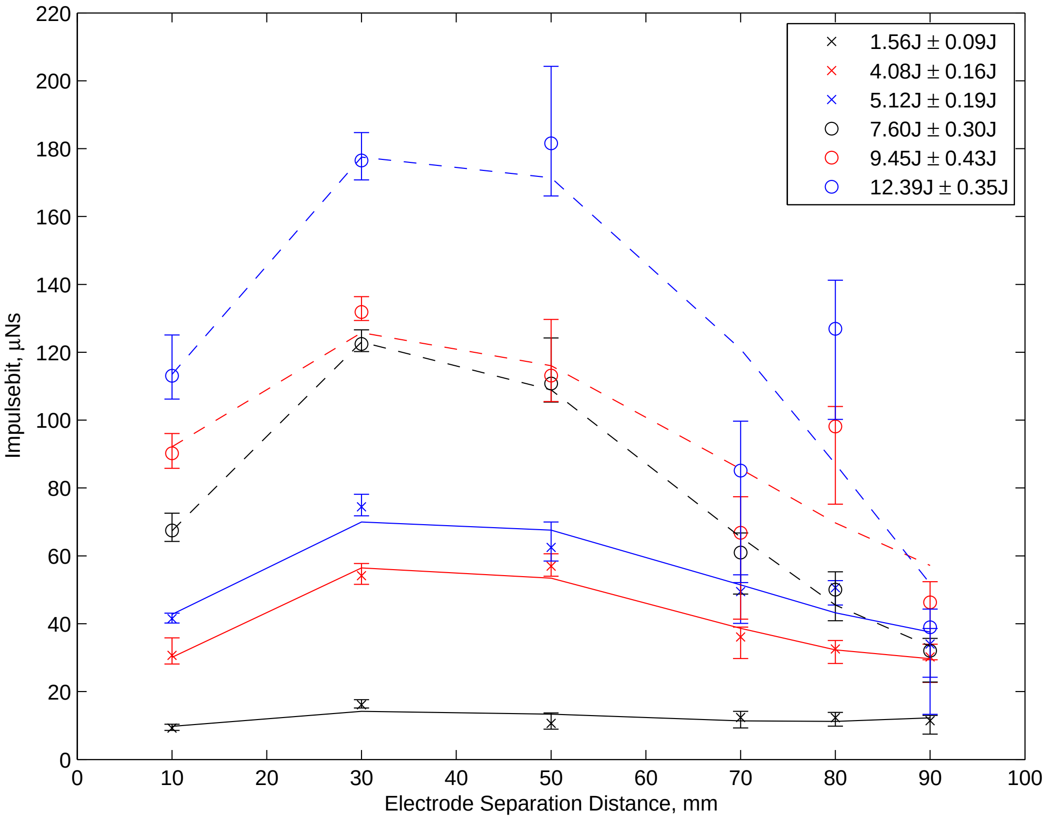

Figure 4.32: Impulse bit as a function of electrode separation for 1.56J, 4.08J, 5.12J, 7.60J, 9.45J and 12.39J discharges

Figure 4.32 shows that as the separation distance increases from 10mm to 90mm there appears to be a peak in the maximum impulse bit between 30mm and 50mm, suggesting that for the given setup and electrical parameters there is an optimum distance to the electrode separation. This feature seems to be independent of the initial energy stored in the capacitor. The decreased performance from 50mm to 90mm is understandable, as the separation distance increases the formed plasma arc needs to traverse over larger distances. This will lead to increased losses that reveal itself as an increased electrical resistance in the LCR circuit causing the current signal to become increasingly over damped. Figure 4.32 also implies that if a PPT is made with electrodes separated at a distance of 10mm, as they erode and the distance increases, the performance of the thruster would improve. This finding is expanded upon in the 'Developing a μPPT for CubeSat Applications' Chapter.

4.3.7 Performance Comparison with and without Teflon^{TM}

During the experiments without Teflon^{TM} it was observed that there was a linear trend between the impulse bit and the PPT discharge energy. However when the PPT was setup in the standard configuration, see Table 4.3, the impulse bit was different when Teflon^{TM}was present to when it was not present, see Figure 4.33.

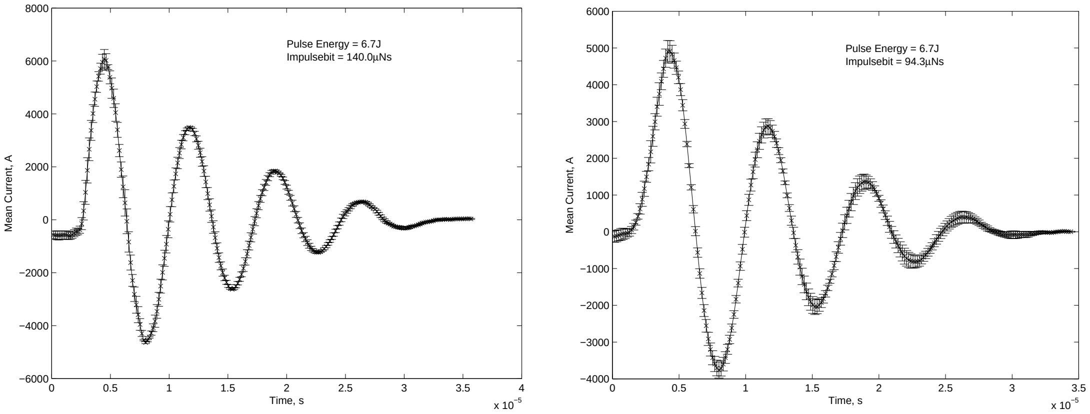

Figure 4.33: Comparison of current signals when the PPT is in the standard configuration discharging at similar energies. Left: With Teflon^{TM}, Right: Without Teflon^{TM}

It can clearly be seen in the value of the current peaks that when the Teflon^{TM} is present the current ringing increases. Additional experiments were conducted with Teflon^{TM}. The data sets for these can be seen in Figure B.45 to B.48. These additional data sets are then combined with the data sets from the 'Discharge Energy Experiments without Teflon' and the 'Teflon^{TM} Width Experiments'. Using these combined data sets a comparison is made with the impulse bit to the PPT discharge energy when Teflon^{TM} is and is not present between the electrodes, see Figure 4.34.

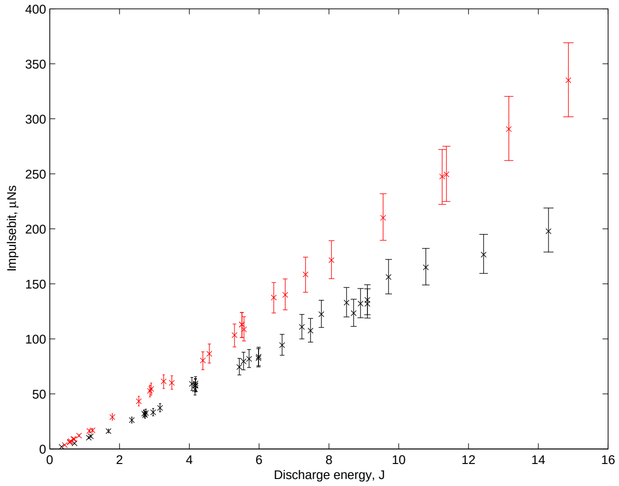

Figure 4.34: Combined data sets showing how the impulse bit relates to the PPT discharge energy when Teflon^{TM} is present (red) and is not present (black) between the electrodes

It can be seen that there is a clear distinction in performance when Teflon^{TM} is and is not present.

The impulse bit of the PPT without Teflon^{TM} is ≈60-75% of the impulse bit with Teflon^{TM}. This result is intriguing because from previous experiments it was shown that the Teflon^{TM}geometry and the variation in eroded mass from the Teflon^{TM}surface did not impact the performance. This new result leads to the conclusion that although the Teflon^{TM}itself does not affect the performance of the thruster, its presence between the electrodes acts as a catalyst during the discharge. In effect its presence creates a surface that during breakdown the discharge can track across more effectively than pure vacuum. This creates an increase in the initial current flow and therefore an increase in the impulse bit. Removing the Teflon^{TM}from the PPT may cause a reduction in the performance but it will aid in miniaturisation of the thruster and remove a major source of carbon that will coat the thruster housing in soot and possibly cause premature failure.

4.3.8 Electrode erosion

Once all the experiments had been conducted the PPT testbed was dismantled. During this process several observations were made about the status of the electrodes. Images of the electrodes can be seen in Figure 4.35. On both electrodes small pitted marks can be seen covering the whole surface. The streaks that can be seen on the cathode arise from the cathode being sanded down. This was done before the main experimental phase and during the trouble shooting phase when the discharge initiator (i.e. sparkplug) was being problematic. The theory was to see if a 'rough' cathode promoted a discharge, as it was found later that this was not the cause of the issue (it was the ignition coil). The cathode also shows a concentration of scorched marks at the end of the electrode. The anode (which was not sanded down) shows a gradual colour change from one end of the electrode to the other, suggesting that more pitting and carbon deposition occurred at the right hand edge (which coincides to the 'back' of the chamber). Two scorched mark areas are also prevalent on the anode, one at the end of the anode (i.e. the nozzle exit) and the other in a region which would be directly opposite to the sparkplug location. This suggests that this is the area of most activity and electrode erosion.

Figure 4.35: The electrode surfaces after exposure to several thousand pulse discharges at various energies. Left: Anode, Right: Cathode, the hole is the location of the sparkplug insert

Electron microscope images where taken of the surfaces of the electrodes. Figure 4.36 shows two images, the left image shows the scorched area on the anode that is directly under the sparkplug and the right image shows a close up of one of the craters seen on the anode. Due to the size of the cathode it was not possible to observe this electrode in the electron microscope facility. The 253x magnification electron microscope image (left) shows a vast area of eroded copper material from the surface. The rough edges seen are due to successive crater formation occurring in the same location. The 2562x magnification electron microscope image (right) shows a single crater of around 20μm, the left side of the crater is quite defined, whilst the right hand side appears to look like molten slag, suggesting high temperatures were involved in the formation of this crater. Also in this image, in the top left hand corner is a macro particle. Using a mass spectrometer that was built into the electron microscope this macro particle was identified as a molten ball of tungsten formed during the discharge initiation experiments when a tungsten electrode was used. This sphere shape is typical of a macro particle that is formed during a discharge [24].

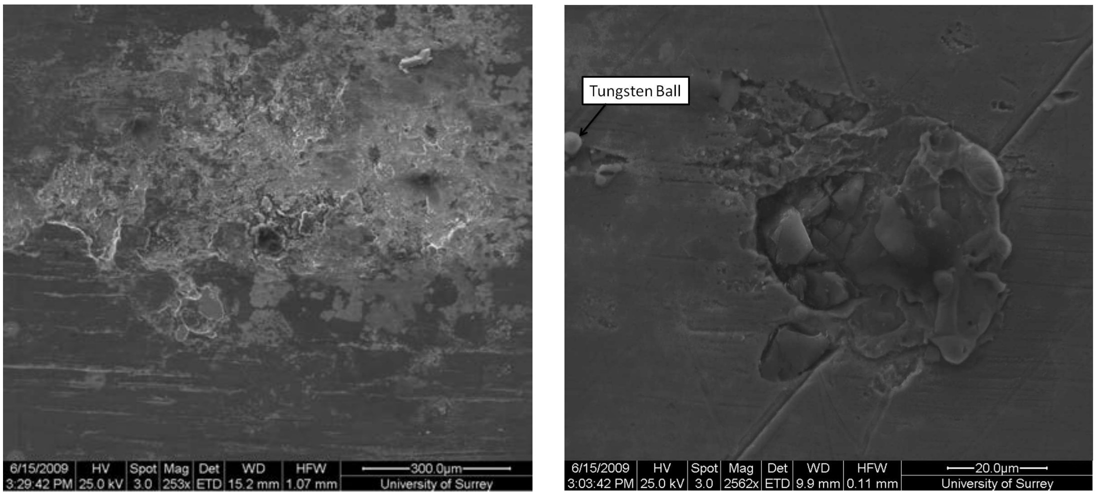

Figure 4.36: Electron microscope images of the anode. Left: Area opposite to the location of the sparkplug, Right: a close up of a single crater

The last observation of note was a ‘rainbow’ colour effect that could be seen on the back of the anode electrode, which was due to metal film deposition, see Figure 4.37. An example of a metal flange from a metal plasma deposition chamber is next to the image for comparison. Copper within the plasma plume would deposit itself on the backside of the electrode and coat it uniformly creating a thin film. The uniform thin film would refract reflected light and depending on the thickness of the film would refract at different wavelengths causing the ‘rainbow’ effect. This suggests the presence of metal within the plasma which would be consistent with the electrode erosion observed.

Figure 4.37: Examples of film deposition Left: Back of PPT anode, Right: surface of metal flange from a plasma deposition chamber

4.4 Summary

Once key components and facilities were identified an experimental program was setup. Originally this had been timetabled to take around nine months to a year to procure, build, test and evaluate a PPT. In reality this was extended to three and a half years. Several factors led to this long experimental program including limited funds for experimentation, the development of three separate PPT testbeds and the procurement and refurbishment of two vacuum chambers. A quote from Albert Einstein would also be apt to explain the reason for three and a half years, ‘If we knew what it was we were doing, it would not be called research, would it?’.

Once the facilities and testbed were proved to be working satisfactory the main set of experiments were conducted and several conclusions were made. However it is worth to note that the calculation of the impulse bit is taken from mathematical manipulation of the current signal to evaluate the electromagnetic contribution of the total impulse bit. The impulse bit calculated in this work does not take into account forces that would occur due to gas dynamics and late time ablation effects that could be observed if an impulse bit stand was used.

Experiments on the discharge initiator showed that it was important to have a breakdown due to a strong electric field but the specific properties of that initial arc did not affect the rest of the PPT pulse discharge. The DI was stripped back to a single filament wire held at negative 15kV and this was able to inject electrons via electron quantum tunnelling into the discharge chamber and initiate a breakdown of the main PPT capacitor.

Experiments looking into the mass loss from the Teflon^{TM} surface showed that the mass erosion was caused by plasma that formed close to the surface. As energy was increased to this plasma more Teflon^{TM} erosion occurred. However the opposite was not the case. When injecting the plasma with more Teflon^{TM} mass (by confining the plasma with sidewalls) an increase in the performance of the PPT did not occur, suggesting the presence of Teflon^{TM} mass within the plasma was not a significant factor in determining the plasma properties.

Experiments showed that the plasma resistance and the evolution of the plasma resistance had a major impact on the ringing of the overall pulse and the total length of the pulse. If the resistance can be kept to a minimum then performance can be increased. The plasma resistance was shown to be significantly affected by the electrode separation distance.

Experiments with the presence of Teflon^{TM} and without the presence of Teflon^{TM} showed a marked difference in performance. From the previous experiments it was concluded that the presence of Teflon^{TM} eroded material within the plasma did not have an effect on the PPT performance. So the only conclusion is that the presence of the Teflon^{TM} acts as a bridge when the arc discharges and that it is easier to arc between the electrodes connected by a material than it is to arc across hard vacuum. A reccomendation for future work would be to look into the materials that are used to 'bridge' the electrode gap as this could significantly increase the performance of the PPT.

Finally the presence of craters and film deposition confirms that electrode erosion occurs and that this is the most probable source that the plasma comes from when there is no Teflon^{TM} present between the electrodes. In the next chapter electrode erosion and cathode spots are used to model the PPT discharge without Teflon^{TM}.

Chapter 5

PPT Modelling

5.1 Introduction

In parallel to the experimental work conducted, modelling of the discharge was also undertaken. During the experimental phase it was important to build up a database of discharges. In all over 400 average discharge data sets were collected at various parameters. These data sets were then used to compare the modelled results with experimental results in order to validate the model. After validation the model was used as an engineering tool to aid in the design of an optimised μPPT.

Modelling within the PPT field has been diverse. Developed models include the analysis of the interaction between the Teflon^{TM} surface and the plasma bulk via a layer model [79, 80], the expansion and evolution of the plasma plume [81, 82], return of carbon molecules to the Teflon^{TM} surface [83], complete three dimensional MHD modelling of the PPT discharge [84, 85] and numerous one dimensional models based on the snowplow and mass slug-shot models [86, 87].

It was important to develop modelling capabilities in-house to aid in the understanding of the pulsed plasma discharge. As this was a parallel effort with the experimental work it was important to balance resources (i.e. time, cost, software etc) available to this aspect of the project. It was also important to use the trends and results found from the experimental phase and incorporate these into the developing model. Due to the avaliable resources the modelling program used to build and compile the program was Matlab. The decision was taken to concentrate on a model that did not use demanding computational resources, yet would still be useable as an engineering tool. The idea of creating a full three dimensional model was dropped and a simpler one dimensional lumped circuit analysis model with a simplified magnetohydrodynamic flow model method was implemented.

The lumped circuit analysis model is based on separating the PPT thruster into its constituent electrical components and allocating discrete values to these, i.e. the electrode inductance, the mutual electrode inductance, the capacitor inductance etc. Figure 5.1 shows the mechanical parts of a PPT overlaid with their allocated electrical parameters.

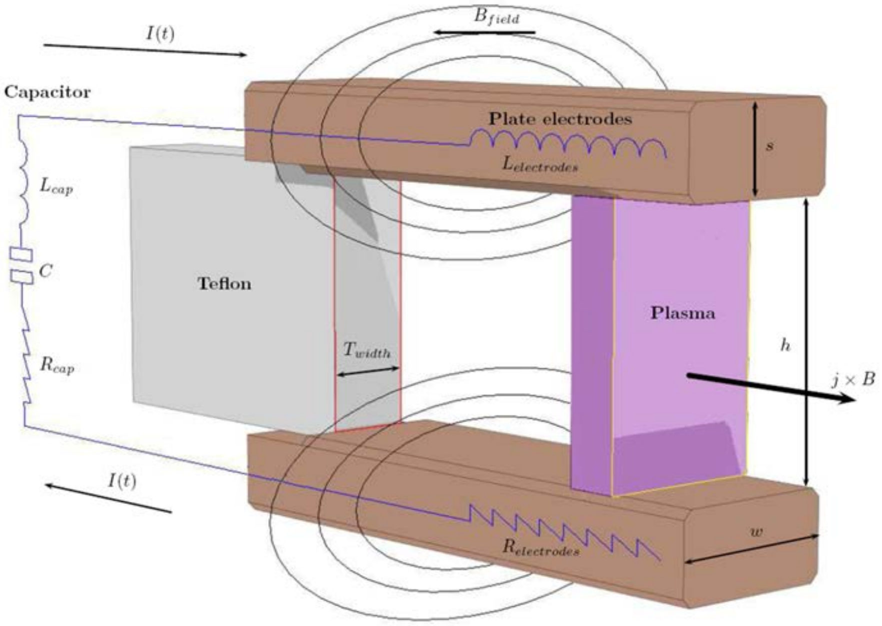

Figure 5.1: A one dimensional circuit schematic overlaid on the components of a PPT

The one dimensional model is then linked with Newtonian mechanics and a mass model to describe how the plasma mass accelerates out of the discharge chamber. Commonly in literature the complex processes that occur within the PPT are simplified to single constants or linear relationships. For instance, Lapierre uses a constant for the plasma resistance during the discharge[86]. These over-simplifications cause a detachment between modelled trends and real data and therefore diminishe the useful return that can be made from using such models.

There is then a need to create a model that is based on experimental experience and observations. Within the next section each parameter is discussed in detail to understand its origin, its significance and how it interacts with other variables during the discharge process. This will then lead to the formulation of a new model. Once the model is formulated and after it has been validated against the experimental results, the model is used to draw conclusions on processes that are occurring within the PPT discharge. Finally the model is then used to identify trends that can lead to optimise a miniaturised PPT.

5.2 PPT Model

5.2.1 Lumped Circuit Model

Formation of the code begins from first principles. Using the circuit depicted in Figure 5.1 Faraday's law (that states 'The induced electromotive force (EMF) in any closed circuit is equal to the time rate of change of the magnetic flux through the circuit') is applied around the circuit and the direction of the electromotive force, ϵ, is given by Lenz's law ('An induced current is always in such a direction as to oppose the motion or change causing it'):

$$\begin{aligned} |\epsilon| &= \left|\frac{d\phi_B}{dt}\right| \\ \epsilon &= -\frac{d}{dt}\left[\phi_B\right] \\ \epsilon &= -\frac{d}{dt}\left[L_{circuit}I\right] \\ \epsilon &= -\left[L_{circuit}\frac{dI}{dt} + I\frac{dL_{circuit}}{dt}\right] \end{aligned} \tag{5.1}$$

The electromotive force causes the flow of current through the current loop and can be alternatively expressed by the difference between the potential before work has been done by the electromotive force and the potential after work has been done by the electromotive force. Also, by considering Kirchhoff's law, Equation 5.1 becomes:

$$\begin{aligned} V_{after} - V_{before} &= -\left[L_{circuit}\frac{dI}{dt} + I\frac{dL_{circuit}}{dt}\right] \\ V_{before} &= IR_{circuit} + L_{circuit}\frac{dI}{dt} + I\frac{dL_{circuit}}{dt} \\ V_0 - \frac{1}{C_{PPT}}\int(I)dt &= IR_{circuit} + L_{circuit}\frac{dI}{dt} + I\frac{dL_{circuit}}{dt} \end{aligned} \tag{5.2}$$

The voltage before work is done by the electromotive force can be realised as being the voltage at time t within the circuit loop. The circuit inductance and resistance can be expressed respectively as:

$$L_{circuit} = L_{capacitor} + L_{electrodes} + L_{plasma} \tag{5.3}$$

$$R_{circuit} = R_{capacitor} + R_{electrodes} + R_{plasma} \tag{5.4}$$

The inductance of the plasma, L_{plasma}, is found from the magnetic flux through the plasma. However, for a closed surface (i.e. a Gaussian surface surrounding the plasma bulk), the magnetic flux is zero:

$$L_{plasma} = \frac{\phi_B}{I} = \frac{1}{I}\oint B.dS = 0 \tag{5.5}$$

5.2.2 Capacitor Model

One area of this work, which has not been explored in detail, is the modelling of the contribution that the capacitor makes to the total circuit inductance and resistance. These values are highly dependant on the manufacturing process, the internal electrode geometry, the method of external connection to the rest of the circuit and the dielectric of the capacitor. After initial investigations looking at using a SPICE model to reflect the higher order frequency behaviour mechanisms of a capacitor, it was concluded that this diversion from the focus of the work would be too costly in resources. The SPICE model for each capacitor would need to be custom built and the publically available information required for each component of the capacitor SPICE model is limited. A generic model would be difficult to create and so was left for future work. However, as the contributions from the capacitor are significant, it was important to experimentally find these values for the 5kV PPR50RD-405 custom capacitor that was used for the experimental tests.

The experimental results from Appendix B indicate that with the 5kV PPR custom capacitor the discharge frequency is consistently 136kHz. Using a HM8018 HAMEG Instruments LCR meter Figure 5.2 shows a log plot of the capacitor resistance and a log plot of the capacitor inductance as a function of driving frequency. By fitting the data to a polynomial best fit and extrapolating at a discharge frequency of 136kHz, an estimation of 33mΩ for the capacitor resistance and 310nH for the capacitor inductance can be made.

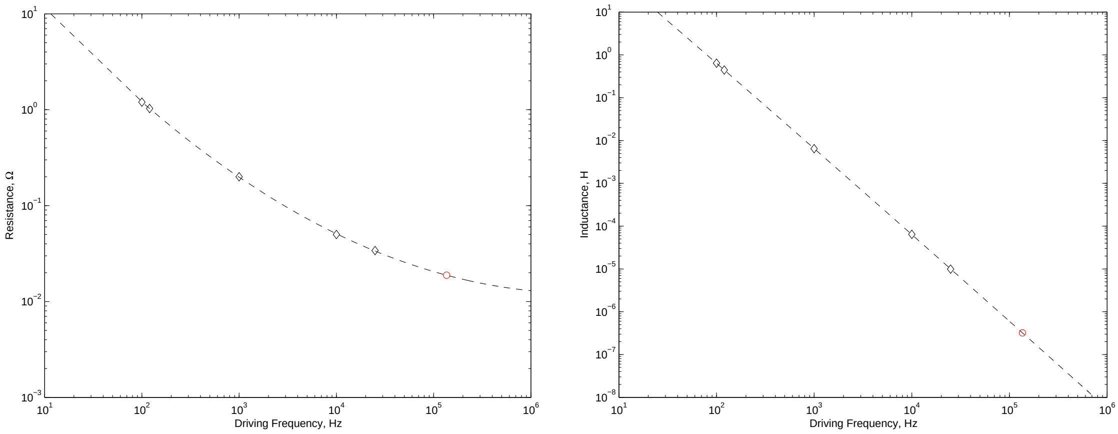

Figure 5.2: Measured as a function of driving frequency. Left: Capacitor resistance, Right: Capacitor inductance. The black diamonds represent the experimental data from the LCR meter and the red circle represents the extrapolated parameter at 136kHz

5.2.3 Electrode Model

Modelling the electrode inductance and resistance is not a straight forward procedure. The discharge occurs in the kilohertz regime and at these frequencies the skin depth is small. At 100kHz the skin depth is around 0.2mm for copper. The skin depth is the distance from the surface in which most of the current flows and is due to the skin effect. The skin effect is caused by rotating eddy currents that are formed by free electrons rotating around field lines setup by a fluctuating H-field within the conductor, see Figure 5.3. The eddy currents oppose the flux that generates them. The rotation of these eddy currents hence causes a reduction in the net flow of current in the centre of the conductor, and a net increase in the flow of current towards its outer edges. Therefore the net flow of current appears to be reduced in the centre and increased in the skin of the conductor. The higher the frequency of the fluctuations in the

H-field the more pronounced the effect will be.

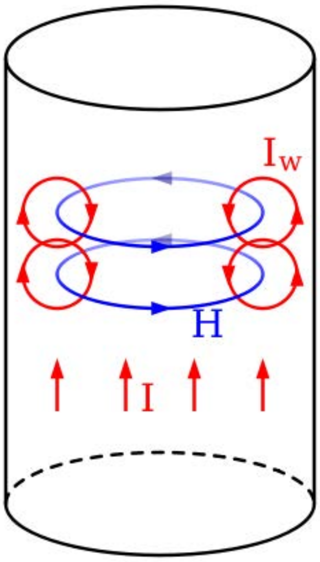

Figure 5.3: The Skin depth is due to the circulating eddy currents (arising from a changing H-field) cancelling the current flow in the centre of a conductor and reinforcing it in the skin

The pushing of the current to the outer edges of the conductor causes the impedance and inductance of the electrode to be frequency dependant. The model that is used in this work is based on research within the microchip industry which model the high frequency effects between rectangular contacts [88]. The electrodes are split into an array of sub conductors, see Figure 5.4. The different colours give a visual representation of how the current is distributed in a rectangular high frequency driven conducting post (electrode). Assuming the dimensions chosen for the sub conductor width and length are sufficiently small, with respect to the skin depth at a particular driving frequency, it can be assumed that the current through each sub conductor is constant.

The self-inductance, L_{sub}, for a rectangular sub conductor, as long as the sub conductor length is at least five times greater than the sub conductor width or thickness, can be expressed as[88]:

$$L_{sub} = 2e-7l_{sub}\left[ln\left(\frac{2l_{sub}}{w_{sub}+t_{sub}}\right)+0.5+0.2235\left(\frac{w_{sub}+t_{sub}}{l_{sub}}\right)\right] \tag{5.6}$$

The resistance for each sub conductor will be:

$$R_{sub} = \frac{l_{sub}}{\sigma_{sub}w_{sub}t_{sub}} \tag{5.7}$$

Due to the proximity of the sub conductors to each other within the same conducting post there will be a mutual inductance between each sub conductor with each other sub conductor in that post. Where the ith row and jth column describe the position of one sub conductor and the mth row and nth column describe the position of the second sub conductor, which are separated by a distance d$_{ij,mn}$ (taken from

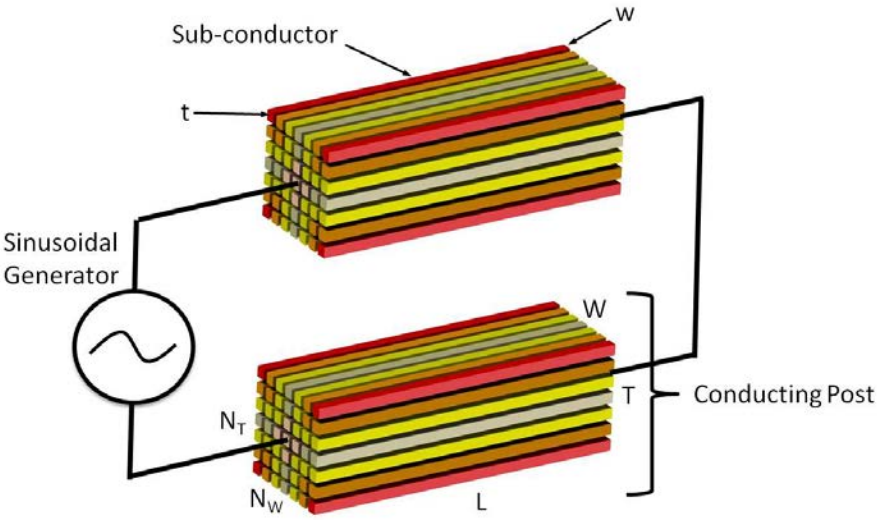

Figure 5.4: Two conducting posts in series driven by a sinosodial generator

the centre axes of each sub conductor). The mutual inductance created can be written as[88]:

$$M_{ij,mn} = 2e-7l_{sub}\left[ln\left(\frac{l_{sub}}{d_{ij,mn}+\sqrt{1+\frac{l_{sub}^2}{d_{ij,mn}^2}}}-\sqrt{1+\frac{d_{ij,mn}^2}{l_{sub}^2}}+\frac{d_{ij,mn}}{l_{sub}}\right)\right] \tag{5.8}$$

Considering just one post of the two seen in Figure 5.4 the self inductance, the resistance and the mutual inductance between each sub conductor with all other sub conductors can be calculated. Invoking Ohm's law which states, the voltage drop (across all the sub conductors equally) will be equal to the impedance multiplied by the current in each sub conductor. The impedance in a high frequency setup is a combination of the resistance, the self inductance and mutual inductance between all other sub conductors. A matrix equation can be solved to then find the currents in each sub conductor:

$$\begin{bmatrix} V_{drop} \\ V_{drop} \\ V_{drop} \\ V_{drop} \\ V_{drop} \\ V_{drop} \end{bmatrix} = \begin{bmatrix} R_{sub}+j\omega L_{sub} & j\omega M_{12,11} & \cdots & j\omega M_{N_TN_W,11} \\ j\omega M_{11,12} & R_{sub}+j\omega L_{sub} & \cdots & j\omega M_{N_TN_W,12} \\ \vdots & \vdots & & \vdots \\ j\omega M_{11,ij} & j\omega M_{12,ij} & \cdots & j\omega M_{N_TN_W,ij} \\ \vdots & \vdots & & \vdots \\ j\omega M_{11,N_TN_W} & j\omega M_{12,N_TN_W} & \cdots & R_{sub}+j\omega L_{sub} \end{bmatrix} \begin{bmatrix} I_{11} \\ I_{12} \\ \vdots \\ I_{ij} \\ \vdots \\ I_{N_TN_W} \end{bmatrix} \tag{5.9}$$

Assuming the voltage drop applied to the post (i.e. the electrode) is known, the matrix can be solved. The total current in the post is given as a summation of all the sub conductor currents. Using Ohm's law the impedance can be calculated as:

$$\frac{V_{drop}}{I_{post}} = Z = R_{post} + j\omega L_{post} \tag{5.10}$$

Once the impedance is known the post resistance is thus the real part of the impedance and the post inductance can be found by manipulating the imaginary part of the impedance. However so far we have only considered a single electrode. In the case of the PPT there are two conducting posts as set out in Figure 5.4. So we have to consider both mutual inductances from sub conductors within the same electrode but also mutual inductances from sub conductors in the second electrode. Equation 5.9 is modified and expanded upon to consider this additional mutual inductance, and care is taken to consider the directions of the currents in the two sub conductors. If the currents are flowing in the same direction, the mutual inductance will be positive; if the currents are flowing in opposite directions, the mutual inductance will be negative. So the mutual inductance from within the same electrode will be positive but the mutual inductance, due to the second electrode with current flowing in the opposite direction, will be negative. The electrodes are assigned the subscripts A and B to differentiate them. Lastly it is realised that, unlike the single electrode case, the voltage is a summation of the voltage drop of a sub conductor in the first electrode and the voltage drop of a sub conductor in the second electrode. Combining these a new matrix equation can be formed to calculate the sub currents in each sub conductor in each electrode.

$$\begin{bmatrix} V_{drop} \\ V_{drop} \\ \vdots \\ \vdots \\ \vdots \\ V_{drop} \\ 0 \end{bmatrix} = \left[\begin{matrix} R_{Asub} + j\omega(L_{Asub} - M_{A11,B11}) & j\omega(M_{A12,A11} - M_{A12,B11}) & \cdots & R_{Bsub} + j\omega(L_{Bsub} + M_{B11,B11}) \\ R_{Asub} + j\omega(L_{Asub} - M_{A11,B11}) & j\omega(M_{A12,A11} - M_{A11,B12}) & \cdots & j\omega(M_{B11,B12} - M_{B11,A11}) \\ \vdots & \vdots & & \vdots \\ \vdots & \vdots & & \vdots \\ \vdots & \vdots & & \vdots \\ \vdots & \vdots & & \vdots \\ 1 & 1 & & -1 \end{matrix} \right.$$

$$\left. \begin{matrix} & \cdots & \\ j\omega(M_{B12,B11} - M_{B12,A11}) & \cdots & j\omega(M_{BN_{BT}N_{BW},B11} - M_{BN_{BT}N_{BW},A11}) \\ R_{Bsub} + j\omega(L_{Bsub} - M_{B12,B11}) & & j\omega(M_{BN_{BT}N_{BW},B12} - M_{BN_{BT}N_{BW},A11}) \\ \vdots & & \vdots \\ \vdots & & \vdots \\ \vdots & & \vdots \\ \vdots & & \vdots \\ -1 & & -1 \end{matrix} \right] \begin{bmatrix} I_{A11} \\ I_{A12} \\ \vdots \\ I_{B11} \\ I_{B12} \\ \vdots \\ I_{BN_{BT}N_{BW}} \end{bmatrix} \tag{5.11}$$

In the two electrode system it should also be realised that the total current is not a summation of all the sub conductor currents but rather a summation of the sub conductor currents in electrode A which is equal to the summation of the sub conductor currents in electrode B. Once the matrix is solved the impedance of each electrode can be calculated, using Equation 5.10. The resistance and inductance of each electrode can then be inferred from the impedance. Note that the inductance here takes into account the self inductance and the mutual inductances from sub conductors found in either post.

During initial testing of the electrode inductance model it was shown that as the frequency (i.e. the value of the complex component of the inductances) was increased, the model became unstable if the total number of sub conductors was too low. The solution was to increase the number of sub conductors but with this came an increase in the total compiling time. Figure 5.5 shows the results using MATLAB of a 968 sub conductor system that took 26 minutes to compile. Due to MATLAB being a 'single' string program the compiling time was defined by the processor of the desktop computer used to run the program.

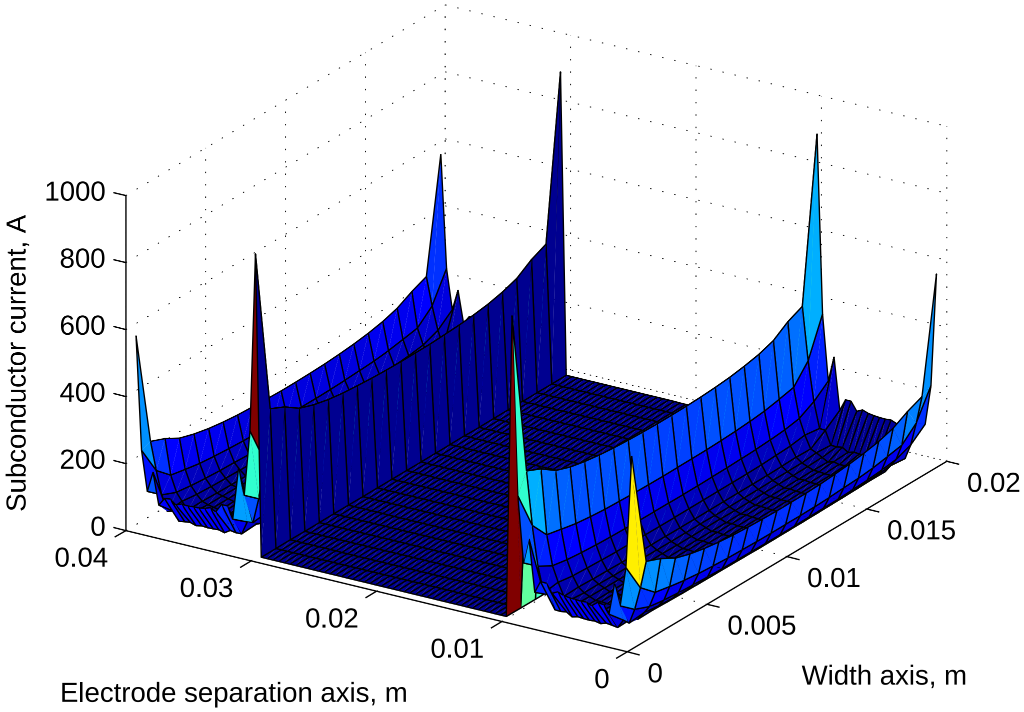

Figure 5.5: Inductance model based on a PPT with dimensions taken from Table 4.3 discharging at a frequency of 136kHz

Figure 5.5 clearly shows several features. At 136kHz the current flowing through the centre of the electrodes is minimal. The current tends to flow in the outer regions of the electrode, specifically congregating in the electrode corners. Also due to mutual inductance from the other electrode, an increased proportion of the current flows in the electrode edges located closest to each other than in the outer edges of the electrode. These results coincide with photos of the electrode surface that show increased activity at the electrode edges (i.e. charred edges), see Figure 5.6.

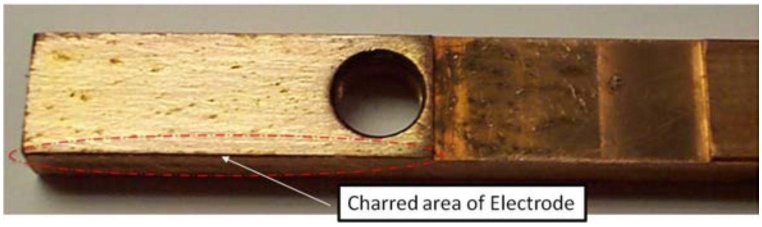

Figure 5.6: Increased activity on electrode coinciding in the area where high currents are present within the electrode

This model is required to run at every time-step because the inductance model requires voltage and effective electrode length inputs that vary with the discharging capacitor and evolving plasma respectively. It was noted, during model testing, that although the voltage affected the magnitude of the current in each sub conductor, it did not vary the relative sub conductor current magnitudes that the sub conductors shared with each other. It was also observed that the magnitude of the voltage did not affect the inductance or the resistance of the electrode (at 136kHz). This meant that the problem could be reduced to a single variable, the effective electrode length. As the plasma is moved within the discharge chamber it expands the effective length of the current loop. The length between the plasma mass and the capacitor is the effective electrode length and is the part of the electrode that carries current in the current loop. The inductance model was run at several lengths and the electrode resistance and inductance was measured. The points were then fitted to a curve, see Figure 5.7. This best fit was used to calculate the inductance and resistance as a function of the effective electrode length based on the PPT which was used in the experiments. Each new PPT electrode geometry would require this process to be undertaken.

It can be seen that the contribution to the total circuit resistance and inductance from the electrodes compared to the capacitor resistance and inductance is minimal with respect to the 5kV PPR50RD-405 custom capacitor used in the experiments. However, this electrode model will be of use when low inductance capacitors are studied and the capacitor and electrode inductances are comparable to each other.

5.2.4 Plasma Flow Model

The plasma model was based on observations found in literature and observations taken during this work's experimental phase. The plasma model developed here is based on discharges that do not include material between the electrodes (i.e. Teflon^{TM}). In this model it is theorised that the source of the plasma mass originates from the electrode surfaces.

High speed photography shown in the literature survey (Figure 2.31), photography of the electrodes post experimentation (Figure 4.35) and electron microscope imagery of the electrodes (Figure 4.36) all

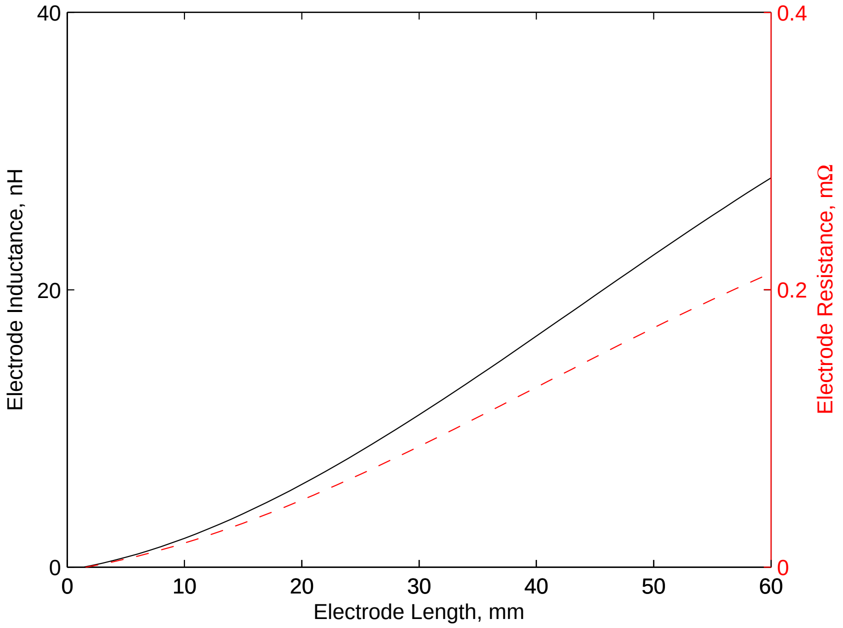

Figure 5.7: Electrode inductance and resistance as a function of length for the parameters set in Table 4.3

suggest that the electrodes are being eroded in condensed areas by a high energy process, which has a byproduct of crater formation. The high speed photographic images show in detail two structures: first, bright spots that occur on the electrode surface and second, from these bright spots it appears that small but intense jets are formed (seen most clearly on the top electrode at 4800ns and 5100ns)[20].

The model developed to explain these structures draws together experimental and modelling work from two areas based on cathode spot emission sites [24, 89] and plasma flows eminating from grouped cathode spot emissions[90, 91, 39]. The process starts with the creation of emission centres, i.e. the bright spots seen located on the cathode. The metal electrodes of the PPT are not smooth surfaces on the microscopic scale. Field emission occurs at geometric sharp points and promotes ion bombardment in these locations, see Figure 5.8. As ion bombardment increases, the emission site rapidly heats and thermionic emissions of electrons occur. The increased presence of electrons promotes further ion bombardment and a thermal runaway occurs. This process rapidly heats the surface of the electrode until it 'explodes' and leaves a visible crater. The crater edge with its rough surface then forms a location for secondary cathode spots to form.

The plasma produced from these 'exploding' bright spots is energetic with the mean ion charge state in the 1+ to 4+ state dependant on the material of the electrode. As the plasma is accelerated and moves away from the emission centre and crater, the plasma properties have been shown to remain fairly consistent even when measured at significant distances[24]. The area in which these properties are stabalisized is known as the 'freezing zone' and will remain in this state until it reaches a region known

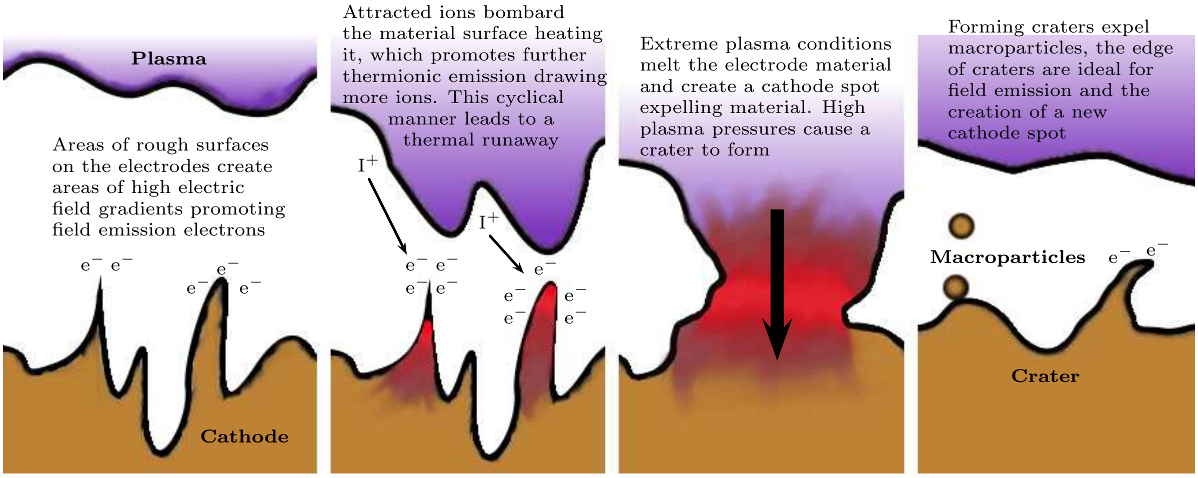

Figure 5.8: Evolution of the cathode spot process and macro particle formation as a result of plasma pressure on the liquid cathode material

as the ‘mixing region’ (i.e. an area where due to external influences the properties of the plasma begin to change once more). The frozen plasma parameters are unique to each element and are summarised by Anders in a periodic table format[24]. The parameters of the frozen plasma for copper are used to describe the plasma conditions close to the cathode electrode in the mixing region and form the initial boundary conditions of the plasma flow.

The current flowing through the plasma during the discharge, are in the kilo ampere range, which induces a self constricting magnetic field within the plasma flow, see Figure 5.9. The magnetic force is balanced out by the ideal gas pressure exerted by the highly energetic electrons (known as the Bennet criterion [92]) and a plasma column is created. If the currents are considerable ($\geq$1kA), a sausage instability occurs within the plasma and a pinch forms within the column. The pinch constriction causes a localised area that has an increased particle number density with an increased chance of particle collisions. The increased collision rate causes the particle temperature to rise substantially and further ionise the plasma into higher ion charge states. This is supported by evidence which used an RFEA probe in PPT experiments, where ions up to 199eV were measured in a typical discharge [23].

The initial plasma parameters originating from the cathode spots using copper electrodes in a PPT are given in Table 5.1. The initial copper plasma has a velocity of 13.2kms^{-1} towards the direction of the anode and has an average mean ion state of Cu^{2+} (72.1% of the total population).

The number of cathode spots observed during a discharge is proportional to the overall arc current flowing through the system. For copper electrodes it has been experimentally observed that the current per observed spot, I_{spot}, is 150±70A [93]. If moderate to high currents are flowing through the system a plasma column forms. The column origin, which is in close proximity to the cathode, is an area of increased cathode spot activity. The close proximity of the cathode spots to each other causes their resulting plasma jets to amalgamate into a single ‘plasma flow’ in an area known as the ‘mixing region’,

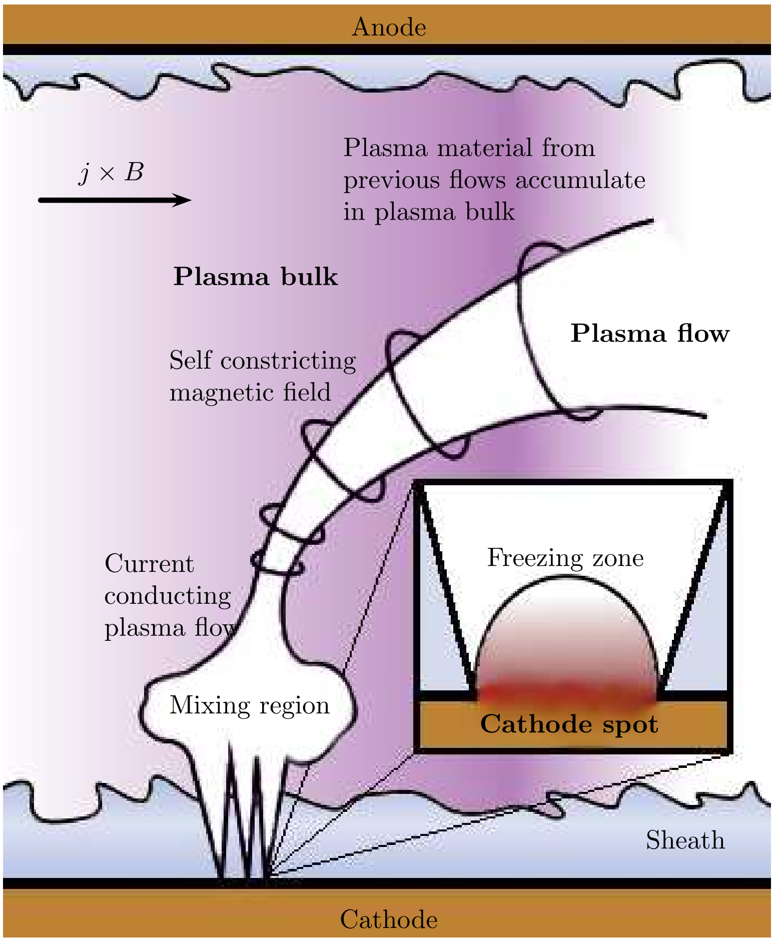

Figure 5.9: Plasma evolution from emission centre to plasma bulk in a cathode spot plasma flow of a PPT

Table 5.1: Initial plasma conditions for copper electrodes [32] [24] [31] [39]

Initial condition	**Value**
Cathode Parameters	
Spot splitting current	150±70 A
Plasma Jet	
Mean ion charge state	2.06
Plasma jet radius	1-2 mm
Freezing zone/mixing region	
- Spot velocity	13.2kms^{-1}
- Ion fraction dist.	1+ =10.7%
	2+ =72.1%
	3+ =17.1%
	4+ =0.014%

located approximately 0.1 to 1mm above the cathode surface [91].

The 'plasma flow' has dimensions which are dependent on the number of plasma jets present within the discharge (equivalent to the number of cathode spots present). There is limited literature on the dimensions of the micro plasma jets, which originate from the cathode spots and this is the biggest uncertainty introduced into the model presented. The plasma jet is thought to expand parabolically with a circular aperture at its end face. The total area of the flow in the mixing region is taken to be a function of the initial surface area from a single plasma jet (originating from a single cathode spot) multiplied by the total number of cathode spots present in the discharge;

$$S_0 = S_{spot}\frac{I_{arc}}{I_{spot}} \tag{5.12}$$

An estimate for the dimensions of the individual cathode spot has been found by using a three frame interforic system [31] [32]. The radius of the spot can be estimated from the electron density distribution plotted on a equidensitogram, see Figure 5.10. It shows that the radius of the cathode spot is around 1-2mm for copper.

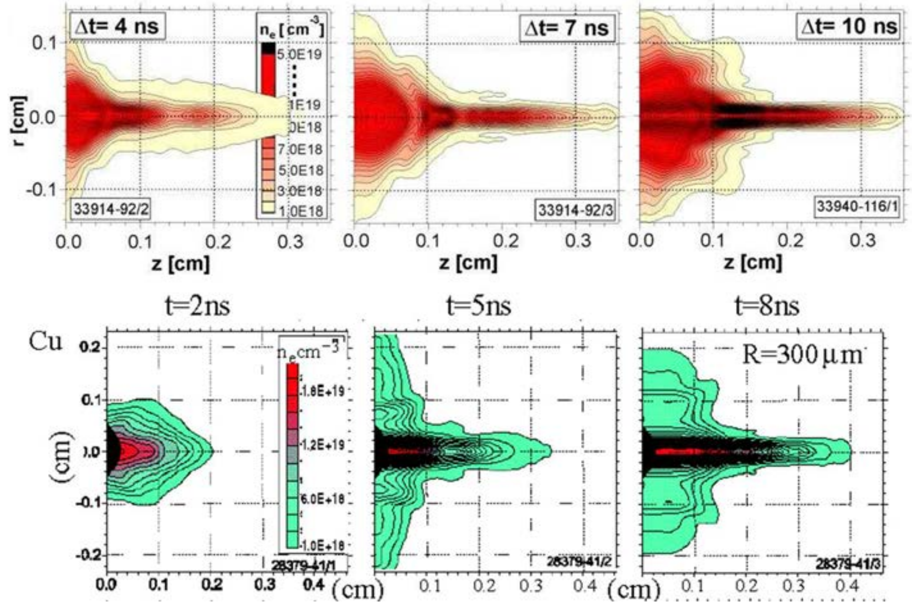

Figure 5.10: Equidensitograms for copper cathode spots [31] [32]

The plasma flow from the cathode mixing region to the anode sheath is described using a simplified set of magnetohydrodynamic equations. The full set of magnetohydrodynamic equations in three spatial dimensions and one temporal dimension becomes a non trivial task to solve. Simplifications can be made if it is assumed that the plasma between the electrodes is in a steady state and that the plasma parameters only change with distance from the cathode. The validity of these assumptions needs closer consideration.

The velocity of the ions emitted from the cathode spot region is similar to the ion velocity speed near the anode sheath, which for copper is around 13.2 kms^{-1}. For the experiments shown in this work with inter-electrode gaps of 1-9cm this equates to an ion particle time of flight (TOF) τ_L of around 0.76-6.8μs. Another timescale involved in these processes is the characteristic time for the ion charge state produced in the cathode spot process to relax to its quasi-steady-state value, τ_S. This has been found to be on the order of 50-100μs for copper [94]. If the current pulse discharge time, τ, meets the inequality $\tau \gg \tau_S \gg \tau_L$, a quasi steady state or vacuum arc takes place. If $\tau \ll \tau_L$ the discharge is considered to be the spark phase of a vacuum discharge (or fast pulse discharge). In the case that $\tau_S \geq \tau \geq \tau_L$ the discharge is considered to be a short pulse discharge where the plasma flow parameters correspond to instant changes in the discharge current and S_0 [91]. However the cathode spot evolution is theorised to be a fractal process with a finite life time [24]. The surface area of the combined plasma jets will then depend on the total pulse duration. Equation 5.12 can be modified to take this into account [91]:

$$S_t = S_0 \frac{I_{arc}}{I_{spot}} \left(1 + \frac{t}{\tau_S}\right) \tag{5.13}$$

In the case of the PPT under study (which has a discharge frequency of 136 kHz) the characteristic time of a single pulse of the total discharge is found to be around 3.68μs. Therefore dependent on the time of flight of the particles through the inter-electrode gap the processes involved can either be thought as a short or fast pulse discharge. The modelling of a fast pulse discharge requires the inclusion of a full set of time dependant magnetohydrodynamic equations. The modelling of a short pulse can be completed with quasi steady state assumptions with only the time dependence of the surface area of the combined plasma jets to be considered, which considerably simplifies the problem. As such the model developed only considers short pulses and limits the model's validity to comparisons with experimental data with an inter-electrode gap of 1cm ($\tau_L \cong 0.76\mu$s) and 3cm ($\tau_L \cong 2.27\mu$s). The developed model for short pulses is invalid for distances larger than 5cm for the experimental data undertaken. However, despite this limitation in the model, developed PPTs are typically copper based electrodes with gap distances of around 3cm, meaning the model is applicable for evaluating within these parameters.

The flow model is based on the following assumptions [95]:

- The plasma flow originates from a single or closely grouped number of cathode spots rather than several individual plasma flows from spots located at distances far apart from each other.
- The discharge is a short pulse arc where quasi steady state can be assumed.
- It is assumed that the compression of the plasma flow by its own magnetic field is identical to the compression of the current flow, which has the same cross sectional area.
- The self generated magnetic field is stronger than the external magnetic field created by current flowing through the electrodes and is limited to a small region near the edge of the plasma column. Thus the self generated magnetic field shields the plasma contained within the column from external magnetic effects, i.e. The conductivity within the plasma column is unaffected by both external magnetic fields and self generated magnetic fields.
- The model uses a one dimensional system of equations which takes into account the plasma flow cross sectional area, $S(z) = \pi r^2$. It is assumed that across the cross sectional area the plasma temperature, electron density, ion velocity, ion charge state and the current density are uniform.

- Electron energy losses due to heat conduction are ignored compared to energy lost due to joule heating and electron-ion collisions.
- The ion pressure is neglected in comparison to the electron pressure given that the electron temperature is much greater than the ion temperature in the cathodic plasma.
- The plasma originates from material eroded by cathodic spot emission sites and these provide the initial boundary conditions of the plasma close to the cathode. All the mass eroded is assumed to be ionised particles and is accelerated within the plasma column. The introduction of neutral particles or particulates into the discharge gap from cooling emission sites on the cathode is ignored.
- The anode is considered a passive collector of the charge and mass which means that the model is only adequate within the inter-electrode gap outside of the anode sheath region. Additional effects on the anode (i.e. anodic spot creation) are neglected and the addition of these processes are left for future work.
- It is assumed that the electron temperature of the plasma flow is limited and is a function of the initial electron temperature in the cathode spot region.

In the following flow model, the z-axis is defined as the axis connecting the midpoint of the electrodes, the y-axis is defined as the axis aligned with the magnetic fields created by the current flow through the electrodes and the x-axis is defined as being perpendicular to z and y axis. In polar co-ordinates the z-axis is the same as the cartisian co-ordinates and the the r-axis is in the x-y plane.

The flow model is based on solving the following MHD equations in cylindrical coordinates for steady state. For the moving plasma the continuinity and momentum transfer equations are used:

$$\frac{\partial \rho}{\partial t} + \nabla \cdot (\rho V) = 0 \tag{5.14}$$

$$\rho \left(\frac{\partial}{\partial t} + V \cdot \nabla \right) V = J \times B - \nabla P \tag{5.15}$$

For the electrical current the conservation law is used:

$$\nabla \cdot J = 0 \tag{5.16}$$

For the self generated magnetic field Ampere's law is used:

$$\nabla \times B = \mu_0 J \tag{5.17}$$

In cylindrical coordinates for steady state these equations can be simplified to [96]:

$$\frac{1}{r}\frac{\partial}{\partial r}\left(r\rho V_r\right)+\frac{\partial}{\partial r}\left(\rho V_z\right)=0 \tag{5.18}$$

$$\rho\left(V_r\frac{\partial V_z}{\partial r}+V_z\frac{\partial V_z}{\partial z}\right)=\frac{\partial P}{\partial z}+J_rB_\theta \tag{5.19}$$

$$\rho\left(V_r\frac{\partial V_r}{\partial r}+V_z\frac{\partial V_r}{\partial z}\right)=\frac{\partial P}{\partial r}-J_zB_\theta+J_\theta B_z \tag{5.20}$$

$$\frac{1}{r}\frac{\partial}{\partial r}\left(rJ_r\right)+\frac{\partial}{\partial r}\left(J_z\right)=0 \tag{5.21}$$

$$B_\theta=\frac{\mu_0}{r}\int_0^r J_zrdr \tag{5.22}$$

The plasma pressure within the flow is a combination of the ion temperature and the electron temperature given by the ideal gas law. However, due to the assumption that the electron temperature is much greater than the ion temperature, the contribution to the total pressure from the ion pressure can be neglected and the plasma pressure, P, becomes:

$$P\simeq k_BT_eN_e \tag{5.23}$$

The properties of electron temperature within the plasma flow are described by the electron heat balance equation [97]:

$$\frac{d}{dz}\left(\frac{3}{2}PV_eS\right)+P\frac{d}{dz}\left(V_eS\right)=\frac{I^2}{\sigma S}-Q_{ei}S \tag{5.24}$$

As the current is related to the velocity of a particle, a relationship can be established between the electron velocity, V_e, and the flow velocity [97]:

$$V_e=V_z\left(1+\frac{1}{\alpha_i}\right) \tag{5.25}$$

α_i is the ion current normalised by the arc current ratio and is explained further in the plasma mass model section.

The electrical conductivity is a measure on how easy it is for the current to flow through the plasma and is heavily dependent on the relative motion and collision frequencies between the ions and the electrons within the plasma. The conductivity is made from three elements; the conductivity that is parallel to the direction of the magnetic field, the conductivity that is perpendicular to the direction of the magnetic field and the conductivity due to relative motion around the magnetic field caused by the

Hall effect. A tensor can be formed to describe the conductivity through the plasma:

$$\sigma = e_0 \begin{bmatrix} \sigma_\perp & -\sigma_H & 0 \\ \sigma_H & \sigma_\perp & 0 \\ 0 & 0 & \sigma_\parallel \end{bmatrix} \tag{5.26}$$

Where the perpendicular, $\sigma_\perp$, Hall, σ_H, and parallel, $\sigma_\parallel$, conductivities are defined as:

$$\sigma_\perp = \frac{\omega_{pe}^2 \left(\upsilon_{ie} - i\omega_{pulse}\right)}{\left(\upsilon_{ie} - i\omega_{pulse}\right)^2 + \Omega_e^2} + \sum_i \frac{\omega_{pi}^2 \left(\upsilon_{ie} - i\omega_{pulse}\right)}{\left(\upsilon_{ie} - i\omega_{pulse}\right)^2 + \Omega_i^2} \tag{5.27}$$

$$\sigma_H = \frac{\omega_{pe}^2 \Omega_e}{\left(\upsilon_{ie} - i\omega_{pulse}\right)^2 + \Omega_e^2} + \sum_i \frac{\omega_{pi}^2 \Omega_i}{\left(\upsilon_{ie} - i\omega_{pulse}\right)^2 + \Omega_i^2} \tag{5.28}$$

$$\sigma_\parallel = \frac{\omega_{pe}^2}{\left(\upsilon_{ie} - i\omega_{pulse}\right)} + \sum_i \frac{\omega_{pi}^2}{\left(\upsilon_{ie} - i\omega_{pulse}\right)} \tag{5.29}$$

The plasma frequency, ω_p, of the particle species, j, is:

$$\omega_{pj} = \left(\frac{N_j Q_n^2 e^2}{m_j e_0}\right)^{\frac{1}{2}} \tag{5.30}$$

In the presence of a magnetic field the particles will begin to rotate around the field lines at a given frequency. This frequency of gyration of the particle species, j, is:

$$\Omega_j = \frac{Q_n e B}{m_j} \tag{5.31}$$

It is noted here that the mass of electrons is in the order of three magnitudes smaller than ions meaning there is a significant difference in the frequency of gyration between the two particles species. Additionally high ion charge states will have high frequencies than lower ion charge states. The frequency dependant effect on the collisional electron-ion frequency is only significant at high frequencies, in the typical range for PPT discharges (hundreds of kilohertz) this effect is minimal and can be neglected, which simplifies Equations 5.27, 5.28 and 5.29.

Within the implemented model it was assumed that there was no interaction between the magnetic field created around the electrodes and with the internal plasma formed within the pinched plasma flow. The reason for this inaccuracy was due to limited resources. Instead of a detailed magnetic field based on the current flows within the electrode (and its sub-conductors), a simplified model of the magnetic field was implemented based on two parallel point sources (discussed later). Near the electrodes the point sources caused issues with the model and results gleaned did not compare well with experimental results. To overcome this issue the magnetic field strength variable within the plasma column was set to zero, from this the conductivity tensor is simplified to consider only the contributions from the parallel and perpendicular conductivity. The re-evaluation of this assumption is set for future work when a more detailed and accurate magnetic field is implemented into the model.

As the electron temperature of the plasma increases so does the collisional frequency of electrons and ions. This causes an increase in the plasma pressure but a decrease in the flow velocity of the plasma. Subsequently as the velocity decreases so does the cross sectional area of the plasma flow which in effect increases the electron density. The increase in the electron density further increases the plasma pressure in a runaway effect that causes the plasma flow to become 'stationary'. To limit this growth it is assumed that the electron temperature within the plasma flow cannot exceed a critical temperature, T_{cr}. The critical temperature is defined as [98]:

$$T_{cr} = \frac{75M^2 T_m \overline{Q_0}}{192\overline{Q}} \tag{5.32}$$

The Mach number for all plasma jets originating from a cathode surface is $\simeq 3.5$. The frequency at which the electrons and ions collide, υ_{ie}, is given as [99]:

$$\upsilon_{ie} = 3.62 \times 10^{-6} \frac{\Lambda N_e T_e^{-\frac{3}{2}}}{\overline{Q}} \tag{5.33}$$

Collisions within the plasma between the electrons and the ions can be considered as binary collisions. However, due to the relative masses, velocities and sizes, an electron is more likely to be scattered by a small amount due to the interaction of the coulomb forces between the particles rather than a larger deflection due to a direct impact between the particles. Due to the small scatter in a single collision event it is more advantageous to describe the effect of numerous small scatter events (as would be present in plasma) rather than describe the collisional processes by a direct collision. The coulomb logarithm, Λ, is the factor by which small-angle collisions are more effective than large-angle collisions. For the plasma conditions most typically found in a short duration vacuum arc the coulomb logarithm is described as [99]:

$$\Lambda = 23 - log\left(N_e^2 \overline{Q} T_e^{-\frac{3}{2}}\right) \tag{5.34}$$

From the ionisation levels of the plasma particle species and the electron temperature an approximation for the ion charge state distribution can be made. An approximate method using the Grizinski$\check{i}$ formula for the electron impact ionisation cross section of ions and averaging over the Maxwell electron velocity distribution is used to find the ionisation coefficient, $k_n(t)$, of the nth charge state level [100]:

$$k_n(t) = 1 \times 10^{-20} \left(\frac{8k_B T_e}{\pi m_e}\right)^{\frac{1}{2}} \left(\frac{13.6e}{I_{i,n}}\right)^2 \exp\left(\frac{-I_{i,n}}{k_B T_e}\right) \tag{5.35}$$

Table 5.2 lists the energy required to raise the ion state from the nth state to the nth + 1 state. The

Table 5.2: Energy required to raise ion state

Ion	**Energy, eV**	**Ion**	**Energy, eV**	**Ion**	**Energy, eV**
Cu	7.73	Cu^{+10}	33.30	Cu^{+20}	107
Cu^{+1}	12.57	Cu^{+11}	103.70	Cu^{+21}	112
Cu^{+2}	16.55	Cu^{+12}	32.00	Cu^{+22}	144
Cu^{+3}	20.54	Cu^{+13}	34.00	Cu^{+23}	122
Cu^{+4}	22.42	Cu^{+14}	49.00	Cu^{+24}	126
Cu^{+5}	23.20	Cu^{+15}	36.00	Cu^{+25}	170
Cu^{+6}	36.00	Cu^{+16}	37.00	Cu^{+26}	109.50
Cu^{+7}	27.00	Cu^{+17}	76.00	Cu^{+27}	8474.88
Cu^{+8}	33.00	Cu^{+18}	37.59	Cu^{+28}	505.24
Cu^{+9}	33.00	Cu^{+19}	1026.41	Cu^{+29}	N/A

ionisation coefficient can be used to estimate the ratio of the number density of the nth charge state to the total number of ions present in the plasma. This is known as the charge state fraction and can be found along the plasma flow using[91]:

$$f_n(z) = C_n \left(\frac{(-z - z_0)\, k_{n+1} N_e}{V_z} \right) - C_{n-1} \left(\frac{(-z - z_0)\, k_n N_e}{V_z} \right) \tag{5.36}$$

where C_n is a function of the charge state fraction distribution f_n^0 at the freezing zone of the cathode spot, see Table 5.1, and is expressed as:

$$C_n = \sum_{n=1} f_n^0 \tag{5.37}$$

The mean ion charge state along the cathode-anode axis is the sum of the charge state fraction distribution along the axis:

$$\overline{Q}(z) = \sum_{n=1} Q_n f_n(z) \tag{5.38}$$

The electron density, which is a function of the arc current, can be calculated from[97]:

$$J_i = J_e \alpha_i \rightarrow \overline{Q} e N_i V_z = \alpha_i \frac{I}{S} \rightarrow N_e = \frac{I \alpha_i}{e S V_z} \tag{5.39}$$

Assuming quasi-state neutrality the ion density is thus, $N_i = \frac{N_e}{Q}$. Finally the rate of energy loss for the ionisation of ions is defined by the the expression [101]:

$$Q_{ie} = N_e N_i \sum_{n=1} I_{i,n+1} k_{n+1} f_n \tag{5.40}$$

Equations 5.18 to 5.40 can be used to simulate the conditions of the plasma in the quasi-steady state plasma flow between the electrodes by solving a differential set of equations. By expanding out the heat balance equation (Equation 5.24) to obtain an expression for $\frac{dT_e}{dr}$ this can then be joined with the following set of equations that were obtained from Equations 5.18 to 5.22 and 5.39 [96]:

$$\frac{d\left(\rho V_z S\right)}{dz} = 0 \tag{5.41}$$

$$\frac{dS}{dz} = 2\pi R \frac{V_r}{V_z} \tag{5.42}$$

$$\frac{dR}{dz} = \frac{V_r}{V_z} \tag{5.43}$$

$$\left(\rho V_z S\right)\frac{dV_z}{dz} = -\frac{d\left(PS\right)}{dz} \tag{5.44}$$

$$\left(\rho V_r S\right)\frac{dV_z}{dz} = \frac{3PS}{R} - \frac{\mu_0 I^2}{2\pi R} \tag{5.45}$$

$$\frac{dN_e}{dz} = \frac{I\alpha_i}{eS^2V_z^2}\frac{dS}{dz}\frac{dV_z}{dz} \tag{5.46}$$

This system of equations was solved using the Matlab ODE23 differential equation solver, given an initial flow area from Equation 5.13 and a given arc current. The initial values of the boundary conditions for the set of equations is summarised in Table 5.1 and 5.3.

Table 5.3: Boundary conditions for the plasma flow model

Boundary condition	**Value**
$(\rho V_z S)$	$\Gamma_i I$
S_0	Equation 5.13
R_0	$\sqrt{\frac{S_0}{\pi}}$
V_{z0}	13.2kms^{-1}
V_{r0}	0
T_e	11605 K
N_e	$\frac{I\alpha_i}{eS_0V_z}$

From the flow model the parameters of the plasma along the flow axis from cathode to anode can be established. The resistance of the plasma flow can be found from the inverse of the conductivity integrated across the distance between the electrodes:

$$R_{plasmaflow} = \int_0^h \frac{1}{\sigma(z)}dz \tag{5.47}$$

The plasma flow resitance however is minimal compared to the effective resistance seen across the voltage drop in the sheath regions. Plasma is ‘insulated’ from the environment that surrounds it by the natural sheaths that are created whenever plasma interacts with a surface. The sheath is a dynamic entity with a structure and thickness that depends on the potential difference between the solid surface and the plasma potential.

In the cathode spot creation process the introduction of charge and mass via emission sites circumnavigates the effect of the cathode sheath. However, the anode sheath needs closer attention. When the potential of the solid surface rapidly changes (as it does in the PPT), the change in the electric field causes the electrons to leave immediately whilst the slower heavier ions remain 'fixed' for a small instance. This type of sheath is known as the ion matrix sheath and the thickness of such a sheath is:

$$d_{sheath} = \sqrt{-\Phi_{wall}\frac{2e_0}{eN_i}} \tag{5.48}$$

The Child-Langmuir Law describes how the species current is effected by the sheath. It states that the current per unit area which can pass through a planar sheath is limited by space-charge effects. We have assumed by invoking the ion matrix sheath that the ion current is negligible and so the limited arc current becomes:

$$J_{e-sheath} = \frac{I_{e-sheath}}{S_{anode}} = \frac{4e_0}{9}\left(\frac{2e}{me}\right)^{\frac{1}{2}}\frac{\Phi_{wall}^2}{d_{sheath}} \tag{5.49}$$

The lumped circuit analysis model is used to calculate Φ_{wall} at any given time, whilst the flow model is used to calculate N_i and S_{anode} near the anode. The limitation in the arc current by space-charge effects can be considered as a pseudo resistance for the purposes of the lumped circuit analysis model. Using Ohm's law, the limited arc current and the potential difference between the sheath and the sheath wall (which is $\simeq \Phi_{wall}$ if the plasma potential is relatively small), then combining with Equation 5.47, the total plasma resistance becomes:

$$R_{plasma} = R_{sheath} + R_{plasmaflow} \simeq \frac{V_{sheath}}{I_{e-sheath}} \tag{5.50}$$

5.2.5 Electrode Errosion Model

The properties of a cathode spot, in which the plasma mass originates, is only dependant on the material the cathode spot is formed on. For the same material one cathode spot compared to another are remarkably similar. This has allowed experimentalists to form certain parameters for many metals, which include the ion normalised by arc current, α_i, which is used to describe the ratio between the ion current and the arc current in a cathodic plasma, see Figure 5.11. This has a value of $\alpha_i = 0.114$ for copper. Another parameter is, Γ_i, the ion erosion rate, which describes the total ion mass eroded from the electrode surface per unit charge. For copper this value is $33.4\mu\text{gC}^{-1}$. This can be used to determine the rate of mass loss from the electrode surface as a function of the discharge current:

$$\frac{dm}{dt} = \frac{dm}{dQ}\frac{dQ}{dt} \Rightarrow \Gamma_i I \tag{5.51}$$

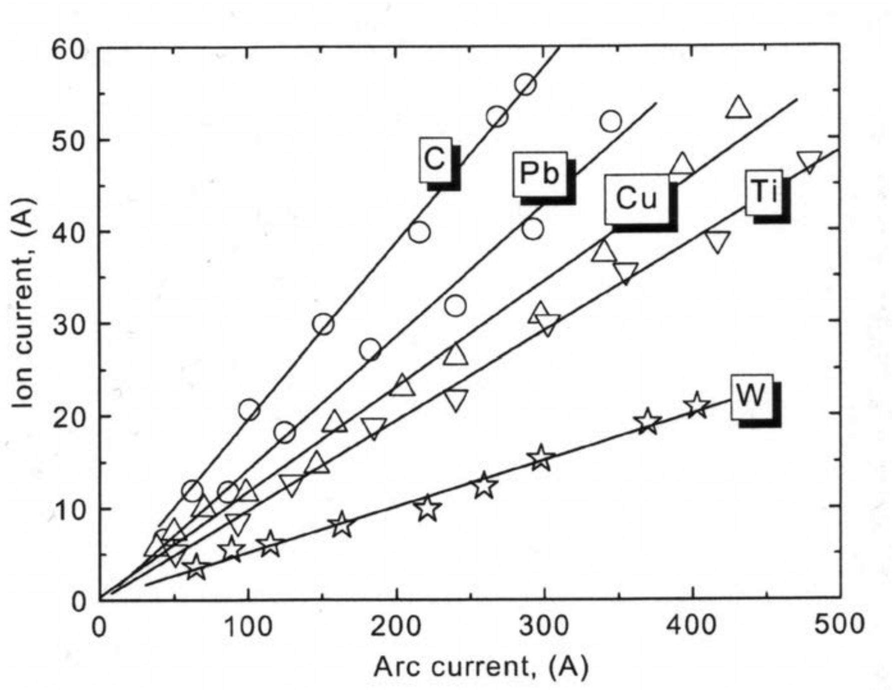

Figure 5.11: Ion current as a function of arc current for different cathode materials[33]

The total mass eroded from the electrodes, if experimentally measured, should be higher than found from Equation 5.51 due to macro particulate and neutral particle ejection that are produced from the cathode crater as it cools down after it has 'exploded'. An example of a macro particulate can be seen in Figure 4.36. Macro particulates are accelerated at a slower rate than the plasma ions and electrons due to their increased mass and so their effect on the dynamics of the plasma flow is neglected.

Neutrals are neglected for a PPT without Teflon^{TM} as there is no significant source of neutrals during the cathode spot process because most of the particles are ions. For copper the mean ion charge state is Cu^{2+} (72.1% of the total population) [24]. In addition neutrals occurring from cooling emission sites are formed on timescales longer than the discharge process and so are assumed not to interact or effect the discharging plasma.

5.2.6 Force Model

During the PPT discharge only the Lorentz force acting upon the 'plasma flow' to move the flow as a bulk system in the direction of the nozzle exit is considered. If Teflon^{TM} was present the flow model would have to account for the additional mass from the Teflon^{TM} and the subsequent neutral particle sheet from the Teflon^{TM} surface. The neutral sheet is not accelerated by electromagnetic forces but would expand out of the nozzle under thermal expansion.

It was noted in the literature review that the location of the neutral particle sheet above the cathode (when Teflon^{TM} was involved) was also the location where the next luminous activity (cathode emission site) would occur when the current through the current loop reversed direction, seen in Figure 2.32.

This would make sense, as the neutral particle sheet (if excited and ionised) would act as a bridge of least resistance between the two electrodes where current could flow. This would promote an area of ion bombardment on the rough cathode surface where an emission site would form. After the initial discharge across the Teflon^{TM} surface, further pulses would begin from the formed neutral sheet at a location specified by the dynamics of the neutral sheet.

In the case of the experiments undertaken in this work where Teflon^{TM} is not present, a neutral particle sheet is thought not to form. Instead, the formation of each new plasma sheet is assumed to be in a location where the circuit resistance is minimal (i.e. where $R_{electrodes}$ is small). This is usually at the closest point to the capacitor, but still within the discharge chamber.

When calculating the Lorentz force between the plasma flow and the magnetic field that is set up around the electrodes, a magnetic field distribution based on two infinitely long copper wires was assumed. The magnetic field distribution was calculated along the axis between the wires. This magnetic field distribution along the axis between the two electrodes was assumed to be similar to a magnetic field around rectangular electrodes, so that across the width of the rectangular electrodes the distribution was assumed to be constant and fringe effects were ignored. The accuracy of this magnetic field distribution is unknown and further work is required to confirm its applicability.

Using the Lorentz force evaluated over the entire plasma flow volume, Newton's second law and Equation (5.51) leads to an expression for the acceleration of the plasma bulk as a whole out of the thruster nozzle;

$$\Gamma_i I \frac{dx}{dt} + \frac{dx^2}{d^2t}\Gamma_i \int_0^t I dt = \int_V (J \times B)\, dV \tag{5.52}$$

Whilst evaluating the Lorentz force the magnetic field contribution from the self induced magnetic field in the x-y plane will cancel itself out and so only the external magnetic field in the y-axis needs to be considered. The external magnetic field in the x-axis and the z-axis is zero as fringe effects are neglected. The current density in the x-y plane is also zero. The Lorentz force integrated over cylindrical co-ordinates is therefore:

$$\int_V (J \times B)\, dV = \int_V \frac{I_z}{\pi R^2(z)} \left(\frac{\mu_0 I_z}{2\pi(z+\phi)} + \frac{\mu_0 I_z}{2\pi(h-z+\phi)} \right) dV = \frac{\mu_0 I_z}{2\pi} log \frac{2h}{\phi + h} \tag{5.53}$$

where ϕ is half the electrode thickness.

5.2.7 Complete PPT Discharge Model

The model implementation used the Matlab dde23 delayed differential equation solver. The toolset of this solver allows 'events' to be set that, if obtained, would terminate the solver. Parameters can then be altered and the solver restarted using the terminated solution and altered parameters to become the new boundary conditions and 'history' for the next pulse. The solver is also capable of providing an estimate of the $\frac{dL_{circuit}}{dt}$ by using the time lag function of the solver with the assumption that:

$$\frac{\Delta L}{\Delta t} \Rightarrow \frac{dL}{dt} \tag{5.54}$$

where the time lag was set sufficiently small at 0.1μs. Equations (5.2), (5.51), (5.53) and (5.54) can be rewritten in state space and solved as a set of simultaneous equations:

$$\begin{aligned}
x\dot{(1)} &= x(3) \\
x\dot{(2)} &= x(4) \\
x\dot{(3)} &= \frac{\frac{\mu_0 I_z}{2\pi} log \frac{2h}{\phi + h} - x(3)x(4)\Gamma_i}{x(6)} \\
x\dot{(4)} &= \frac{V_0 - \frac{x(2)}{C_{PPT}} - x(4)x\dot{(5)} - x(4)R_{circuit}}{L_{circuit}} \\
x\dot{(5)} &= \frac{L_{circuit} - L_{circuit-lag}}{1 \times 10^{-7}} \\
x\dot{(6)} &= \Gamma_i x(4)
\end{aligned} \tag{5.55}$$

When the integral of the current, $x\dot{(2)}$, reached either a maximum or minimum (i.e. zero current) the dde23 solver would pause. It was at this stage experimental observations suggested that a new plasma bulk would be created and accelerated out of the PPT. So the distance travelled by the plasma bulk, x(1), the plasma bulk speed, x(3) and the plasma bulk mass, x(6), were reset to their initial conditions and the other values remained unaltered. The dde23 solver was then restarted. The initial conditions for the set of differential equations is shown in Table 5.4. The initial conditions were arbitrarily chosen to be relatively small but non-zero values.

Table 5.4: Boundary conditions for the lumped circuit analysis model

Boundary condition	**Value**
$x(1)$	0.1 mm
$x(2)$	0
$x(3)$	1 ms^{-1}
$x(4)$	10 A
$x(5)$	0
$x(6)$	0.001 μg

There are processes that are not modelled within the lumped circuit analysis which may also affect the plasma bulk properties. The accuracy of the magnetic field distribution has a significant role in determining the Lorentz force which in turn determines the bulk plasma speed. If the bulk speed is 'slow' when the current in the circuit loop reverses, there may still be a previous plasma bulk in the discharge channel. In reality the circuit would then be closed by that plasma bulk and the discharge would carry on from wherever the plasma bulk might be at that time. However, in the model it is assumed a new sheet is initiated and so it is possible to have two or more plasma bulks occurring in the same discharge channel. If the bulk speed is ‘fast’ and the bulk plasma has left the discharge chamber before the current reverses then multiple plasma bulks cannot occur.

The effect of the plasma bulk canting is also not taken into consideration as it is beyond this simplified model. It is theorised that the canting effect originates from the vectored velocity between the plasma flow (which is in the direction of the anode) and the velocity of the plasma bulk (which is in the direction of the nozzle and is a function of the Lorentz force). The two combined create a vectored plasma bulk velocity. By applying diverging electrodes to the PPT the vectored velocity can be realigned with the axis in which the nozzle is in to increase performance. From the frame of reference of the ion motion within the plasma flow the canting will cause the accelerated ion to experience an off axis electric field which may alter the properties of the plasma flow. Incorporating these processes is left for future work.

The complete code for the PPT discharge model can be found in Appendix A.

5.3 Model Validation

The model was validated against experimental results by comparing the predicted current profile with the experimentally observed current profile. The radius of an individual cathode spot has been shown to expand between 1-2mm in the first 10ns, see Figure 5.10. On timescales greater than this no references of the radius of the cathode spot for high current discharges were found. The properties of the plasma flow at the anode sheath are a function of the initial flow area (which is a function of the individual cathode spot area). By comparing the predicted current profile with experimental results (in the quasi steady state assumption range i.e. below 3cm) for individual cathode spot radii from 0.5mm to 4.5mm, a best fit match was found, see Figure 5.12. For the 1cm gap distance the 1.5mm and 2.5mm radii under-predicted the current profile, whilst for the 3cm gap distance the 0.5mm and 4.5mm radii under-predicted the current profile. By a process of elimination a cathode spot radius of 3.5mm was found to best fit the data sets. This value was then fixed when comparing all other data sets.

Further optimisation of the radius of the individual cathode spot is left for future work as it requires the modelling of anode spot processes in the flow model and a more accurate value for the capacitor inductance and resistance in the lumped circuit analysis model.

Figure 5.13 shows the validity of the model to predict the current profile at 1443V discharge at an electrode gap separation of 3cm. The comparison shows two features that are not modelled accurately. The first is that the current peak from the experimental results and the modelled results are artificially placed in line with each other. This is because the model does not predict the occurrence of the exponential increase in the current waveform seen in the first few microseconds of the experimental data. This physical phenomenon is thought to be from the discharge gap breakdown mechanism, which is not

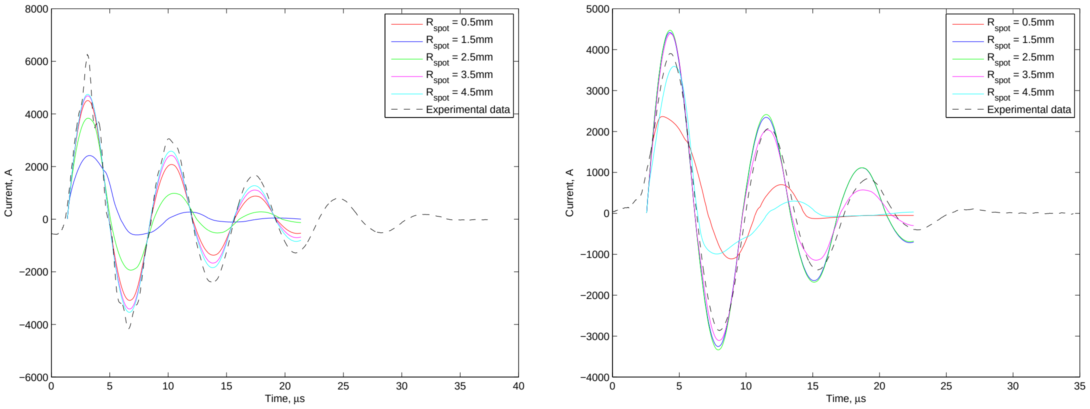

Figure 5.12: Optimisation of R_{spot} by creating a best fit between the predicted and experimentally observed current profiles at 1cm (Left) and 3cm (Right) electrode separation

modelled.

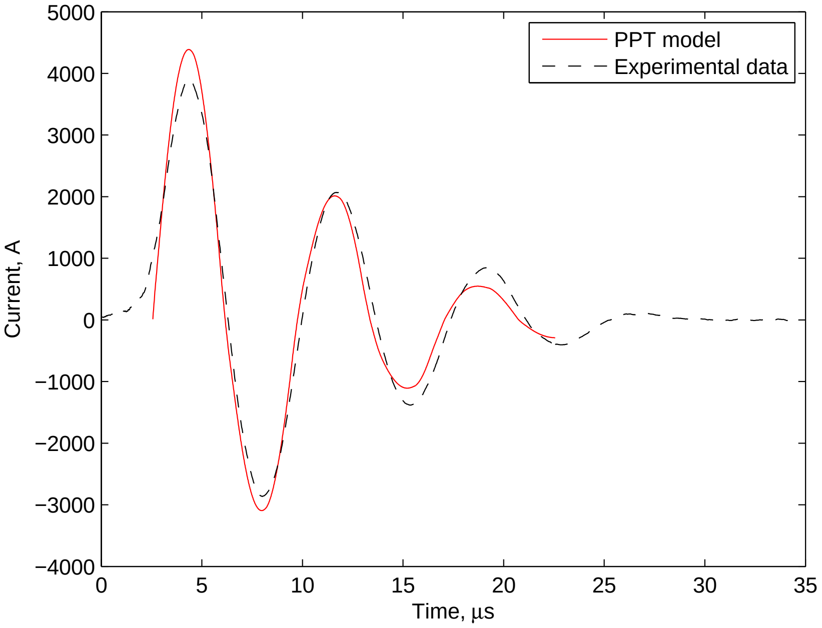

Figure 5.13: Comparison of the predicted and experimentally observed current profiles at 1443V and 3cm electrode separation

The second feature is the over prediction of the current pulse in the first peak. This may be linked to the breakdown mechanism or it may also be linked to the possible inaccuracy in the simplified model of how the cathode spot radius changes with time (Equation 5.13). Figure 5.14 compares the validity of the model over a range of experimental measurements from 748V to 2493V at a discharge gap of 3cm.

In context with the previous observations Figure 5.14 generally shows good correlation between the predicted and observed current profiles. Figure 5.15 compares the validity of the model over a range of experimental measurements from 770V to 2600V at a discharge gap of 1cm.

Figure 5.15 shows a reasonable correlation between the predicted and modelled data. However, as the

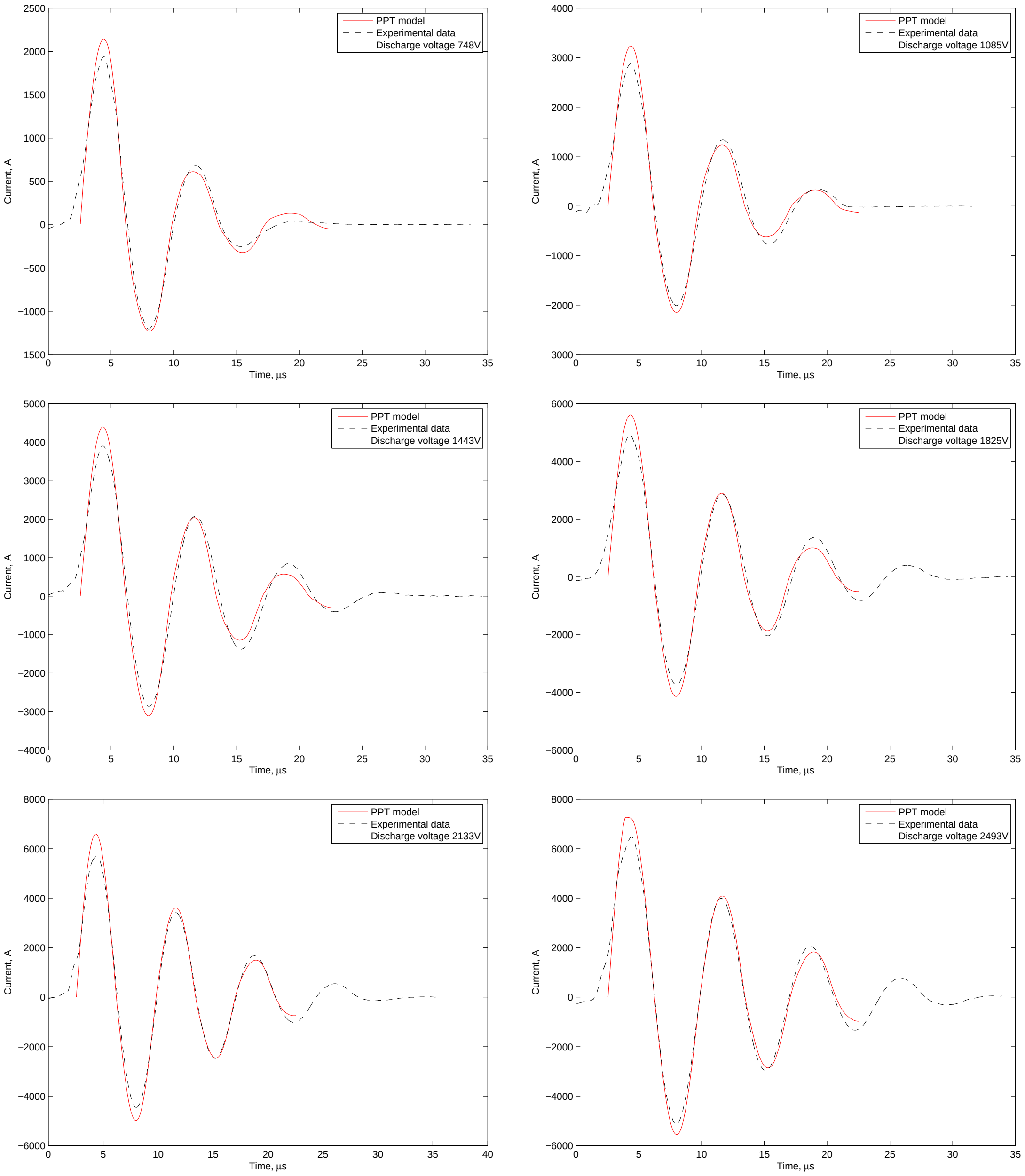

Figure 5.14: The modelled current (red) compared to experimentally obtained current measurements (black dash) for discharges between 748V and 2493V at an electrode separation distance of 3cm

discharge voltage is increased the model increasingly under-predicts the current profile. This is thought to be because the model does not take into account anode spot creation processes, which is thought to be the cause of the visible spikes seen in the first (and sometimes second) peaks of the experimental data curves.

Figure 5.16 shows that the peak plasma bulk speed for a 1443V discharge at a 3cm electrode separation distance is just under 12kms^{-1}. A selection of peak ion speed velocities measured in literature, with time of flight probes are: 26-40kms^{-1} [102], 4-15kms^{-1} [22] and 15.5-35kms^{-1} [20]. The model predicts the range of peak ion velocities for 1cm and 3cm between 748V and 2600V discharges to be 3.5-22kms^{-1}. This range predicted by the model is within the order of magnitude from literature but future work

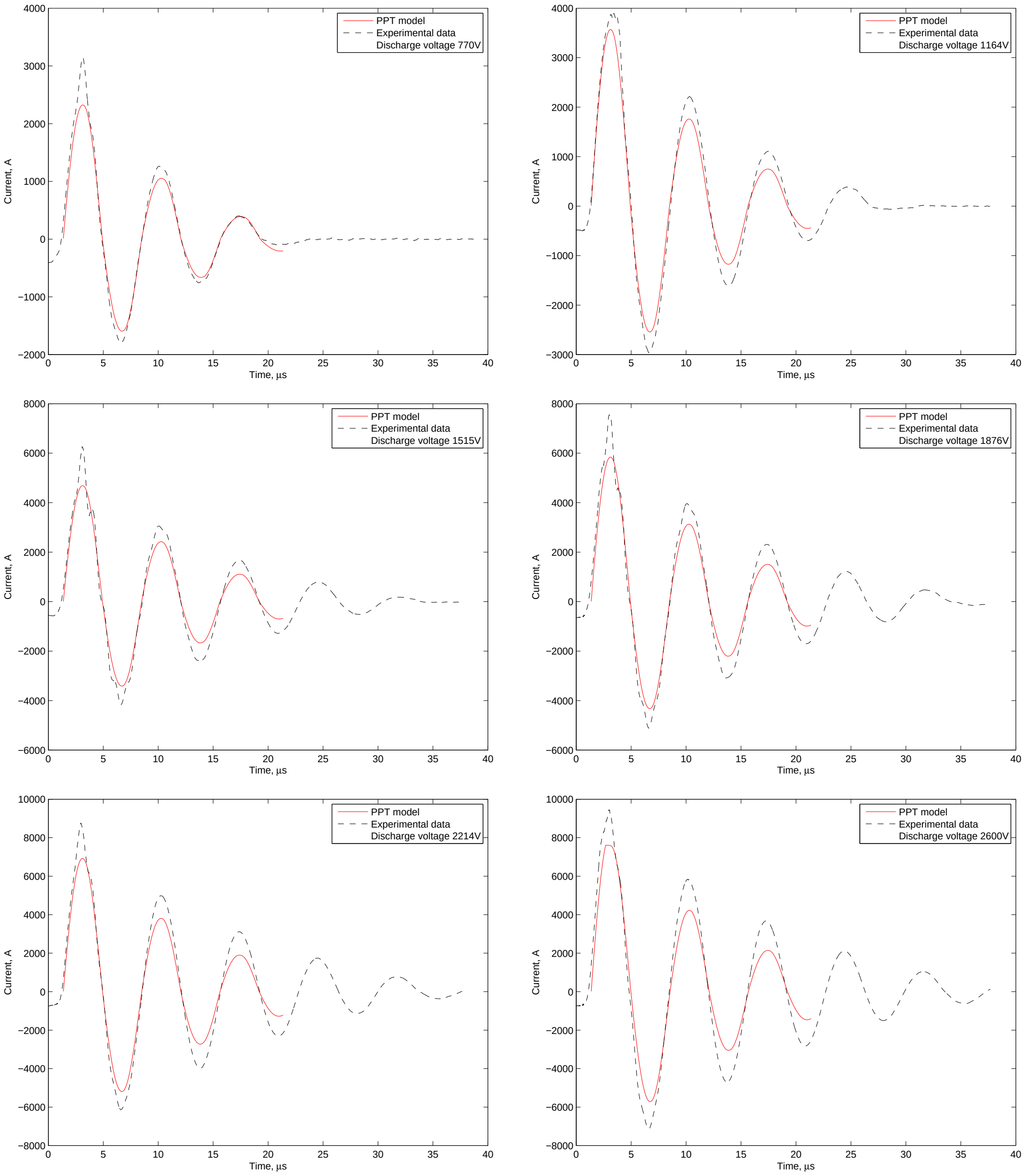

Figure 5.15: The modelled current (red) compared to experimentally obtained current measurements (black dash) for 770V and 2600V discharges at an electrode separation distance of 1cm

and experiments will be required to measure the peak ion speeds exactly with a time of flight probe. The accuracy of the Lorentz force model will depend significantly on the accuracy of the magnetic field distribution model.

Within the limited parameters to validate the compiled model with experimental values, the model has been shown to give relatively accurate results for the discharge current profiles over a range of discharge parameters, as long as they remain within the boundaries of the quasi steady state assumption. The model also provides a relative good match between predicted and experimentally observed peak ion speed velocities.

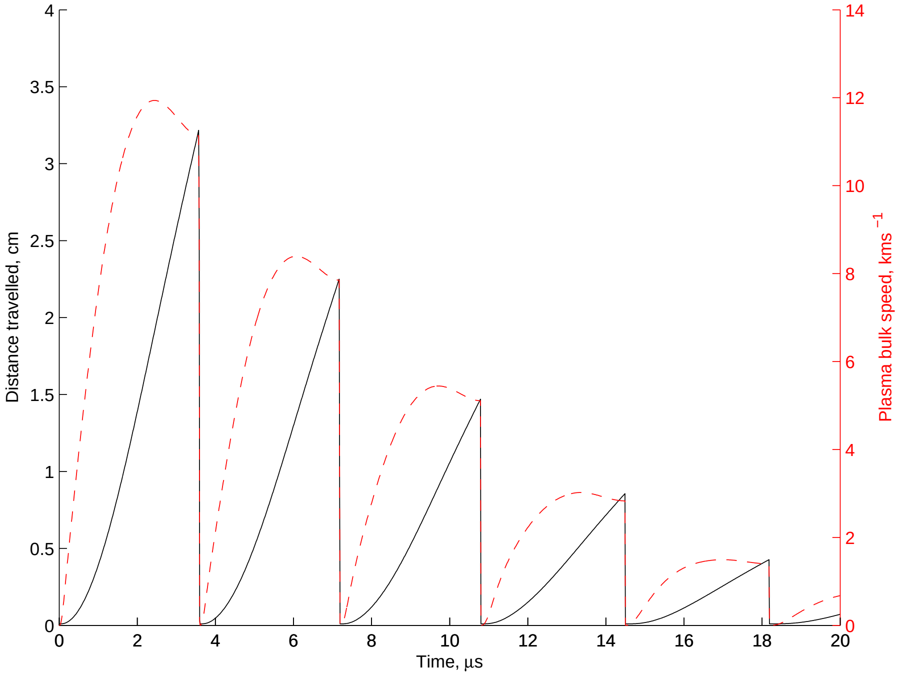

Figure 5.16: The bulk plasma speed accelerated by the $J \times B$ product for a 1443V discharge at a 3cm electrode separation distance. Dashed: Plasma bulk speed, Solid: Distance travelled

5.4 PPT Analysis

The completed model can be used to investigate the internal plasma processes of the PPT and possibly highlights features that have been seen in experimental literature but unexplained in theory. The analysis will look at the properties of the plasma flow, assumed to be in quasi steady state, across the electrode discharge gap and how the quasi steady state plasma properties change over the discharge time. For the analysis of the plasma the model was set up with the parameters given in Table 5.5.

Figure 5.17 shows the current profile of the first pulse. The times of interest are at 0.05μs, 0.70μs and 1.75μs, which represent the start of the pulse, halfway through the pulse rise and the peak of the current pulse respectively.

Table 5.5: Parameters of the modelled PPT

PPT Parameter	**Value**
High Voltage Capacitor	
Capacitance	4.06μF
Charging voltage	1443V
Cap. Inductance	310nH
Cap. Resistance	33mΩ
Electrodes	
Setup	Parallel bar
Material	Copper
Width	20mm
Thickness	10mm
Discharge channel length	60mm
Separation	30mm

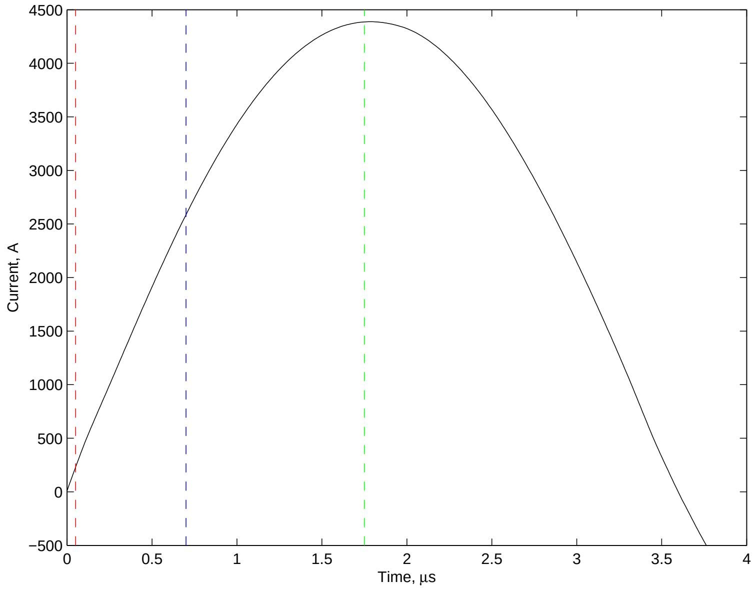

Figure 5.17: Predicted current profile of the first pulse discharge showing the relative current values at the analysis times of 0.05μs (red), 0.70μs (blue) and 1.75μs (green)

The flow radius distribution of the plasma flow between the electrodes at these times is shown in Figure 5.18, with the addition of a plot to show how the flow radius varies over the complete discharge.

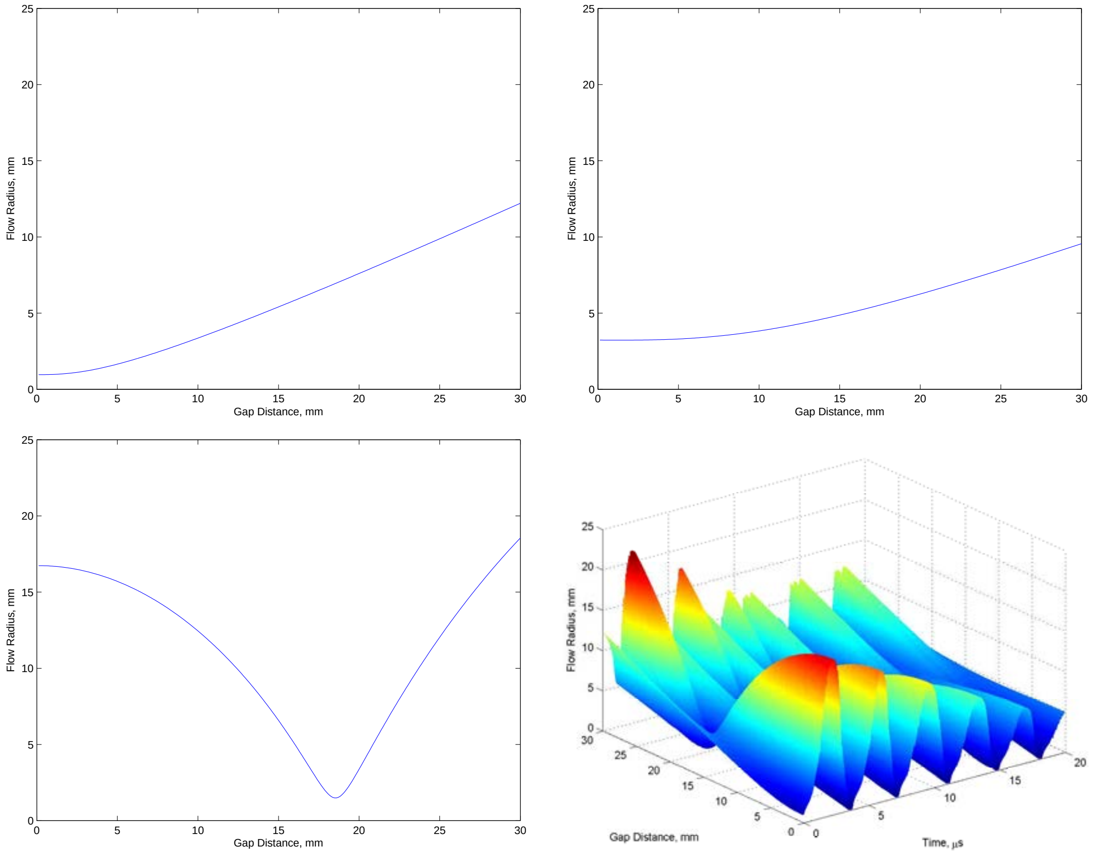

Figure 5.18: Predicted flow radius, Top left: 0.05μs, Top Right: 0.70μs Bottom Left: 1.75μs Bottom Right: Complete discharge

At 0.05μs and 235A, the flow radius shows a conical like expansion that starts at 2-3 mm from the cathode surface. Before this the flow radius is relatively constant at approximately 1mm but during the conical expansion of the flow area this increases to approximately 12mm close to the anode surface. As the current rises to 2800A at 0.70μs the flow radius distribution looks similar, however the initial flow radius has increased to approximately 3mm. The start of the conical expansion has shifted to approximately 5mm. The radius of the flow at the anode has also decreased to approximately 9-10mm. A 3D representation of the plasma flow at 0.70μs can be seen in Figure 5.19. When this is compared to images of the current density profile mapping between 2-3μs in Figure 2.26 [16] similarities can be seen. Although caution should be taken the structure at this stage of the pulse in both images shows a cylindrical coloumn towards the cathode that expands out conically towards the anode.

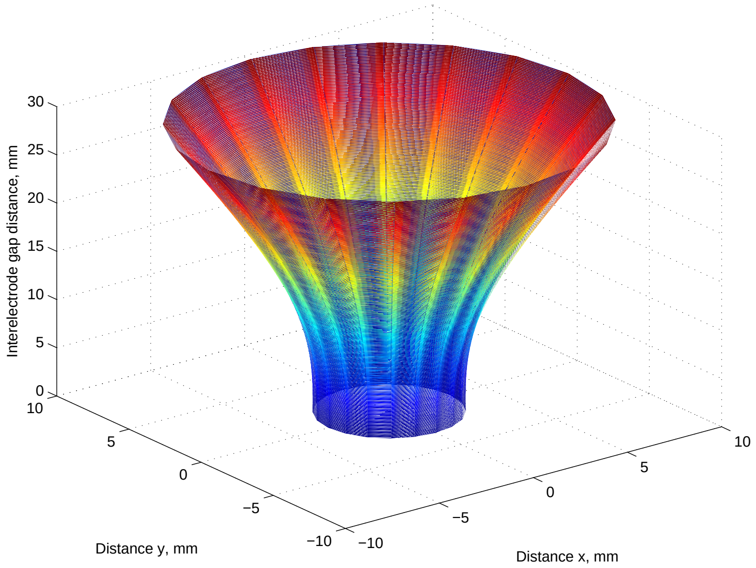

Figure 5.19: 3D representation of the plasma flow at 0.70μs

As the current approaches the peak current of 4330A at 1.75μs a 'choke' formation is seen around 18-19mm from the cathode. In addition to this the initial flow radius has significantly increased to approximately 17mm. This is expected as the number of cathode spots increases with the discharge current. However, due to the change of dynamics of the flow caused by the choke, instead of the flow radius decreasing as the initial radius increases, (as seen from 0.05μs to 0.70μs), here the flow radius seems to have increased once again to approximately 18mm. The flow radius over the whole discharge shows that as the discharge progresses the 'choke' remains at the same distance from the cathode surface. Further modelling has shown that this is the case for all electrode geometries tested and in cases where the internal conductivity of the plasma column is unaffected by internal magnetic fields. In the absence of internal magnetic fields this 'choke distance' could be thought of as a material property of the electrode itself. The 'choke' has an effect on all the other plasma flow parameters.

At 0.05μs and 235A, the electron temperature shows a peak of 2eV at around 2.5mm from the cathode.

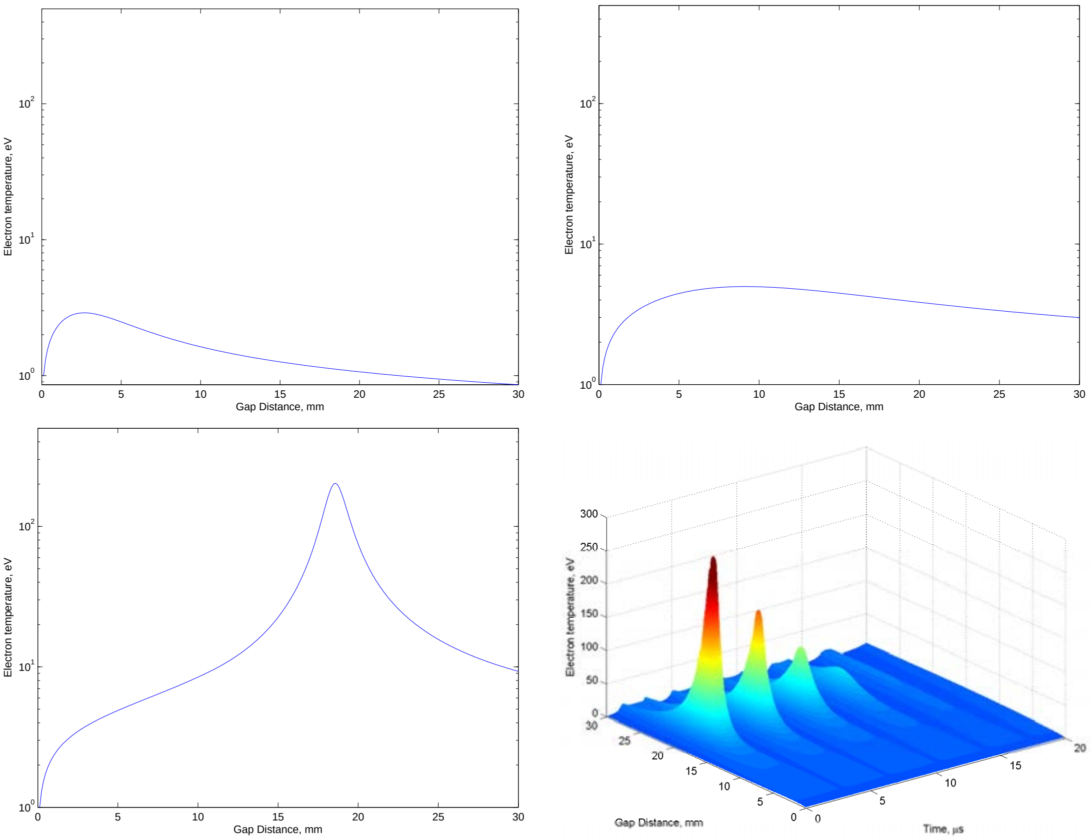

Figure 5.20: Predicted electron temperature, Top left: 0.05μs, Top Right: 0.70μs Bottom Left: 1.75μs Bottom Right: Complete discharge

The distribution initially rises rapidly to its peak and then gradually decays. At the anode the electron temperature has dropped to around 0.8eV. As the current rises to 2800A at 0.70μs the distribution looks similar although the peak temperature has risen to 5eV and the peak has shifted away from the cathode to approximately 9-10mm. This distribution has been seen in the experimental phase of this work.

Figure 4.28 shows the distribution of carbon back flux on Teflon^{TM} samples that were placed between the electrodes in some of the experiments. For energies of 5-11J a clear patch is seen on some of the Teflon^{TM} samples close to the cathode. It is also of benefit to note the relative position of the plasma column at 0.05μs and 0.70μs compared to the location at the peak current (1.75μs), see Figure 5.21. At 0.05μs and 0.70μs the plasma column is within 2mm of its initial start position but by 1.75μs at the peak of the discharge this has increased to approximately 1cm.

Although the model does not take into account the effect of Teflon^{TM} it is of interest to note that the distribution of the electron temperature at 0.05μs and 0.70μs, when the plasma column is within 1-2mm from the initial position (and if Teflon^{TM} was present would be in very close proximity) is similar to the distribution of the carbon back flux. Where the electron temperature is at its highest there is no back flux on the Teflon^{TM} samples. Further work to combine the effects of Teflon^{TM} into the model will be required to conclusively say if this is a real effect or a coincidence.

As the current approaches the peak current of 4330A at 1.75μs a new feature is observed and is

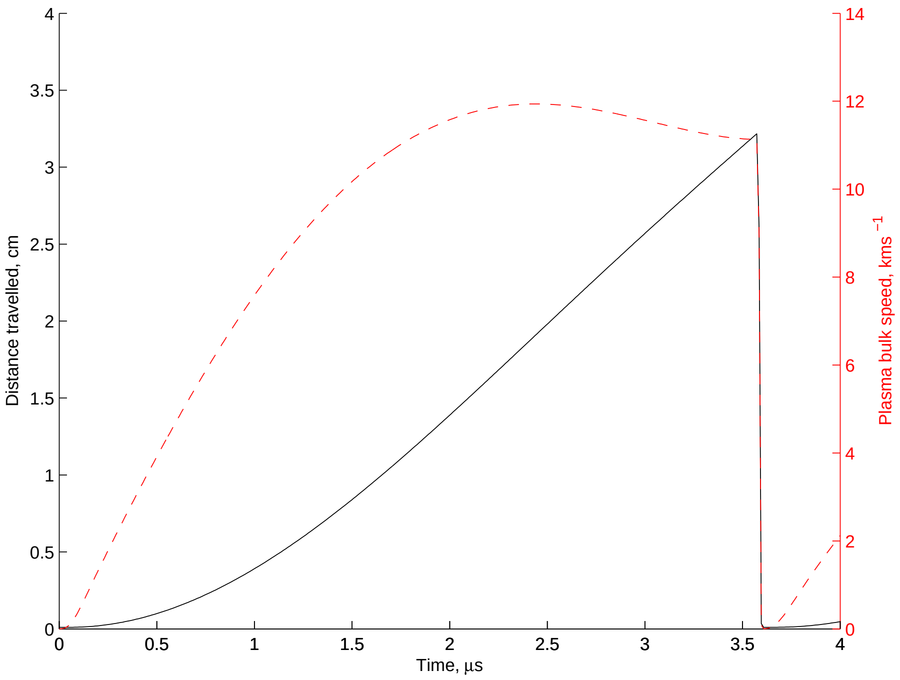

Figure 5.21: The speed and distance travelled by the plasma column in the discharge chamber for a single pulse. Dashed: Plasma bulk speed, Solid: Distance travelled

attributed to the choke in the plasma flow. At the location of the choke the electron temperature sharply increases to approximately 200eV. Further modelling has shown that the magnitude of the peak temperature within the choke is a proportional function of the discharge current. The rise in the electron temperature is also linked with the electron density, see Figure 5.22.

The electron density in several respects shows similar relationships in time with the electron temperature. Figure 5.22 shows that as the plasma flow is restricted by the choke the electron density increases. As well as increasing due to the physical volume within the choke being small compared to the rest of the flow, the electron density also increases due to a secondary effect. As the plasma flow is constricted, the electron temperature significantly increases and further ionisation of the copper ions within the flow occurs. At the extreme temperatures mean ion charge states of Cu^{+25} are predicted, see Figure 5.23. The additional influx of electrons from the highly ionised copper particles adds to the total electron density.

The distribution and magnitude of the peak electron density has been observed in literature, see Figure 2.28. Although the data in the graph has been 'centralised' it can be deduced from the reference that the peak is located approximately 18-20mm from the cathode surface, which is in good correlation to the developed model.

The high ion charge states that are predicted to form in the choke by the model have been observed in literature. Figure 5.24 shows the ion signals for a 2kV discharge with a 2μF at 40nH capacitor [34]. It can be seen from the signal data that the ions with the highest ion charge state are observed first

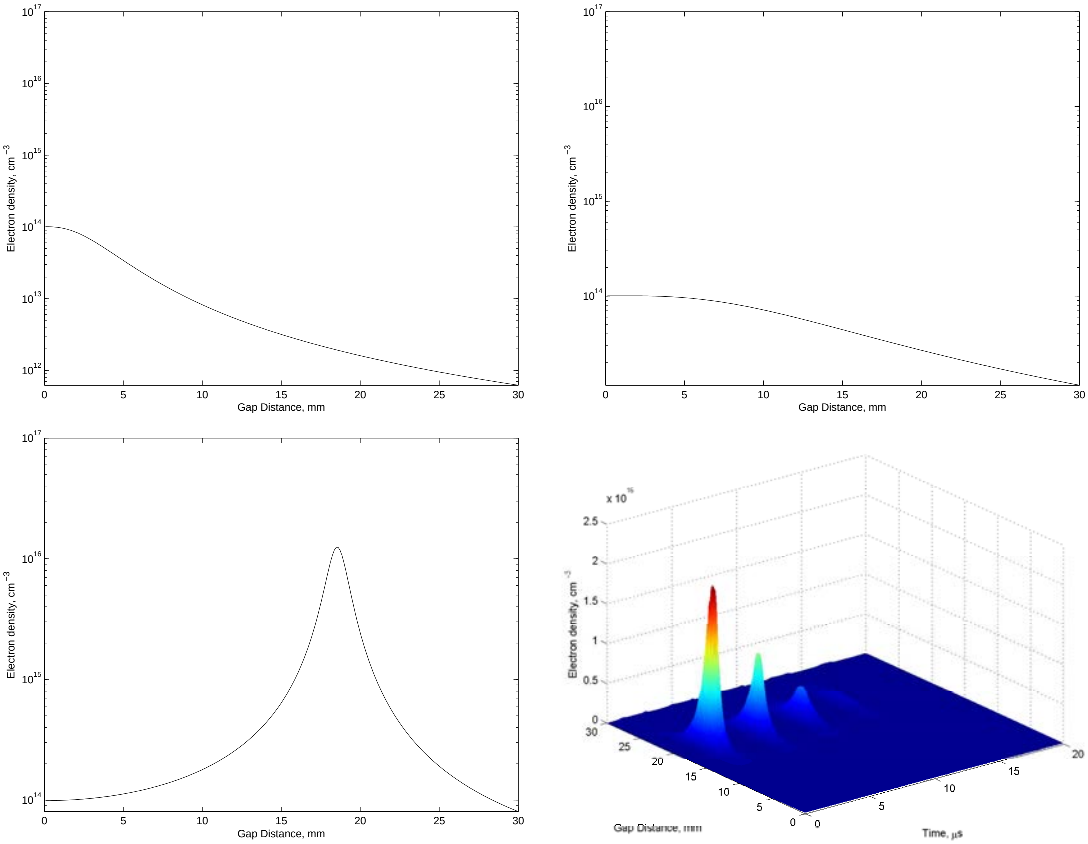

Figure 5.22: Predicted electron density, Top left: 0.05μs, Top Right: 0.70μs Bottom Left: 1.75μs Bottom Right: Complete discharge

and as time progresses the ion charge state number decays. Plotting the decay of the ion charge state from the signal probe shows that with crude interpolation the ion charge state predicted by the model is reasonable compared to avaliable literature.

The ion charge state, electron temperature and electron density have a significant impact on the electron-ion collisional frequency and the plasma frequencies of the different species of particles. In turn these distributions affect the conductivity of the plasma as depicted in Figure 5.25 for the complete discharge.

The plot shows some interesting features; foremost that the plasma flow conductivity is not constant across the discharge gap. Close to the cathode the conductivity is at its lowest and hence plasma resistivity is at its highest. When a moderate current is flowing through the plasma flow the conductivity increases rapidly to a peak as the ion charge state also rises. However this rise in conductivity is limited and after a threshold current the conductivity falls to a steady state for the majority of the pulse and for a majority of the discharge gap. As the discharge continues the location of the peak conductivity centres, traverses towards the choke point in the plasma flow (around 20mm).

The plasma resistance is small compared to the space-charge limiting effect of the anode sheath. The total circuit resistance and inductance is shown in Figure 5.26. The spikes in the plasma resistance are

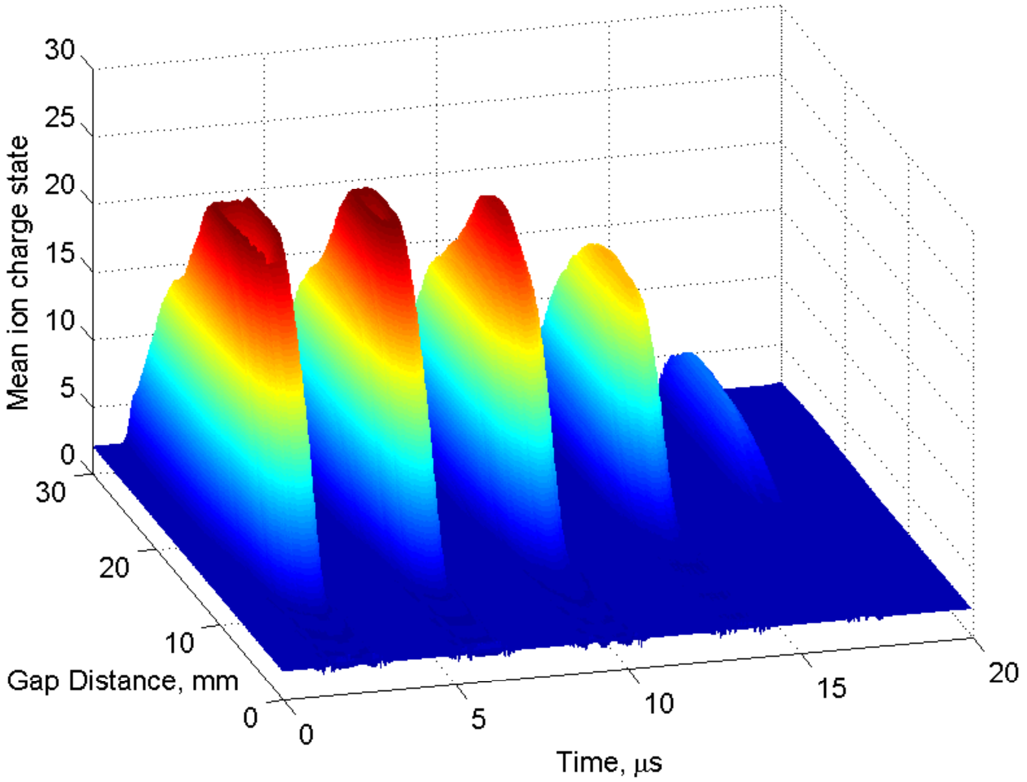

Figure 5.23: Predicted mean ion charge state for the complete discharge

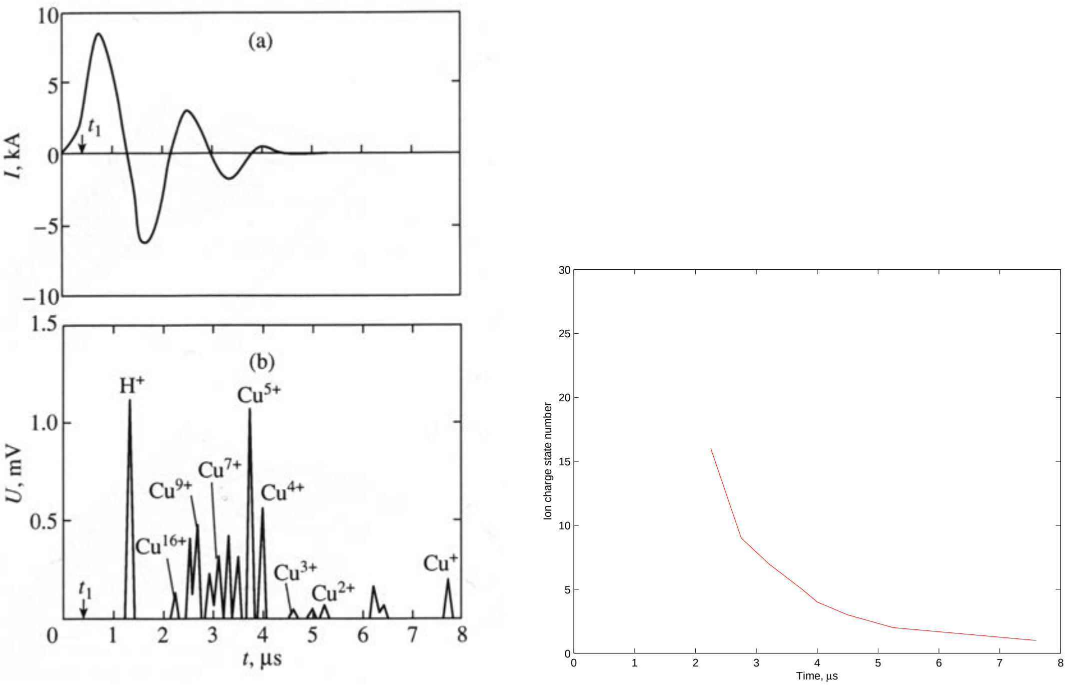

Figure 5.24: Left: Observed ion states for a 2kV discharge with a 2μF at 40nH capacitor. Right: Decay of the ion charge state over time [34]

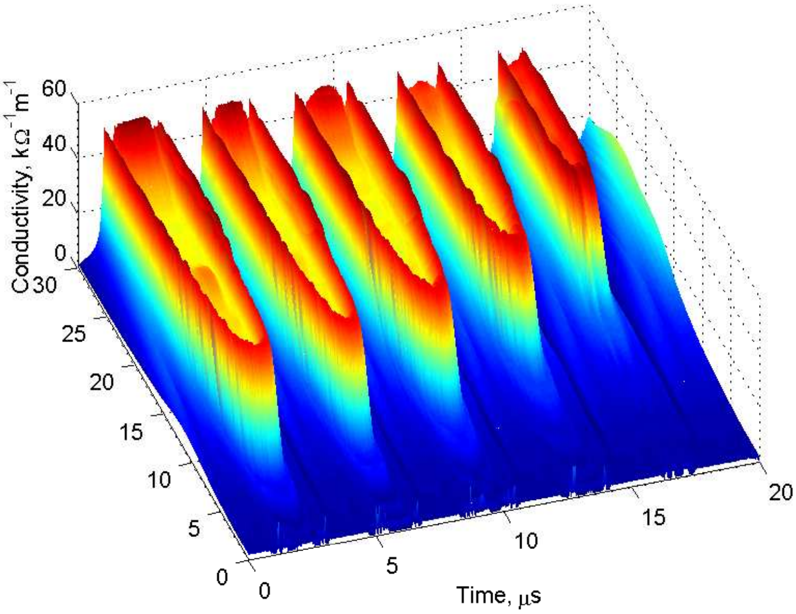

Figure 5.25: Predicted conductivity for the complete discharge

the locations where the current tends to zero and should be taken with caution. It has been observed in the literature that even as the discharge current tends to zero, a small amount of activity can still be seen within the discharge chamber, which in effect will limit the spike seen in the modelled data, see Figure 2.30. The profile of the circuit resistance shows that the resistance varies inversely with the current (which is to be expected), between 33mΩ to around 400mΩ. Also at the peak of the discharge current, the resistance of the plasma and sheath drops significantly and the total circuit resistance is only limited by the capacitor resistance.

The model has predicted that within the PPT discharge gap a choke point forms due to instabilities of the plasma flow which in turn causes a pinch effect. The dynamics of the choke significantly increases the electron density, the electron temperature and the mean ion charge state of the inter-electrode plasma. These predicted effects are also observed with similar magnitudes within the available literature, further validating the developed model.

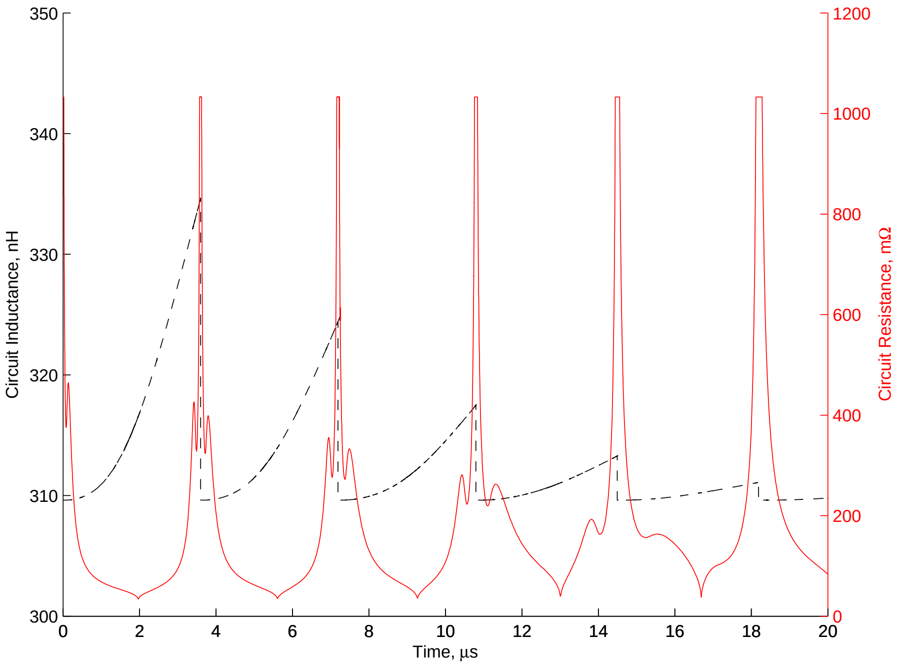

Figure 5.26: Total plasma resistance of the plasma flow for the complete discharge

5.5 PPT Optimisation

The flow model has been able to predict the current profile reasonably compared to experimental results. The accuracy of the model in estimating the Lorentz force is less well known. Without experimental time of flight data to verify the relative ion speeds it is difficult to be confident in the accuracy of the force model. However, the Lorentz force is a product of the magnetic field and the current density. The current density as predicted by the flow model fits experimental data well. The magnetic fields produced in the discharge are a proportional function of the current. Therefore even if the specific values of the magnetic field distribution are not entirely accurate, it can still be used to discover performance trends.

During the formulation of the Lorentz force model the magnetic field distribution was altered in different ways, including a draft model based on a rectangular bar electrode. However as seen in Figure 5.5, the current distribution within the electrode was not even due to the skin effect. This added additional complications and with limited computational resources meant the mapping of the magnetic field was left for future work.

As expected the predicted bulk plasma speed was significantly dependant on the field distribution, however the overall current profile was hardly affected. This lack of coupling is because $L_{Capacitor} \gg L_{electrode}$ and $R_{Capacitor} \gg R_{electrode}$, so the change in the effective electrode length within the closed circuit as the plasma propagated through the discharge channel had little overall impact. As part of the optimisation work the capacitor resistance and inductance will be lowered and so the coupling effect will become stronger. As this occurs, confidence in the results will lower, however the trends seen should show some insight into developing an optimised PPT.

Due to the approach used in this work many of the variables that are usually loosely defined in other models have been set by the material properties of the electrode, the dynamics of the cathode spot process or negated by the removal of the Teflon^{TM} propellant. The changeable variables are physical values, variables set by real electrical components and the electrical characteristics of the capacitor. Here these are the dimensions of the parallel bar electrodes, the inductance, capacitance and resistance of the high voltage PPT capacitor and the voltage the capacitor is charged to. The electrode material could also be changed to other metal types, e.g. Aluminium, Carbon or Titanium. However, to obtain a full set of input parameters (conductivity, ionisation energies, plasma jet parameters etc) for each of the metals proved difficult. There was a necessity to ensure the correct cathode spot radius was used for the specific metal, which the flow model is very sensitive to. Both factors combined meant that this part of the optimisation was left for future work.

To optimise the performance of the PPT it is necessary to focus on two areas. The first is to increase the efficiency of converting electrical energy provided by the capacitor into kinetic energy to accelerate the bulk plasma. The second area is to maximise the impulsive force provided by the discharge, whilst keeping the material mass loss per discharge as low as possible. This will ensure the electrodes will last longer and so the PPT will be able to provide a larger total impulse. By varying the electrode geometry and the capacitor parameters it will be seen if this can be achieved.

The specific criteria looked at will be: the specific impulse, I$_{sp}$, the impulse bit, I$_{bit}$, the mass bit, m$_{bit}$ and the efficiency of converting electrical energy into kinetic energy, η_{PPT}. The specific impulse, I$_{sp}$, is a measure of the thrust to the rate of use of propellant by sea level weight for any engine:

$$I_{sp} = \frac{\frac{dm}{dt}u_e}{\frac{dm}{dt}g_0} = \frac{u_e}{g_0} \tag{5.56}$$

The impulse bit, I$_{sp}$, is a measure of the momentum transferred by the engine in a short period of time. For the PPT this is the total Lorentz force (ignoring contributions from neutral particle gas and macro particulate dynamics) over the bulk volume for the complete discharge:

$$I_{bit} = mu_e = \int_{t_0}^{t_f} \int_V J \times BdVdt \tag{5.57}$$

The mass bit is found by integrating Equation 5.51:

$$m_{bit} = \int_{t_0}^{t_f} \Gamma_i I dt \tag{5.58}$$

It should be noted that this is only the mass eroded by the passing current, it does not take into account mass evaporating from cooling emission sites which would increase the total mass loss per pulse without providing significant and useful thrust. Neglecting this mass will have an effect on the calculated total efficiency of the system. It is more appropriate to specify that the efficiency that is being optimised,

Table 5.6: Setup of the PPT in the standard configuration

PPT Parameter	**Value**
High Voltage Capacitor	
Capacitance	4.06μF
Charging voltage	1700V
Cap. Inductance	310nH
Cap. Resistance	33mΩ
Electrodes	
Setup	Parallel bar
Material	Copper
Width	20mm
Thickness	10mm
Separation	30mm

is the efficiency of the system to convert electrical energy into thrust to accelerate the plasma bulk by the Lorentz force:

$$\eta = \frac{E_{kinetic}}{E_0} = \frac{\frac{1}{2}mu_e^2}{\frac{1}{2}CV_0^2} = \frac{I_{bit}}{CV_0^2} \tag{5.59}$$

A standard approach is taken to the optimisation process. The PPT model is set up as laid out, arbitrarily, in Table 5.6. This will be known as the 'standard configuration'. From here one of the parameters under consideration is altered between a range of values whilst all the others are kept the same.

Due to the pulsed nature of the thruster the specific impulse and electrical to kinetic energy conversion efficiency, scales with the plasma bulk speed that varies with time. Figure 5.27 shows the specific impulse of the PPT in the standard configuration. It also shows the mean and peak specific impulses. The optimisation of the specific impulse and the energy conversion efficiency will consider both the mean and peak values.

The first parameter considered is the charging voltage of the discharge capacitor and is varied between 500V to 2500V, see Figure 5.28. The upper limit was set to 2500V as above this value for the standard configuration the peak currents produced were of the order of 10kA. Above this peak current the flow model fails to predict the dynamics of the 'choke' region satisfactorily and the model accuracy diminishes. Despite this, the lumped circuit analysis model shows that, as the voltage is increased, all the performance parameters also increase. This is because, as the voltage is increased, the energy of the pulse increases as well. Despite the increase in energy the mean efficiency of the system remains fairly constant but with a gentle rise. Similar distributions are seen when the capacitance of the PPT discharge capacitor is varied over the range of 0.5-8.0μF, see Figure 5.29. These trends tell us that the efficiency of the system in its ability to use the inputted energy is mostly independent from the energy supplied to the system.

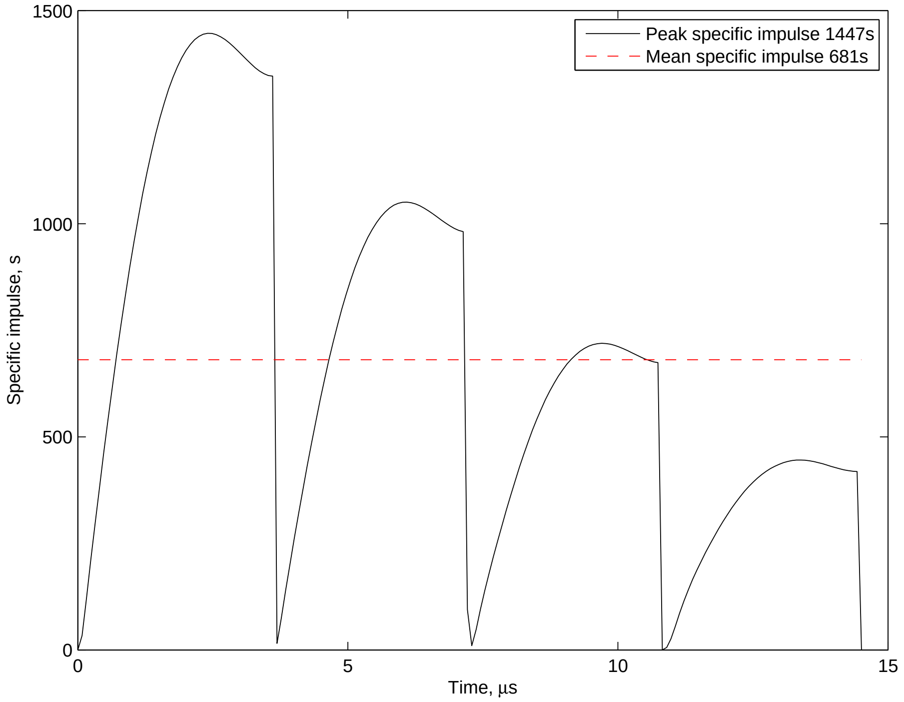

Figure 5.27: Predicted specific impulse for a PPT setup in the standard configuration. The red dashed line is the mean specific impulse over the whole discharge

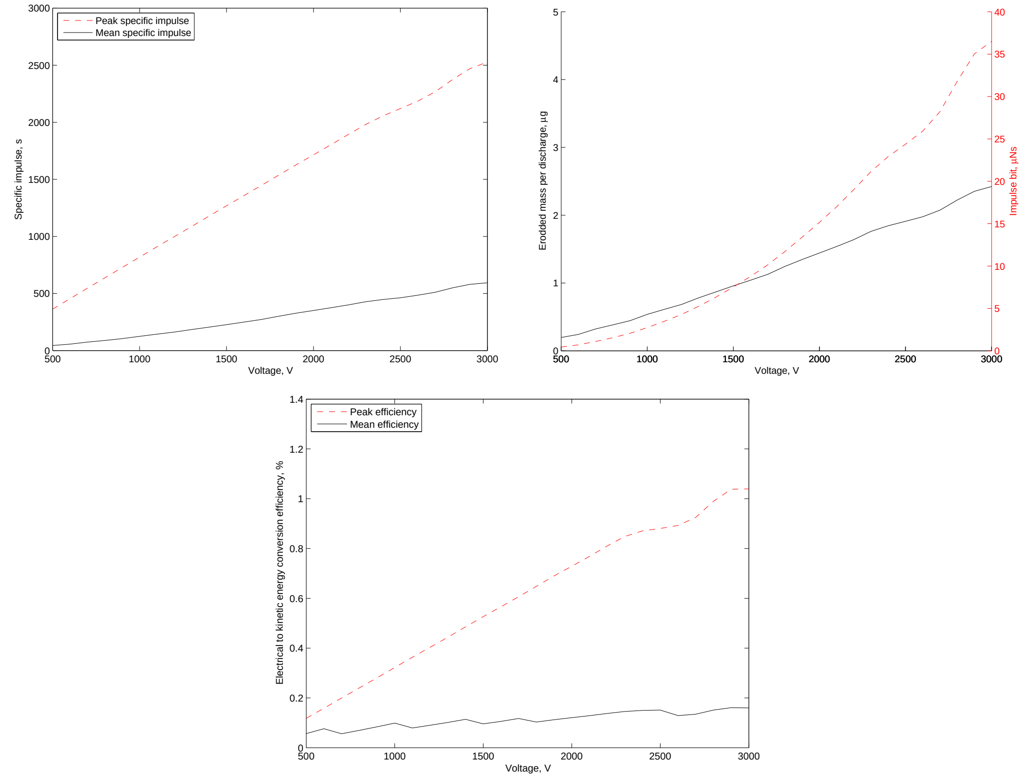

Figure 5.28: Predicted performance of a PPT setup in the standard configuration but with the discharge voltage being varied from 500-2500V. Top Left: Specific Impulse, Top Right: Impulse bit and mass bit, Bottom: Electrical to kinetic energy conversion efficiency

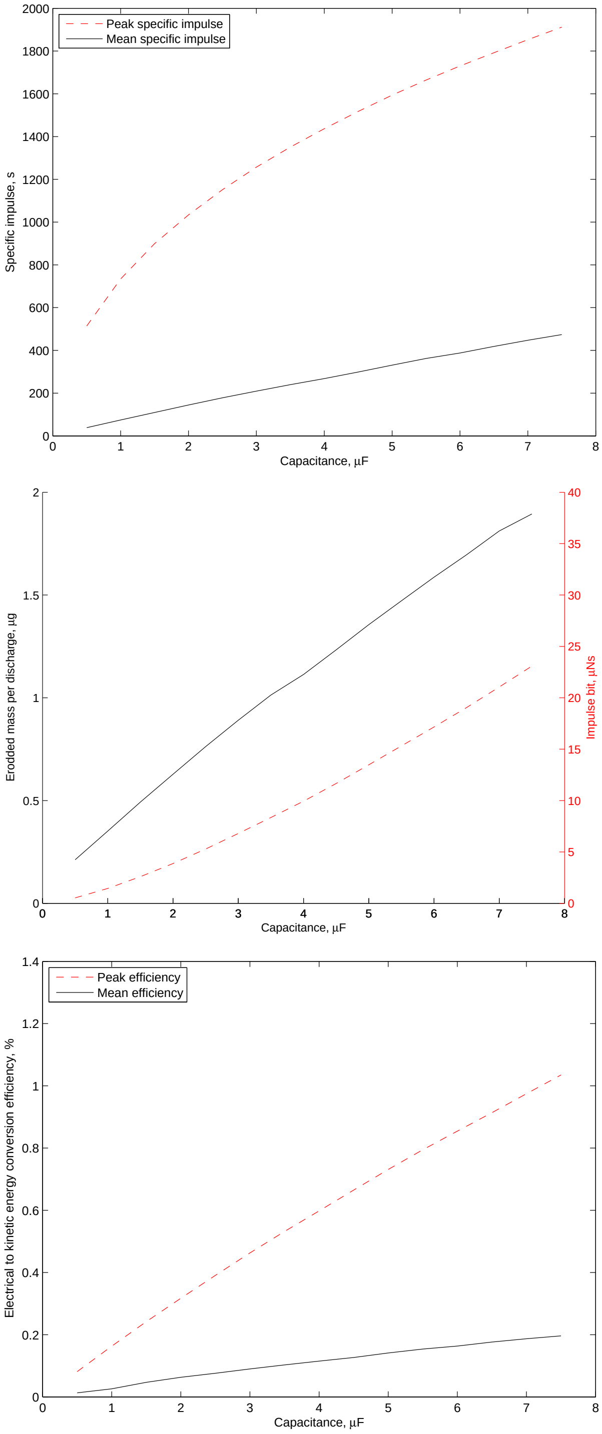

Figure 5.29: Predicted performance of a PPT setup in the standard configuration but with the PPT capacitor capacitance being varied from 0.5-8.0μF. Top: Specific Impulse, Middle: Impulse bit and mass bit, Bottom: Electrical to kinetic energy conversion efficiency

The inductance of the circuit, which has a significant contribution from the capacitor, was varied between 20-400nH. It is shown that for the standard configuration there is a peak in the impulse bit at approximately 100nH. In general, for the other parameters, as the inductance is increased the performance of the PPT decreases. In the case of the mean specific impulse it remains relatively constant. To improve the PPT performance these trends show that there is a need for the inductance to be matched to the discharge circuit.

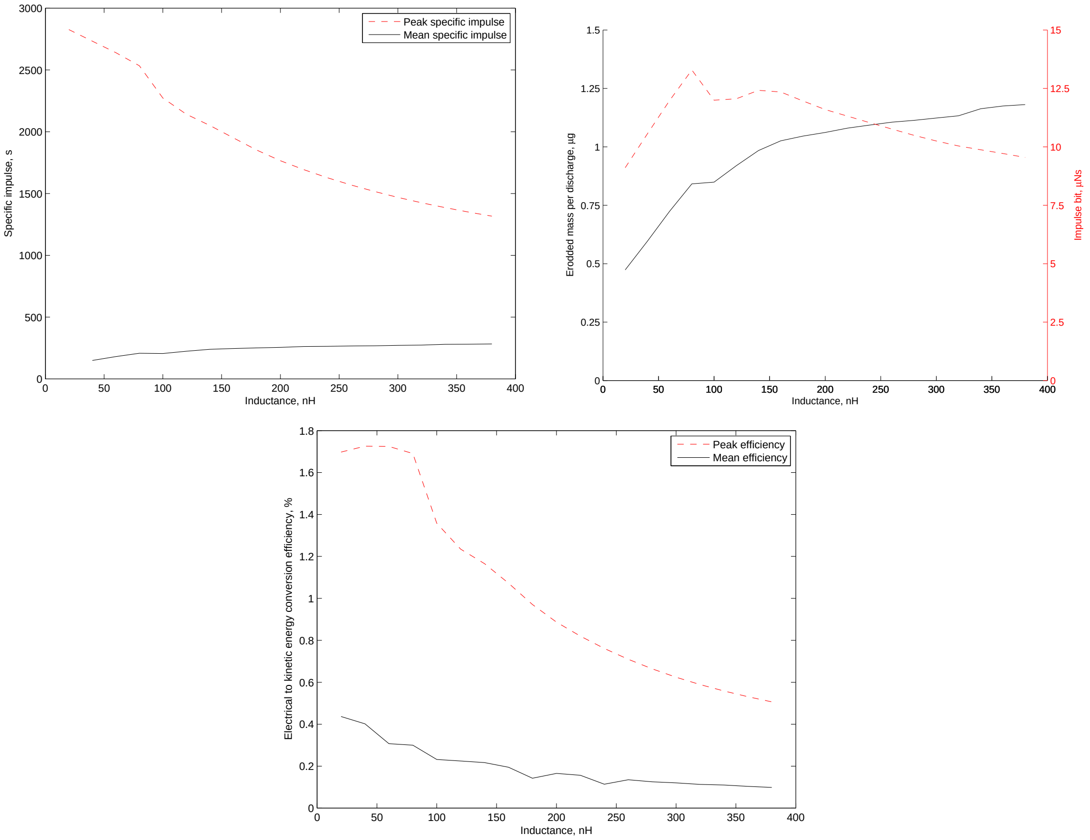

Figure 5.30: Predicted performance of a PPT setup in the standard configuration but with the circuit inductance being varied from 20-400nH. Top Left: Specific Impulse, Top Right: Impulse bit and mass bit, Bottom: Electrical to kinetic energy conversion efficiency

The total circuit resistance, not including the plasma resistance, was altered from 2-60mΩ. It was observed in Figure 5.26 that the plasma resistance for the standard configuration can rise up to and above 400 mΩ. Therefore the effect of altering the circuit resistance will be diminished. Figure 5.31 shows that when the circuit resistance is lowered the impulse bit and specific impulse of the PPT improves. However, the mean efficiency remains relatively constant.

The trends in the circuit resistance and the circuit inductance show that reducing these values in general will lead to performance increases, but care should be taken when lowering the inductance so as not to affect the circuit's ability to store energy in the magnetic field as the pulse rings. Reducing the inductance too much will have a negative effect on the current pulse and the total mass eroded and hence will impact on the impulse bit of the thruster. PPTs should then be developed with low total circuit resistances but properly matched inductances.

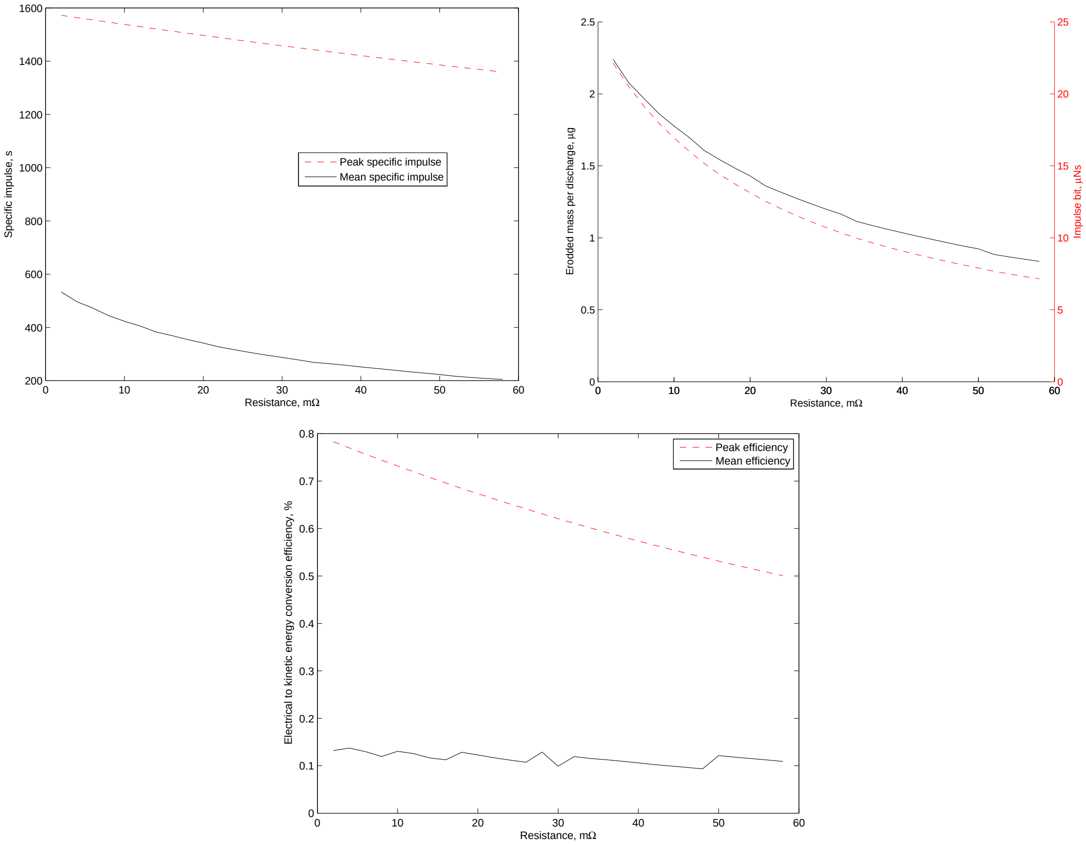

Figure 5.31: Predicted performance of a PPT setup in the standard configuration but with the circuit resistance being varied from 2-60mΩ. Top Left: Specific Impulse, Top Right: Impulse bit and mass bit, Bottom: Electrical to kinetic energy conversion efficiency

The geometry of the PPT was altered by investigating the electrode gap distance and the electrode thickness. In reality the changes in the geometry to the electrode thickness will not be the same as predicted in this model. In this model the electrode thickness is one of the variables used to map out a rudimentary magnetic field distribution that is used in the Lorentz force model. In that model the midpoint of the electrode thickness represents the distance between the origin point from which the magnetic field distribution emanates (based on two infinitely long wires) and the edge of the electrode, see Equation 5.53. In the electrode model, see Figure 5.5, it is shown that the current is not at the centre of the electrodes but towards the corners due to the skin effect. However, despite this inherent inaccuracy of the magnetic field distribution, the variation in the electrode thickness in the force model should provide insight into how to optimise the magnetic field, see Figure 5.32. The thickness was altered from 1-19mm. In effect the plots show that the closer the origin point of the magnetic field is brought to the electrode surface (i.e. the electrode thickness is reduced) the stronger the magnetic field becomes. This in turn increases the performance of the PPT without affecting the current profile and the mass bit. This trend shows that the performance of the PPT can be enhanced by optimising the magnetic field distribution or by applying an external magnetic field.

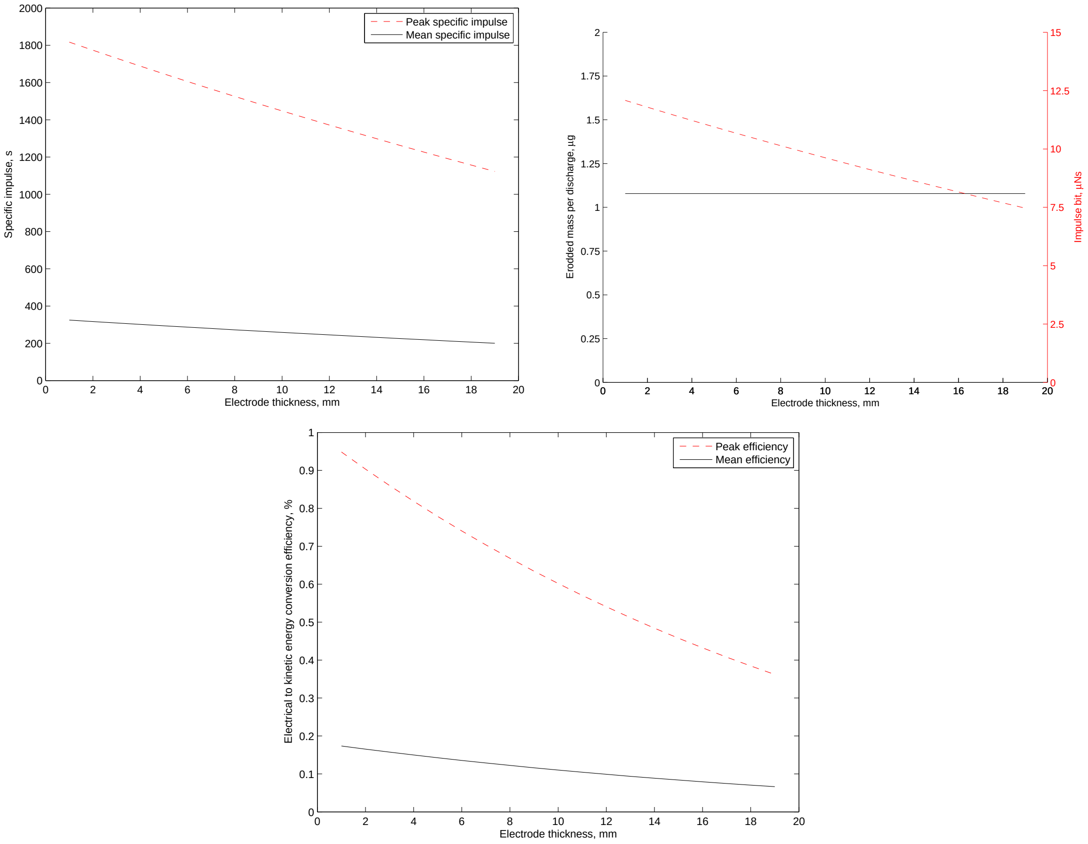

Figure 5.32: Predicted performance of a PPT setup in the standard configuration but with the electrode thickness being varied from 1-19mm. Top Left: Specific Impulse, Top Right: Impulse bit and mass bit, Bottom: Electrical to kinetic energy conversion efficiency

Finally the electrode gap distance was varied from 5mm to 50mm, see Figure 5.33. The upper limit of 50mm was chosen because this was the limit of the quasi steady state assumption. As the gap distance is increased to 50mm caution and confidence in the predicted values should be taken. It can be seen that at 18mm, 33mm and 43mm the performance of the PPT dips. Unsurprisingly these coincide with the location of the first and subsequent chokes seen in the plasma flow. In these areas the modelled choke point coincides with the anode and alters the charge-space limited current, predicted by the Child-Langmuir law. However, apart from these dips, the trends show that as the electrode gap is increased the performance rises to a maximum value and remains constant. The location of the choke point as discussed earlier is reliant on the initial flow area and possible anode spot formation processes that are not modelled. The trend shows that for the standard configuration setup the further the electrodes are separated the better the performance will be up to a maximum value. The trends also show that when designing a μPPT the electrodes should be separated as far as possible to maximise the performance.

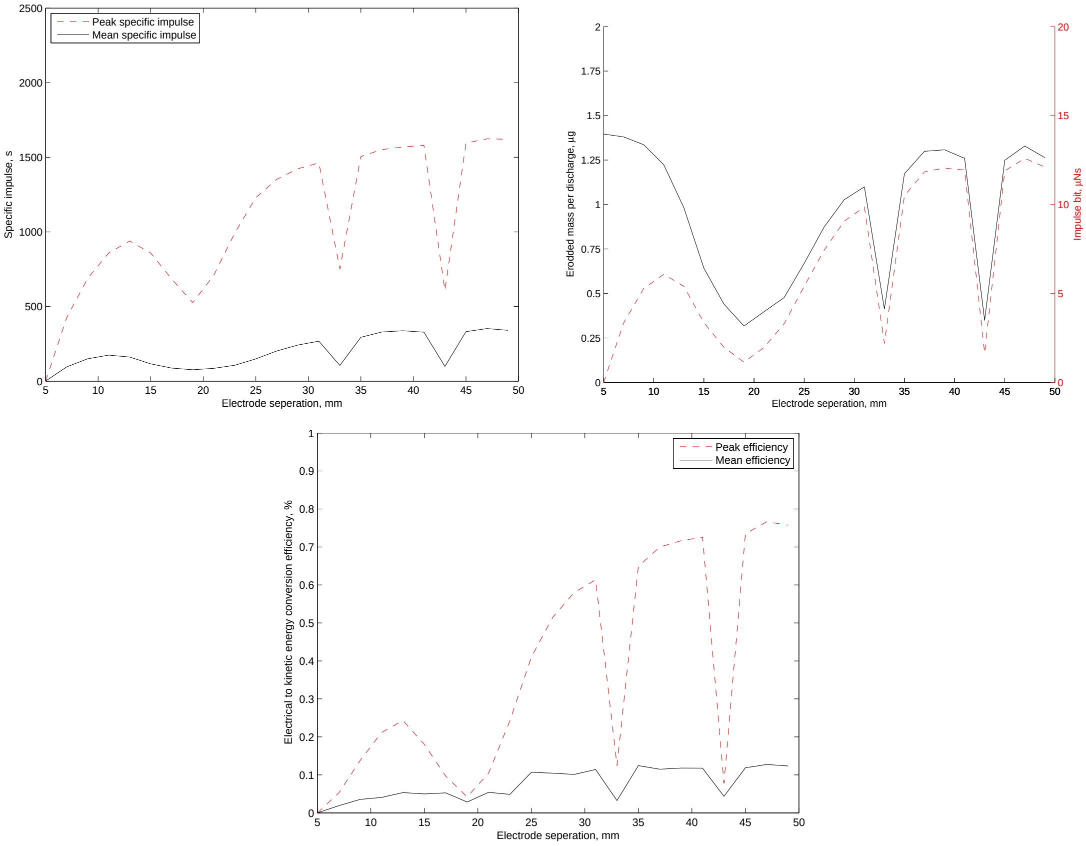

Figure 5.33: Predicted performance of a PPT setup in the standard configuration but with the electrode separation distance being varied from 5-30mm. Top Left: Specific Impulse, Top Right: Impulse bit and mass bit, Bottom: Electrical to kinetic energy conversion efficiency

It is clear that the PPT discharge is an inefficient process that only converts on average a very small percentage, dependant on the setup, of the total inputted energy into kinetic energy which accelerates the plasma bulk out of the nozzle. Although the peak efficiencies of the individual pulses have been shown to reach higher efficiencies, on the whole the process is still inefficient. It would seem that most of the energy is lost in the charge-space limitation effect brought about by the anode sheath. To improve the performance of the PPT requires the manipulation of the anode sheath in such a way as to limit this effect. Until that can be done the energy conversion efficiency of the PPT from electrical to kinetic energy will remain low.

In summary caution should be taken when evaluating the specific values of the predicted data due to the inaccuracies that may be inherent in the magnetic field distribution of the Lorentz force model and the initial flow radius of the flow model. Despite these, trends can be seen in the produced data that suggest the following should be carried out to optimise the performance of the PPT:

- The circuit resistance, especially that of the capacitor, should be lowered as much as possible.
- The inductance of the circuit should be specifically matched to the PPT to optimise the capability of the circuit to store energy in its magnetic fields as the capacitor discharges.
- The magnetic field distribution should be maximised by optimising the geometry of the PPT or by enhancing the discharge chamber with an external magnetic field.
- The electrode separation distance for copper electrodes should be increased to around 3-5cm but caution should be applied on this upper value as the quasi steady state limit is reached.

5.6 Summary

The developed model to predict the performance of the PPT was built with the available computational software and hardware resources in mind. The model was based on a lumped circuit analysis model with several additional sub models to predict the behaviour or certain aspects of the thruster. These sub models included a detailed analysis of the discharge electrodes based on splitting the conductor into a number of sub conductors. The resistance, self inductance and mutual inductance was then calculated. It was found that compared to the relative resistance and inductance of the capacitor the electrode resistance and inductance was minimal.

One of the limiting factors of currently avaliable lumped circuit analysis models is the assumption of constant values to describe the plasma that do not fluctuate with time or current. To overcome this lack in modelling a simplified magnetohydrodynamic flow model based on quasi steady state assumptions was put forward. The flow model was based on the assumptions that the plasma mass originated from the electrode surface and flowed towards the anode rather than a plasma bulk originating from a solid propellant between the electrodes (i.e. Teflon^{TM}). The flow model shows that along the flow the plasma at certain distances creates a 'choke', where the flow radius is small. In the 'choke' the electron temperature, electron density and mean ion charge state, significantly rise to values that have been observed in the available literature. The dynamics of the flow has a significant impact on the anode sheath and its ability to limit the arc current. It has been shown that it is this limiting effect that affects the PPT's ability to convert electrical energy to kinetic energy efficiently. If it is possible to manipulate the charge-space of the anode sheath then this is where most gains in performance can be made.

The model has been shown to be a reasonable representation of the effects that occur within a PPT, which does not have Teflon^{TM} present between the electrodes. Future work on improving the model should be focussed on:

- Developing an accurate SPICE model for the discharge capacitor.
- The introduction of anode spots to the flow model.
- Improvement and validation of the Lorentz force model. This will include a more accurate description of the magnetic field distribution from a current carrying rectangular bar in the high frequency domain to account for skin effects and ion speed measurements from time of flight probes.
- Introducing the effects that canting has on the plasma flow.
- Accounting for the initial arc breakdown.
- Optimisation work on the individual cathode spot radii for copper and other materials.
- Reworking the flow model to be time dependant and removing the necessity for steady state assumptions to increase the usability of this model.

Chapter 6

Developing a μPPT for CubeSat Applications

6.1 Introduction

The picosatellite is a very disruptive technology to the established satellite market, due to its low production cost and ever-increasing capability of its payloads. This technology has the possibility of seriously impacting on the economics of space. Distributed networking will allow swarms of picosatellites to communicate with each other without the need to link through a ground station allowing for close formation flying satellite swarms to be established. This could lead to some conventional payloads from larger satellites being distributed amongst a number of smaller and low cost picosatellites, providing new directions for future mission concepts. However, a significant issue is the limited options for an active on board propulsion system for a picosatellite. If the picosatellite is to be used in advanced mission concepts it will need an in-space propulsion element to its design.

During the later stages of this work a rare opportunity presented itself. The company Surrey Satellite Technology Limited (SSTL) required a propulsion system for a three unit CubeSat. This 10cm × 10cm × 30cm satellite was required as a precursor technology demonstration mission for a series of follow on missions. The main payload of this satellite, called STRaND-1, is a HTC smart phone with the Google Android operating system. The reason for this was that the smart phone's digital camera, processor, data storage, position sensors and WiFi capabilities surpassed the technology currently available within the volume and power constraints of a satellite of this size.

To increase the satellite's capabilities a propulsion system would also need to be developed to possibly compensate for atmospheric drag, provide high precision pointing, complete orbit maintenance manoeuvres and provide a capability to 'dump' momentum. The SSTL in-house μresistor jet with propellant tank and feed lines proved to be too cumbersome for a full 3-axis control system. Surrey Space Centre offered an alternative in the form of eight μPPTs and it was accepted as part of the Attitude Determination and Control System (ADCS). The current launch date is scheduled for November 2011. This chapter covers the design, development and testing of the μPPT system for the first Surrey Technology Research and Nanosatellite Demonstration mission (STRaND-1).

6.2 μPPT Design Phase

The goal in designing a μPPT was to use what had been discovered during the course of this work in both the experimental efforts and the modelling efforts to build an optimised propulsion payload. The experimental work showed that the PPT operated sufficiently without the presence of Teflon^{TM}. It also showed that the performance of the PPT without Teflon^{TM} was approximately 60-75% of the performance with Teflon^{TM}. The PPT model indicated methods of increasing the performance by lowering the circuit resistance, matching the inductance of the circuit and optimising the shape and spacing of the electrode discharge gap. The insights found from the model were put into practice wherever possible within the constraints of the design process. The decision was made early on to develop a PPT without Teflon for several reasons:

- The removal of the Teflon and propellant feed mechanism saved valuable space and volume which could be used to place additional PPTs within the system.
- Teflon contains a lot of carbon, which when broken down, would coat the inside surface of the thruster with a film of carbon. When enough carbon builds up on the surfaces connecting the two electrodes it would lead to arc tracking and failure of the PPT.
- It allowed the use of the model developed during this thesis to be used to size the PPT. Once built the PPT could be thoroughly tested and the experimental data could be used to further evaluate and validate the model.

Without the Teflon propellant the developed model could then be used to give a guideline into the design of the μthruster. The iterative process began by modelling a PPT with similar characteristics to the one tested experimentally, so a capacitance of 4μF was chosen for the capacitor. The voltage rating of the capacitor dictated its size, the higher the voltage rating the larger the capacitor would be. An initial voltage rating of 700V was chosen for the CubeSat PPT as this was the minimum voltage during experimentation at which the PPT would regularly discharge.

The electrode spacing and geometry was chosen based on the knowledge gained from the electrode and flow model and observations from the charred areas of the electrodes during experimentation. The electrode separation was chosen to be as wide as possible but to remain clear from the possible ‘choke’ regions that were predicted to exist but also to keep the micro thrusters small. From Figure 5.31, an electrode separation distance of 11mm was chosen. The shape of the electrode was chosen to be a thin blade-like electrode, see Figure 6.1.

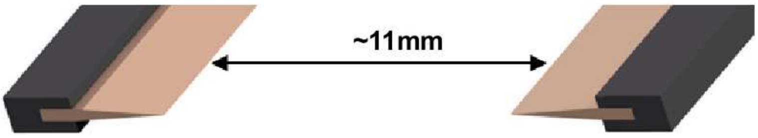

Figure 6.1: PPT with a new form of electrode design based on a blade geometry

This geometry was chosen for two reasons. Firstly, the blade edge would promote areas of cathode spot errosion and physically ensure they remained in the same location when multiple spots formed. Secondly, the current flow was promoted in the corner and edges of the electrode bar. By having two of the corner edges in close proximity to each other whilst the other two edges are further away meant that the current flow looked more like four point sources and better resembled a magnetic field distribution from two pairs of two infinitely long wires, see Figure 6.2.

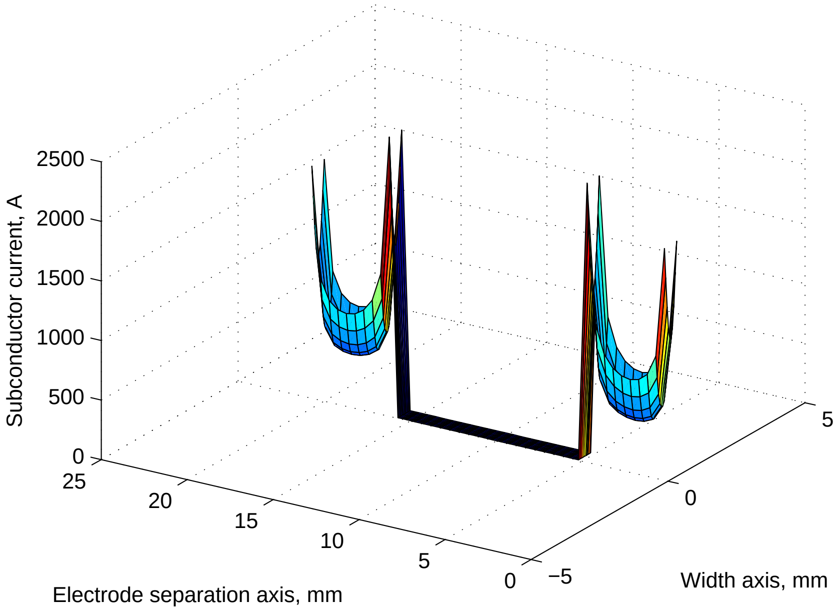

Figure 6.2: The current distribution in a thin electrode parallel bar PPT

The bladed electrode concept integrated with the decision not to use Teflon was further expanded upon to create a mock up of what a propulsion system may look like, see Figure 6.3. The propulsion system was initially split into three modules, where 8 PPTs were split into two modules of 4 PPTs per module and a third module was dedicated to a PPU to convert 5V to a high voltage output. The amalgamation of the three modules can be situated within a 2 or 3 unit CubeSat chassis and the placement of the modules within the chassis is flexible to allow for other components and payloads. The design offers control and propulsion in pitch, roll, yaw, X-axis and Y-axis.

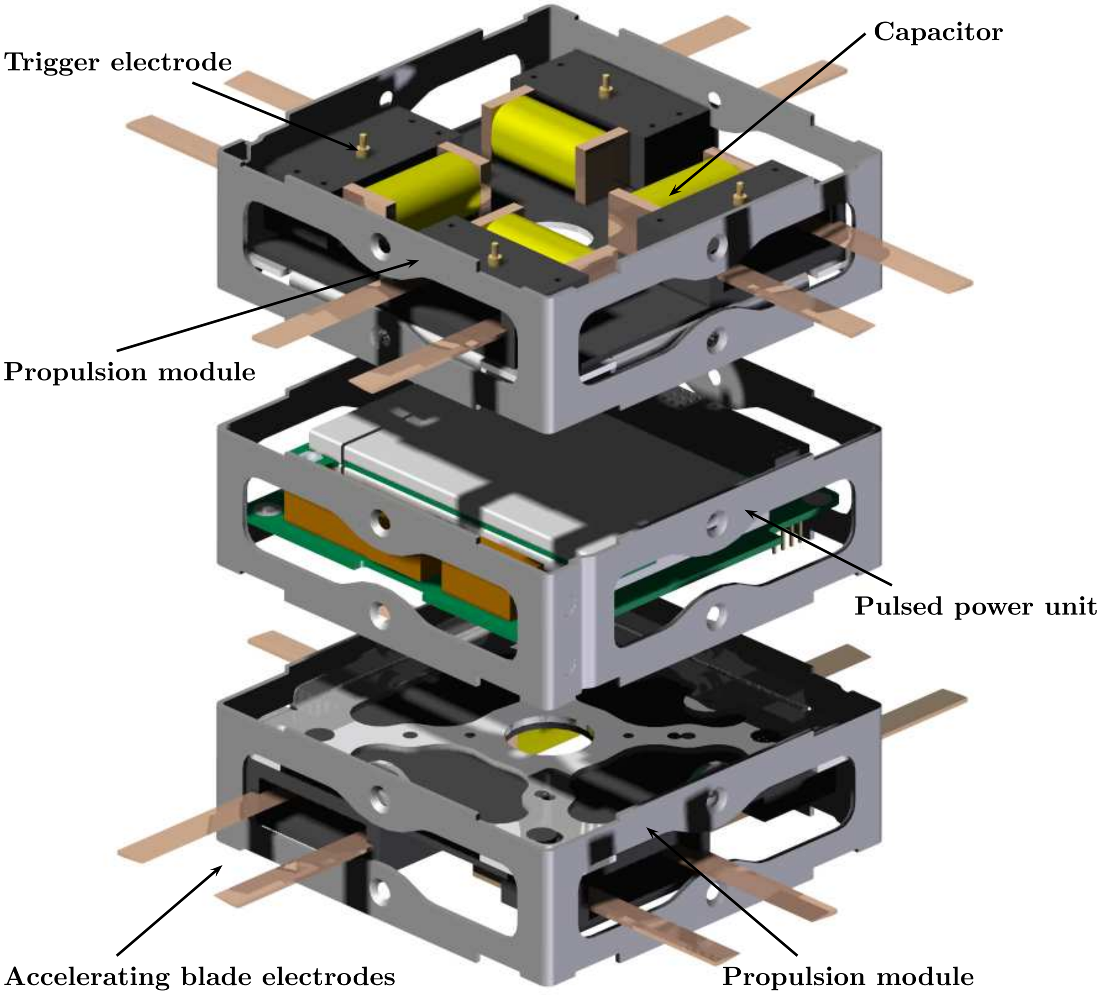

Figure 6.3: Conceptual design of a CubeSat propulsion system comprised of 3 modules with a total of 8 PPTs to provide X-axis, Y-axis, pitch, roll and yaw motion control in a CubeSat

Initially it was thought that the plane electrodes could be lengthened to provide more material to be eroded and hence increase the overall ΔV of the propulsion system. However, CubeSats are designed to be modular and adding protruding electrodes would have meant a redesign of the deployment pod that the CubeSat is launched from, which would have been both costly and complex. Therefore the electrodes were shortened to remain within the CubeSat chassis. This however decreased the amount of electrode propellant available to the system. To overcome this the electrode width was increased to 0.5mm.

During the design phase careful consideration was taken into developing the discharge initiator. In total there were three concepts that were looked into; the field electron emission effect by the traditional spark plug, thermal electron excitation by semiconductor lasers and a mechanical trigger formed from high voltage contacts breaking. Early on it was shown that laser excitation would be too complex a process to procure, build and control, so it was dismissed. Closer consideration was given to the other concepts. Initially the field electron emission effect was thought to be the ideal choice, as EMCO High Voltage Inc. sold a 5V DC to negative 10kV voltage multiplier in a 1.7cm^3 package. The issue though was total volume. Having one multiplier per thruster sparkplug was an unworkable solution, as space was required for other payloads. To try to overcome this a network of state of the art reed relay switches linked to a single multiplier was investigated. However with each relay being 25 to 30mm long this still took up considerable space.

The high voltage contact breaking method of creating a spark via a mechanical trigger was further developed. The system consisted of a contact arm, a lever arm, a torsion spring, an electromagnet and a retaining pin, see Figure 6.4. The torsion spring is not shown but should be located around the cylindrical part of the contact arm with one spring leg slotting into the cut out section of the lever arm and the other spring leg attached to the thruster housing (not shown). The lever arm and electromagnet was made from steel and will be used to create a downward force that will pivot the contact arm to make contact with the grounded electrode. Once the electromagnet is turned off the lever arm is restored to its original position by the torsion spring.

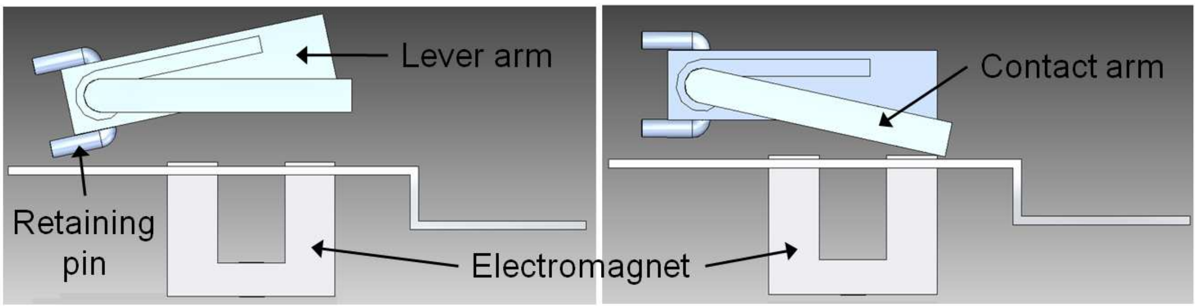

Figure 6.4: The high voltage contact breaking trigger system in the up and down positions

Using the high voltage contact breaking method caused the contact arm to erode and so the separation distance between the electromagnet and lever arm needed to allow for this erosion in its design. The material the contact arm was made from also affected the erosion rate. Using a material with a low erosion rate would extend the lifetime of the contact arm. Although for bread boarding the contact arm would be made from aluminium the actual flight hardware contact arm will be made from Elkonite (75% Tungsten, 25% Copper) due to its low erosion rate but relative ease in manufacture (compared to pure Tungsten), see Figure 6.5.

The capacitor, electrodes and contact arm needed to be isolated from the rest of the spacecraft and its payloads. Ultem^{TM} has previous flight experience with flown PPTs and also has a high dielectric strength, so this material was chosen for the thruster housing. The design of the thruster housing, capacitor, electrodes and trigger system can be seen in the cut away diagram shown in Figure 6.6.

The thruster housing measures 40mm × 40mm × 12mm and four of these housings can be situated on a PC104 board in a rotational symmetric off axis configuration see Figure 6.7. The PC104 require-

Figure 6.5: Contact arms. Left: Aluminium, Right: Elkonite

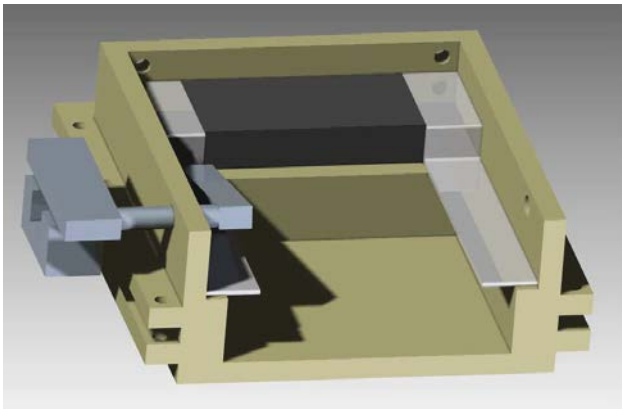

Figure 6.6: Mock up of the thruster housing with the electrodes, capacitor and trigger system

ments are a set of standards that the CubeSat industry uses to provide and allow for modularity. The PC104 system requirements specifically relating to board dimensions were adhered to, to ensure smooth integration with other payloads. However, there was a design conflict with the structural supports and the thruster housings, so additional PC104 boards were placed above and below the thruster module to ensure integration with other payloads but to allow the structural supports within the thruster module to be relocated.

The PPU was designed to charge up the high voltage capacitors within the eight PPTs. The target was set to charge two 4μF capacitors within one second allowing the satellite to fire two thrusters at any one time at a discharge rate of 1Hz. The capacitors were designed to be charged to 700V by using a DC to HV DC multiplier. The multipliers were supplied by EMCO High Voltage Inc. and were packaged into a 12.7mm^3 cube. Four multipliers were put into the PPU design. On their input lines 1kV rated diodes were added to provide reverse polarity protection and 10μF capacitors were added to reduce reflected ripple currents on the input supply lines. The PPT capacitors needed to be isolated from each other so when one triggered it would not cause a cascade effect and discharge all the others. To do this low pass filters made from 33nF capacitors and 10kΩ resistors were made. The low pass filters were placed before the 4μF high voltage capacitors. Figure 6.8 shows the built PPU and PPT module after the design phase but before they were tested in the breadboard phase. The requirements set by ESA for a CubeSat propulsion system are given in Table 3.2 and represent a broad but attainable goal for the performance

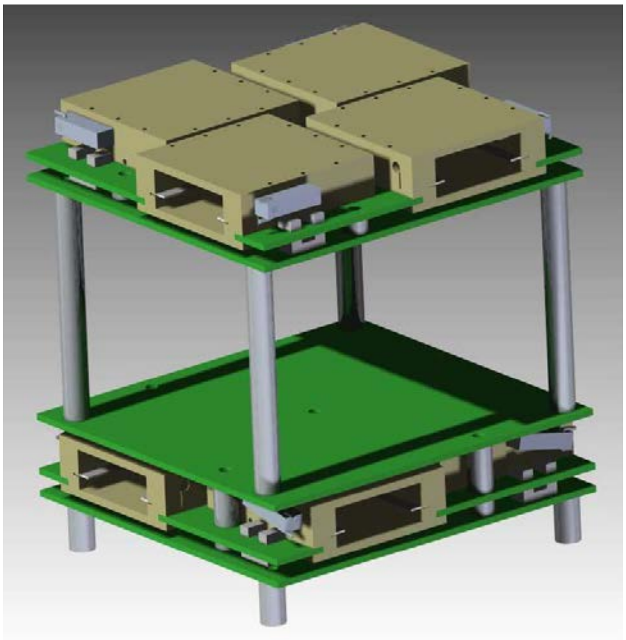

Figure 6.7: Mockup of the propulsion module showing the location of all eight μPPT units

of the designed μPPT.

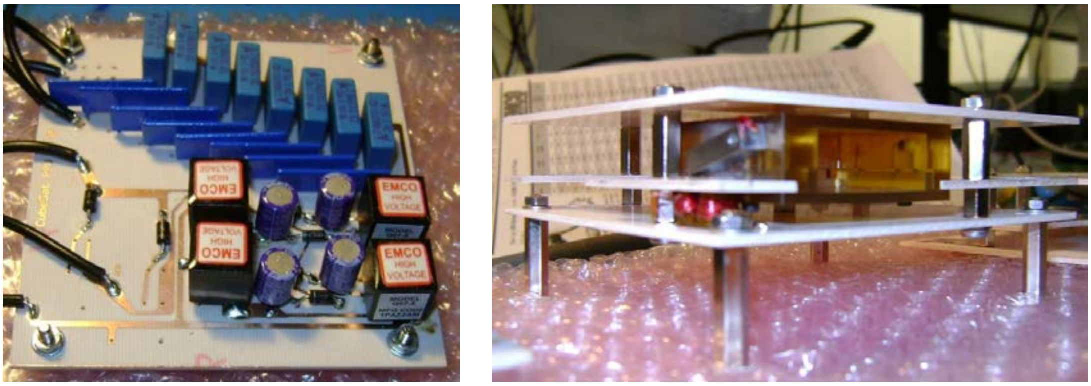

Figure 6.8: Left: STRaND-1 PPU before bread boarding. Right: STRaND-1 PPT before bread boarding

6.3 μPPT Breadboarding Phase

The PPT and PPU were modified after bread boarding the initial design. Several flaws were found in the original design. The design was based on a 4μF capacitor rated at 700V, however the volume available for the capacitors was 3cm^3. It was a challenge to find a pulse capacitor that would be rated to high voltages and fit into the available volume. The custom capacitor manufacturer Calramic (USA) were able to manufacture two CR09 capacitors fixed by copper tabs in parallel to provide a total capacitance of 0.76μF at 700V, rated for more than 1 million pulses, see Figure 6.9.

The electrodes were soldered directly onto the PPT capacitor to reduce circuit inductance and resistance between the two elements. The electrode geometry was 25mm in length, 5mm in thickness, 0.5mm

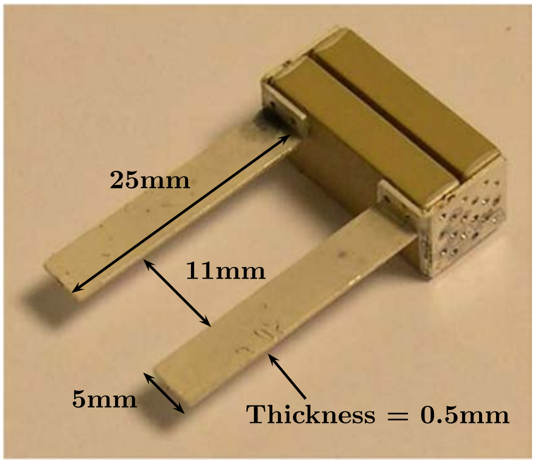

Figure 6.9: Calramic CR09 pulse capacitor for the STRaND-1 PPT

in width and separated from each other by 11mm.

The low pass filter designed to isolate the discharging capacitors from each other had a cut-off frequency of 482Hz. The PPT has a discharge frequency between 30-200kHz. In theory the filter was expected to work however it did not operate satisfactorily. Often when one of the capacitors was discharged or one of the triggers operated, all of the capacitors in the system discharged. This was initially negated by using a 20M resistor instead of the 10KΩ resistor which reduced the cut off frequency to 4Hz. However, this increased the capacitor charge time to around 60 seconds and so was unworkable. The solution was to use a high voltage diode instead of a low pass filter which did not limit the current flow to the capacitor but did stop the transient effects that caused the other capacitors to discharge.

The charge time of the capacitors was an issue. Using four EMCO DC to HV DC multipliers and bread boarding the initial PPU with a 2.2μF ceramic capacitor (also from Calramic) showed the charge time was around six seconds. Although the CR09 capacitor was only 0.76μF, it was an indication that the PPU would struggle to charge two capacitors in one second. To rectify this, the number of DC to HV DC convertors was increased from four to eight, see Figure 6.10. This was achievable due to the space saved from the removal of the low pass filters.

The working principle of creating a spark by a lever contact mechanism proved to be a viable option during bread boarding but the design of the original trigger mechanism proved to be troublesome. The original concept used a steel lever arm and electromagnet to provide a downward force and a torsion spring to provide a returning force. However, when assembled there were several problems with this design. When compressed, the torsion spring would press on the pivoting arm creating additional frictional forces. The magnetic field produced by the electromagnet within the set power budget was too weak to overcome the torsion spring stiffness. Finally magnetic remanence within the steel caused it to become permanently magnetised, which would interfere with other systems on the CubeSat.

The electromagnet and lever arm assembly was replaced with a P653 piezo electric motor, see Figure

Figure 6.10: Revised PPU developed during bread boarding for the STRaND-1 CubeSat

6.11. The μmotor from Physik Instrumte (PI) GmbH & Co had a 0.15N push-pull capability with a movement range of 2mm and a power consumption of 0.5W. Compared to the electromagnet and lever arm assembly the μmotor increased the timing accuracy in which discharges could be triggered.

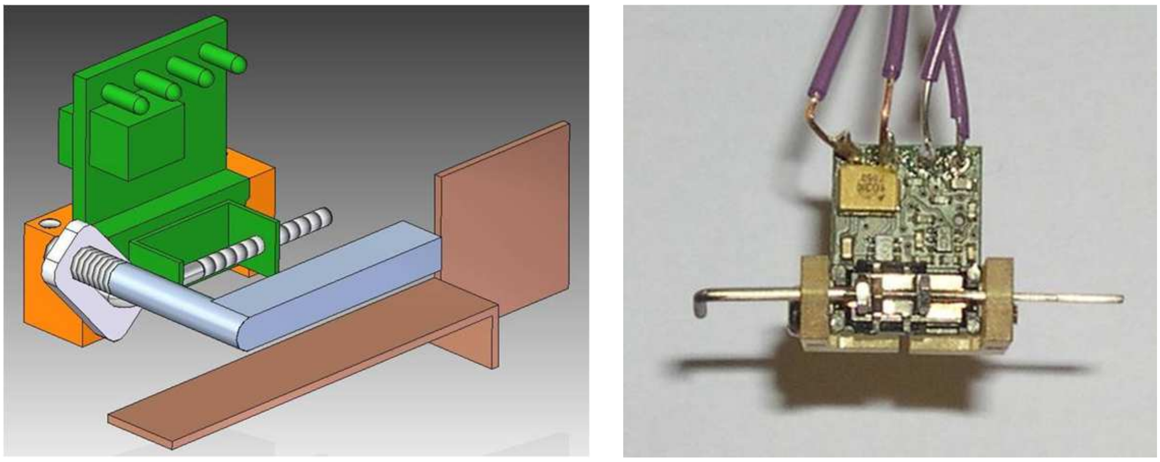

Figure 6.11: The redesign of the trigger system using a P653 piezo electric motor

Once the system had been built it was found to be extremely delicate. The holder in which the push rod was mounted was susceptible to becoming stuck. In the harsh vibrating environment of a launch, this was an overwhelming risk. Also the holder in general was not stable and so the rod would rub against the guiding holes in the motor mount which caused frictional forces that the motor was not able to overcome. These issues meant that this avenue of development was dropped and other solutions were investigated.

The next candidate was a simple system using Nitinol wire and a returning force spring. Nitinol wire is a shape memory alloy which has the useful property of contracting when heated. The total contraction is around 10% of its total length. Contraction occurs when the crystalline structure in the wire shortens when heat is applied. The wire has a naturally high resistance compared to nominal metal wires and when a current is passed through the Nitinol wire its own resistance became the source of heat. The

Nitinol wire activates and contracts between 70-75^{o}C depending on the specific composition of the wire. Convection was the main method of cooling the wire down once it had contracted. During the cooling down phase a returning force spring would return the wire to its original length. The movement created was enough to move the contact trigger arm. A system was designed for the μPPT, see Figure 6.12, which operated nominally in the laboratory environment.

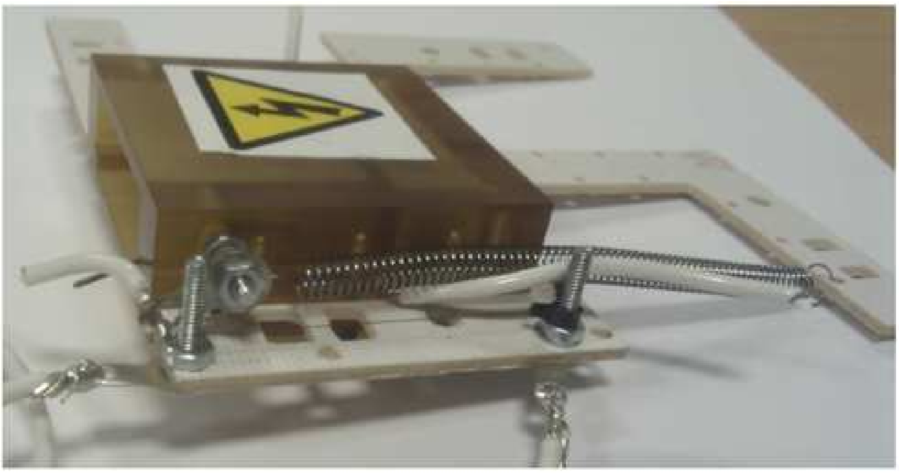

Figure 6.12: The redesign of the trigger system using a Nitinol wire and spring mechanism

Once placed in the vacuum environment, due to the change in the thermal properties of the system, a reduced current was required to contract the wire. However, the main method in cooling was now conduction through the Nitinol wire structural supports and this took around 20 seconds before the trigger mechanism could be operated again. The Nitinol wire was relatively thin and brittle and broke on several occasions whilst under high stress conditions, which, coupled with the slow repetition rate of this mechanism, called into question the survivability of this system during launch.

The last system developed returned to the method of using a piezo electric motor. The SQUIGGLE linear micro motor is manufactured by Newscale Technologies. It uses a system of four pads made from piezoelectric material located around a central threaded rod. The pads are oscillated in such a manner to resemble a 'hula' motion that causes the central threaded rod to rotate around its central axis, which can cause it to move to the extent of the rod length (in this case up to 6mm). The motor has nanometre resolution, provides a force up to 5N and can change the translation speed of the rod from 1-10mms^{-1}. The design of this system is shown in Figure 6.13. Once built the trigger system was tested by being operated 10,000 times, during this test the system operated flawlessly.

An additional problem with all the trigger mechanisms was the possibility that spot welding would occur. The trigger contact arm is charged up to 700V and when brought into contact with the ground electrode caused a spark to occur that would melt the surface of the electrodes, which can cause them to bond or weld together. Limiting the current through the contact arm assembly can reduce the chance of spot welding. Initially a COTS 9Ω resistor was used but after a few tests this resistor blew. The COTS

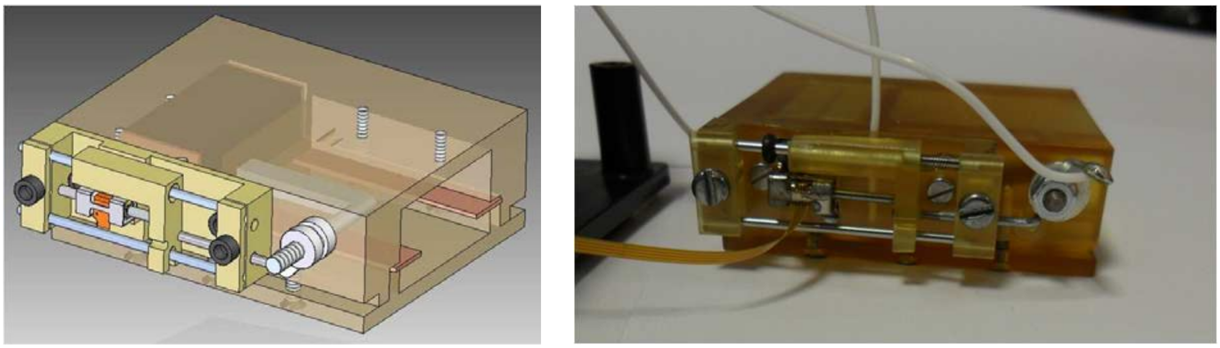

Figure 6.13: The redesign of the trigger system using a SQUIGGLE motor

resistor was replaced with a miniature 9Ω resistor rated to 5W and 1kV from the Precision Resistor Company. The new resistor worked well in parallel with the motor which provided enough force to overcome any spot welding that occurred.

Due to some power lines being up to 700V the standard PC104 headers in the CubeSat standard were not implemented into the design. The additional space was used to either accomadate a thruster unit on the propulsion module boards or make space for clearances around HV lines located on the PPU board. A harness manufactured by Axon cables was constructed and integrated into the design. The connecting wires were made to ESCC 3901.013.01 standards, with connectors made to MIL-M-24519 standards out of a liquid crystal polymer. The harness was rated to 1kV, but when tested in the Surrey Space Centre's large vacuum chamber no breakdown occurred up to the maximum test of 2.5kV.

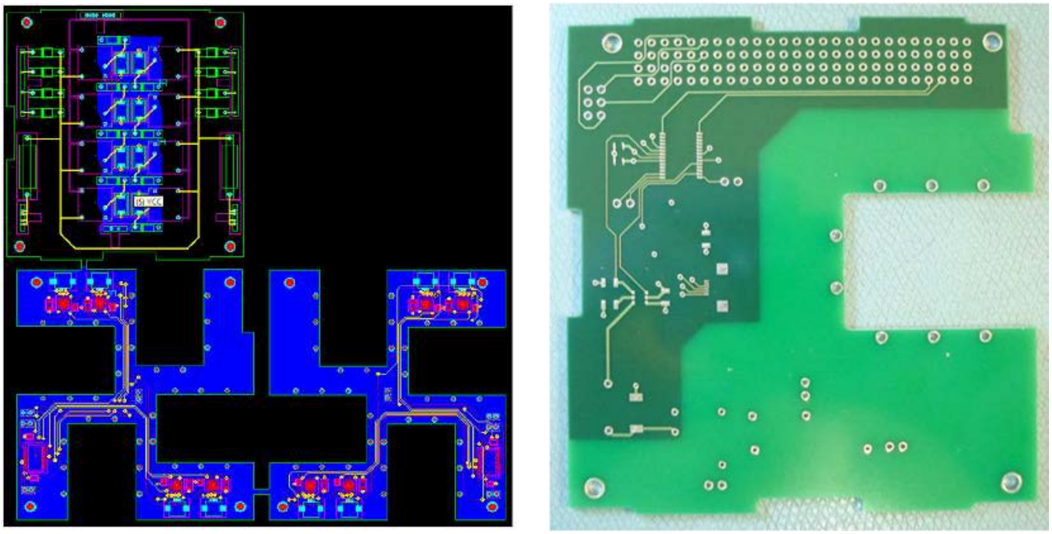

Figure 6.14: The PCB layout for the STRaND μPPT flight module and the manufactured PCB for the qualification model

The low voltage electronics were then developed. A Texas Instruments power distribution switch was used to limit the current into the PPU to prevent the PPT capacitors drawing too much load too fast from the main satellite battery. Another issue was controlling the SQUIGGLE motors. The motors came with their own NSD 2101 drivers with their own I^2C commands, which were incompatible with the satellite I^{2}C commands. A μ-controller was added as a buffer to interpret I^{2}C commands from the satellite and translate these into I^{2}C commands which the NSD 2101 driver could handle. Once the electronics had been selected they were placed into a PCB layout ready for manufacture. The PCB was a four layer FR4 PCB with a lead Hot Air Solder Level (HASL) finish for ease of component integration.

It was around this time that a second flight oppertunity arose to fly a single μPPT on the 3U CubeSat UKUBE-1 mission. The UKUBE-1 mission is the maiden CubeSat mission for the UK Space Agency and although unsuccessful chosen the PPT was downselected to the final six payloads. During this time the UKUBE-1 PPT was developed. After the down selection process it was decided to continue with the manufacture off the PPT board and use it as a qualification module for the STraND PPT program. Figure 6.14 shows the PCB layout for the flight module and the manufactured PCB for the qualification model.

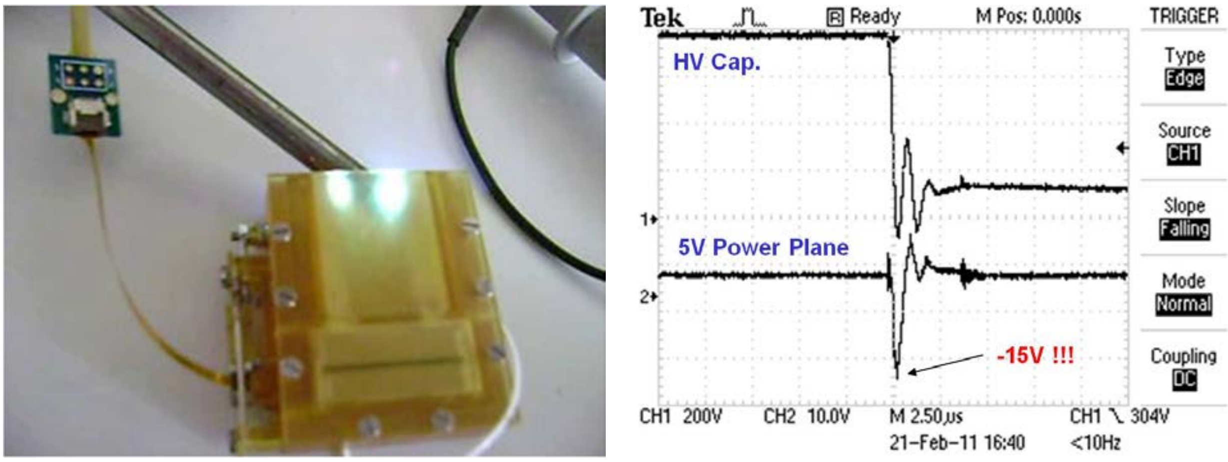

Figure 6.15: Left: μPPT being discharged in a laboratory environment. Right: Voltage profile across terminal of electrodes and across the power plane

Once the μPPT units had been built preliminary testing was conducted in the laboratory environment. Concerns were raised about possible electromagnetic interference from the pulsing PPTs with the sensitive electronics of the other subsystems. Figure 6.15 shows the voltage profile of the discharging capacitor and the low electronics power plane. It is noted that in a vacuum environment the frequency of the discharge is less than the one shown. It can be seen that when the PPT fires, a negative 15V spike is seen in the power plane. This would in effect cause all the electronics in the satellite seeing this signal to 'reset'. Obviously this was undesirable and a solution to the issue was sought. The previously introduced current limiting switch only limited the spike to a negative 0.2V on the 5V line with an overall drop in voltage of 5.2V. A second solution was to incorporate a low pass filter. However, this only reduced the magnitude of the ripple rather than eliminating it. The ripple was reduced to approximately 2V. With limited space for filter electronics it was difficult to have a multistage or large low pass filter. The next solution was to try a 5th order Butterworth low pass filter, which was a single chip device. The Butterworth filter worked well. However, it was designed for filtering signal lines rather than power lines and so the outputted filtered line was significantly current limited. As this fed directly into the DC to HV DC multiplier this meant the peak voltage seen by the PPT capacitor was only 200V. This rendered this solution unworkable. The final solution came from using a Murata NFM31 single chip power filter with a footprint of 3.2mm × 1.6mm. The filter was placed both on the 5V line and the ground line to the DC to HV DC multipliers. The filters provided adequate protection and damping of the discharge ripples to less than 100mV on the power planes. However, to incorporate the filters into the flight design two of the DC to HV DC multipliers had to be removed.

Another secondary effect of the discharging PPT was the effect by induction. As the PPT discharged a voltage was induced in nearby electronics. Figure 6.16 shows the effect of this induction on a dipole antenna as a function of distance. The μPPT is discharged in a laboratory environment during these tests. The secondary high burst frequency discharges seen should be ignored as these are due to resonance effects between high and low voltage oscilloscope probes which were inputted to the same oscilloscope. The plots show that even at the maximum distance of 30cm, equivalent to the length of the STRaND-1 satellite, an induced ripple of approximately two hundred millivolts was produced and at close distance was over 1.5V. This induced ripple can cause electronic components to reset within the whole of the satellite.

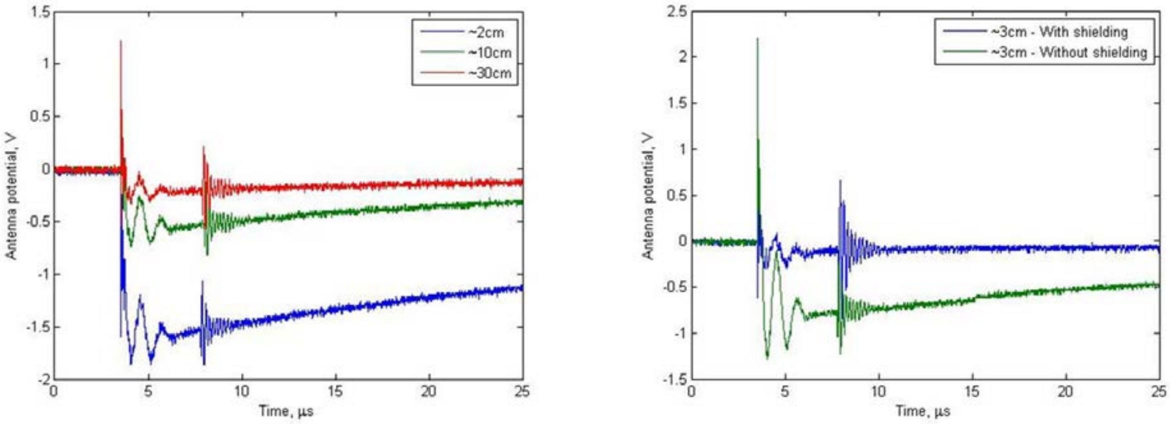

Figure 6.16: Left: Induced voltage in a dipole antenna as a function of distance. Right: Shielded and unshielded signals

To overcome this a Faraday's cage was placed around the laboratory μPPT which provided adequate protection, see Figure 6.16. For the qualification model an aluminium Faraday's cage was designed but in practice due to size and volume constraints copper tape with conductive adhesive was affixed around the Ultem housing and grounded, see Figure 6.17.

After the bread boarding phase was completed the qualification model and the flight model were built in a clean room environment, see Figure 6.18. The flight model is partially built, still requiring a Faraday's cage to be applied to each thruster and the trigger mechanisms to be attached.

To accurately measure the current waveform in the discharging PPT requires a rogowski coil, but

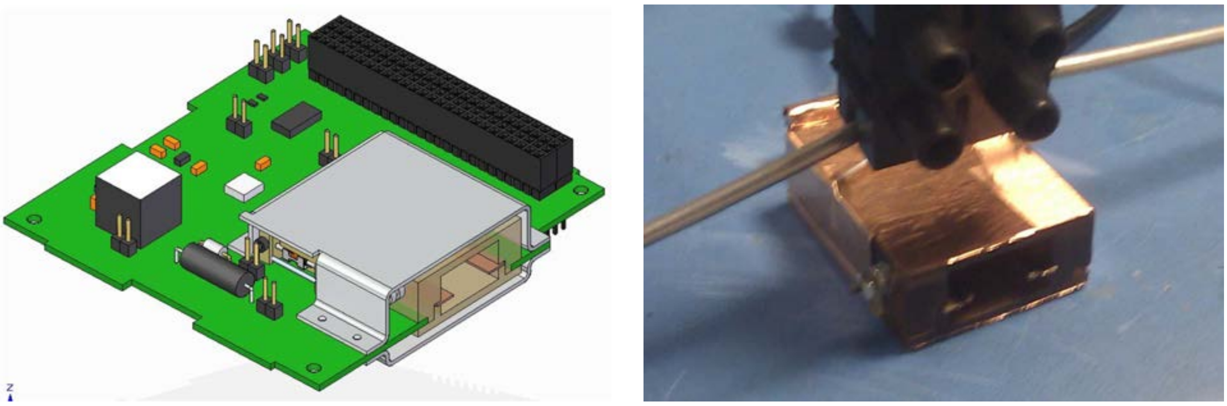

Figure 6.17: Left: CAD design of the Faraday's cage for the qualification model. Right: Actual Faraday's cage implemented into flight hardware

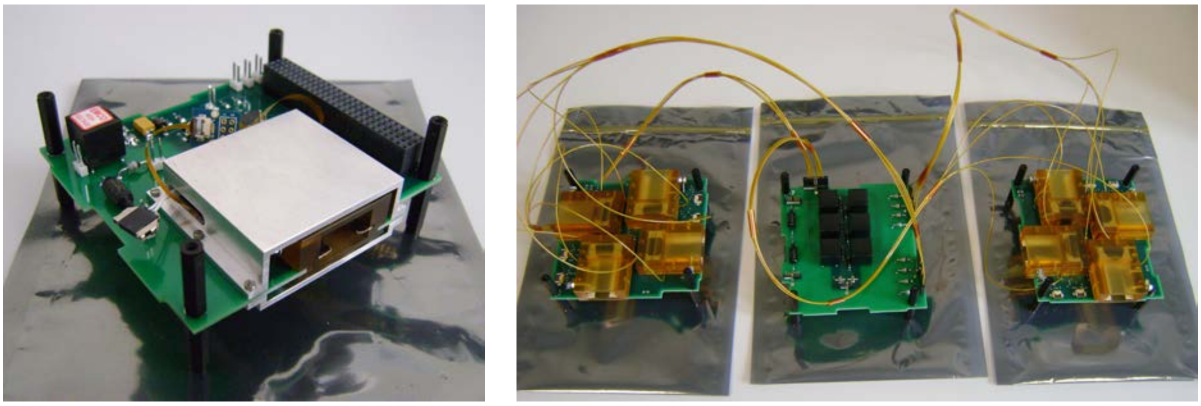

Figure 6.18: Left: Qualification and lifetime testing module. Right: STRaND-1 PPT flight module

due to the size and close integration of the electrodes to the capacitor, placing a rogowski coil would directly interfere with the dynamics of the discharge gap. A high voltage probe across the capacitor terminals however can give the frequency of the discharge in the vacuum environment. Figure 6.19 shows the qualification module in the Surrey Space Centre's small vacuum chamber and the typical discharge voltage profile of the μPPT. The voltage profile infers, due to its form, that there is a single strong pulse followed by two or three weaker pulses. Interestingly after the third pulse a secondary sharp peak occurs between 1.65μs to 1.75μs. The location of this peak is not consistent in time due to the averaging of the data the spike appears to be 100V. However, when investigating the original data the spike was between 260V to 355V. This phenomenon may be caused by the PPT capacitor because it is made from two parallel joined chip capacitors, but further work is required to establish this. It can be estimated from the voltage profile that the frequency of the discharge is 1.25MHz.

Using the frequency the predicted capacitor inductance and resistance can be extrapolated. Following a similar procedure with the LCR meter as was used for the experimental PPR capacitor, the resistance of the CR09 capacitor was estimated to be 4.1mΩ and the inductance to be 18nH. The frequency was also used in the electrode model to predict how the inductance and resistance altered over the effective electrode length, see Figure 6.20. Compared to the PPT set up from the experimental phase the electrode

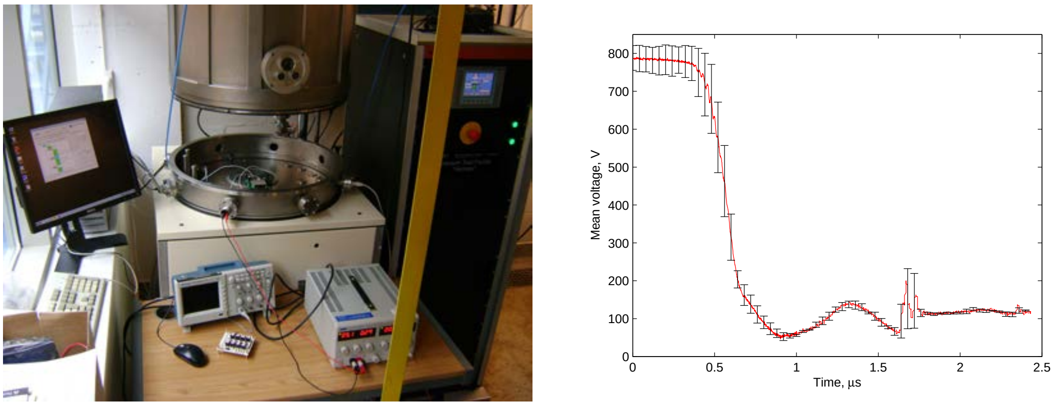

Figure 6.19: Left: Qualification model in the vacuum chamber discharging. Right: Voltage discharge profile across the capacitor terminals

inductance and resistance of the μPPT are significantly higher. The inductance has doubled and the resistance has risen by an order of magnitude. Both of these effects can be contributed to the higher discharge frequency of 1.25MHz for the μPPT.

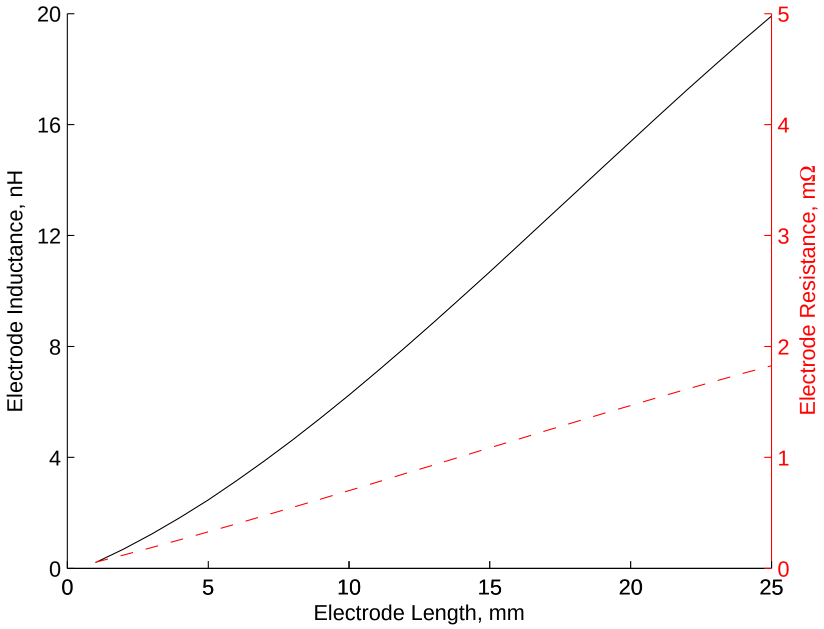

Figure 6.20: Electrode resistance and inductance for the blade style electrodes as a function of effective electrode length

Using the experimental results from the built modules and implementing these into the developed model, the predicted performance of the STRaND-1 μPPT flight unit is found, see Table 6.1. In comparison to the ESA CubeSat propulsion requirements, see Table 3.2, all the requirements are met or surpassed, except for the thrust.

The accuracy of these results needs to be confirmed through flight based experiments. Impulse balances have been developed with resolutions of up to 1-10μNs [78]. However, from these preliminary

Table 6.1: SSC μPPT target performance based on the results from the developed model

Parameter	**SSC μPPT predicted performance**
Propulsion module mass, kg	0.336
Number of μthruster modules	8
Power available to μthruster modules, W	1.5
Bus voltage, V	5.0
Volume required by full μthruster assembly, cm^3	480
Thrust per PPT, μN	0.09
Impulse bit, μNs	0.56
Specific impulse, s	321.8
Mass bit, μg	0.17

results the impulse bit from the modelled μPPT would be under its observable limit. A second issue in ground based tests would be the disturbance caused by the movement of the contact trigger arm and the SQUIGGLE motor. It is thought that this disturbance alone will cause enough noise to invalidate any ground based thrust measurements. However, in the space environment the momentum gained by accelerating and expelling material from the thruster should be detectable in the low gravitational environment with long duration tests. It is therefore important to gain flight heritage with these μPPTs to properly characterise their performance.

In the current configuration the combined PPTs have a total propellant mass of 1.12g, which equate to a total ΔV for the 8 μPPT module for a 3U CubeSat with a mass of 4.5kg to be 2.72ms^{-1}. In the mission analysis section the required ΔV per year of 2-2.2ms^{-1} to account for drag compensation, gravity gradient stabilisation and pointing maintenance was established. The current design would be able to meet this yearly ΔV requirement for a one year mission.

With the insertion of copper blocks into the established discharge chamber of the current design the total propellant mass could be increased to 31.3g, which equates to a total ΔV of 76.34ms^{-1}. According to the calculations in the mission analysis section the required ΔV to move from an initial insertion orbit into an orbit that would meet deorbit requirements for a 3U CubeSat was between 24^{-1} and 164ms^{-1}. With the addition of these copper blocks and depending on the initial orbit conditions, the μPPTs could fulfil this requirement.

The STRaND-1 satellite is currently in the build phase with qualification to begin in August 2011. Since inception the satellite has been used as a tool to train young engineers, both at SSC and SSTL, and has been used to challenge existing manufacturing procedures to understand where costs can be saved in developing future satellites. The CAD model of the STRaND-1 satellite of the complete CubeSat and its internal subsystems can be seen in Figure 6.21

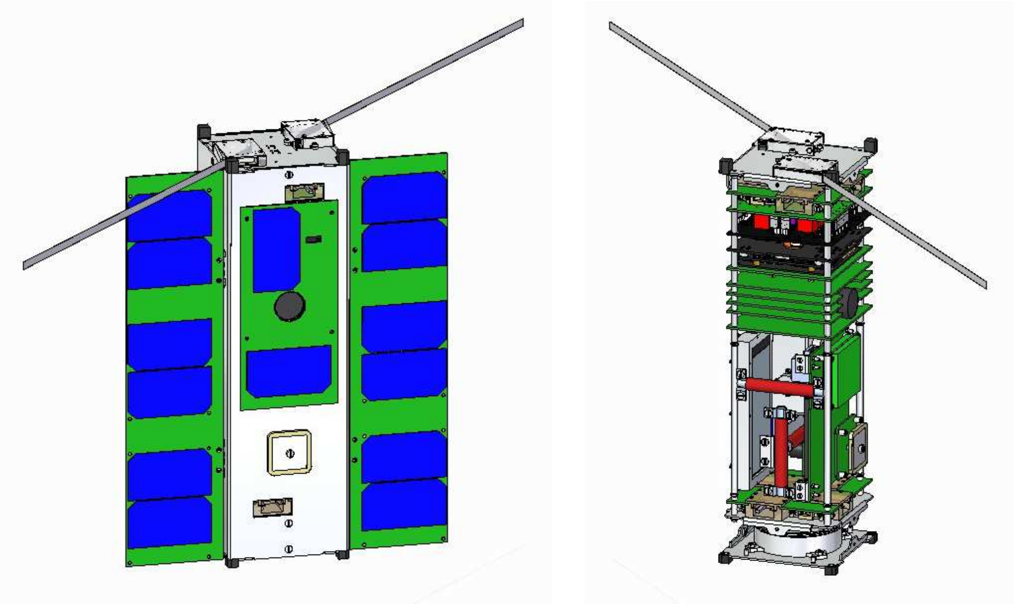

Figure 6.21: CAD model of the STRaND-1 CubeSat. Left: External view Right: Internal view

6.4 Summary

Based on experimental and modelled observations an electric propulsion module with eight μPPTs has been designed for a 3U CubeSat. During bread boarding the design was evaluated and altered as necessary. The μPPT module has been specifically designed to meet the PC104 and CubeSat requirements. The μPPTs have two unique design features not seen in other PPT flown hardware. The first is a contact trigger mechanism that is used to initiate the discharge which replaces the usual sparkplug. The second is the removal of the standard Teflon^{TM} propellant which has aided in the miniaturisation of the thruster and allows for four thrusters to be compacted on to a single PC104 board.

Two propulsion modules were developed for two 3U CubeSats: one was for STRaND-1 and the second was for UKUBE-1. STRaND-1 is a joint project between the Surrey Space Centre and Surrey Satellite Technology Limited and was a technology demonstration mission. UKUBE-1 was also a technology demonstration mission run by the UK Space agency. After the unsuccessful down selection of the UKUBE-1 PPT, the module development was continued as a qualification module for the STRaND-1 mission. This was because both μPPTs used in the modules had an identical design. The qualification and flight units have been built for further testing during the Summer of 2011.

The propulsion module was designed for a 3U CubeSat. Initial results predict that a μPPT with a specific impulse of 321s, an impulse bit of 0.56μNs and a mass bit of 0.17μg has been developed. Although the current design only provides a predicted ΔV of 2.72ms^{-1}, with a relatively simple modification this can be increased to 76.34ms^{-1}. This would be able to compensate for drag, gravity gradient perturbations and maintain pointing to a high degree of accuracy. Depending on the initial orbit insertion the propulsion module may also provide the ability for the CubeSat to meet its deorbit requirements.

If the launch in November 2011 is successful, STRaND-1 will break two propulsion records: it will be the first CubeSat to have full 3-axis propulsive capabilities and it will be the first time electric propulsion has been used on the CubeSat class of satellite platform. If STRaND-1 is successful this will be a great achievement and will highlight the advantages of using the Pulsed Plasma Thruster on small satellites.

Chapter 7

Conclusions & Future Work

7.1 Summary of Conclusions

7.1.1 Literature Review

There has been over five decades of research into the Pulsed Plasma Thruster which has left a rich legacy of literature. This review began with a focus on PPTs that have been flight qualified or flown. Up until the turn of the millennium the PPT was nominally used on spin axis stabilised satellites. The PPTs on the TIP and NOVA satellites operated for a total of 20 years and fired over 50 million pulses. As technology improved the mass and volume of a satellite began to decrease. The PPT was then designed and qualified to give three axis attitude control but with a number of satellite launch failures and delays there have only been two successfully flown PPTs since 2000.

A comprehensive review of experiments in the areas of hardware development and fundamental science was undertaken. The pertinent points of the experiments were distilled and presented allowing parallels to be drawn with other works within the PPT field. The review finished off with a description on the PPT discharge process which gave an account on the current theories of what processes occur and also highlighted areas in which there is currently a lack of understanding. These areas are listed below:

- Off axis thrust production - A significant component to the thrust vector is in the cathode-anode axis originating from the cathode and directed towards the anode. Currently this force producing mechanism is not understood.

- Plasma production from the electrodes - The mass erosion mechanism from the electrodes is not fully understood.

- Role of the neutral particle sheet in the re-ignition process - The neutral particle sheet seems to dictate the position in the discharge chamber where a re-ignition event takes place. But it is not known whether the re-ignition is caused because the neutral particle layer breaks down or whether the presence of the neutral particle sheet promotes some other process or mechanism.

- Magnetic Field - The magnitude and distribution of the magnetic field that is produced around the inductors (electrodes) has a direct impact on the acceleration process of the particles. To increase the coupling between the magnetic field and the plasma it is important to understand how the topology of the magnetic field changes with time during the discharge.

7.1.2 CubeSat Mission Design & Analysis

The CubeSat standard has led to a growth of nanosatellite development since it was first introduced to the academic field in 1999. The past ten years of development have focussed on providing heritage to COTS components for future use and novel scientific research. The modular format of the CubeSat standard has allowed the research community to expand, where individual members can either provide a whole CubeSat or parts there of to the rest of the community.

Based on trends within literature the performance of a μPPT was postulated and a CubeSat mission analysis was conducted. A limiting factor of the CubeSat platform is the 25 year deorbit limit legislation and the situation that CubeSats are nominally secondary payloads on launch vehicles. The legislation means that a CubeSat (dependant on its size and mass) needs to be placed in an orbit between 513km to 651km. As these satellites are secondary payloads, they may be inserted into orbits greater than these, up to 820km for the Soyuz launch vehicle. A propulsion system delivering ΔV between 24ms^{-1} to 164ms^{-1} would ensure that CubeSats achieve the limits set out by the 25 year legislation whilst not being limited to the launch they are placed on.

A CubeSat with propulsion could also counter orbital disturbances i.e. atmospheric drag, solar radiation pressure, gravitational effects from other bodies etc. Dependant on the platform, the incorporated thruster and the orbit the yearly ΔV requirement is estimated to be approximately 2ms^{-1} to 6ms^{-1}.

The μPPT provides additional benefits; it is low cost to manufactuer, the propellant is inert and not pressurised (which is a safety concern from launch providers where secondary payloads are concerned), it has a discreet small repeatable impulse bit allowing the CubeSat to have precise pointing accuracy and it can be used to dump accumulated momentum from reaction wheels.

7.1.3 PPT Experiments

Once the facilities and testbed were proved to be working satisfactory the main set of experiments were conducted and several conclusions were made. However it is worth to note that the calculation of the impulse bit is taken from mathematical manipulation of the current signal to evaluate the electromagnetic contribution of the total impulse bit. The impulse bit calculated in this work does not take into account forces that would occur due to gas dynamics and late time ablation effects that could be observed if an impulse bit stand was used.

Experiments on the discharge initiator showed that it was important to have a breakdown due to a strong electric field but the specific properties of that initial arc did not affect the rest of the PPT pulse discharge. The DI was stripped back to a single filament wire held at negative 15kV and this was able to inject electrons via electron quantum tunnelling into the discharge chamber and initiate a breakdown of the main PPT capacitor.

Experiments looking into the mass loss from the Teflon^{TM} surface showed that the mass erosion was caused by plasma that formed close to the surface. As energy was increased to this plasma more Teflon^{TM} erosion occurred. However the opposite was not the case. When injecting the plasma with more Teflon^{TM} mass (by confining the plasma with sidewalls) an increase in the performance of the PPT did not occur, suggesting the presence of Teflon^{TM} mass within the plasma was not a significant factor in determining the plasma properties.

Experiments showed that the plasma resistance and the evolution of the plasma resistance had a major impact on the ringing of the overall pulse and the total length of the pulse. If the resistance can be kept to a minimum then performance can be increased. The plasma resistance was shown to be significantly affected by the electrode separation distance.

Experiments with the presence of Teflon^{TM} and without the presence of Teflon^{TM} showed a marked difference in performance. From the previous experiments it was concluded that the presence of Teflon^{TM} eroded material within the plasma did not have an effect on the PPT performance. So the only conclusion is that the presence of the Teflon^{TM} acts as a bridge when the arc discharges and that it is easier to arc between the electrodes connected by a material than it is to arc across hard vacuum. A reccomendation for future work would be to look into the materials that are used to 'bridge' the electrode gap as this could significantly increase the performance of the PPT.

Finally the presence of craters and film deposition confirms that electrode erosion occurs and that this is the most probable source that the plasma comes from when there is no Teflon^{TM} present between the electrodes. In the next chapter electrode erosion and cathode spots are used to model the PPT discharge without Teflon^{TM}.

7.1.4 PPT Modelling

The developed model to predict the performance of the PPT was built with the available computational software and hardware resources in mind. The model was based on a lumped circuit analysis model with several additional sub models to predict the behaviour or certain aspects of the thruster. These sub models included a detailed analysis of the discharge electrodes based on splitting the conductor into a number of sub conductors. The resistance, self inductance and mutual inductance was then calculated.

It was found that compared to the relative resistance and inductance of the capacitor the electrode resistance and inductance was minimal.

One of the limiting factors of currently avaliable lumped circuit analysis models is the assumption of constant values to describe the plasma that do not fluctuate with time or current. To overcome this lack in modelling a simplified magnetohydrodynamic flow model based on quasi steady state assumptions was put forward. The flow model was based on the assumptions that the plasma mass originated from the electrode surface and flowed towards the anode rather than a plasma bulk originating from a solid propellant between the electrodes (i.e. Teflon^{TM}). The flow model shows that along the flow the plasma at certain distances creates a 'choke', where the flow radius is small. In the 'choke' the electron temperature, electron density and mean ion charge state, significantly rise to values that have been observed in the available literature. The dynamics of the flow has a significant impact on the anode sheath and its ability to limit the arc current. It has been shown that it is this limiting effect that affects the PPT's ability to convert electrical energy to kinetic energy efficiently. If it is possible to manipulate the charge-space of the anode sheath then this is where most gains in performance can be made. The model has been shown to be a reasonable representation of the effects that occur within a PPT, which does not have Teflon^{TM} present between the electrodes.

7.1.5 Developing a μPPT for CubeSat Applications

Based on experimental and modelled observations an electric propulsion module with eight μPPTs has been designed for a 3U CubeSat. During bread boarding the design was evaluated and altered as necessary. The μPPT module has been specifically designed to meet the PC104 and CubeSat requirements. The μPPTs have two unique design features not seen in other PPT flown hardware. The first is a contact trigger mechanism that is used to initiate the discharge which replaces the usual sparkplug. The second is the removal of the standard Teflon^{TM} propellant which has aided in the miniaturisation of the thruster and allows for four thrusters to be compacted on to a single PC104 board.

Two propulsion modules were developed for two 3U CubeSats: one was for STRaND-1 and the second was for UKUBE-1. STRaND-1 is a joint project between the Surrey Space Centre and Surrey Satellite Technology Limited and was a technology demonstration mission. UKUBE-1 was also a technology demonstration mission run by the UK Space agency. After the unsuccessful down selection of the UKUBE-1 PPT, the module development was continued as a qualification module for the STRaND-1 mission. This was because both μPPTs used in the modules had an identical design. The qualification and flight units have been built for further testing during the Summer of 2011.

The propulsion module was designed for a 3U CubeSat. Initial results predict that a μPPT with a specific impulse of 321s, an impulse bit of 0.56μNs and a mass bit of 0.17μg has been developed. Although the current design only provides a predicted ΔV of 2.72ms^{-1}, with a relatively simple modification this can be increased to 76.34ms^{-1}. This would be able to compensate for drag, gravity gradient perturbations and maintain pointing to a high degree of accuracy. Depending on the initial orbit insertion the propulsion module may also provide the ability for the CubeSat to meet its deorbit requirements.

If the launch in November 2011 is successful, STRaND-1 will break two propulsion records: it will be the first CubeSat to have full 3-axis propulsive capabilities and it will be the first time electric propulsion has been used on the CubeSat class of satellite platform. If STRaND-1 is successful this will be a great achievement and will highlight the advantages of using the Pulsed Plasma Thruster on small satellites.

7.2 Novelty and Research Achievements

Within the course of this work, the following novel contributions have been made to the current state of the art, for the Pulsed Plasma Thruster field:

- From critical analysis of the literature review and with observations during experimentation that a PPT, without Teflon^{TM} propellant, produces plasma from the errosion of the electrode surface.
- It is postulated that in most PPTs, with or without standard Teflon^{TM} propellant, the plasma originates from the errosion of the electrode surface.
- It has been highlighted with circumstantial evidence from the literature review that within the PPT, the process of cathode spots is the cause of electrode errosion.
- It has been shown through experimentation that the current discharge profile in the circuit loop of the PPT is a function of the stored energy but is not a function of the eroded Teflon^{TM} mass.
- It is postulated with experimental evidence that the presence of Teflon^{TM} acts as an arc bridge. When the discharge is initiated this bridge acts as a 'path of least resistance' in which the initiated discharge tracks across. The presence of the bridge allows for larger currents to flow and stronger magnetic fields to form which enhance and elongate the LCR ringing effect of the discharging circuit.
- It has been highlighted with analytic evidence from the literature review that each pulse of the ringing discharge relates to a new plasma formation. It is also highlighted that beyond the first pulse the location of each new plasma formation coincides with the location of the neutral particle sheet (if present).
- Based on models from the literature a simplified MHD plasma flow model that originates from the production of plasma from cathode spots has been formed. This model, which takes cathode spot data from the plasma coating field and a flow model from research into short pulse high current cathodic plasmas, is implemented to explain the internal dynamics of the PPT. The simplified

MHD plasma flow model coupled with a lumped circuit analysis model, a Lorentz force model, an electrode skin effect model and a plasma errosion model make the completed novel PPT model. The PPT model, within the confinements of quasi steady state is able to accurately predict the current profile of a discharging PPT. The PPT model also predicts, within reasonable magnitudes, values of plasma parameters that are seen within literature, including the mean ion charge state and the electron density. The PPT model predicts temperature distributions in the early stages of the plasma formation that coincide with the observed back flux of carbons seen on Teflon^{TM} samples. Lastly the PPT model, in the early stages of the plasma formation, predicts similar shapes of the plasma flow to that seen in current density distribution data.

- It is postulated from observations made using the developed PPT model, that within the plasma flow ‘choke’ points form due to instabilities within the plasma flow. These lead to localised areas of high ion mean charge states, high electron temperatures and high electron number densities. I also postulate that the main limiting factor of arc current within the plasma flow is due to the charge-space limitation of the anode sheath. I postulate that until this limitation is reduced by careful manipulation of the plasma flow near the anode sheath the efficiency of PPTs to convert electrical energy to kinetic energy will remain low.
- The developed model was used to design a novel type of PPT electrodes that were based on a blade like configuration. This configuration was chosen as it would hopefully promote cathode spot formation in a single area along the blade edge.
- A novel propulsion module for a sub 5kg satellite platform has been developed with eight μPPTs that will provide two axis with pitch, roll and yaw attitude control. The μPPT boasts several novelties including a contact trigger discharge initiator, low circuit inductances and resistances using a custom pulse capacitor and no Teflon^{TM} propellant. All these innovations have meant that four μPPT can be mounted on a single PC104 board.

7.3 Future Work

This thesis opens up the opportunity for others to expand upon the work that has been started, in particular the following areas of study need to be continued as a direct continuation of this work:

- Alternative methods of mass loss measurement: It was found during the experimental phase of this work that when the PPT fired, there was a momentary rise in the vacuum chamber pressure. The maximum pressure obtained was linked to the energy of the pulse discharge. It was also shown that the rise in pressure was independent of electromagnetic interference. Theoretically, if the vacuum gauge has good resolution, accuracy and sensitivity, if the dimensions of the vacuum chamber are known and if the pumping capacity of the vacuum chamber is stable, the vacuum chamber pressure could be used to estimate the total mass loss per pulse from the PPT. The advantages of this method would be the direct comparison of mass loss between individual pulses, rather than taking mean mass measurements of the propellant before and after an experimental regime. However, this work would require a thorough understanding on the working principles and particle flows within a vacuum chamber and require sensitive costly vacuum gauges.

- Arc bridge material: In the literature review and observations made during experimentation with and without Teflon^{TM} it was shown that the material between the electrodes acted like an arc bridge during initial breakdown of the discharge. During the initial phases of the discharge it was seen that when Teflon^{TM} was present, the flow of current was greater through the PPT, which had the effect of storing more energy in the self created magnetic fields that formed around the electrodes. The increased current and stronger magnetic fields would cause an increase in the performance of the PPT. However, it was also shown that the mass lost from the Teflon^{TM} did not play a significant role in the dynamics of the plasma. Based on these conclusions alternative materials could be used between the electrodes. They would need to be initially non conducting, so the PPT capacitor can charge to the desired voltage. But once the discharge is initiated the material would have to enhance the formation of the initial arc so larger current flows would form. Due to the possibility of being eroded, the material has to be made from elements that are non conducting when they are deposited upon the thruster chamber walls.

The developed model within this work is a reasonable start to a more complete and complex model to describe the PPT discharge. Several areas within the current model need to be expanded upon to enhance its applicability:

- SPICE model: The capacitor is currently modelled as single values in the lumped circuit analysis model. However, when high frequencies are involved additional processes occur. A SPICE or generic high frequency capacitor model is thus required to model these effects.
- Additional propellant: The developed model is based on a system with no propellant material between the electrodes. Additional propellant introduced as a solid, liquid or gas may have an effect on the dynamics of the flow model. As such the flow model needs to incorporate the effects from additional species of elements within the plasma which would primarily effect the plasma conductivity and mean ion charge state.
- Electrode material: To analyse the effect of using different materials for the PPT electrodes it is important to gather data on the cathode spot properties that would form from these materials. In many cases of simple metals this has been already done in literature. However, what is less known

is the evolution of the cathode spot dimensions in time. Developing an accurate model to describe the time dependant dimensions of the cathode spot will aid in estimating boundary conditions of the plasma flow.

- Initial arc breakdown: The charge-space properties of the discharge gap and their effect on the formation of the initial arc need to be modelled. It was shown that there is an exponential rise in the current pulse which is not adequately modelled. This breakdown needs to take into account the properties of the discharge gap and any materials that are placed between the electrodes to enhance the initial breakdown.
- Anode spots: In the literature and the experiments it was shown that at certain conditions anode spots form. The experiments show that the forming anode spots cause a significant increase in the current flow and that as such the performance of the PPT increases. The introduction of additional ions into the plasma flow region effects how the plasma flow behaves. The conditions of formation of the anode spot need to be discovered and the properties of these spots need to be known so they can describe the relevant anode boundary conditions. Also the interaction from two competing flows from the anode and cathode surface need to be understood. By capitalising on the increased current flow from anode spot formation, performance increases in the PPT can be made.
- Lorentz force model: The Lorentz force model used in this work assumes that the flow of current originates radially from the midpoint of the rectangular bar electrodes. Modelling of the electrode has shown this not to be the case and that current actually flows in the skin regions. In future work the coupling between these two observations will have to be made to get a more accurate model of the magnetic field distribution in the PPT. To validate this model experimentally ion speed measurements from time of flight probes need to be made.
- Canting and time dependency: The developed model is only valid in the quasi steady state regime and ignores the effect of canting on the system. In future a Particle in Cell (PIC) simulation will need to be developed so the plasma flow can be described in three dimensions that will take into account time dependencies and canting caused by the interaction of the particles with the magnetic field. Currently using simplified partial differential equations to solve the flow dynamics means that some observed phenomena are being neglected.
- Multiple flows: Literature has shown that the current density flow is not always made from a single flow. If cathode spots form at significant distances from each other at multiple locations, multiple flows will form. This process needs to be explained and the effect of these multiple flows needs to be accounted for within the developed flow model.

Development of a flight μPPT module for a 3U CubeSat and the observations from using the developed model have shown areas in which novel hardware can be developed for the future:

- Hybrid magnotorque PPT system: It was shown that enhancing the magnetic field can positively affect the PPT performance. A coaxial μPPT could therefore be constructed that fits inside the core of a magnotorque. As well as using the interaction of the magnotorque magnetic field with the Earth's magnetic field to stabilise the CubeSat, the same magnetic field could also be used to enhance the dynamics of the PPT.
- Cathode spot propulsion: The production of cathode spots themselves can accelerate ions to high velocities, in the case of copper this is around 13.2kms^{-1}. A relatively simple μpropulsion system can be created that could be used to exploit this thrust mechanism alone.

7.4 Publications

The current list of publications relating to this work that have been published are;

Shaw P. V., Lappas V. J., Underwood C. I. 'Development of a PPT for CubeSat Applications', International Journal of Aerospace Engineering, 2011 (In preperation)

Shaw P. V., Lappas V. J., 'Observations on the effect of high current cathodic plasma discharges between copper electrodes with and without the presence of a Teflon dielectric between the electrodes', Journal of Physics D: Applied Physics or Technical Physics letter, 2011 (In preperation)

Shaw P. V., Lappas V. J., 'High current cathodic arc plasma flow model for a Lorentz force accelerator' Journal of Physics D: Applied Physics or Technical Physics letter, 2011 (In preperation)

Shaw P. V., Lappas V. J., Underwood C. I. 'Development of the μPPT propulsion module for STRaND-1 a 3U CubeSat',1st IAA Conference on University Satellites Missions and CubeSat Workshop in Europe, Rome, Italy, 2011.

Shaw P. V., Lappas V. J., 'Pulsed Plasma Thruster: Simple Design, Complex Matter', Space Propulsion Conference 2010, Sans Sebastian, Spain, May, 2010.

Shaw P. V., Lappas V. J., 'Mathematical Modelling of High Efficiency Pulsed Plasma Thrusters for Microsatellites', International Aerospace Conference, AIAA IAC-06-C4.P.4.4, Valencia, Spain, 2006.

Bibliography

[1] Zakrzwski, C., Benson, S. W., Sanneman, P., and Hoskins, A., "On-orbit testing of the EO-1 pulsed plasma thruster," *38th Joint propulsion conference*, AIAA, Indianapolis, Indiana, 2002.

[2] Ziemer, J. K., Cubbin, E. A., Choueiri, E. Y., Oraevsky, V., and Dokukin, V., "Pulsed plasma propulsion for a small satellite: Mission COMPASS P3OINT," *32nd Joint propulsion conference*, AIAA, 1996.

[3] Marques, R. I., Gabriel, S. B., and Costa, F. d. S., "High frequency burst pulsed plasma thruster research at the university of Southampton," *30th International electric propulsion conference*, Florence, Italy, 2007.

[4] Markusic, T., Polzin, K. A., Levine, J. Z., McLeavey, C., and Choueiri, E. Y., "Ablative Z-pinch pulsed plasma thruster," *36th Joint propulsion conference*, AIAA, Huntsville, Alabama, 2000.

[5] Nawaz, A., Auweter-Kurtz, M., Herdrich, G., and Kurtz, H. L., "Investigation and optimization of an instationary MPD thruster at IRS," *29th International electric propulsion conference*, IEPC, Princeton University, New Jersey, 2005.

[6] Pottinger, S., Krejci, D., and Scharlemann, C., "Pulsed plasma thruster performance for miniaturised electrode configurations and low energy operation," *Acta Astronautica*, Vol. 68, No. 11-12, 2008, pp. 1996–2004.

[7] Kawakami, M., Lin, W.-W., Igari, A., Horisawa, H., and Kimura, I., "Plasma behaviours in a laser-assisted plasma thruster," *39th Joint propulsion conference*, AIAA, Huntsville, Alabama, 20/7/03 2003.

[8] Scharlemann, C. A. and York, T. M., "Alternative propellants for pulsed plasma thrusters," *38th Joint propulsion conference*, AIAA, Indianapolis, Indiana, 2002.

[9] Kakami, A., Koizumi, H., Komurasaki, K., and arakawa, Y., "Performance study on liquid propellant pulsed plasma thruster," *39th Joint propulsion conference*, AIAA, Huntsville, Alabama, 2003.

[10] Keidar, M., Boyd, I. D., Gulczinski III, F. S., Antonsen, E. L., and Spanjers, G. G., "Analyses of Teflon surface charring and near field plume of a micro-pulsed plasma thruster," *International electric propulsion conference*, 2001.

[11] Spanjers, G. G., Lotspeich, J. S., Mcfall, K. A., and Spores, R. A., "Propellant ineffeciency due to particulates in a pulsed plasma thruster," *Space technology and applications forum*, Albuguergue, NM, 1997.

[12] Spanjers, G. G., Mcfall, K. A., Gulczinski III, F. S., and Spores, R. A., "Investigation of propellant inefficiencies in a pulsed plasma thruster," *32nd Joint propulsion conference*, AIAA, Lake Buena Vista, Florida, 1996.

[13] Keidar, M., Boyd, I. D., and Beilis, I. I., "Model of particulate interaction with plasma in a teflon pulsed plasma thruster," *Journal of propulsion and power*, Vol. 17, No. 1, 2001.

[14] Alexeev, Y. A., Kazeev, M. N., and Kozlov, V. F., "Energy transfer to the propellant in high power PPT," *4th International spacecraft propulsion conference*, ESA, Cagliari, Sardinia, Italy, 2004.

[15] Markusic, T. and Spores, R. A., "Spectroscopic emission measurements of a pulsed plasma thruster plume," *33rd Joint propulsion conference*, AIAA, Seattle, Washington, 1997.

[16] Berkery, J. and Choueiri, E. Y., "Characterization of current sheet evolution in a pulsed electromagnetic accelerator," *28th International electric propulsion conference*, Toulouse, France, 2003.

[17] Kazeev, M. N., Popov, G. A., antropov, N. N., Diakonov, G. A., Orlov, M. M., Posokhin, V. S., Tyutin, V. K., and Yakovev, V. N., "Dynamics and distribution of electron density in the channel of pulsed plasma thruster," *Joint propulsion conference*, AIAA, Indianapolis, Indiana, 2002.

[18] Kamhawi, H., Turchi, P. J., Mikellides, P. G., and Mikellides, I. G., "Experimental and theoretical investigation of an inverse-pinch coaxial pulsed plasma thruster," *36th Joint propulsion conference*, AIAA, Huntsville, Alabama, 2000.

[19] Kumagai, N., Igarashi, M., Sato, K., Tamura, K., Kawahara, K., and Takegahara, H., "Plume diagnostics in pulsed plasma thruster," *38th Joint propulsion conference*, AIAA, Indianapolis, Indiana, 2002.

[20] Nawaz, A., Bauder, U., Bohrk, H. K., Herdrich, G., and Auweter-Kurtz, M., "Electrostatic probe and camera measurements for modeling the iMPD SIMP-LEX," *Jet propulsion conference*, AIAA, 2007.

[21] Koizumi, H., Noji, R., Komurasaki, K., and Arakawa, Y., "Study on plasma acceleration in an ablative pulsed plasma thruster," *43rd Joint propulsion conference*, AIAA, Cincinnati, Ohio, 2007.

[22] Gatsonis, N. A., Zwahlen, J. C., Wheelock, A., Pencil, E. J., and Kamhawi, H., "Characterization of a pulsed plasma thruster plume using a quadruple langmuir probe method," *38th Joint propulsion conference*, AIAA, Indianapolis, Indiana, 2002.

[23] Parker, K., "Pulsed plasma thruster plume analysis," *Acta astronautica*, Vol. 53, 2003, pp. 789–795.

[24] Anders, A., *Cathodic arcs: From fractal spots to energetic condensation*, Atomic, optical and plasma physics 50, Springer, 1st ed., 2008.

[25] Kamhawi, H., Pencil, E. J., and Haag, T. W., "High thrust-to-power rectangular pulsed plasma thruster," *38th Joint propulsion conference*, AIAA, Indianapolis, Indiana, 2002.

[26] Long, M., Lorenz, A., Rodgers, G., Tapio, E., Tran, G., Jackson, K., Twiggs, R., and Bleier, T., "A cubesat derived design for a unique academic research mission in earthquake signature detection," *16th Annual AIAA USU Conference on Small Satellites*, Utah State University, Logan, Utah USA, 12/8/2002 2002.

[27] Kitts, C., Ronzano, K., Rasay, R., Mas, I., Williams, P., and Mahacek, P., "Flight Results from the GeneSat-1 Biological Microsatellite Mission," *21st Annual AIAA USU Conference on Small Satellites*, Utah State University, Logan, Utah USA, 13/8/07 2007.

[28] Mauthe, S., Pranajaya, F., and Zee, R. E., "The design and test of a compact propulsion system for CanX nanosatellite formation flying," *19th Annual AIAA USU Conference on Small Satellites*, Utah State University, Logan, Utah USA, 8/8/2005 2005.

[29] Rysanek, F. and Hartman, J. W., "Micro vacuum arc thruster design for a cubesat class satellite," *16th Annual AIAA USU Conference on Small Satellites*, Utah State University, Logan, Utah USA, 12/8/02 2002.

[30] Myers, R. M., "Electromagnetic propulsion for spacecraft," Tech. Rep. NASA-CR-191186, NASA, 1993.

[31] Nicolai, P., Tikhonchuk, V. T., Kasperczuk, A., Pisarczyk, T., Borodziuk, S., Rohlena, K., and Ullschmied, J., "Plasma jetsproduced in single laser beam interaction with a planar target," *33rd Conference on Plasma Physics*, Rome, Italy, 19/6/06 2006.

[32] Kasperczuk, A., Pisarczyk, T., Kalal, M., Ullschmied, J., Krousky, E., Masek, K., Pfeifer, M., Rohlena, K., Skala, J., Velarde, P., Gonzalez, M., Garcia, C., Oliva, E., and Pisarczyk, P., "Direct and indirect methods of the plasma jet generation," *35th EPS Conference on Plasma Physics*, Hersonissos, Crete, Greece, 9 - 13 June 2008.

[33] Anders, A., Oks, E., Yushkov, G. Y., Savkin, K. P., Brown, I. G., and Nikolaev, A., "Measurements of the total ion flux from vacuum arc cathode spots," *IEEE Transactions on plasma science*, Vol. 33, No. 5, 2005, pp. 4.

[34] Artamonov, M. F., Krasov, V. I., and Paperny, V., "Registration of accelerated multiply charged ions from the cathode jet of a vacuum discharge," *Journal of Experimental and Theoretical Physics*, Vol. 93, No. 6, 2001, pp. 5.

[35] Palumbo, D., "Solid propellant pulsed plasma propulsion system development for N-S stationkeeping," *14th International electric propulsion conference*, IEPC, Princeton, New Jersey, 1979.

[36] Tamura, K., Igarashi, M., Kumagai, N., Sato, K., Kawahara, K., Takegahara, H., Sugiki, M., and Hashimoto, H., "Evaluation of low power pulsed plasma thruster for -LabSat II," *38th Joint propulsion conference*, AIAA, Indianapolis, Indiana, 2002.

[37] Schein, J., Gerhan, A., Rysanek, F., and Krishnan, M., "Vacuum arc thruster for cubesat propulsion," Tech. rep., Alameda Applied Sciences Corporation, San Leandro, CA, USA, 2002.

[38] "Medium delta V, low power, low voltage, microthruster module breadboarding," Statement of work, European Space Agency, Directorate of Directorate of Technical and Quality Management, 29th October 2009.

[39] Krasov, V. I., Krinberg, I. A., Paperny, V., Korobkin, Y. V., Romanov, I. V., Rupasov, A. A., and Shikanov, A. S., "Ion acceleration in a high-current cathode plasma jet expanding in vacuum," *Technical Physics Letters*, Vol. 33, No. 11, 2007, pp. 941–944.

[40] Burton, R. L. and Turchi, P. J., "Pulsed plasma thruster," *Journal of propulsion and power*, Vol. 14, No. 5, 1998, pp. 716–735.

[41] Cassady, R. J., Meckel, N. J., Hoskins, W. A., Myers, R. M., Oleson, S. R., and McGuire, M., "Pulsed plasma thruster systems for spacecraft attitude control," *10th Annual AIAA USU Conference on Small Satellites*, Utah State University, Logan, Utah USA, 1996.

[42] Hoskins, W. A., Rayburn, C. D., and Sarmiento, C., "Pulsed plasma thruster electromagnetic compatibility: History, theory and the flight validation on EO-1," *39th Joint propulsion conference*, AIAA, Huntsville, Alabama, 2003.

[43] Rayburn, C. D., Campbell, M. E., and Mattick, A. T., "Pulsed plasma thruster system for microsatellites," *Journal of spacecraft and rockets*, Vol. 42, No. 1, 2005, pp. 161–170.

[44] Campbell, M. E. and Bruckner, A. P., "UW Dawgstar: One third of ION-F," *13th Annual AIAA USU Conference on Small Satellites*, Utah State University, Logan, Utah USA, 23/8/99 1999.

[45] Gulczinski III, F. S., Dulligan, M., Lake, J., and Spanjers, G. G., "Micropropulsion research at AFRL," *36th Joint propulsion conference*, AIAA, Huntsville, Alabama, 2000.

[46] Pottinger, S., Krejci, D., and Scharlemann, C. A., "Development of a mPPT for cubesat applications," *44th AIAA Joint propulsion conference and exhibit*, AIAA, Hartford, Connecticut, 2008.

[47] Campbell, M. E. and Schetter, T., "Formation flying mission for the UW Dawgstar satellite," *IEEE Aerospace conference*, IEEE, Big Sky, Montana, 18/3/00 2000.

[48] Hoskins, W. A. and Cassady, R. J., "Applications for pulsed plasma thrusters and the development of small PPTs for microspacecraft," *36th Joint propulsion conference*, Huntsville, Alabama, 2000.

[49] Pencil, E. J., Kamhawi, H., and arrington, L. A., "Overview of NASA's pulsed plasma thruster development program," *40th Joint propulsion conference*, AIAA, Fort Lauderdale, Florida, 2004.

[50] Rysanek, F. and Burton, R. L., "Effect of heatloss on thrust of a coaxial PPT," *38th Joint propulsion conference*, AIAA, Indianapolis, Indiana, 2002.

[51] Bushman, S. S. and Burton, R. L., "Heating and plasma properties in a coaxial gasdynamic pulsed plasma thruster," *Journal of propulsion and power*, Vol. 17, No. 5, 2001, pp. 959–965.

[52] Popov, G. A. and Antropov, N. N., "Ablative PPT. New quality, new perspective," *Acta astronautica*, Vol. 59, 2006, pp. 175–180.

[53] Hrbud, I., Rose, M. F., and White, P., "Performance of a multilayer ceramic capacitor power system for pulsed plasma thrusters," *34th Joint Propulsion Conference and Exhibit*, AIAA, Cleveland, Ohio, USA, 13/7/98 1998.

[54] Arrington, L. A., "Evaluation of pulsed plasma thruster micropulsing," *40th Joint propulsion conference*, AIAA, Fort Lauderdale, Florida, 2004.

[55] Keidar, M. and Boyd, I. D., "Electromagnetic effects in the near field plume exhaust of a pulsed plasma thruster," *37th Joint propulsion conference*, AIAA, Salt Lake City, Utah, 2001.

[56] Kamhawi, H., Arrington, L., Pencil, E. J., and Haag, T. W., "Performance evaluation of a high energy pulsed plasma thruster," *41st Joint propulsion conference*, AIAA, Tucson, Arizona, 2005.

[57] Nawaz, A., Herdrich, G., Kurtz, H. L., Schonherr, T., and Auweter-Kurtz, M., "SIMP-LEX: Systematic geometry variation using thrust balance measurements," *30th International electric propulsion conference*, IEPC, Florence, Italy, 2007.

[58] Laystrom, J. K., Burton, R. L., and Benavides, G. F., "Geometric optimization of a coaxial pulsed plasma thruster," *39th Joint propulsion conference*, AIAA, Huntsville, Alabama, 2003.

[59] Kimura, I., Yanagi, R., and Inoue, S., "Preliminary experiments on pulsed plasma thrusters with applied magnetic fields," *13th International Electric Propulsion Conference*, AIAA, San Diego, California, USA, 25/4/78 1978.

[60] Cooley, J. and Choueiri, E. Y., "IR-Assisted discharge initiation in pulsed plasma thrusters," *38th Joint propulsion conference*, AIAA, Indianapolis, Indiana, 2002.

[61] Cooley, J. and Choueiri, E. Y., "Fundamentals of PPT discharge initiation: Undervoltage breakdown through electron pulse injection," *39th Joint propulsion conference*, Huntsville, Alabama, 2003.

[62] Simon, D., Land, H. B., and Emhoff, J., "Experimental evaluation of a micro liquid pulsed plasma thruster concept," *42nd Joint propulsion conference*, AIAA, Sacramento, California, 2006.

[63] Kakami, A., Koizumi, H., Komurasaki, K., and arakawa, Y., "Design and performance of liquid propellant pulsed plasma thruster," *Vacuum*, Vol. 73, 2004, pp. 419–425.

[64] Koizumi, H., Kakami, A., Furuta, Y., Komurasaki, K., and Arakawa, Y., "Liquid propellant pulsed plasma thruster," *28th International electrical propulsion conference*, Toulouse, France, 2003.

[65] Arrington, L. A., Haag, T. W., Pencil, E. J., and Meckel, N. J., "A performance comparison of pulsed plasma thruster electrode configurations," *25th International electric propulsion conference*, IEPC, Cleveland, Ohio, 1997.

[66] Keidar, M., Boyd, I. D., Antonsen, E. L., Gulczinski III, F. S., and Spanjers, G. G., "Propellant charring in pulsed plasma thrusters," *Journal of propulsion and power*, Vol. 20, No. 6, 2004, pp. 978–984.

[67] Antonsen, E. L., Burton, R. L., Spanjers, G. G., and Spores, R. A., "Microsecond timescale surface temperature measurements in micro-pulsed plasma thrusters," *39th Joint propulsion conference*, Huntsville, Alabama, 2003.

[68] Byrne, L. T., Seling, H. S., Wetlock, A. T., Gatsonis, N. A., and Pencil, E. J., "Design of a triple probe experiment to measure the PPT plume from the exit plane to the backflow region," *36th Joint propulsion conference*, AIAA, Huntsville, Alabama, 2000.

[69] Byrne, L. T., Gatsonis, N. A., and Pencil, E. J., "Triple langmuir probe measurements in the plume and backflow region of a pulsed plasma thruster," *37th Joint propulsion conference*, AIAA, Salt Lake City, Utah, 2001.

[70] Keidar, M., Boyd, I. D., and Beilis, I. I., "Ionisation and ablation phenomena in an ablative plasma accelerator," *Journal of Applied Physics*, Vol. 96, No. 10, 2004.

[71] Arrington, L. and Haag, T. W., "Multi-axis thrust measurements of the EO-1 pulsed plasma thruster," *35th Joint propulsion conference*, AIAA, Los Angeles, California, 1999.

[72] Ashida, H., Fujihashi, K., Inagawa, S., Miura, Y., Omagari, K., Konda, Y., Miyashita, N., and Matunaga, S., "Design of Tokyo tech nanosatellite Cute-1.7 + APD II and its operation," IAF, 29/9/2008 2008.

[73] Steyn, W. H. and Lappas, V., "Cubesat solar sail 3-axis stabilization using panel translation and magnetic torquing," *Aerospace Science and Technology*, Vol. 15, No. 6, 2010, pp. 476–485.

[74] Mueller, J., Hofer, R., and Ziemer, J. K., "Survey of propulsion technologies applicable to CubeSats," Tech. rep., Jet Propulsion Laboratory, Calafornia Institute of Technology, National Aeronautics and Space Administration, 3rd May 2010.

[75] Larson, W. J. and Wertz, J. R., editors, *Space Mission Analysis and Design*, Space Technology Series, Microcosm Press, 3rd ed., 2004.

[76] "U.S. Standard atmosphere 1976," 1976.

[77] Brady, M. E. and Aston, G., "Pulsed plasma thruster ignitor plug ignition characteristics," *3rd Joint thermophysics, fluids, plasma and heat transfer conference*, AIAA, St. Louis, Missouri, 1982.

[78] Krejci, D., Seifert, B., and Scharlemann, C. A., "Thrust measurement of a micro pulsed plasma thruster for CubeSats," *1st IAA Conference on University Satellites Missions and CubeSat Workshop in Europe*, Rome, Italy, 24-29 January 2011.

[79] Keidar, M., Boyd, I. D., and Beilis, I. I., "On the model of Teflon ablation in an ablation-controlled discharge," *Journal of Physics D: Applied Physics*, Vol. 34, 2001, pp. 1675–1677.

[80] Keidar, M. and Boyd, I. D., "Optimisation issues for a mico-pulsed plasma thruster," *Journal of propulsion and power*, Vol. 22, No. 1, 2006, pp. 48–55.

[81] Awadallah, R. S., Freund, D. E., and Simon, D., "Electromagnetic emission modelling for micro pulsed plasma thrusters," *41st Joint propulsion conference*, AIAA, Tucson, Arizona, 2005.

[82] Surzhikov, S. T. and Gatsonis, N. A., "A splitting method of unsteady 3-D magnetogasdynamic flows applied to pulsed plasma thruster plumes," *32nd Plasmadynamics and lasers conference*, AIAA, Anaheim, California, 2001.

[83] Lange, C., "Carbonisation studies on pulsed plasma thruster Teflon propellant," Tech. rep., Universitat Stuttgart, 2008.

[84] Rhodes, R., Keefer, D., and Thomas, H., "A numerical study of a pulsed plasma thruster," *37th Joint propulsion conference*, AIAA, Salt Lake City, Utah, 2001.

[85] Rooney, D., Moeller, T., Keefer, D., Rhodes, R., and Merkle, C., "Experimental and computer studies of a pulsed plasma accelerator," *43rd Joint propulsion conference*, AIAA, Cincinnati, Ohio, 2007.

[86] Laperriere, D. D., Gatsonis, N. A., and Demetriou, M. A., "Electromechanical modelling of applied field micro pulsed plasma thrusters," *41st Joint propulsion conference*, AIAA, Tucson, Arizona, 2005.

[87] Ziemer, J. K. and Choueiri, E. Y., "Scaling laws for electromagnetic pulsed plasma thrusters," *Plasma Sources Sci. Technol.*, Vol. 10, 2001, pp. 395–405.

[88] Bar, A. W., "Calculation of frequency-dependent impedance for conductors of rectangular cross section," *AMP Journal of Technology*, Vol. 1, 1991, pp. 9.

[89] Anders, A., Anders, S., Forsters, A., and Brown, I. G., "Pressure ionisation: its role in metal vapour vacuum arc plasma and ion sources," *Plasma Sources Sci. Technol.*, Vol. 1, 1992, pp. 263–270.

[90] Krinberg, I. A. and Paperny, V., "Cathode jet pinching as the effective mechanism of plasma heating and acceleration," *IEEE 19th International symposium on discharges and electrical insulation in vacuum*, 2000.

[91] Krinberg, I. A. and Paperny, V., "Pinch effect in vacuum arc plasma sources under moderate discharge currents," *Journal of Physics D: Applied Physics*, Vol. 35, 2002, pp. 549–562.

[92] Fridman, A. and Kennedy, L. A., *Plasma physics and engineering*, Taylor and Francis, New York, 2004.

[93] Beilis, I. I., Djakov, B. E., Juttner, B., and Pursch, H., "Structure and dynamics of high-current arc cathode spots in vacuum," *Journal of physics D: Applied physics*, Vol. 30, 1997, pp. 119–130.

[94] Oks, E., Yushkov, G. Y., and Anders, A., "Temporal development of ion beam mean charge state in pulsed vacuum acr ion sources," *The review of scientific instruments*, Vol. 79, No. 2, 2008, pp. 3.

[95] Krinberg, I. A. and Zverev, E. A., "Additional ioization of ions in the inter-electrode gap of a vacuum arc," *Plasma sources sci. Technol.*, Vol. 12, 2003, pp. 7.

[96] Krinberg, I. A., "Three modes of vacuum arc plasma expansion in the absence and presence of a magnetic field," *IEEE Transactions on plasma science*, Vol. 33, No. 5, 2005, pp. 5.

[97] Krinberg, I. A. and Matafonov, G. K., "Control of ion charge states in vacuum arc ion source by imposition of a non-uniform magnetic field," *Surface and Coatings Technology*, Vol. 201, 2007, pp. 4.

[98] Krinberg, I. A., "Plasma flow crisis and the limiting electron temperature in a vacuum arc in axial magnetic field," *Technical Physics Letters*, Vol. 31, No. 3, 2004, pp. 3.

[99] D., H. J., "NRL Plasma Formulary," Tech. rep., Beam Physics Branch, Plasma Physics Division, Naval Research Laboratory, 2007.

[100] Zverev, E. A. and Krinberg, I. A., "The current coloumn contraction and ion charge increase induced by the current build up in a pulsed vacuum discharge," *Technical Physics Letters*, Vol. 26, No. 4, 2000, pp. 3.

[101] Korobkin, Y. V., Paperny, V., Romanov, I. V., Rupasov, A. A., and Shikanov, A. S., "Micropinches in laser induced moderate power vacuum discharge," *Plasma Phys. Control. Fusion*, Vol. 50, 2008, pp. 14.

[102] Zwahlen, J. C., *Investigation of a pulsed plasma thruster plume using a quadruple langmuir probe technique*, Ph.D. thesis, Worcester Polytechnic Institute, 2002.

Appendix A

PPT Model Computational Code

```
function PPT_Model_2011_krinberg_final()
%% Parallel Plate Pulsed Plasma Thruster Model
%%
% Version April 2011
% Copyright 2011 Surrey Space Centre, University of Surrey, UK
% Author: Peter V. Shaw
% Contact Address:
% Postal: Peter Shaw,
%         Surrey Space Centre,
%         University of Surrey,
%         Guildford,
%         Surrey,
%         GU2 7XH,
%         UK

% Email: p.shaw@surrey.ac.uk
% Phone: +44(0)1483 684710
% Fax:   +44(0)1483 689503
%% Disclaimer
%%
% Although the author has attempted to find and correct any bugs in
% this software program, the author is not responsible for any damage
% or losses of any kind caused by the use or misuse of this program.

% The author is under no obligation to provide support, service,
% corrections, or upgrades to the software program. Any reproduction
% or unauthorised use of the program contained herin is prohibted
% without the express permission of the author or Surrey Space Centre,
% University of Surrey, UK.

% This material is protected under copyright law of the United Kingdom.
%% Introduction
%%
% This model is based on the work published by of Andre Anders from the
% cathode spot and thin field deposition field and Igor Krinberg from the
% Pinched high current plasma flow field.

% This model calculates several parameters and characteristics of a
% discharging pulsed plasma thruster, using a lumped circuit analysis
```

```
% model. Where the circuit is modelled as a LCR circuit. The model has been made
% so that only real or experimentally obatined values for components need
% to be entered.

% The model is designed for a parallel plate pulsed plasma thruster that
% uses electrodes that are parallel to each other and are in the form of a
% rectangular bar with an imputted width, length, thickness and seperated by
% a given distance. The model is specifically designed for the energy
% supply (bank, storage device etc) to be in the form of a capacitor.
% Lastly the design is set up for the case where NO Teflon or other
% propellant is located between the electrode spacing. The propellant is
% assumed to come from the erroded mass from the electrodes.

%% Upkeep
%%
% This section clears the workspace and command window of all previously
% stored variables and past work. The 'tic' function begins the count of
% total computation time for the program.
clc
clear
tic
%% Global Variables
%%

% Mechanical Setup
global PPT_V0            % Initial discharge voltage of capacitor
global PPT_C             % Capacitance of High voltage capacitor
global PPT_Height        % Speration distance between the electrodes
global PPT_Thickness     % Thickness of the electrodes
global PPT_Width         % Width of the electrodes
global L_Cap             % Inductance of main PPT capacitor
global R_Cap             % Equivalent Series Resistance (ESR) of main
                         % PPT capacitor
global freq_discharge    % Discharge frequency of PPT
global B_ext_across      % Cross magnetic field experienced by plasma within
                         % pinched coloumn. Should be 0.
global B_ext_axial       % Axial magnetic field experienced by plasma within
                         % pinched coloumn.

% Initial electrode and plasma conditions
global mass_no           % Total mass number of electrode material
global Elec_Conductivity % Conductivity of the electrode material
global E_Q               % Complete set of ionisation energies for electrode
global Cn                % Initial distribution of the ion charge state
                         % in the mixing region
global PPT_I_r           % Ion errosion rate for the electrode
global Z0                % Initial mean ion charge state of plasma flow
global PPT_i_e           % Ion current normalised by arc current
global PPT_m_i           % Particle mass of electrode material
global Te_spot           % Temperature of plasma jet near the mixing region
global rmin              % Distance from cathode that mixing region forms
global Tem               % Maximum electron temperature within a microjet
global M0                % Mach number (same for all cathode materials)
global Cu_spot           % Max current per spot for electrode material
global ts_spot           % Time for the ion charge state distribution to
                         % reach steady state for the specific electrode material
global R0_per_spot       % Initial radius of the plasma flow at the mixing
                         % region
```

```
% Simulation variables
 global t_end                % Computation time at the end of each discharge
 global delays               % Small change in time to work out d/dt in dde23
 global Subconductor_number % In the electrode model X is the X by X number
                             % of conductors that the electrode should be
                             % split into
 global xyz                  % Simulation count variable
 global Res_flow; global Q_flow; global Coll_flow; %Sim variables

 global v1; global v2; global v3; % variables to extract data for graphs
 global v4; global v5; global v6;
 global v7; global v8; global v9;
 global v10; global v11; global v12;
 global v13; global v14; global v15;
 global v16; global v17; global v18;
 global v19; global v20; global v21;
 global v22; global v23; global v24;
 global v25; global v26;

%% Input Components
%%
% Constants
 e = 1.60217646e-19;        % Fundamental charge

% Mechanical Setup
 V_interest = 1700;         % Data of interest for the model to be compared with
 PPT_Height = 0.03;         % Speration distance between the electrodes
 PPT_Thickness = 0.01;      % Thickness of the electrodes
 PPT_Width = 0.02;          % Width of the electrodes
 Elec_Conductivity = 59.595e6; % Conductivity of the electrode material
 PPT_C = 4.06e-6;           % Capacitance of High voltage capacitor
 L_Cap = 310e-9;            % Inductance of main PPT capacitor
 R_Cap = 33e-3;             % Equivalent Series Resistance (ESR) of main
                            % PPT capacitor
 freq_discharge = 136e3;    % Discharge frequency of PPT
 B_ext_across = 0;          % Cross magnetic field experienced by plasma within
                            % pinched coloumn. Should be 0.
 B_ext_axial = 0;           % Axial magnetic field experienced by plasma within
                            % pinched coloumn. Should be 0.1d

% Electrode and Plasma Properties
 E_Q = [7.72638;12.566;16.5486;20.539;22.42;23.2;36;27;33;33;33.3; ...
     103.7;32;34;49;36;37;76;37.588;1026.412;107;112;144;122;126; ...
     170;109.5;8474.88;505.237;].*e; % Complete set of ionisation energies for
                                     % electrode material
 mass_no = 29;              % Total mass number of electrode material
 PPT_m_i = 63.55*1.66053886e-27; % Particle mass of electrode material
 PPT_I_r = 33.4e-9;         % Ion errosion rate for the electrode
 PPT_i_e = 0.114;           % Ion current normalised by arc current
 Z0 = 2.06;                 % Initial mean ion charge state of plasma flow
 Te_spot = 1*11605;         % Temperature of plasma jet near the mixing region
 rmin = 0.1e-3;             % Distance from cathode that mixing region forms
 Tem = 2.8*11605;           % Maximum electron temperature within a microjet
 M0 = 3.5;                  % Mach number (same for all cathode materials)
 Cu_spot = 150;             % Max current per spot for electrode material
                            % For Copper this value is +/- 70A
 ts_spot = 60e-6;           % Time for the ion charge state distribution to
```

```
                          % reach steady state for the specific electrode
                          % material. For copper this value is +/- 10e-6s

R0_per_spot = 0.0035;      % Initial radius of the plasma flow at the mixing
                          % region THIS IS THE MOST UNCERTAIN VALUE AND
                          % WAS USED TO FIT DATA

F_n_0 = zeros(mass_no,1);% Create array for the initial distribution
F_n_0(1,1) = 0.107;       % of the ion charge states in the plasm mixing
F_n_0(2,1) = 0.721;       % region
F_n_0(3,1) = 0.171;
F_n_0(4,1) = 1.4e-4;
F_n_0(5,1) = 0;
Q=1;
Cn = zeros(mass_no,1);
while Q <= mass_no
    Cn(Q,1) = sum(F_n_0(1:Q,1));
    Q = Q+1;
end

% Simulation variables
Subconductor_number = 8; % In the electrode model X is the X by X number
                          % of conductors that the electrode should be
                          % split into
delays = 1e-7;            % Small change in time to work out d/dt in dde23
t_end = 0;                % Computation time at the end of each discharge
xyz = 1;                  % Simulation count variable

% variables to extract data for graphs
v1 = zeros(250,10); v2 = zeros(250,10); v3 = zeros(250,10);
v4 = zeros(250,10); v5 = zeros(250,10); v6 = zeros(250,10);
v7 = zeros(250,10); v8 = zeros(250,10); v9 = zeros(250,10);
v10 = zeros(250,10); v11 = zeros(250,10); v12 = zeros(250,10);
v13 = zeros(250,10); v14 = zeros(250,10); v15 = zeros(250,10);
v16 = zeros(250,10); v17 = zeros(250,10); v18 = zeros(250,10);
v19 = zeros(250,10); v20 = zeros(250,10); v21 = zeros(250,10);
v22 = zeros(250,10); v23 = zeros(250,10); v24 = zeros(250,10);
v25 = zeros(250,10); v26 = zeros(250,10);

Res_flow=1;Q_flow=1; Coll_flow=1;%Sim variables

%% Read in Experimental data

if PPT_Height == 0.01;
    TT = 1.3705e-6;       % Time constants to ensure the first peaks of the
                          % modelled and experimental data allign
    load(['F:\Pete_Backup_all_Mar_2011\PhD\Results\Mlab_2011\AR0.5_' ...
        num2str(V_interest) '.mat']);
elseif PPT_Height == 0.03;
    TT = 2.563e-6;        % Time constants to ensure the first peaks of the
                          % modelled and experimental data allign
    load(['F:\Pete_Backup_all_Mar_2011\PhD\Results\Mlab_2011\AR1.5_' ...
        num2str(V_interest) '.mat']);
elseif PPT_Height == 0.05;
    TT = 2.563e-6;        % Time constants to ensure the first peaks of the
                          % modelled and experimental data allign
    load(['F:\Pete_Backup_all_Mar_2011\PhD\Results\Mlab_2011\AR2.5_' ...
        num2str(V_interest) '.mat']);
```

```
end

PPT_V0 = V_mean_avg;      % Initial discharge voltage of the capacitor discharge
                          % taken from experimental data
t_space = length(Time);   % Total number of data points collected experimentally

%% Differential Equation Solver
%%
%TIME = length(Time)*2e-8;
TIME = 20e-6;

history = [1e-4 0 1e-3 10 0 1e-12]; % Boundary conditions
options = ddeset('Events',@Plasmae_v2,'RelTol',1e-4,'AbsTol',1e-4);
sol = dde23(@Plasma_v2,delays,history,[0 TIME],options);

Mass_Tot = zeros(20,1); %Pre-allocate vectors
aaa = 1;
while sol.x(end) < TIME
    t_end = sol.x(1,end); % Find time of the end of each discharge

    Mass_Tot(aaa) = sol.y(6,end); % Total mass erroded during discharge

    % Reset some boundary condition at new discharge
    sol.y(1,end) = 1e-4;
    sol.y(3,end) = 1e-3;
    sol.y(6,end) = 1e-12;

    sol = dde23(@Plasma_v2,delays,sol,[sol.x(end) TIME],options);
    aaa = aaa + 1;
end

%% Data Processing
%%
t = linspace(0,TIME,t_space-1);     %#ok<NASGU> % Create a time matrix that
                                                % emulates the number of samples
                                                % from the real data
Distance_plasma = deval(sol,t,1);  %#ok<NASGU> % This is the distance that
                                                % the plasma coloumn has travelled
I_int = deval(sol,t,2);             %#ok<NASGU> % This is the Intergral of the
                                                % current waveform
speed = deval(sol,t,3);             %#ok<NASGU> % This is the speed of the plasma
                                                % coloumn accelerated by the
                                                % lorentz force
I = deval(sol,t,4);                 %#ok<NASGU> % This is the current waveform
                                                % of the discharge
Inductance = deval(sol,t,5);        %#ok<NASGU> % This is the total circuit
                                                % inductance
Mass = deval(sol,t,6);              %#ok<NASGU> % This is the mass loss of the
                                                % electrodes
filename = ['PPT_Data_' num2str(V_interest) ...
    '_' num2str(0.03*100) 'cm.mat'];
save(filename)     % Save the modelled data
toc                % The 'toc' function ends the count to find the total
                   % computation time for the program.
end


%% DDE Interupt function
```

```
function [value, isterminal, direction] = Plasmae_v2(t,x,z)
% This function finds the termination point so that the the solver can be
% interupted
value = Plasma_v2(t,x,z);
isterminal = [0 1 0 0 0 0];
direction = zeros(6,1);
end


%% Plot graphs of interelectrode gap
function graph_data(xyz,t,sol,x,Vc,Lc,Rc,Lorentz,S0)

global Res_flow; global Q_flow;
global Coll_flow; global con_s;
global rmin; global PPT_Height

global v1; global v2; global v3;
global v4; global v5; global v6;
global v7; global v8; global v9;
global v10; global v11; global v12;
global v13; global v14; global v15;
global v16; global v17; global v18;
global v19; global v20; global v21;
global v22; global v23; global v24;
global v25; global v26;

extent = sol.x(1,end);
r = linspace(rmin,extent,250);
v1(:,xyz) = deval(sol,r,1)';%#ok<NASGU>
v2(:,xyz) = deval(sol,r,2)';%#ok<NASGU>
v3(:,xyz) = deval(sol,r,3)';%#ok<NASGU>
v4(:,xyz) = deval(sol,r,4)';%#ok<NASGU>
v5(:,xyz) = deval(sol,r,5)';%#ok<NASGU>
v6(:,xyz) = deval(sol,r,6)';%#ok<NASGU>
v7(:,xyz) = deval(sol,r,7)';%#ok<NASGU>
v8(:,xyz) = deval(sol,r,8)';%#ok<NASGU>
v9(:,xyz) = deval(sol,r,9)';%#ok<NASGU>
v10(:,xyz) = deval(sol,r,10)';%#ok<NASGU>
v11(:,xyz) = Vc;%#ok<NASGU>
v12(:,xyz) = Lc;%#ok<NASGU>
v13(:,xyz) = Rc;%#ok<NASGU>
v14(:,xyz) = x(1);%#ok<NASGU>
v15(:,xyz) = x(2);%#ok<NASGU>
v16(:,xyz) = x(3);%#ok<NASGU>
v17(:,xyz) = x(4);%#ok<NASGU>
v18(:,xyz) = x(5);%#ok<NASGU>
v19(:,xyz) = x(6);%#ok<NASGU>
v20(:,xyz) = t;%#ok<NASGU>
v21(:,xyz) = Lorentz;%#ok<NASGU>
v22(:,xyz) = S0;%#ok<NASGU>

% Extract Resistivity
space = (PPT_Height)/length(Res_flow);
dist = space:space:PPT_Height;

A = [dist' Res_flow'];
A = sortrows(A); B1 = smooth(A(:,1),3); B2 = smooth(A(:,2),3);
A = [B1 B2]; P = polyfit(B1,B2,20);
```

```
Res_flow2 = polyval(P,r);
v23(:,xyz) = Res_flow2';%#ok<NASGU>

% Extract Mean ion charge state
space = (PPT_Height)/length(Q_flow);
dist = space:space:PPT_Height;

A = [dist' Q_flow'];
A = sortrows(A); B1 = smooth(A(:,1),3); B2 = smooth(A(:,2),3);
A = [B1 B2]; P = polyfit(B1,B2,20);
Q_flow3 = polyval(P,r);
v24(:,xyz) = Q_flow3';%#ok<NASGU>

% Extract Collisional frequency
space = (PPT_Height)/length(Coll_flow);
dist = space:space:PPT_Height;

A = [dist' Coll_flow'];
A = sortrows(A); B1 = smooth(A(:,1),3); B2 = smooth(A(:,2),3);
A = [B1 B2]; P = polyfit(B1,B2,20);
Coll_flow2 = polyval(P,r);
v25(:,xyz) = Coll_flow2';%#ok<NASGU>

% Extract Conductivity
space = (PPT_Height)/length(con_s);
dist = space:space:PPT_Height;

A = [dist' con_s'];
A = sortrows(A); B1 = smooth(A(:,1),3); B2 = smooth(A(:,2),3);
A = [B1 B2]; P = polyfit(B1,B2,20);
con_s2 = polyval(P,r);
v26(:,xyz) = con_s2';%#ok<NASGU>

v1(isnan(v1)) = 0; %#ok<NASGU>
v2(isnan(v2)) = 0; %#ok<NASGU>
v3(isnan(v3)) = 0; %#ok<NASGU>
v4(isnan(v4)) = 0; %#ok<NASGU>
v5(isnan(v5)) = 0; %#ok<NASGU>
v6(isnan(v6)) = 0; %#ok<NASGU>
v7(isnan(v7)) = 0; %#ok<NASGU>
v8(isnan(v8)) = 0; %#ok<NASGU>
v9(isnan(v9)) = 0; %#ok<NASGU>
v10(isnan(v10)) = 0; %#ok<NASGU>
v11(isnan(v11)) = 0; %#ok<NASGU>
v12(isnan(v12)) = 0; %#ok<NASGU>
v13(isnan(v13)) = 0; %#ok<NASGU>
v14(isnan(v14)) = 0; %#ok<NASGU>
v15(isnan(v15)) = 0; %#ok<NASGU>
v16(isnan(v16)) = 0; %#ok<NASGU>
v17(isnan(v17)) = 0; %#ok<NASGU>
v18(isnan(v18)) = 0; %#ok<NASGU>
v19(isnan(v19)) = 0; %#ok<NASGU>
v20(isnan(v20)) = 0; %#ok<NASGU>
v21(isnan(v21)) = 0; %#ok<NASGU>
v22(isnan(v22)) = 0; %#ok<NASGU>
v23(isnan(v23)) = 0; %#ok<NASGU>
v24(isnan(v24)) = 0; %#ok<NASGU>
v25(isnan(v25)) = 0; %#ok<NASGU>
```

```
v26(isnan(v25)) = 0; %#ok<NASGU>

end


%% LCR solver
%%
function dx = Plasma_v2(t,x,z)
t
% Read in global variables
global PPT_V0
global PPT_C
global delays
global PPT_Height
global PPT_Thickness
global PPT_I_r
global L_Cap
global R_Cap
global t_end
global xyz

% Constants
M_perm = 4e-7*pi();         % Magnetic Permeability of free space
e0 = 8.85418782e-12;        % Permitivity of free space
e = 1.60217646e-19;         % Fundamental charge

dx = zeros(6,1); %Pre-allocate vectors
ylag1 = z(:,1);  %Contains the data for the lag function

%% Calculate Current Voltage
%%
Vc = PPT_V0 - (1/PPT_C)*x(2);

%% Calculate Electrode Variables
%%
Choice = 1; % 0 = Absolute value using electrode model
            % 1 = Polynominal fit of electrodes used in Thesis

[L_electrode R_electrode] = Electrode(Choice,abs(x(1)),Vc);

%% Calculate Plasma Variables
%%
[R_plasma R_anode Ni_anode sol S0] = Krinberg_2011(t,t_end,abs(x(4))); %#ok<NASGU>

%% Calculate Anode Sheath Variables
%%
if Ni_anode <= 1e17;
    Ni_anode = 1e17;
end

V_sheath = abs(Vc/2);
d_sheath = ((2*V_sheath*e0)/(e*Ni_anode))^0.5;
I_sheath = pi()*(R_anode^2)*2.33e-6*((V_sheath^1.5)/(d_sheath^2));
R_sheath = (V_sheath)/I_sheath;
if R_sheath >= 1;
    R_sheath = 1;
end
```

```
%% Calculate Circuit Inductance and Resistance
%%
Lc = L_Cap + L_electrode;    % L_plasma = 0 due to magnetic flux
                             % through a closed surface (which plasma is)
Rc = R_Cap + R_plasma + R_electrode + R_sheath;

if abs(x(4)) < 100 % For graph purposes to remove model spikes
    Rcp= R_Cap + R_electrode + R_sheath;
else
    Rcp = Rc;
end
%% Calculate Lorentz Force
%%
Lorentz = (((M_perm*(x(4)^2))/(2*pi()))* ...
    log(2*PPT_Height/(PPT_Height + (PPT_Thickness/2))));

%% Differential equations
%%
dx(1) = x(3);                        % Rate of change of the distance
                                     % travelled by the plasma coloumn
dx(2) = x(4);                        % Rate of change of the intergral
                                     % of the current waveform

% Assumes magnetic field based on the geometery of two electrodes
% that are cylindrical and the the plasma forms a distance PPT_Thickness/2
% away from centre of magnetic field
dx(3) =(Lorentz - (x(3)*abs(x(4))*PPT_I_r))/(x(6)); % The Rate of change
                                          % in the speed of the moving
                                          % plasma coloumn
dx(4) = (Vc - x(4)*dx(5) - (x(4)*Rc))/(Lc); % Rate of change of
                                             % the current waveform
dx(5) = (Lc - ylag1(5,1))/delays; % Rate of change in the total
                                   % inductance of the circuit
dx(6) = abs(x(4))*PPT_I_r;           % Rate of mass loss of the electrodes

graph_data(xyz,t,sol,x,Vc,Lc,Rcp,Lorentz,S0);
xyz = xyz + 1;
end


%% Electrode Model
function [L_electrode R_electrode] = Electrode(Choice,Distance,voltage)
global PPT_Thickness
global PPT_Height
global PPT_Width
global Subconductor_number
global freq_discharge
global Elec_Conductivity

% The model assumes that the distance travelled by the coloumn is the same
% on both the anode and the cathode. If this is not the case than this can
% be taken into account here by altering L_A and L_B.
L_A = Distance;
L_B = L_A;

if Choice == 0 % Absolute value using electrode model
    [R_post_1 R_post_2 L_post_1 L_post_2] = ...
        Electrode_double(Subconductor_number,PPT_Thickness,PPT_Width, ...
```

```
        PPT_Height,L_A,L_B,freq_discharge , voltage , Elec_Conductivity);

elseif Choice == 1 % Polynominal fit of electrodes used in Thesis
    if PPT_Height == 0.01
        L_R_data = [0,0,0;
            0.001,2.6100e-011,2.8892e-007;
            0.002,9.5323e-011,9.7633e-007;
            0.003,2.0034e-010,2.1319e-006;
            0.004,3.3487e-010,3.7388e-006;
            0.005,4.9414e-010,5.7481e-006;
            0.006,6.7437e-010,8.1113e-006;
            0.007,8.7249e-010,1.0786e-005;
            0.008,1.0860e-009,1.3737e-005;
            0.009,1.3127e-009,1.6931e-005;
            0.01,1.5510e-009,2.0343e-005;
            0.02,4.3270e-009,6.2354e-005;
            0.03,7.4430e-009,1.1170e-004;
            0.04,1.0686e-008,1.6400e-004;
            0.05,1.3986e-008,2.1771e-004;
            0.06,1.7316e-008,2.7218e-004;];
    elseif PPT_Height == 0.03
        L_R_data = [0,0,0;
            0.001,3.0973e-011,2.7955e-007;
            0.002,1.1501e-010,9.1619e-007;
            0.003,2.4486e-010,1.9577e-006;
            0.004,4.1426e-010,1.9577e-006;
            0.005,6.1835e-010,4.1426e-006;
            0.006,8.5326e-010,7.1388e-006;
            0.007,1.1157e-009,9.3935e-006;
            0.008,1.4030e-009,1.1850e-005;
            0.009,1.7127e-009,1.4481e-005;
            0.01,2.0429e-009,1.7263e-005;
            0.02,6.1552e-009,5.0421e-005;
            0.03,1.1154e-008,8.8603e-005;
            0.04,1.6605e-008,1.2902e-004;
            0.05,2.2307e-008,1.7063e-004;
            0.06,2.8162e-008,2.1294e-004;];
    elseif PPT_Height == 0.05
        L_R_data = [0,0,0;
            0.001,3.2612e-011,2.7885e-007;
            0.002,1.2158e-010,9.1131e-007;
            0.003,2.5966e-010,1.9435e-006;
            0.004,4.4056e-010,3.3465e-006;
            0.005,6.5945e-010,5.0679e-006;
            0.006,9.1241e-010,7.0588e-006;
            0.007,1.1962e-009,9.2779e-006;
            0.008,1.5080e-009,1.1692e-005;
            0.009,1.8455e-009,1.4273e-005;
            0.01,2.2065e-009,1.6998e-005;
            0.02,6.7931e-009,4.9211e-005;
            0.03,1.2530e-008,8.5898e-005;
            0.04,1.8926e-008,1.2447e-004;
            0.05,2.5729e-008,1.6404e-004;
            0.06,3.2800e-008,2.0420e-004;];
    end
    P = polyfit(L_R_data(:,1),L_R_data(:,2),3);
    L_post_1 = polyval(P,L_A);
    L_post_2 = polyval(P,L_B);
```

```
    P = polyfit(L_R_data(:,1),L_R_data(:,3),3);
    R_post_1 = polyval(P,L_A);
    R_post_2 = polyval(P,L_B);
end

R_electrode = R_post_1 + R_post_2; % Combined resistance of each
                                   % electrode
L_electrode = L_post_1 + L_post_2; % Combined inductance of each
                                   % electrode

% Filters Inf and NaN results for data
L_electrode(isnan(L_electrode)) = 0;
L_electrode(L_electrode == abs(Inf)) = 0;
R_electrode(isnan(R_electrode)) = 0;
R_electrode(R_electrode == abs(Inf)) = 0;
end


%% Calculate Resistance and Inductance from a double set of rectangular
%% electrodes
function [R_post_1 R_post_2 L_post_1 L_post_2] = ...
    Electrode_double(Nw,T,W,H,L_A,L_B,frequency,V_Drop,Elec_Conductivity)

% Create a geometrix xatrix of the subconductors
[Distance_x_y Distance_x_y_plot Dij_mn_y Dij_mn_x] = ...
    Geo_matrix(Nw,T,W,H); %#ok<NASGU>

% Calculates the mutual inductances between the electrodes
[R_post_1 R_post_2 L_post_1 L_post_2 I_Subconductor] = ...
    Mutual_Inductance(Distance_x_y,frequency,V_Drop, ...
    Elec_Conductivity,L_A,L_B); %#ok<NASGU>
end


%% Find Inductance of the electrode system
function [R_post_1 R_post_2 L_post_1 L_post_2 I_Subconductor] = ...
    Mutual_Inductance(Distance_x_y,frequency,V_Drop, ...
    Elec_Conductivity,L_A,L_B)
%% Introduction
%%
% This function works out the resistance, self inductance and mutual
% inductance of two rectangular shapes in close proximity to each other by
% splitting it into a matrix of 'subconductors'. This work is based on the
% paper A. W. Bar, 'Calculation of Frequency-Dependant Impedance for
% Conductors of Rectangular Cross Section', AMP Journal of Technology
% Vol. 1 November, 1991.

% This model is true if the hypotenuse of Subconducter with width and
% thickness is smaller than the seperation distance of the electrodes.
%%

% ANGULAR FREQUENCY
omega = 2*pi()*frequency; %#ok<NASGU> %Converting to Angular frequency

% Thickness of Subconductors
t_A = Distance_x_y(2,1,1) - Distance_x_y(1,1,1);
t_B = t_A;
```

```
% Width of Subconductors
w_A = Distance_x_y(1,2,1) - Distance_x_y(1,1,1);
w_B = w_A;

%% Resistance Subconductor
R_Asub = L_A/(w_A*t_A*Elec_Conductivity);
R_Bsub = L_B/(w_B*t_B*Elec_Conductivity);

%% Self Inductance of Subconductor
L_Asub = (0.2*L_A*(0.5  +  log((2*L_A)/(w_A + t_A))  +  ...
    0.2235*((w_A + t_A)/L_A)))*1e-6;
L_Bsub = (0.2*L_B*(0.5  +  log((2*L_B)/(w_B + t_B))  +  ...
    0.2235*((w_B + t_B)/L_B)))*1e-6;

[Nt Nw N] = size(Distance_x_y);

%% Mutual Inductance between elements of conductor
L_MUTUAL_ij_mn = zeros(Nt,Nw,N);

m = 1;
while m <= N
    a = 1;
    while a <= Nw
        b = 1;
        while b <= Nt
            d = Distance_x_y(b,a,m);
            if m <= N/2
                L = L_A;
            else
                L = L_B;
            end
            L_MUTUAL_ij_mn(b,a,m) = (0.2*L*1e-6*(log(L/d + ...
                sqrt(1+(L^2/d^2))) - sqrt(1+(d^2/L^2)) + d/L));
            b = b + 1;
        end
        a = a + 1;
    end
    m = m + 1;
end
L_MUTUAL_ij_mn(L_MUTUAL_ij_mn==Inf) = 0;

%% Create subroutine so right M Inductance is picked from database
% times by omega complex function
L_MUTUAL_ij_mn = L_MUTUAL_ij_mn.*i.*omega;

m=1;
while m <= N
    if m <= N/2
        [a,b] = find(L_MUTUAL_ij_mn(:,:,m)==0);
        L_MUTUAL_ij_mn(a,b,m)= R_Asub + L_Asub.*i.*omega;
    else
        [a,b] = find(L_MUTUAL_ij_mn(:,:,m)==0);
        L_MUTUAL_ij_mn(a,b,m)= R_Bsub + L_Bsub.*i.*omega;
    end
    m=m+1;
end
```

```
%% Manipulate for first part of Matrix equation

m=1;
while m <= N
    b = 1;
    c = 1;
    while b <= Nt
        a = 1;
        while a <= Nw
                L_MUTUAL_A_ij_mn(1,c,m) = ...
                    L_MUTUAL_ij_mn(b,a,m); %#ok<AGROW>
            a=a+1;
            c = c + 1;
        end
        b=b+1;
    end
    m = m + 1;
end
L_MUTUAL_ij_mn = L_MUTUAL_A_ij_mn;

c=1;
MUTUAL_MATRIX_PART_ONE = zeros(N/2,N/2);
MUTUAL_MATRIX_PART_TWO = zeros(N/2,N/2);
while c <= N/2
    m = 1;
    while m <= N/2
        b = 1;
        while b <= N/2
            MUTUAL_MATRIX_PART_ONE_a(b,m) = ...
                L_MUTUAL_ij_mn(1,1+(c-1),m) - ...
                L_MUTUAL_ij_mn(1,(N/2+1)+(b-1),m); %#ok<AGROW>
            if m==1
                MUTUAL_MATRIX_PART_TWO_a(b,m) = ...
                    L_MUTUAL_ij_mn(1,(N/2+1)+(b-1),(N/2+1)+(m-1)) - ...
                    L_MUTUAL_ij_mn(1,1+(c-1),(N/2+1)+(m-1)); %#ok<AGROW>
            else
                MUTUAL_MATRIX_PART_TWO_a(b,m) = ...
                    L_MUTUAL_ij_mn(1,(N/2+1)+(b-1),(N/2+1)+(m-1)) - ...
                    L_MUTUAL_ij_mn(1,1+(c-1),(N/2+1)+(m-1)); %#ok<AGROW>
            end
            b = b + 1;
        end
        m = m + 1;
    end
    MUTUAL_MATRIX_PART_ONE = [MUTUAL_MATRIX_PART_ONE; ...
        MUTUAL_MATRIX_PART_ONE_a]; %#ok<AGROW>
    MUTUAL_MATRIX_PART_TWO = [MUTUAL_MATRIX_PART_TWO; ...
        MUTUAL_MATRIX_PART_TWO_a]; %#ok<AGROW>
    c = c + 1;
end
MUTUAL_MATRIX_PART_ONE(1:(Nt/2*Nw),:) = [];
MUTUAL_MATRIX_PART_TWO(1:(Nt/2*Nw),:) = [];

%% Add in boundary conditions...
[X Y] = size(MUTUAL_MATRIX_PART_ONE); %#ok<NASGU>
MUTUAL_MATRIX_PART_ONE = [MUTUAL_MATRIX_PART_ONE; ones(1,Y)];

[X Y] = size(MUTUAL_MATRIX_PART_TWO); %#ok<NASGU>
```

```
MUTUAL_MATRIX_PART_TWO = [MUTUAL_MATRIX_PART_TWO; ones(1,Y)*-1];

MUTUAL_MATRIX = [MUTUAL_MATRIX_PART_ONE MUTUAL_MATRIX_PART_TWO];
 [X Y] = size(MUTUAL_MATRIX); %#ok<NASGU>

 V_Drop = ones((X-1),1).*V_Drop;
 V_Drop1 = [V_Drop; 0];
%% Current in Subconductor
 I_Subconductor = MUTUAL_MATRIX\V_Drop1;

%% Extract values for Post
 Impedance_Post = mean(V_Drop)/(sum(I_Subconductor(1:N/2)));
 Impedance_Post2 = mean(V_Drop)/(sum(I_Subconductor(N/2+1:N)));
 R_post_1 = real(Impedance_Post);
 L_post_1 = imag(Impedance_Post)/omega;
 R_post_2 = real(Impedance_Post2);
 L_post_2 = imag(Impedance_Post2)/omega;

 end


%% Make a Matrix for the program
 function [Distance_x_y Distance_x_y_plot Dij_mn_y Dij_mn_x] = ...
      Geo_matrix(Nw,T,W,H)

%% For simplicity the electrodes are kept to be the same dimensions
% Electrode Width
W_A = W;
W_B = W;

% Electrode Thickness
T_A = T;
T_B = T;

%% SUBCONDUCTORS
% For each electrode the number of subconductors is kept equal
N_Aw = Nw;
N_Bw = Nw;

N_At = Nw; %Number of subconductors in the 'Thickness' axis
N_Bt = Nw;

% Subconductor dimensions
w_A = W_A/N_Aw;
t_A = T_A/N_At;

% Subconductor dimensions
w_B = W_B/N_Bw; %#ok<NASGU>
t_B = T_B/N_Bt; %#ok<NASGU>

%% Model cross sectional view of both conductors using a simple matrix
% Calculate
%       ---Nw---
%       %%%%%%|
%       %%%%%%Nt   --- A
%       %%%%%%|
%
%        000000|
```

```
%      000000|
%      000000|
%      000000 Distance between electrodes
%      000000|
%      000000|
%
%      %%%%%%
%      %%%%%%    -- B
%      %%%%%%

% Calculate location of centre of each subconductor

% Create the y position distances
a = 1;
while a <= (N_At + N_Bt + round(H/t_A))
    Dij_mn_y(a) = 0.5*t_A + (a-1)*t_A; %#ok<AGROW>
    a = a + 1;
end

% Create the x position distances
a=1;
while a <= N_Aw
    Dij_mn_x(a) = 0.5*w_A + (a-1)*w_A; %#ok<AGROW>
    a = a + 1;
end

% Create an array that numbers each subconductor
% in both electrodes
a=1;
Subconductor_number=1;
while a <= N_At + N_Bt + round(H/t_A)
    b=1;
    while b <= N_Aw
        Subconductor_number_position(a,b) = ...
            Subconductor_number; %#ok<AGROW>
        Subconductor_number = Subconductor_number+1;
        b=b+1;
    end
    a=a+1;
end

% Create a routine to measure the distance from Dij to Dmn
m = 1;
N = N_Aw*(N_At + N_Bt + round(H/t_A));
%Distance_x_y = zeros(N_At + N_Bt + abs(H/t_A),N_Aw,N);
while m <= N
    [c,v] = find(Subconductor_number_position==m);
        a = 1;
        while a <= N_Aw
            b = 1;
            while b <= N_At + N_Bt + round(H/t_A)
                Distance_x = Dij_mn_x(v) - Dij_mn_x(a);
                Distance_y = Dij_mn_y(c) - Dij_mn_y(b);
                Distance_x_y(b,a,m) = ...
                    sqrt(Distance_x^2 + Distance_y^2); %#ok<AGROW>
                b = b + 1;
            end
            a = a + 1;
```

```
        end
    m = m + 1;
end

%% Cut out data of points between the electrodes
x1 = N - N_Aw*(N_Bt + round(H/t_A));
x2 = N - N_Aw*N_Bt;

Distance_x_y_plot = Distance_x_y(:,:,1); % Export uncut version
                                         % for graph plotting
                                         % purposes
Distance_x_y(:,:,(x1+1):x2) = [];
Distance_x_y((N_Bt+1):(N_Bt + round(H/t_A)),:,:) = [];
end


%% Plasma flow model
%% Introduction
%%
% This function works out the conditions of the plasma between the electrodes.
% Steady state assumptions have been made and it is assumed that the plasma
% flow variables are a function of the current flowing through the plasma.

% Only the boundary condition of the suface area of the mixing region has
% a time dependancy. As such this model is valid for short duration pulses
% where the pulse discharge time is greater than the time it takes for an ion
% to cross the interlectrode gap but is smaller than the time it takes the
% the newly formed plasma to reach it's steady state ion charge state
% distribution. This model is invalid if this inequality is not kept too.

% This model is based on the work of Igor Krinberg and Andre Anders.

% Any discharge below 100Hz will be considered as no frequency

function [R_plasma R_anode Ni_anode sol S0] = Krinberg_2011(t,t_end,I)
global sss
global r_s
global con_s
global Q_flow
global Cu_spot
global R0_per_spot
global ts_spot
global M0
global Z0
global Tem
global PPT_m_i
global PPT_i_e
global PPT_I_r
global PPT_Height
global rmin

%New Global Variables
global R0
global Te_spot
global Ne_spot
global Ne
global Current
```

```
% Reset simulation variables
sss = 1;
con_s = 1;
r_s = 1;
Current = I;
Q_flow = 2.06;

% Constants
e = 1.60217646e-19;
kB = 1.3806504e-23;

% Current specific values
Spot_Num = I/(Cu_spot);              % Number of cathode spots present
S0_per_spot = pi()*(R0_per_spot^2); % Surface area for single spot at
                                     % mixing region
S0 = S0_per_spot*Spot_Num*(1+(t-t_end)/ts_spot); % Surface area for all
                                                  % spots at mixing region

R0 = (S0/pi())^0.5;                  % Initial radius of flow at mixing
                                     % region

V_spot = M0*(5*Z0*kB*Tem/(3*PPT_m_i))^0.5; % Axial velocity of ions at
                                           % mixing region
Ne_spot = ((PPT_i_e/Z0)*I)/(e*V_spot*pi()*(R0^2)); % Initial electron
                                                    % number density
Ne = Ne_spot;                        % Electron number density

%% Initial conditions
x_1_init = PPT_I_r*I;   % Initial product of rho*Vz*S
x_2_init = V_spot;      % Initial axial velocity
x_3_init = I;           % Current through flow
x_4_init = S0;          % Initial flow area
x_5_init = 0;           % Initial radial velocity
x_6_init = R0;          % Initial R
x_7_init = 0;           % Spare
x_8_init = Ne_spot;     % Initial Ne
x_9_init = Te_spot;     % Initial Te
x_10_init = 0;          % Initial dTe

%% Differential Equation Solver
%%

history = [x_1_init x_2_init x_3_init x_4_init ...
    x_5_init x_6_init x_7_init x_8_init x_9_init x_10_init];

options = ddeset('RelTol',1e-3,'AbsTol',1e-3);
sol = ode23(@krinsolve,[rmin PPT_Height],history,options);

%% Data Processing
%%
extent = sol.x(1,end);
r = linspace(rmin,extent,250);
v6 = deval(sol,r,6);%#ok<NASGU>
v6(isnan(v6)) = 0; %#ok<NASGU> % Filters NaN results for data
v8 = deval(sol,r,8);%#ok<NASGU>
v8(isnan(v8)) = 0; %#ok<NASGU> % Filters NaN results for data

% Calculate Anode Sheath region properties
```

```
Q_sheath = sortrows(Q_flow);
Q_sheath = smooth(Q_sheath,3);
Ni_anode = v8(end)./Q_sheath(end);
R_anode  = v6(end);

% Calculate Plasma Resistance
A = [r_s' con_s'.^-1];
A = sortrows(A);
B1 = smooth(A(:,1),3);
B2 = smooth(A(:,2),3);
A = [B1 B2];
R_plasma = trapz(A(:,1),A(:,2));

% Filters Inf and NaN results for data
Ni_anode(isnan(Ni_anode)) = 0;
Ni_anode(Ni_anode == abs(Inf)) = 0;
R_anode(isnan(R_anode)) = 0;
R_anode(R_anode == abs(Inf)) = 0;
R_plasma(isnan(R_plasma)) = 0;
R_plasma(R_plasma == abs(Inf)) = 0;

end

%% Main Solver
function dx = krinsolve(r,x,z) %#ok<INUSD>
% Inputs
global PPT_m_i
global mass_no
global E_Q
global Cn
global Current
global B_ext_axial
global Tem
global M0
global freq_discharge
global PPT_i_e
global sss

global Res_flow; global Q_flow; global r_s;
global con_s

dx = zeros(10,1); % Create a zero matrix

M_perm = 4e-7*pi();
e = 1.60217646e-19;
kB = 1.3806504e-23;
me = 9.10938215e-31;

I = Current;

%% Calculate mean ion charge state
Q = 1;
coff_ion = zeros(mass_no,1);
wave_n = zeros(mass_no,1);
while Q <= mass_no
    coff_ion(Q,1) = 1e-20*(((8*x(9)*kB)/(pi()*me))^0.5)* ...
        ((13.6*e/E_Q(Q,1))^2)*exp((-E_Q(Q,1))/(x(9)*kB));
   Q=Q+1;
```

```
end

[a,b] = find(coff_ion(:,:)==0);
coff_ion(a,b)=1e-50;
wave_n(:,1) = x(2)./(coff_ion(:,1).*x(8));

Q = 1;
F_n = zeros(mass_no,1);
F_n_Q = zeros(mass_no,1);
while Q <= mass_no - 1;
    if Q==1
        F_n(Q,1) = Cn(Q,1)*exp((-r)/wave_n(Q+1,1));
    else
        F_n(Q,1) = Cn(Q,1)*exp((-r)/wave_n(Q+1,1)) - ...
            Cn(Q-1,1)*exp((-r)/wave_n(Q,1));
    end
    F_n_Q(Q,1) = Q*F_n(Q,1);
    Q=Q+1;
end

mean_Q_r = abs(sum(F_n_Q));

%% Limiting Conductivity by limiting the electron temperature
Ve_coff = (1 + 1/PPT_i_e);
Ne = x(8);

%% Calculate conductivity
% This assumes that the self magnetic field of the pinch sheilds the
% plasma from outside disturbances and so conductivity is a measure of
% the current flowing through the internal plasma unaffected by the PPT
% magnetic field

Tcr = (Tem*75*M0^2*2.06)/(192*mean_Q_r);
if x(9) >= Tcr
    [con_tensor coll_freq_ie_ei Q_ion] = ...
        cond_ten(Tcr,Ne,mean_Q_r,F_n,E_Q,coff_ion,freq_discharge,sss);
else
    Te = x(9);
    [con_tensor coll_freq_ie_ei Q_ion] = ...
        cond_ten(Te,Ne,mean_Q_r,F_n,E_Q,coff_ion,freq_discharge,sss);
end

% Conductivity between electrodes 1 = Ex, 2 = Ey(Hall), 3 = Ez(in line with
% B field and is E_parallel)
conductivity = con_tensor*[1;0;0];
conductivity = abs(conductivity(1));

%% Differential equations
%%
% MUST REMAIN IN THIS ORDER!!!!
dx(1) = 0;                     % Change in the product rho*Vz*S along the axis
dx(3) = 0;                     % Change in the current along the axis
dx(4) = 2*pi()*x(6)*x(5)/x(2); % Change of the flow area along the axis
dx(2) = ( - kB*(x(8)*x(9)*dx(4) + x(4)*x(9)*((PPT_i_e/(e*x(2)*x(4)))*dx(3) ...
    - (x(8)/x(4))*dx(4) - (x(8)/x(2))*dx(2)) ...
    + x(4)*x(8)*dx(9)) )/x(1); % Change in the axial velocity along the axis
dx(8) = ((PPT_i_e/(e*x(2)*x(4)))*dx(3) ...
    - (x(8)/x(4))*dx(4) - (x(8)/x(2))*dx(2)); % Change in the electron number
```

```
                                              % density along the axis
dx(9) = ((I^2/(conductivity*Ve_coff*(x(4)^2))) ...
    - (Q_ion/Ve_coff) - 1.5*kB*x(2)*x(9)*dx(8) ...
    - 2.5*kB*x(9)*x(8)*((x(2)/x(4))*dx(4) ...
    + dx(2))  )/(1.5*x(2)*kB*x(8)); % Change in the electron temperature along
                                   % the axis
dx(5) = ((  (3*kB*x(8)*x(9)*x(4)/x(6)) - ((M_perm*I^2)/(2*pi()*(x(6)))) ...
    - ((e*(B_ext_axial^2)*x(5))/(coll_freq_ie_ei*me*x(2)))*(I + ...
    (e*mean_Q_r*x(1))/PPT_m_i))/x(1)); % Change in the radial velocity along
                                      % the axis
dx(6) = x(5)/x(2); % Change of the radius of the plasma flow along the axis

Q_flow(sss) = mean_Q_r;
con_s(sss) = conductivity;
Res_flow(sss) = conductivity^-1;
r_s(sss) = r;
sss = sss + 1;
end
%% Conductivity tensor
function [con_tensor coll_freq_ie_ei_e Q_ion] = ...
    cond_ten(Te,Ne,mean_Q_r,F_n,E_Q,coff_ion,freq_discharge,sss)

global B_ext_across; global PPT_m_i; global mass_no
global Coll_flow

% Constants
e = 1.60217646e-19;
me = 9.10938215e-31;
e0 = 8.85418782e-12;

% Change frequency to angular frequency
freq_discharge_omega = 2*pi()*freq_discharge;

%% Calculate Conductivity Tensor for electrons

% For Electrons
% Ion - electron Collision frequency
log_coul = 23 - log(Ne^0.5 * mean_Q_r * Te^-1.5); %NRL Data sheet
coll_freq_ie_ei_e = abs(log_coul*3.62e-6*(Ne/mean_Q_r)*Te^-1.5);

plasma_freq_e = ((Ne*e^2)/(me*e0))^0.5;
gyro_freq_e = -e*B_ext_across/me;

if coll_freq_ie_ei_e <= abs(gyro_freq_e)
    coll_freq_ie_ei_e = abs(gyro_freq_e);
end

col_mod_e = (coll_freq_ie_ei_e - i*freq_discharge_omega);

con_perp_e_contrib = (plasma_freq_e^2)*col_mod_e/(col_mod_e^2 ...
    + gyro_freq_e^2);
con_hall_e_contrib = (plasma_freq_e^2)*gyro_freq_e/(col_mod_e^2 ...
    + gyro_freq_e^2);
con_parallel_e_contrib = (plasma_freq_e^2)/col_mod_e;

%% Calculate Conductivity Tensor for ions

% Ion - electron Collision frequency
```

```
log_coul = 23 - log(Ne^0.5 * mean_Q_r * Te^-1.5); %NRL Data sheet
coll_freq_ie_ei_i = abs(log_coul*3.62e-6*(Ne/mean_Q_r)*Te^-1.5);

Ni_tot = Ne/mean_Q_r;
Q = 1;
N_n = zeros(mass_no,1);
Q_ion = zeros(mass_no,1);
while Q <= mass_no - 1;
    N_n(Q,1) = Ni_tot*F_n(Q,1);
    Q_ion(Q,1) = Ne*N_n(Q,1)*F_n(Q,1)*E_Q(Q+1,1)*coff_ion(Q+1,1);
    plasma_freq_i = ((N_n(Q,1)*Q^2*e^2)/(PPT_m_i*e0))^0.5;
    gyro_freq_i = Q*e*B_ext_across/PPT_m_i;

    if coll_freq_ie_ei_i <= gyro_freq_i
        coll_freq_ie_ei_i = gyro_freq_i;
    end

    col_mod_i = (coll_freq_ie_ei_i - i*freq_discharge_omega);

    con_perp_i_contrib = (plasma_freq_i^2)*col_mod_i/(col_mod_i^2 ...
        + gyro_freq_i^2);
    con_hall_i_contrib = (plasma_freq_i^2)*gyro_freq_i/(col_mod_i^2 ...
        + gyro_freq_i^2);
    con_parallel_i_contrib = (plasma_freq_i^2)/col_mod_i;

    Q=Q+1;
end

con_perp     = e0*(con_perp_e_contrib + sum(con_perp_i_contrib));
con_hall     = e0*(con_hall_e_contrib - sum(con_hall_i_contrib));
con_parallel = e0*(con_parallel_e_contrib + sum(con_parallel_i_contrib));

con_tensor = [con_perp -con_hall 0; con_hall con_perp 0; 0 0 con_parallel];

Coll_flow(sss) = coll_freq_ie_ei_i;
Q_ion = sum(Q_ion);
end
```

Appendix B

Data Sets

B.1 Discharge Initiation Experiments

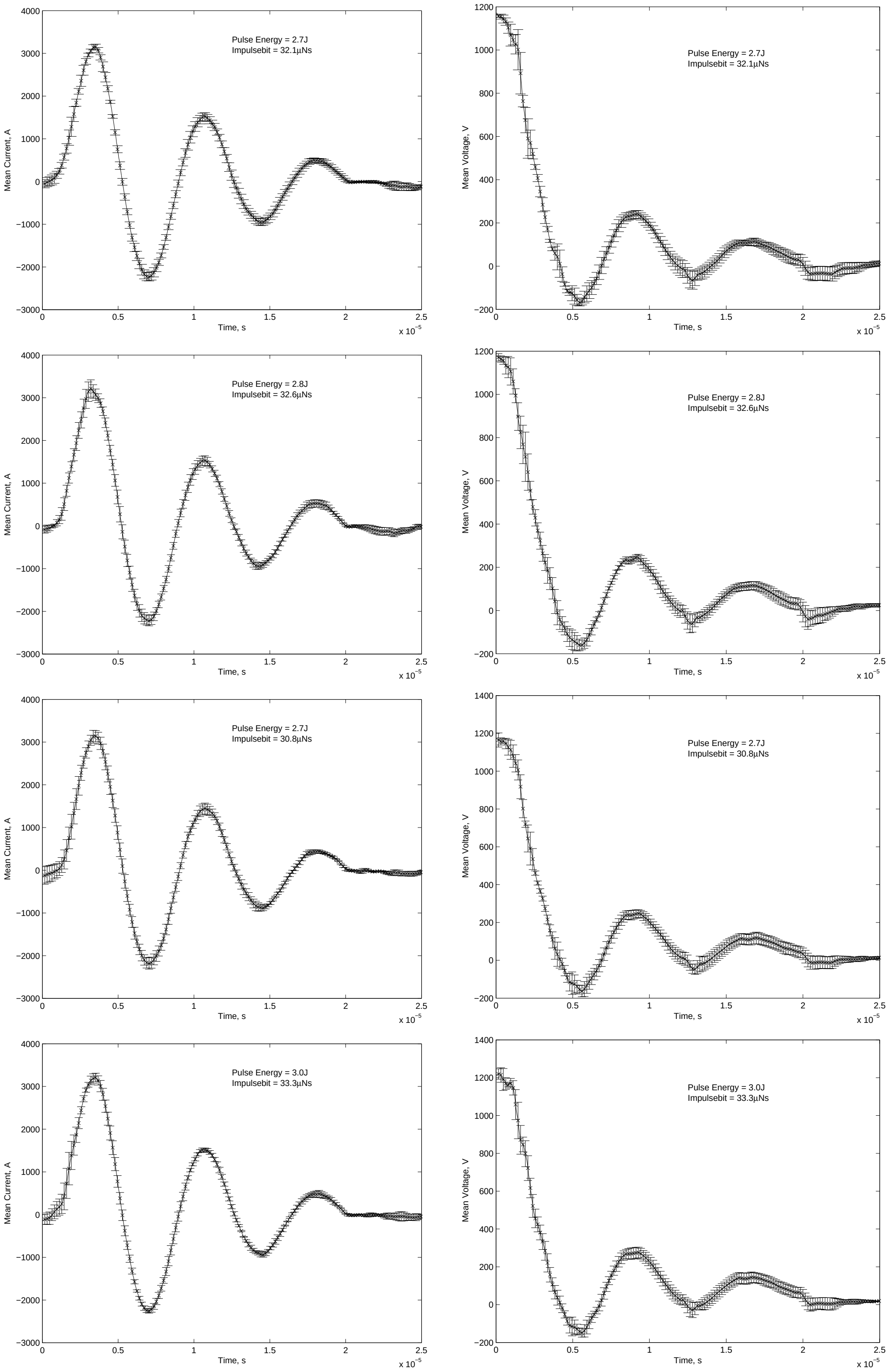

Figure B.1: Profiles 1-4: Standard configuration, Teflon^{TM} width = 3mm. 1: Sparkplug initiated at 15kV, 2: Sparkplug initiated at 20kV, 3: Sparkplug initiated at 25kV, 4: Sparkplug initiated at 30kV

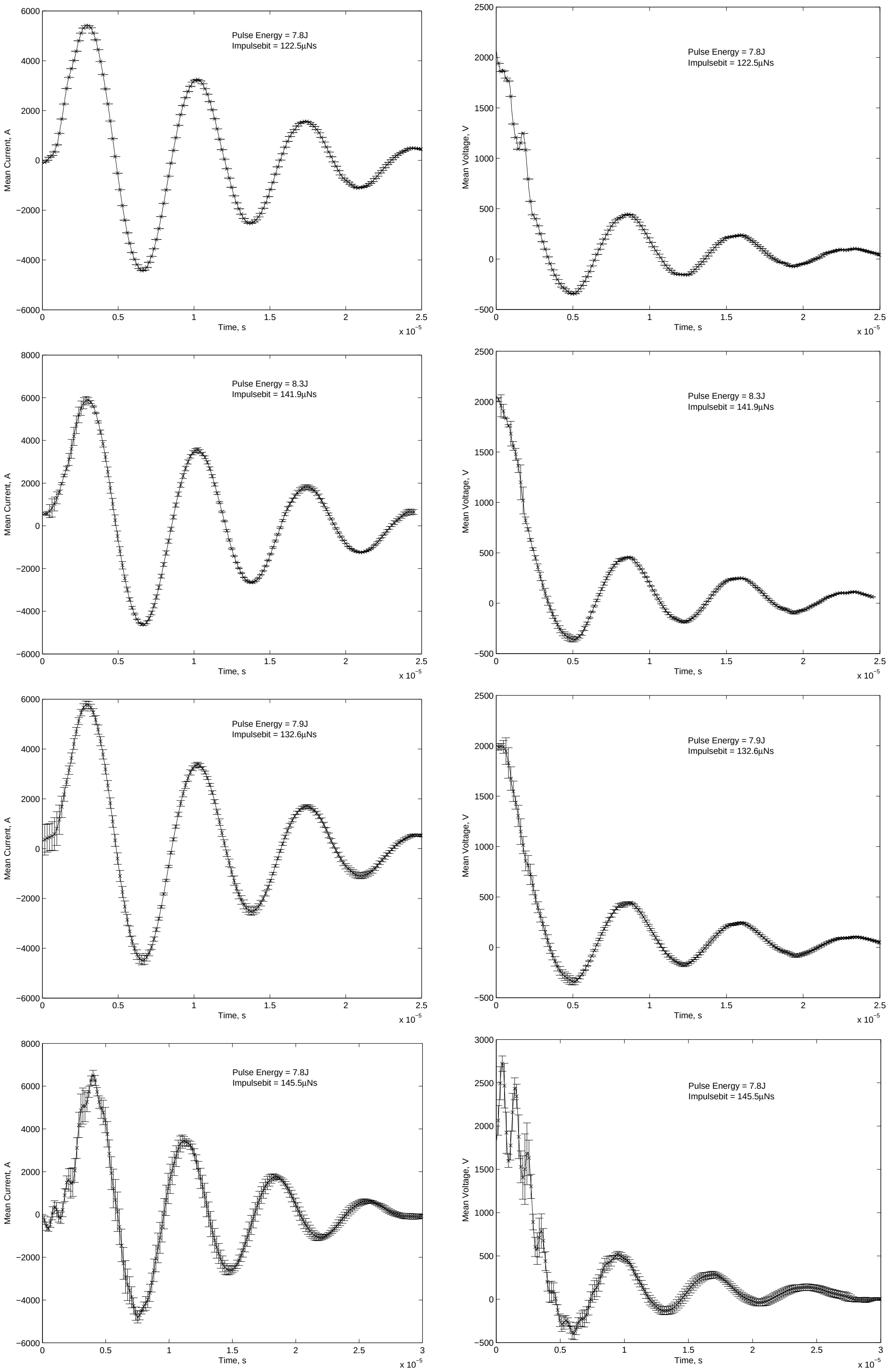

Figure B.2: Profiles 1-4: Standard configuration, no Teflon^{TM}. 1: Two 10nF capacitors placed in parallel with the sparkplug, 2: Sparkplug initiated at 15kV with 100M resistor in series, 3: Sparkplug with no capacitor in parallel with the sparkplug, 4: DI changed to a single tungsten filament with no capacitor in parallel with it

B.2 Mass Errosion Experiments

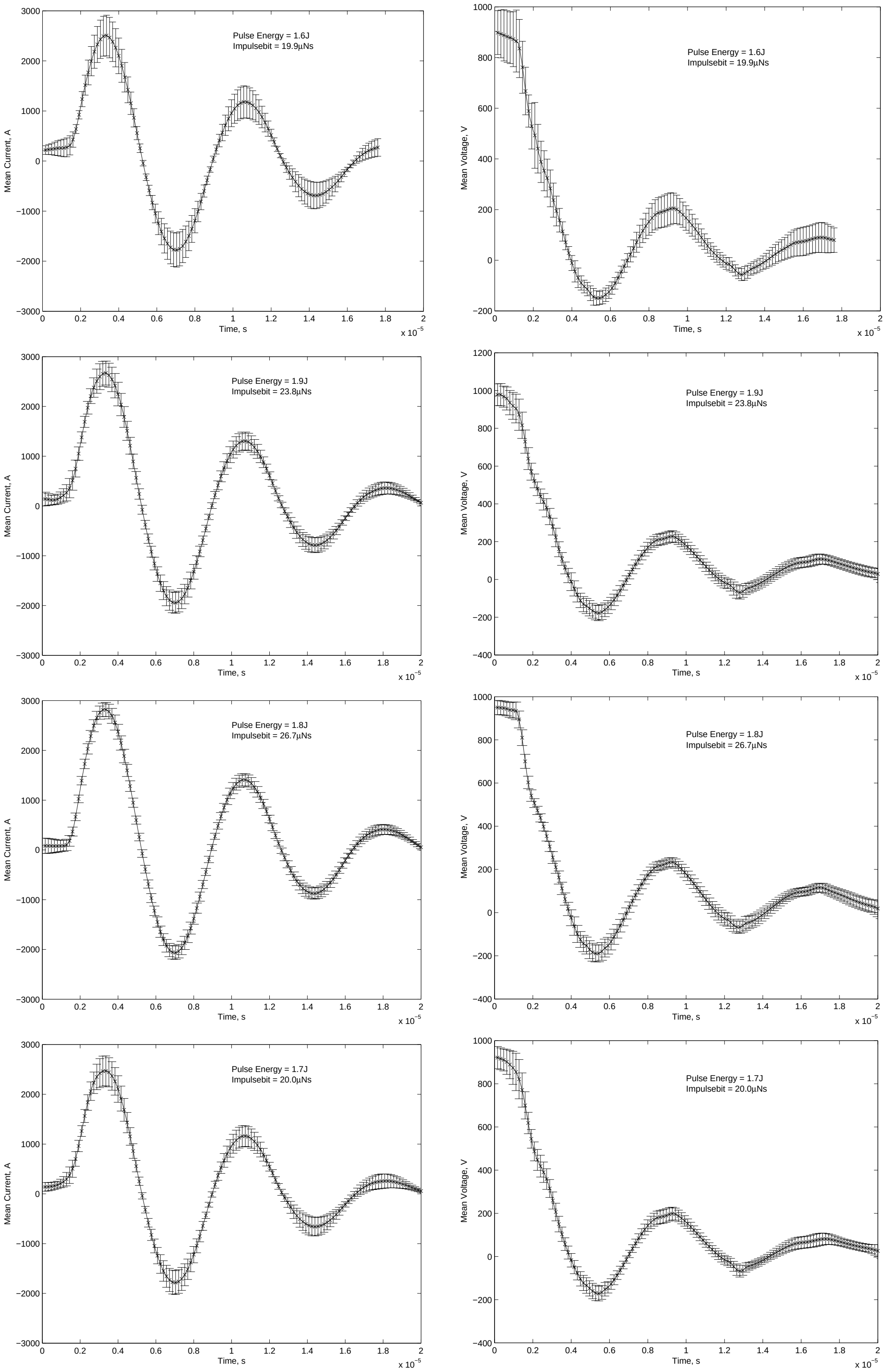

Figure B.3: Profiles 1-4: Standard configuration, Teflon^{TM} width = 3mm. 1: Total pulses = 100, 2: Total pulses = 301, 3: Total pulses = 501, 4: Total pulses = 887

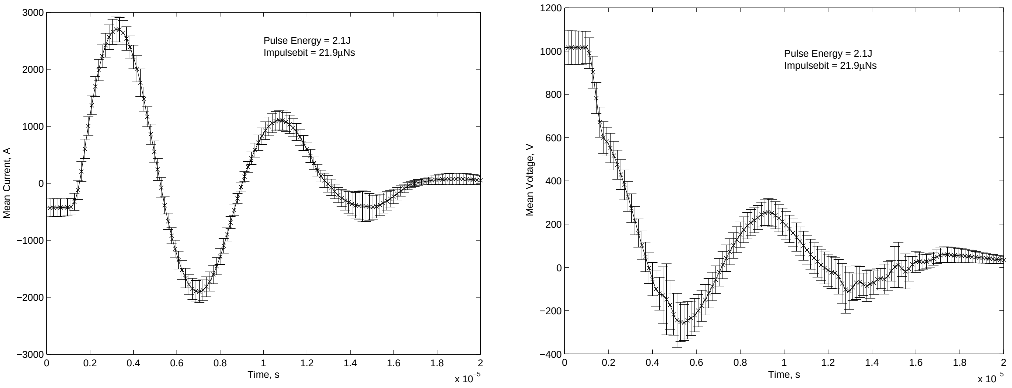

Figure B.4: Profiles 1: Standard configuration, Teflon^{TM} width = 3mm. 1: Total pulses = 178, Teflon^{TM} was enclosed by sidewalls

B.3 Teflon^{TM} Width Experiments

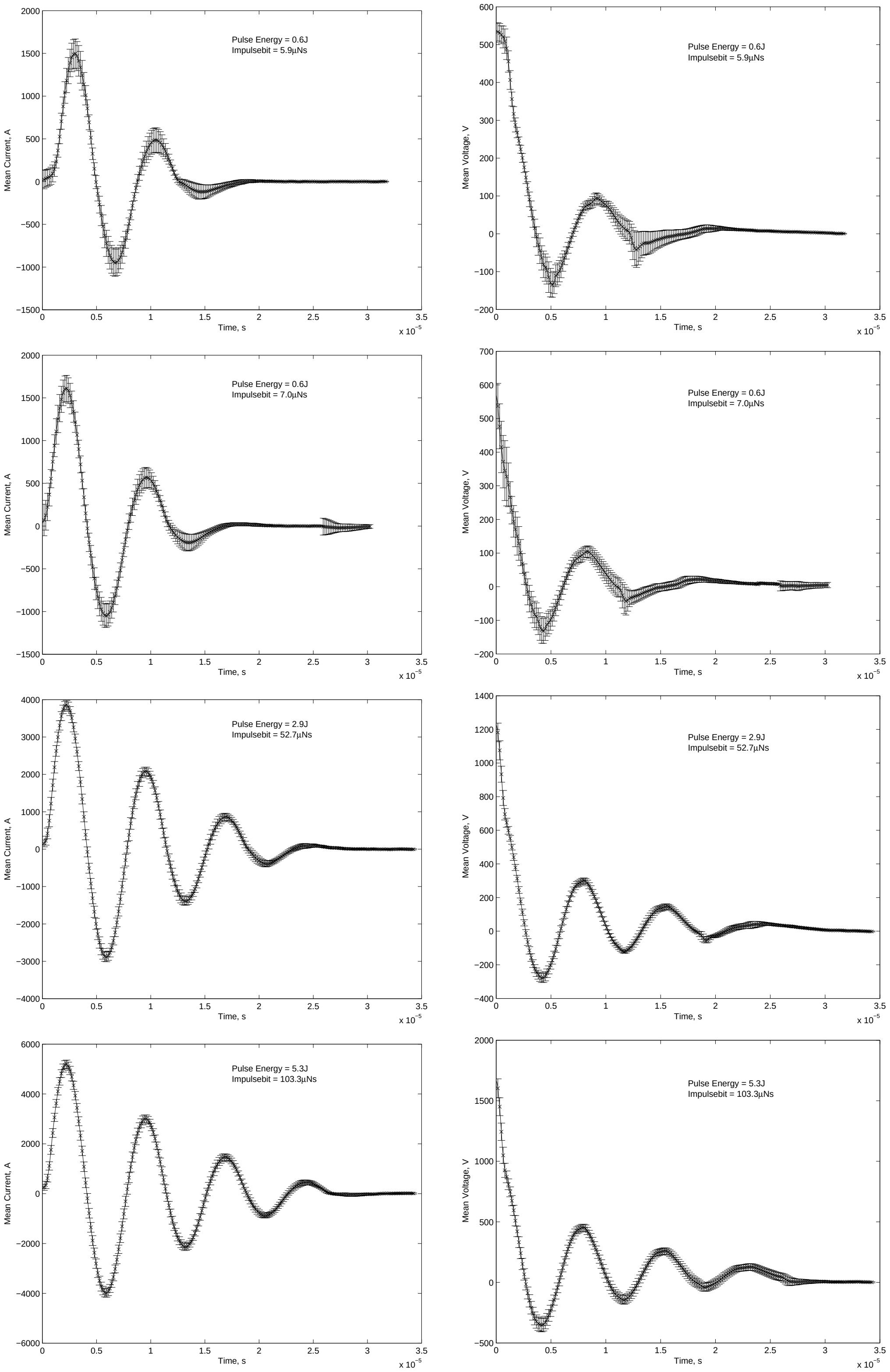

Figure B.5: 1: Teflon^{TM} width = 3.00mm, Profiles 2-4: Teflon^{TM} width = 3.53mm

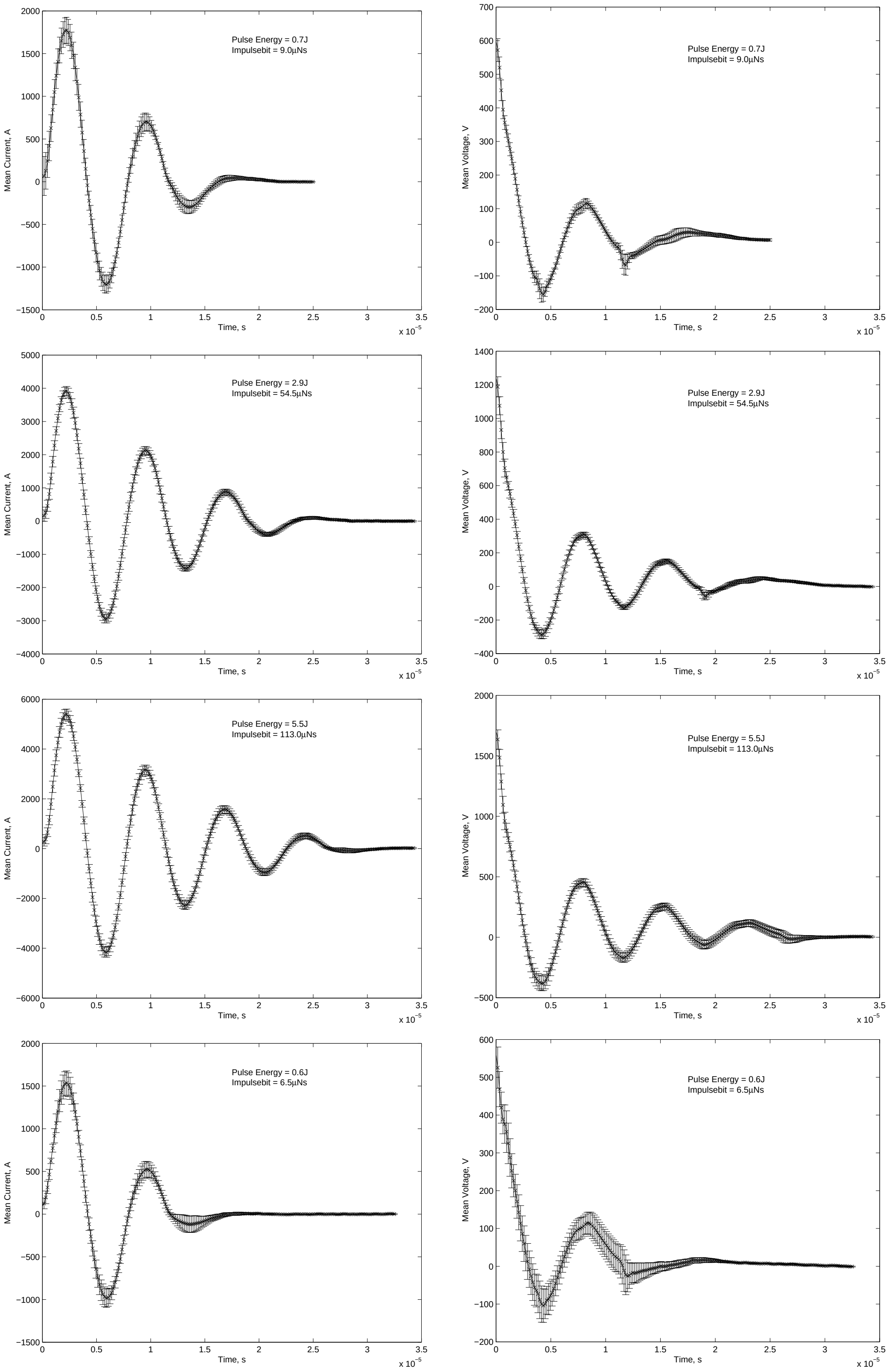

Figure B.6: Profiles 1-3: Teflon^{TM} width = 3.75mm, 4: Teflon^{TM} width = 4.00mm

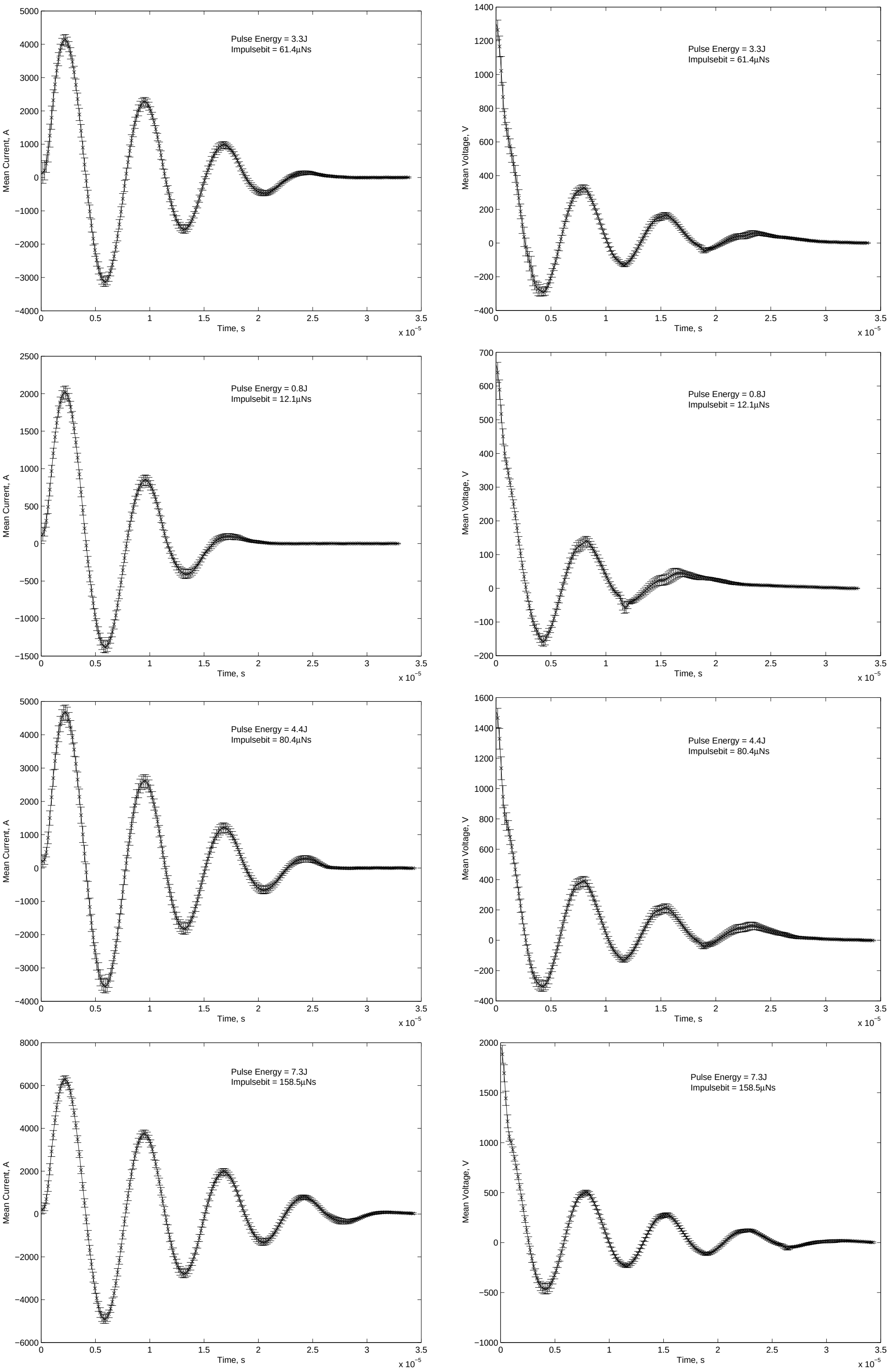

Figure B.7: 1: Teflon^{TM} width = 4.00mm, Profiles 2-4: Teflon^{TM} width = 5.00mm

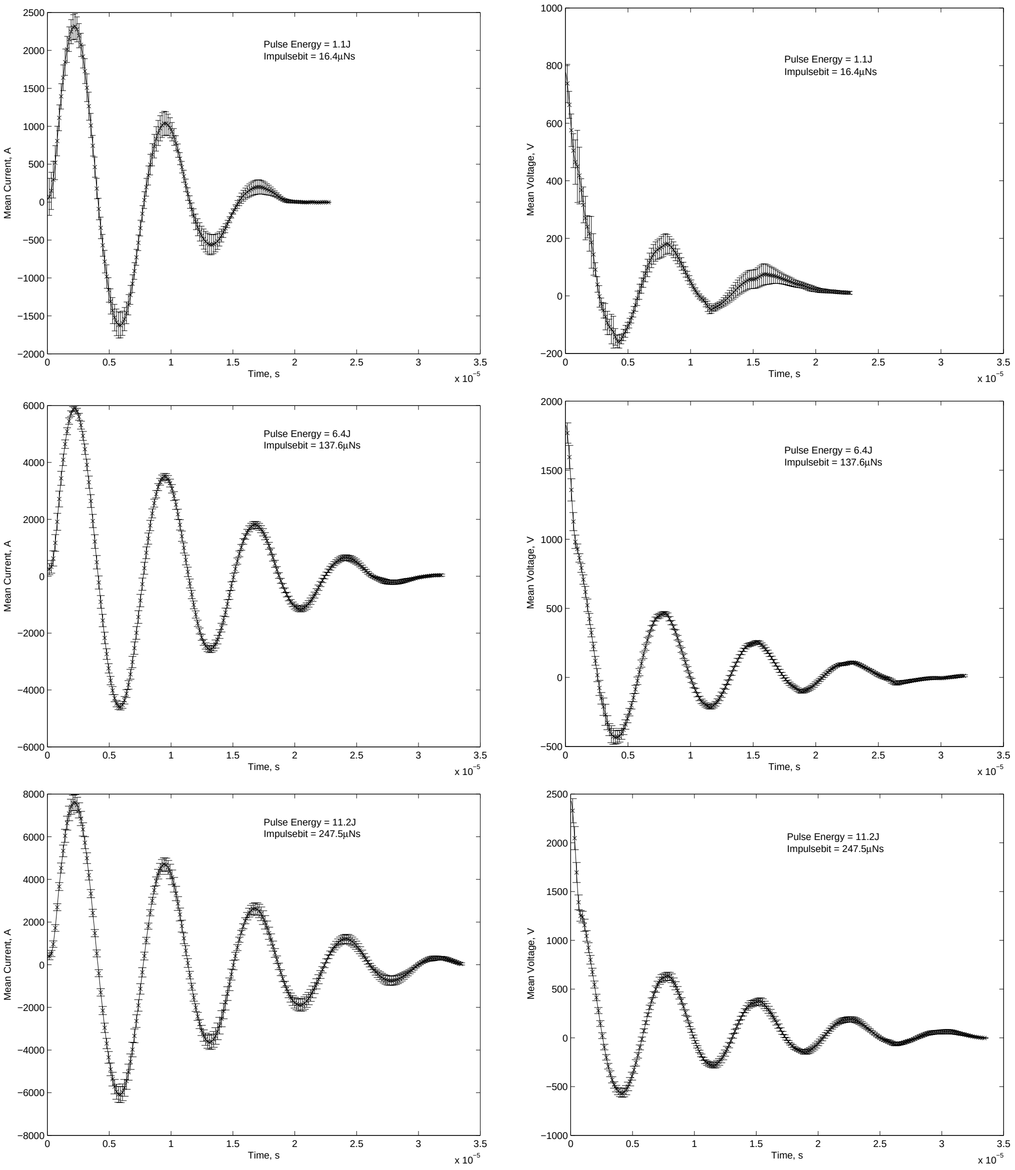

Figure B.8: 1: Teflon^{TM} width = 6.00mm, Profiles 2-3: Teflon^{TM} width = 7.50mm

B.4 Discharge Energy Experiments without Teflon^{TM}

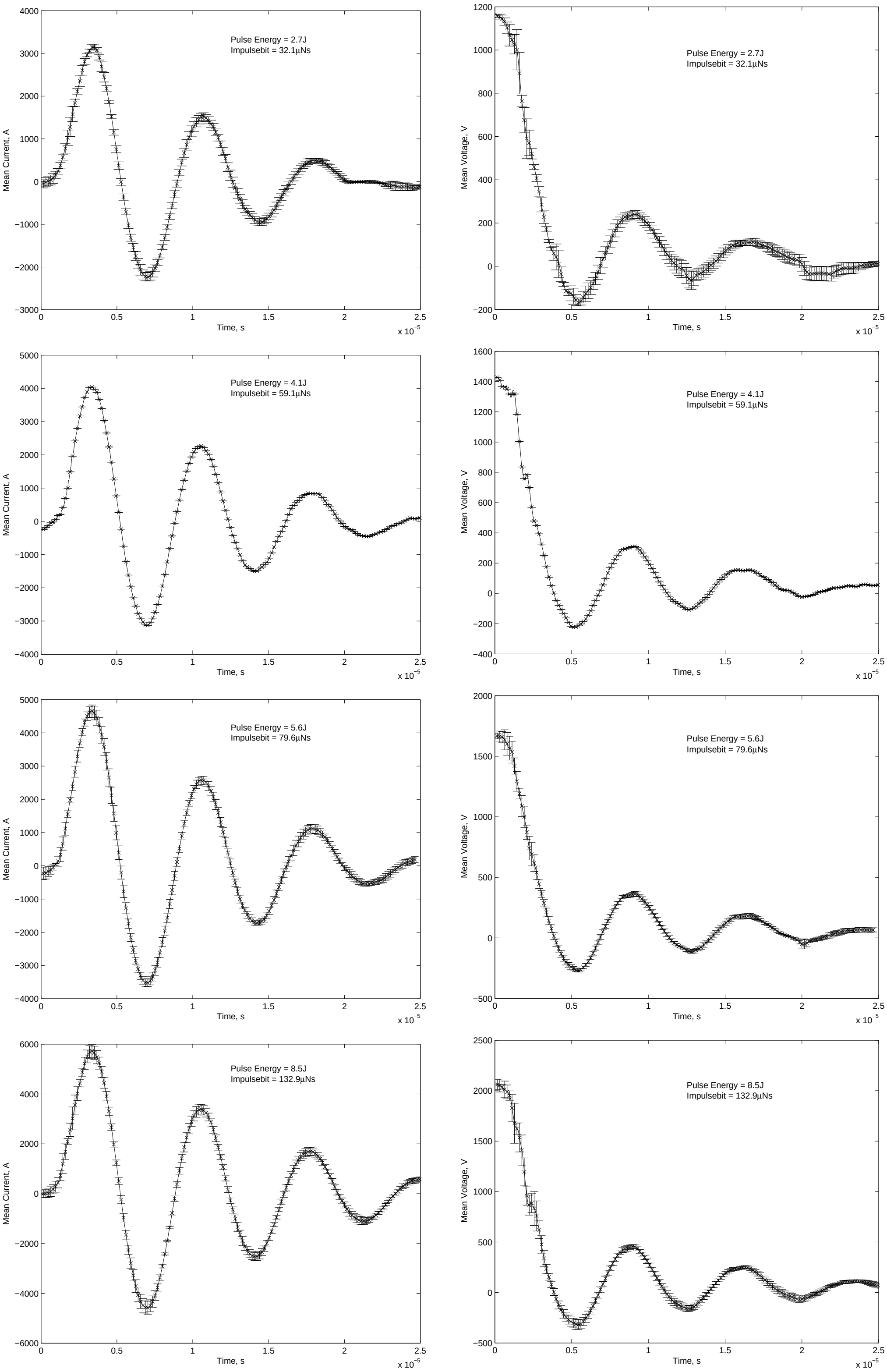

Figure B.9: Profiles 1-4: Sparkplug initiated at 15kV, no Teflon^{TM}

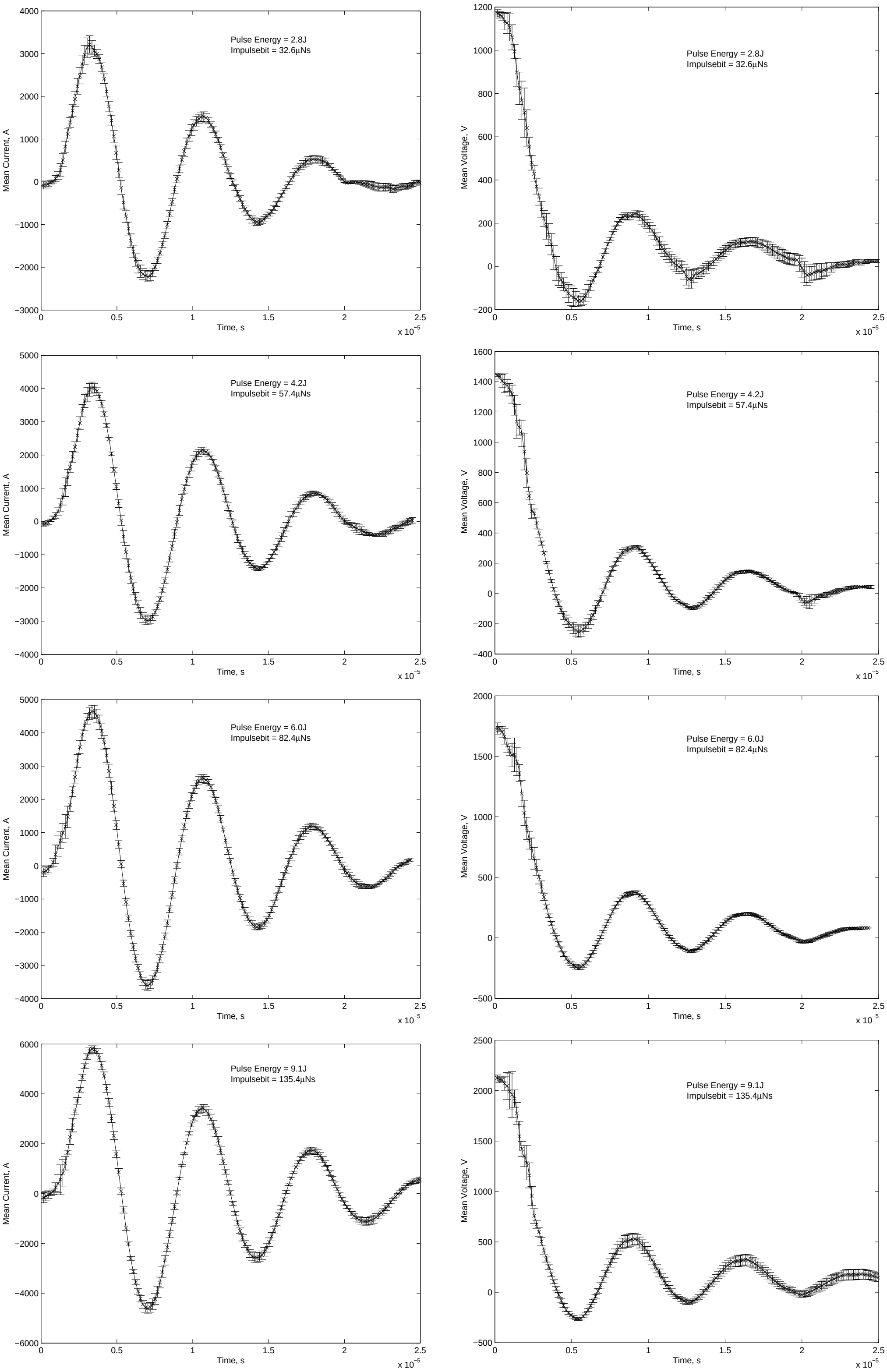

Figure B.10: Profiles 1-4: Sparkplug initiated at 20kV, no Teflon^{TM}

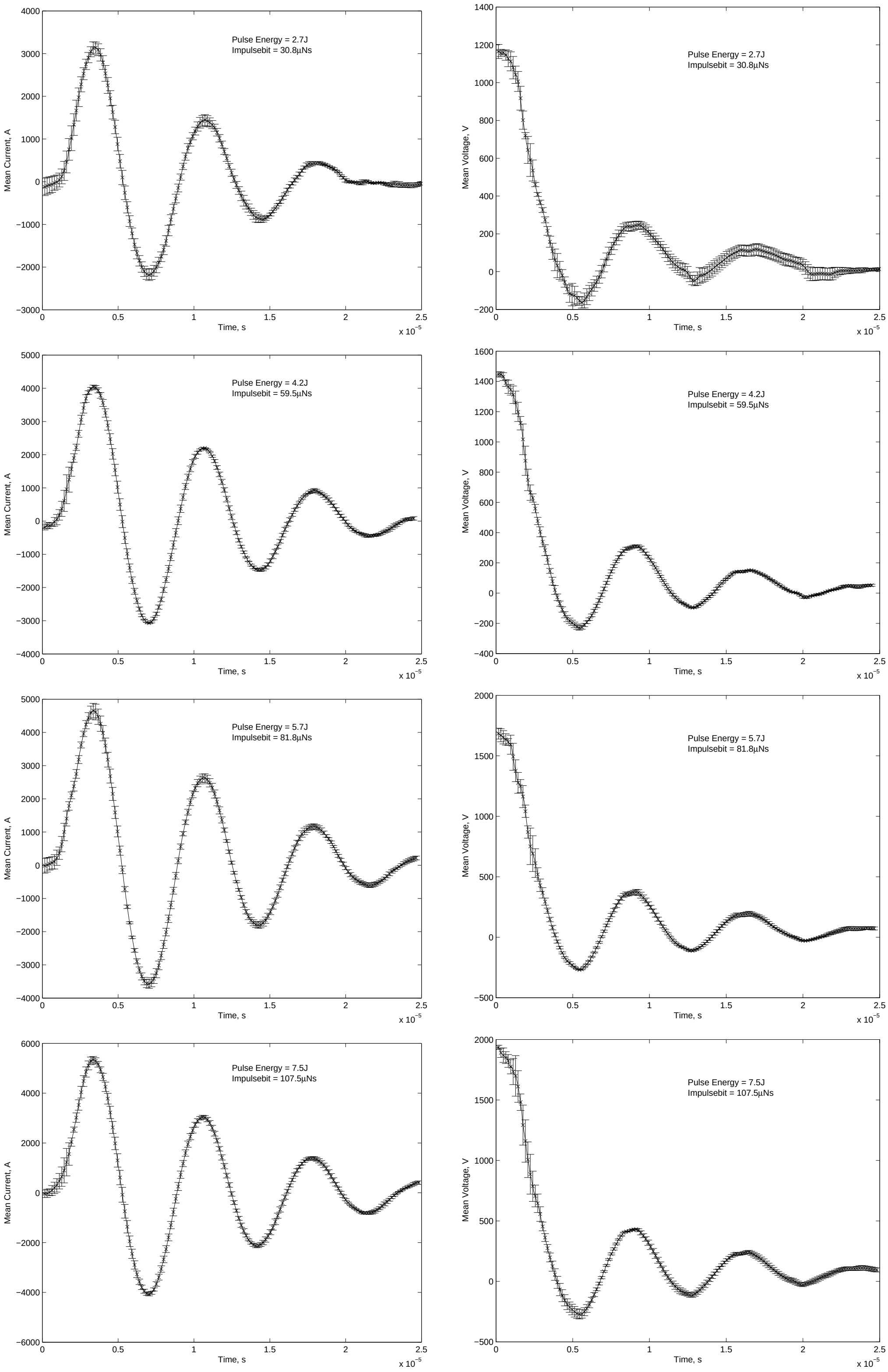

Figure B.11: Profiles 1-4: Sparkplug initiated at 25kV, no Teflon^{TM}

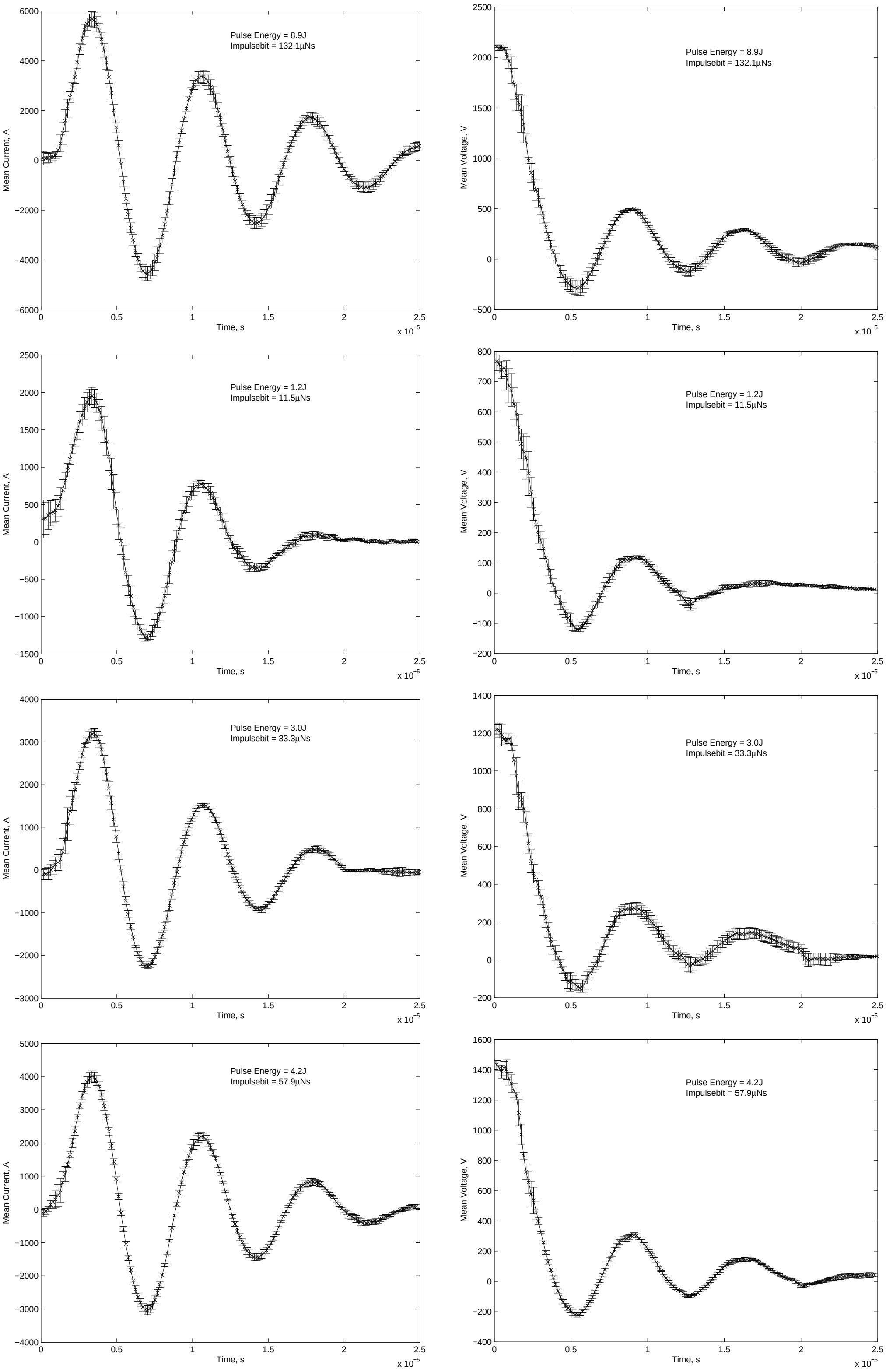

Figure B.12: Profile 1: Sparkplug initiated at 25kV, no Teflon^{TM}. Profiles 2-3: Sparkplug initiated at 30kV, no Teflon^{TM}

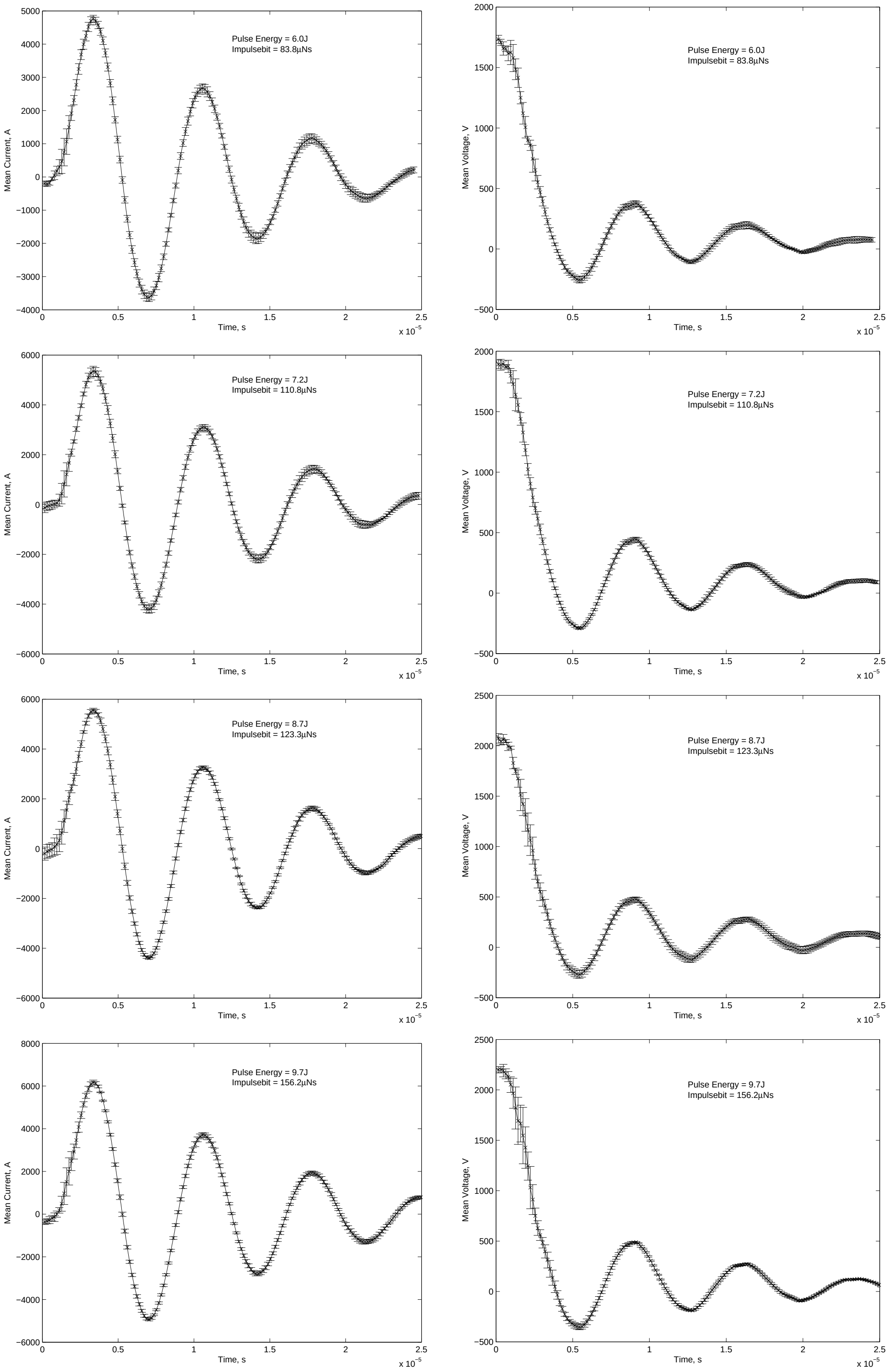

Figure B.13: Profiles 1-4: Sparkplug initiated at 30kV, no Teflon^{TM}

B.5 Electrode Separation Experiments

B.5.1 10mm Electrode Separation

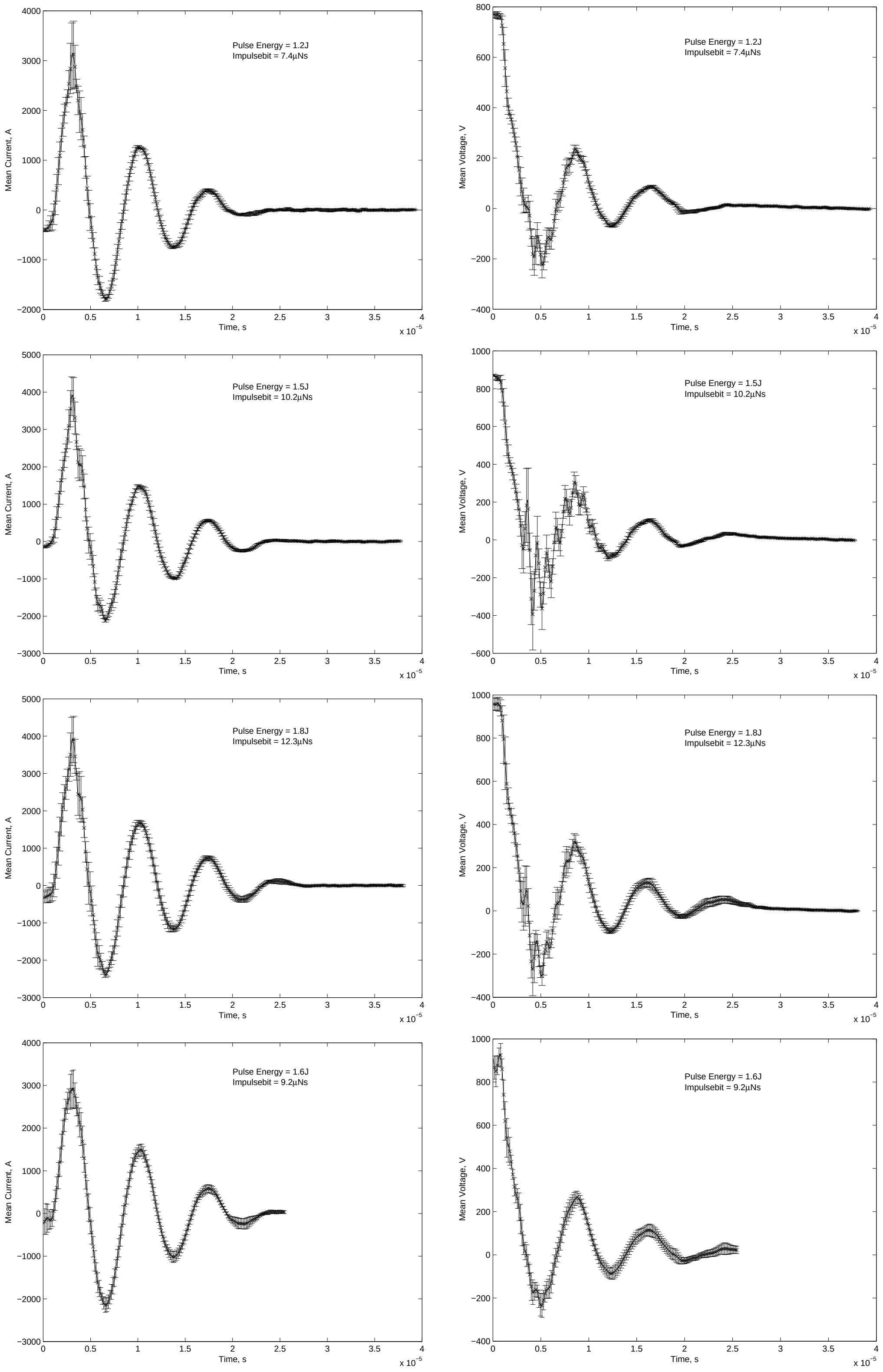

Figure B.14: Profiles 1-4: Electrode separation = 10mm, no Teflon^{TM}

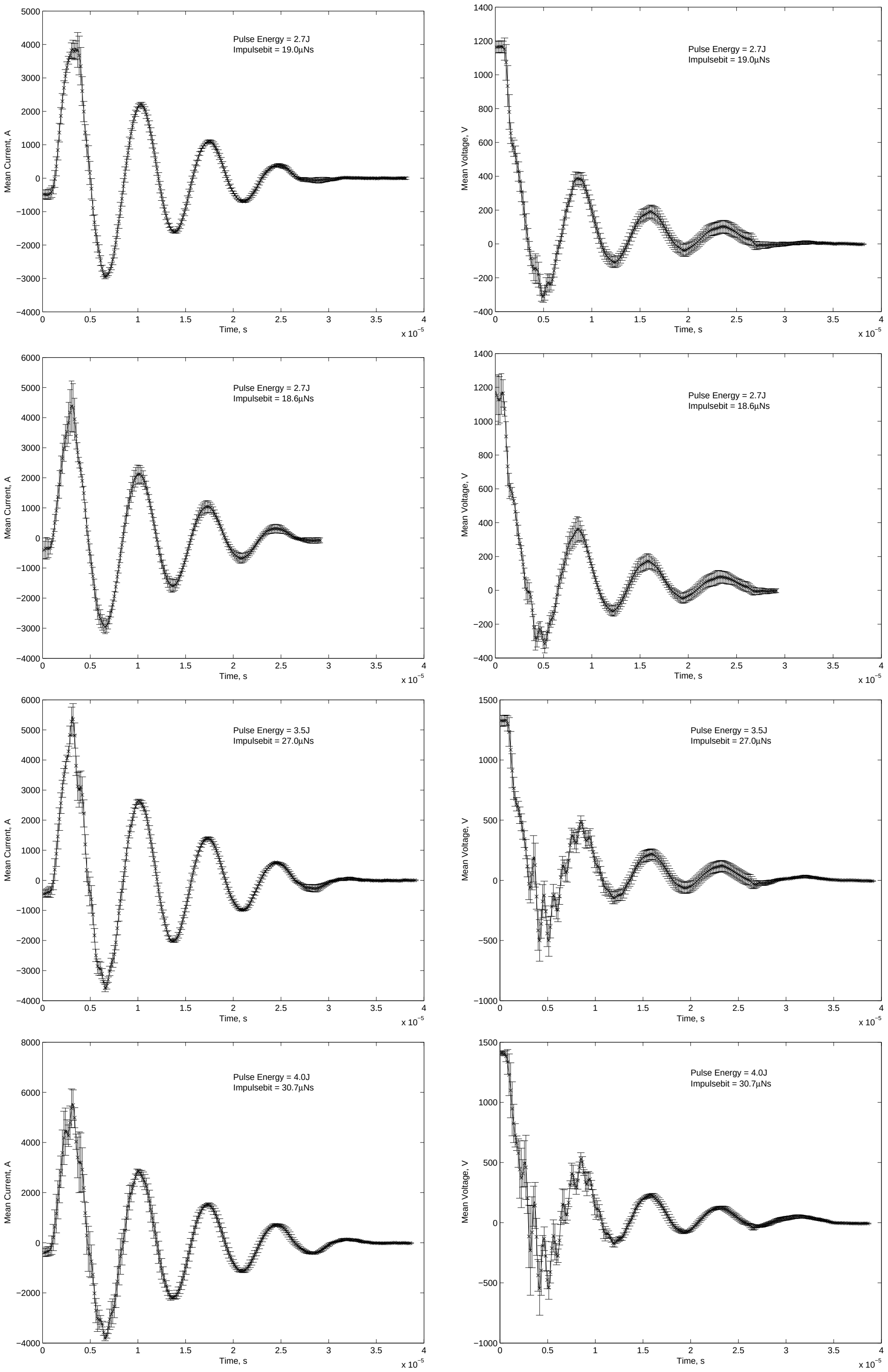

Figure B.15: Profiles 1-4: Electrode separation = 10mm, no Teflon^{TM}

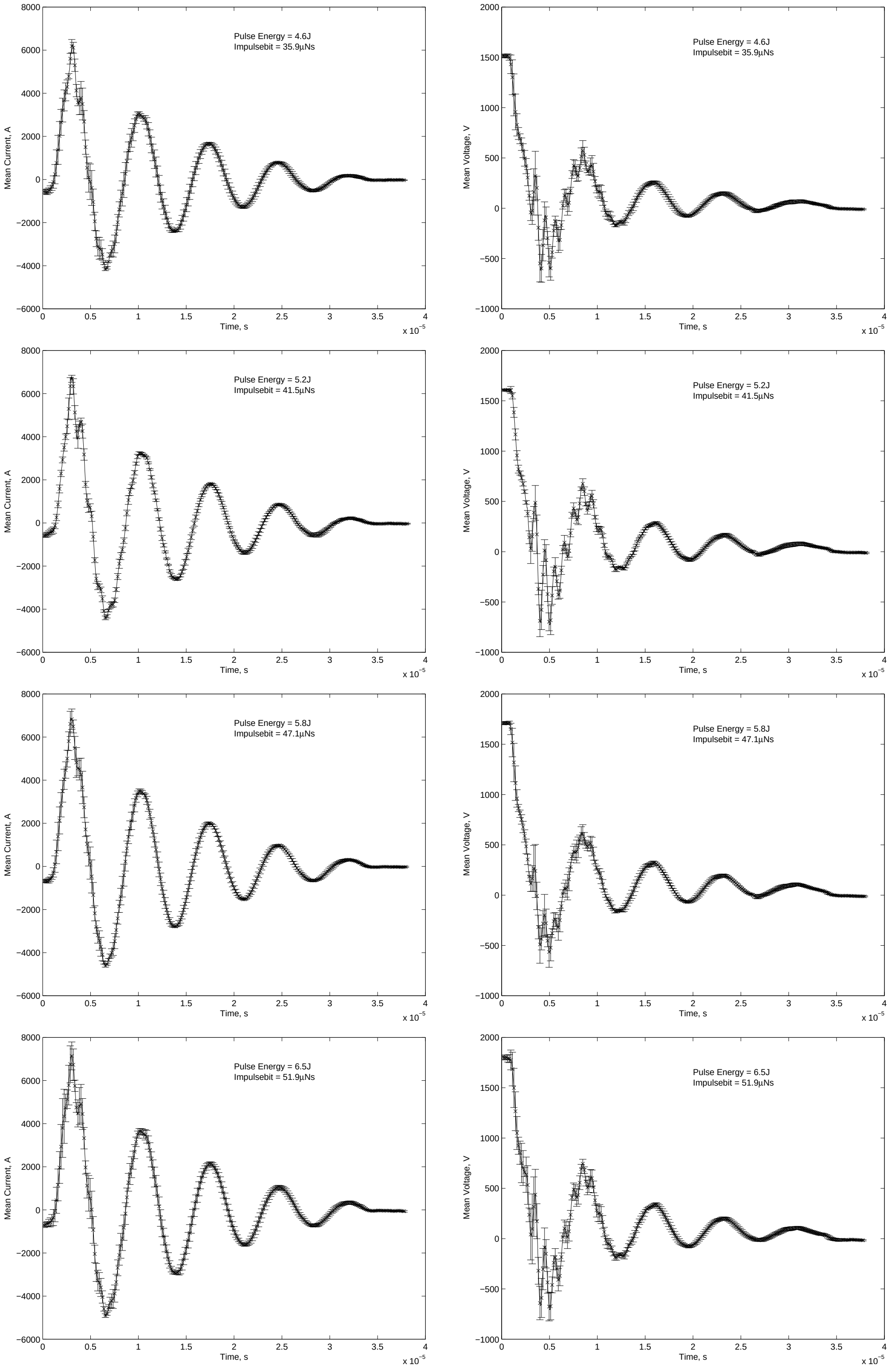

Figure B.16: Profiles 1-4: Electrode separation = 10mm, no Teflon^{TM}

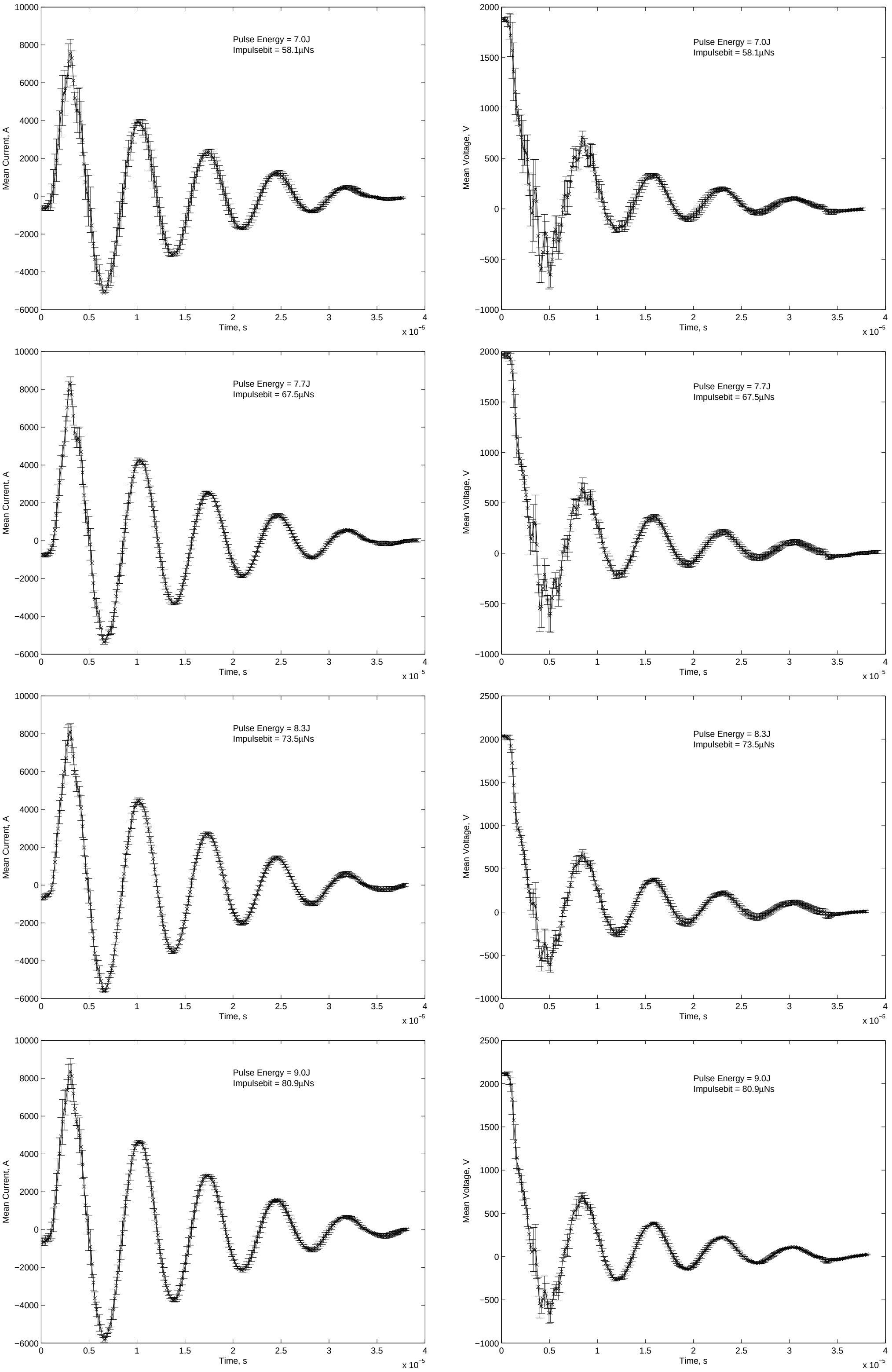

Figure B.17: Profiles 1-4: Electrode separation = 10mm, no Teflon^{TM}

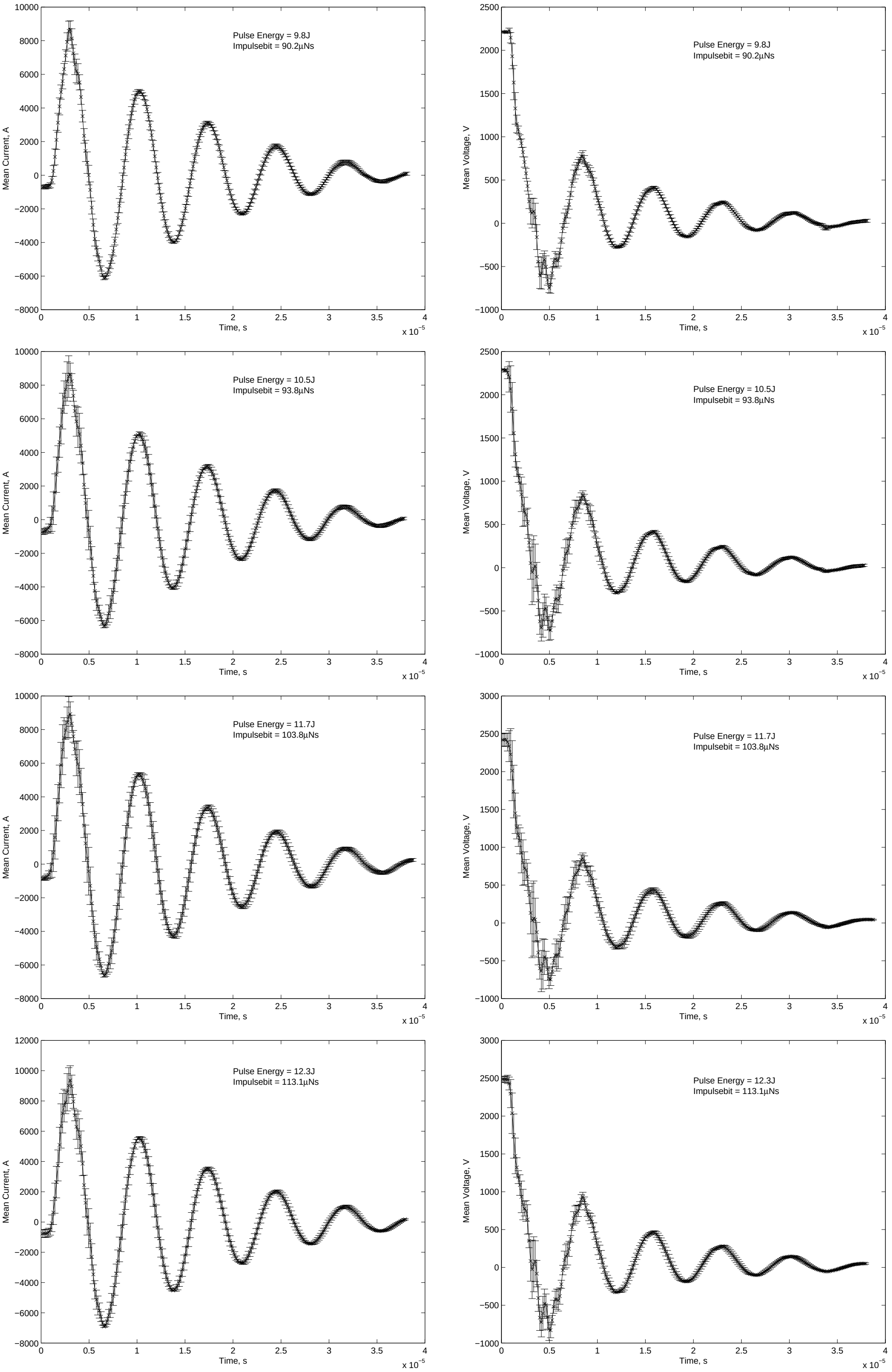

Figure B.18: Profiles 1-4: Electrode separation = 10mm, no Teflon^{TM}

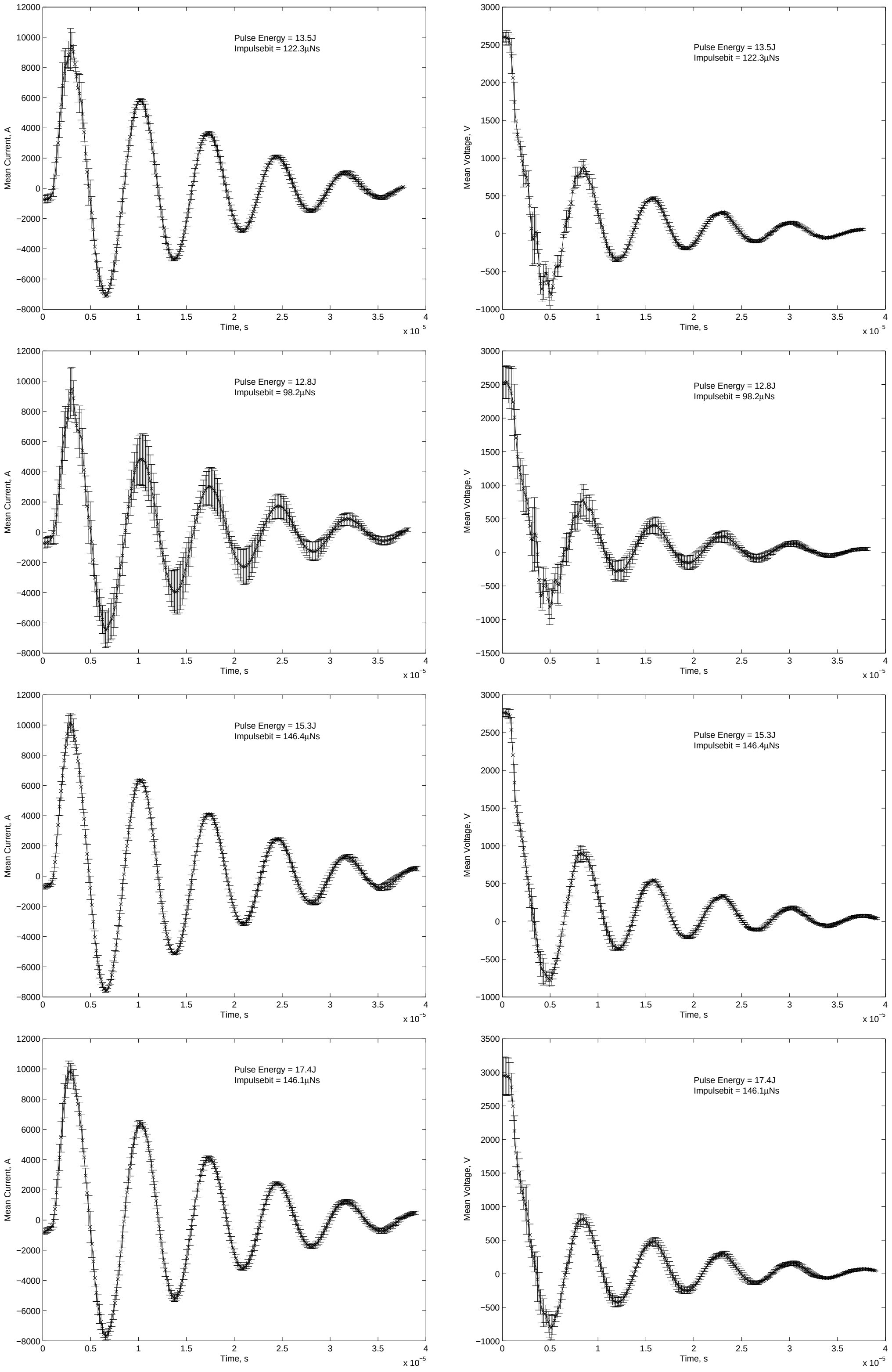

Figure B.19: Profiles 1-4: Electrode separation = 10mm, no Teflon^{TM}

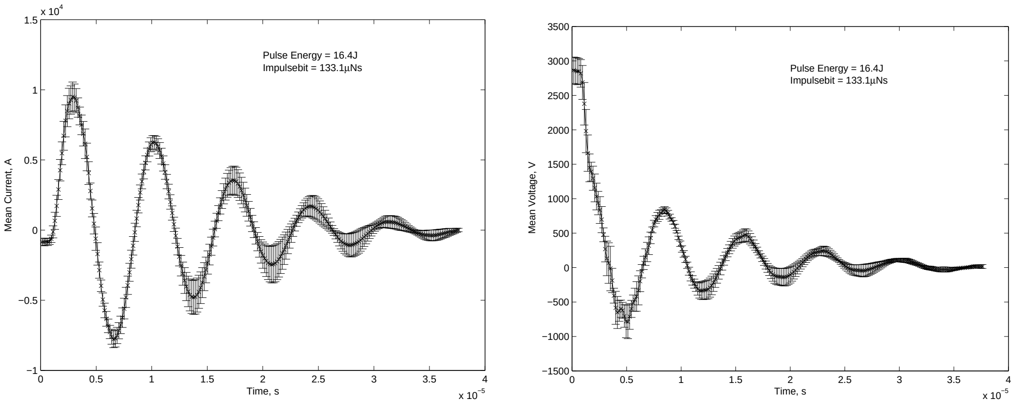

Figure B.20: Profile 1: Electrode separation = 10mm, no Teflon^{TM}

B.5.2 30mm Electrode Separation

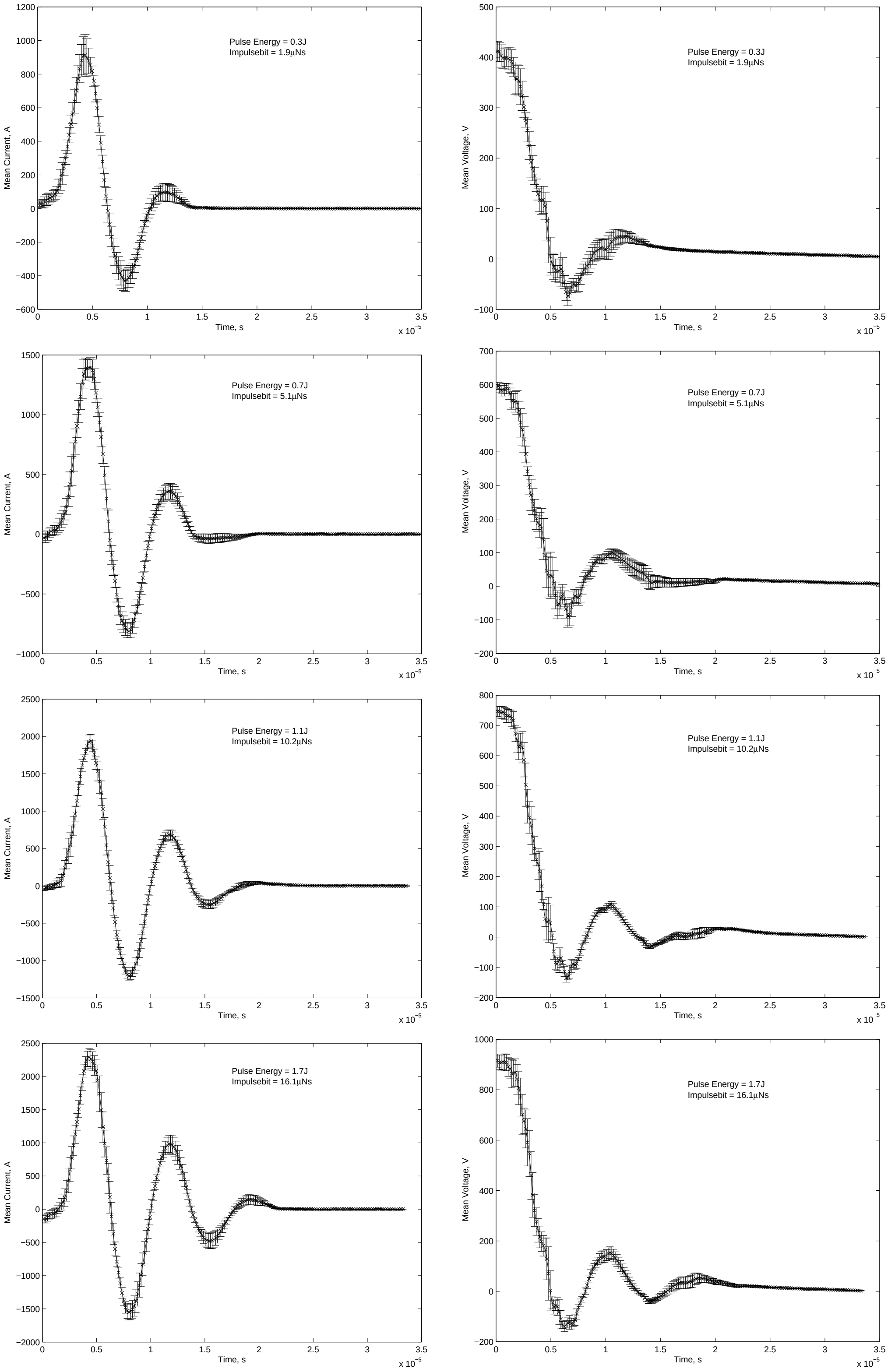

Figure B.21: Profiles 1-4: Electrode separation = 30mm, no Teflon^{TM}

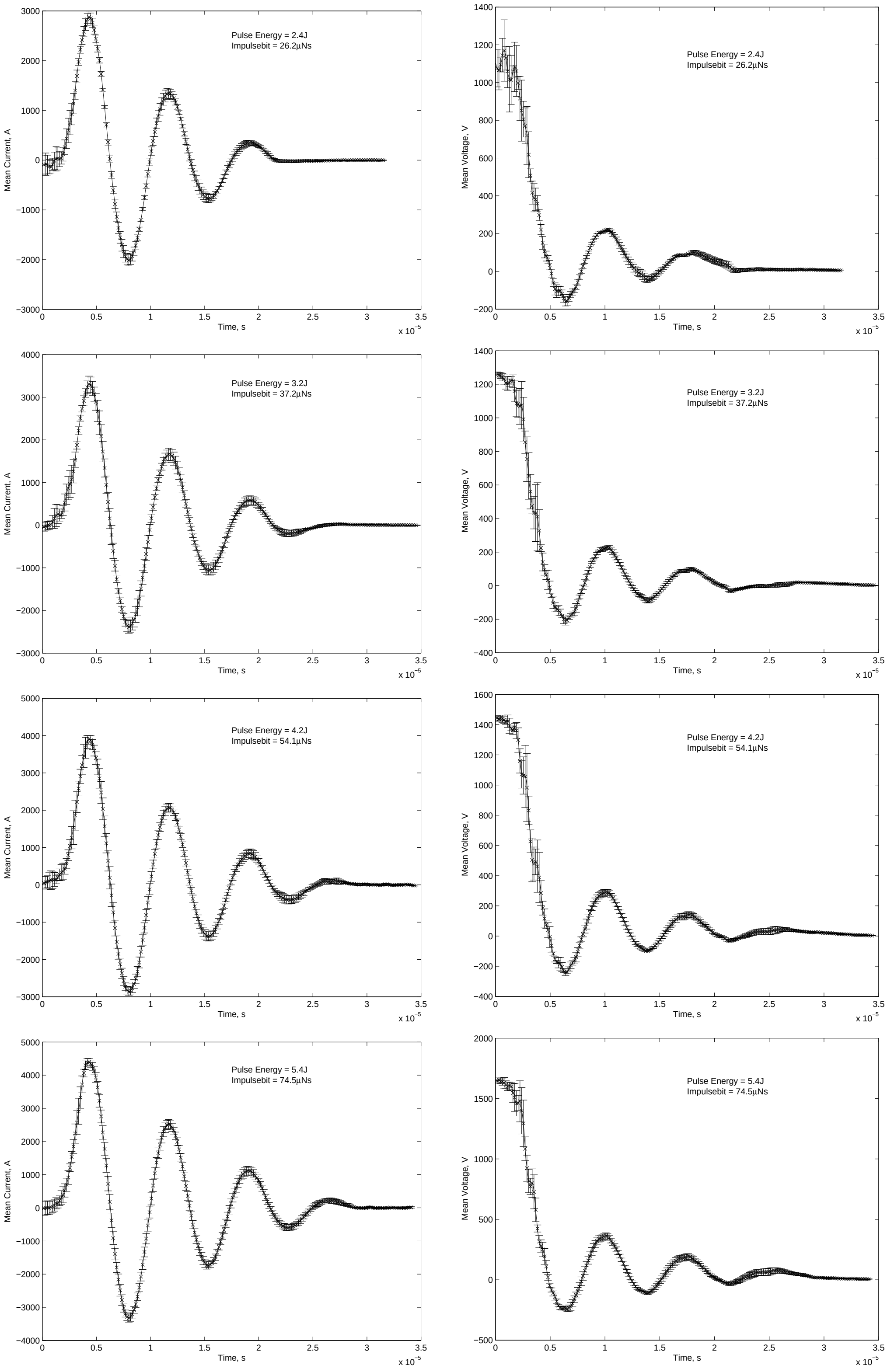

Figure B.22: Profiles 1-4: Electrode separation = 30mm, no Teflon^{TM}

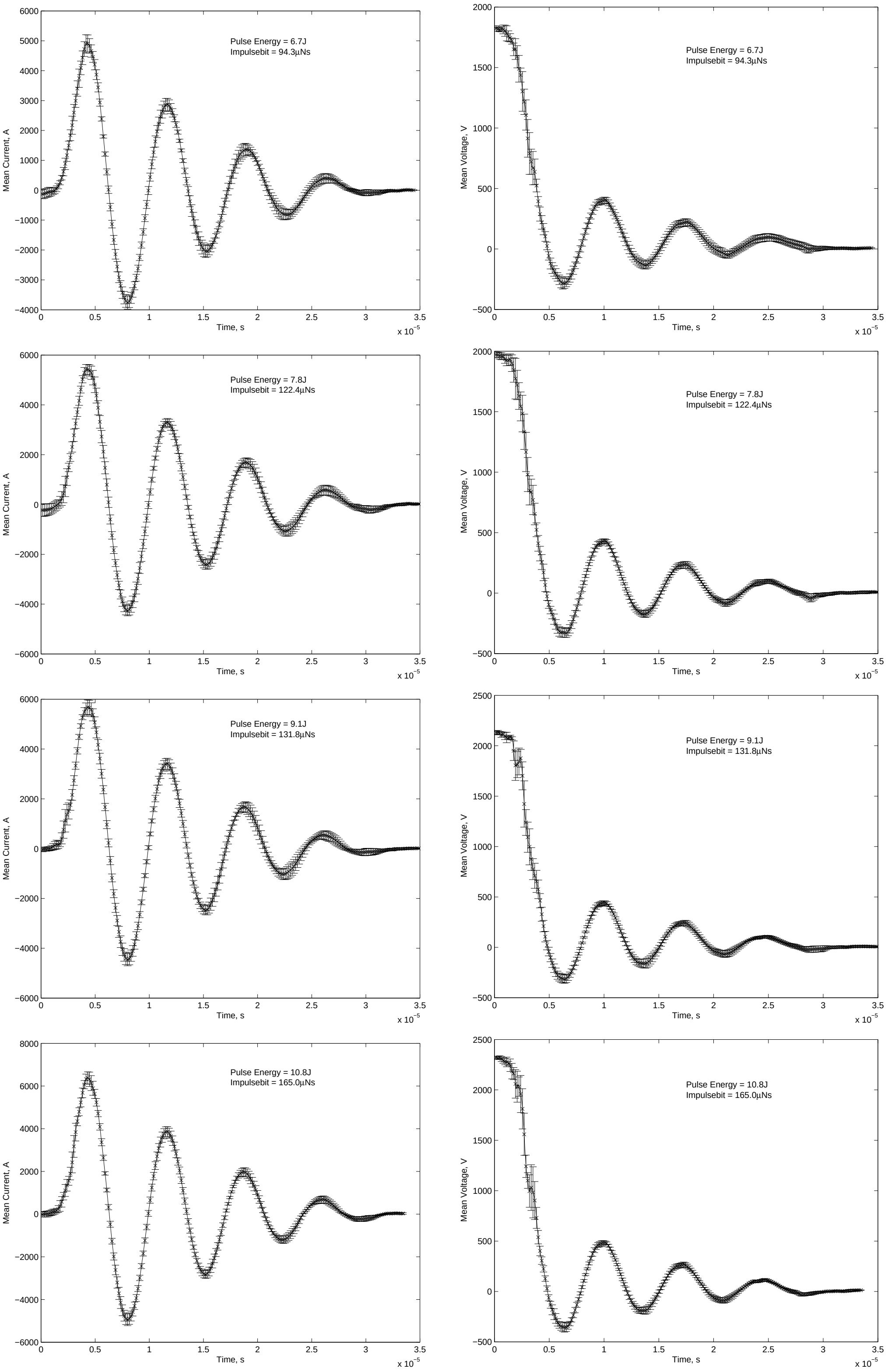

Figure B.23: Profiles 1-4: Electrode separation = 30mm, no Teflon^{TM}

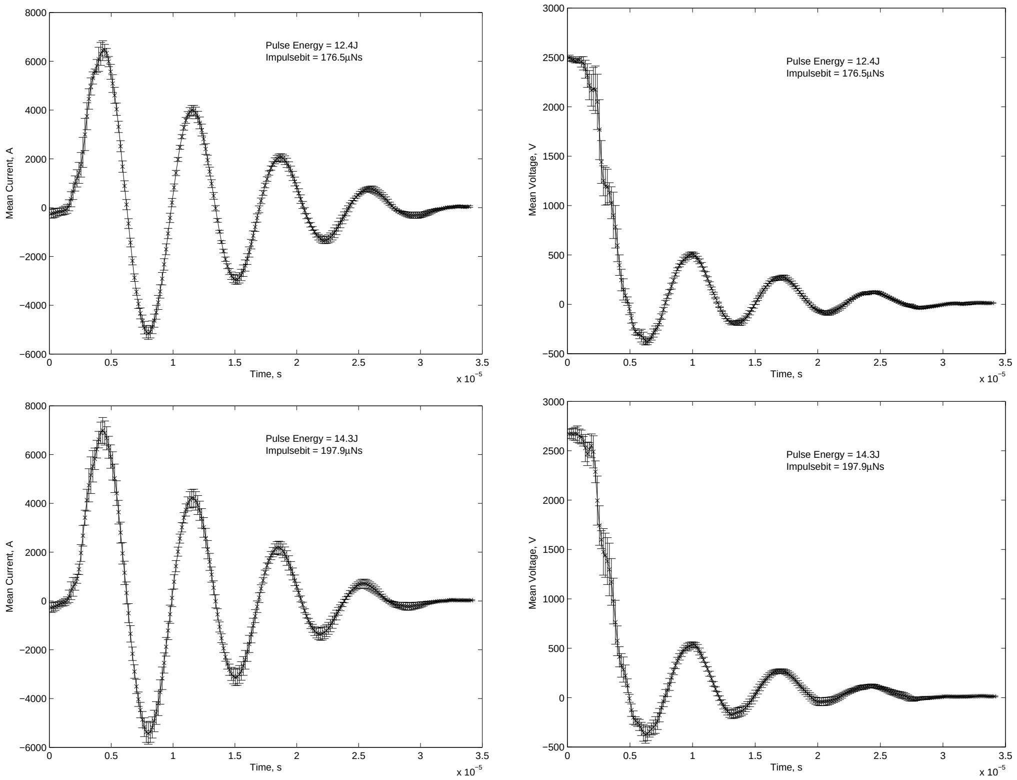

Figure B.24: Profiles 1-2: Electrode separation = 30mm, no Teflon^{TM}

B.5.3 50mm Electrode Separation

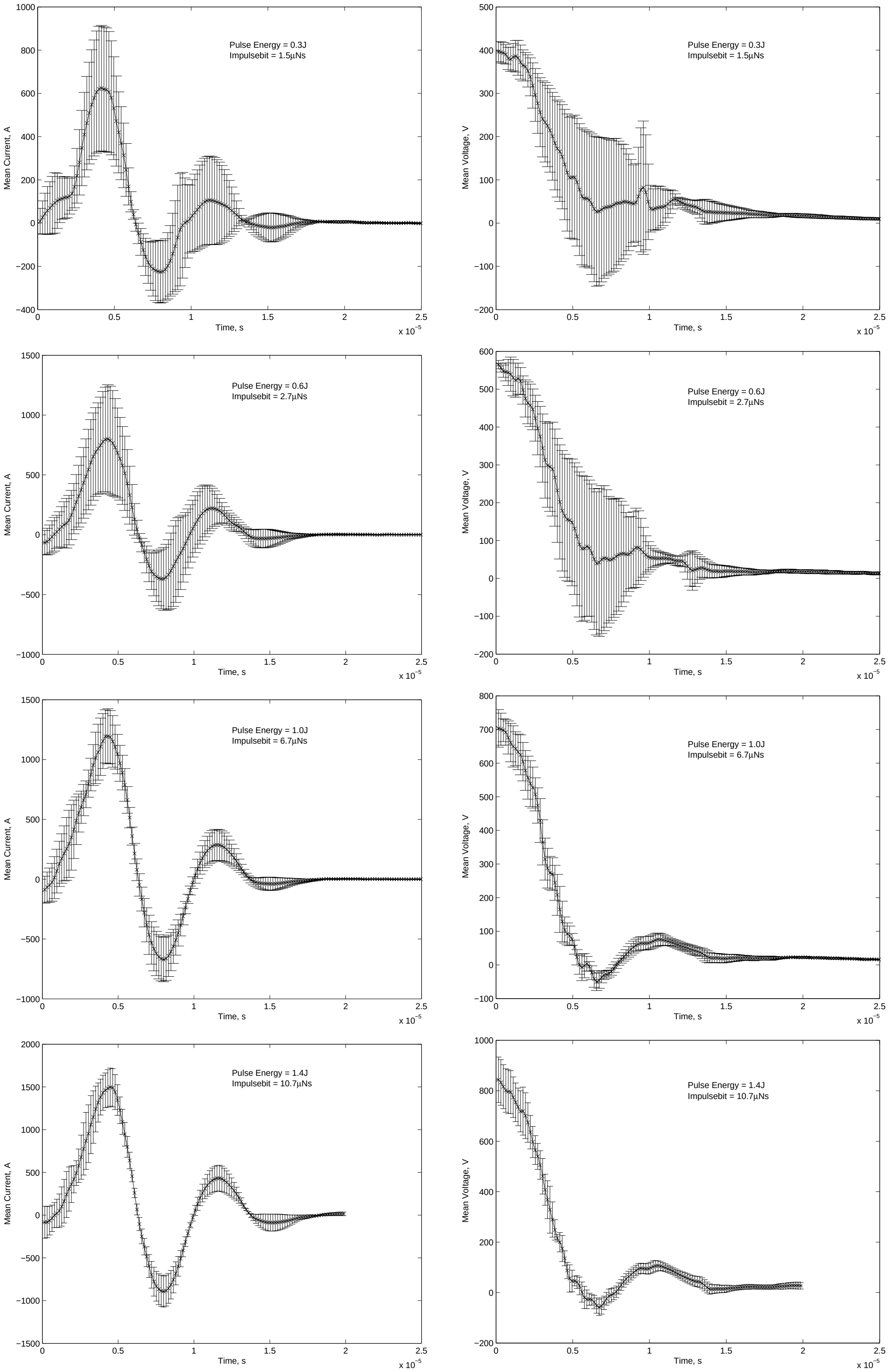

Figure B.25: Profiles 1-4: Electrode separation = 50mm, no Teflon^{TM}

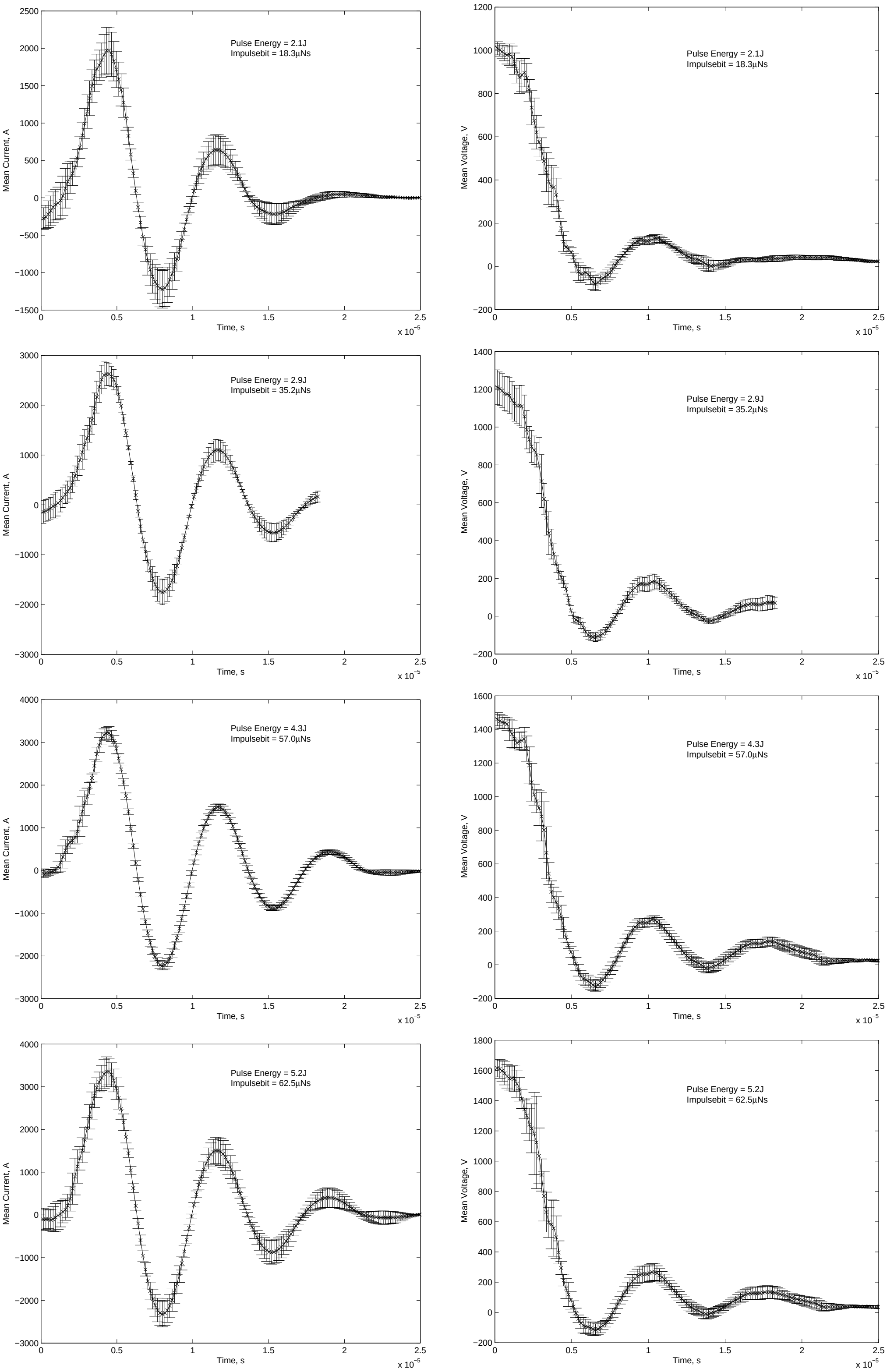

Figure B.26: Profiles 1-4: Electrode separation = 50mm, no Teflon^{TM}

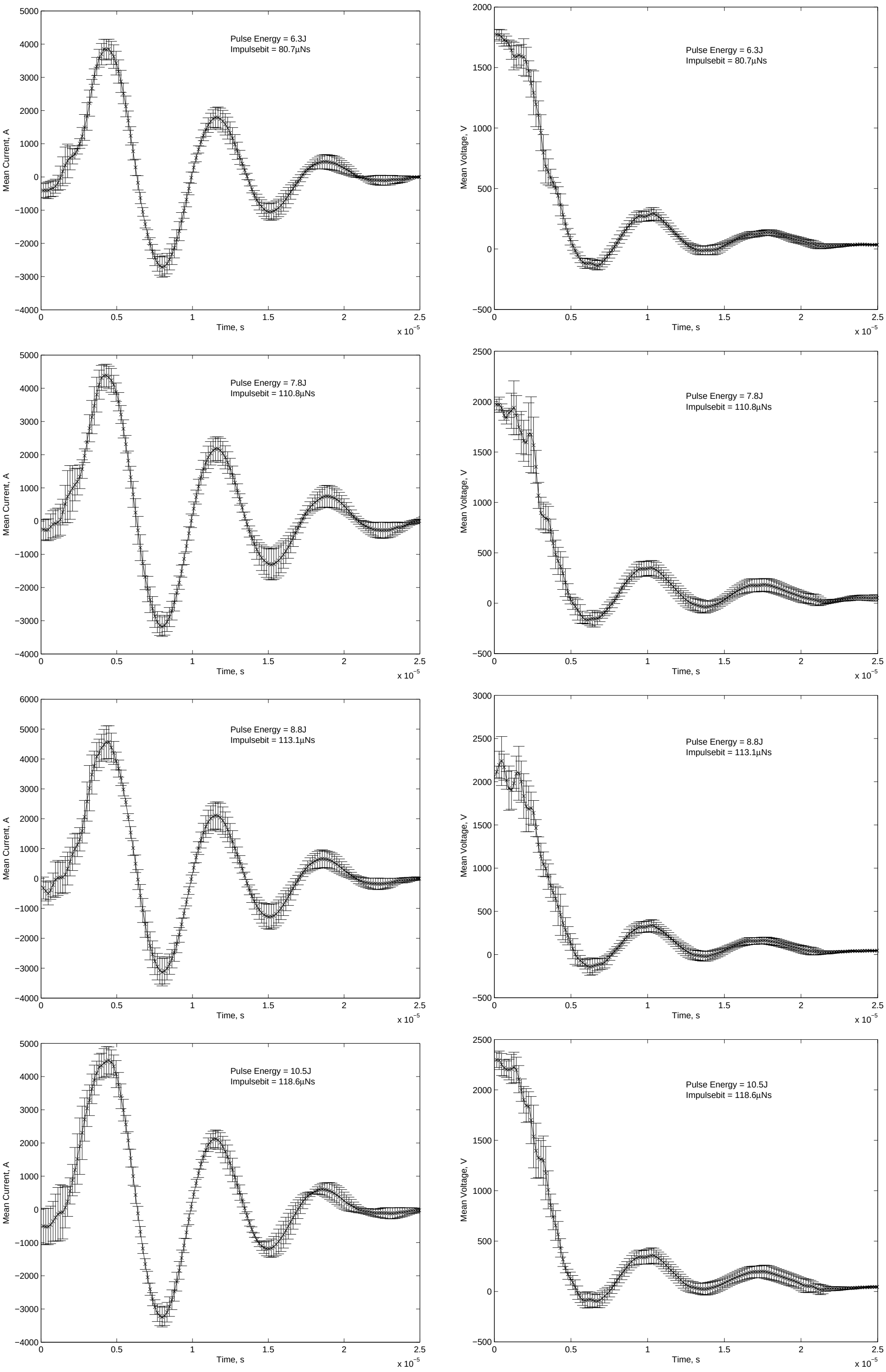

Figure B.27: Profiles 1-4: Electrode separation = 50mm, no Teflon^{TM}

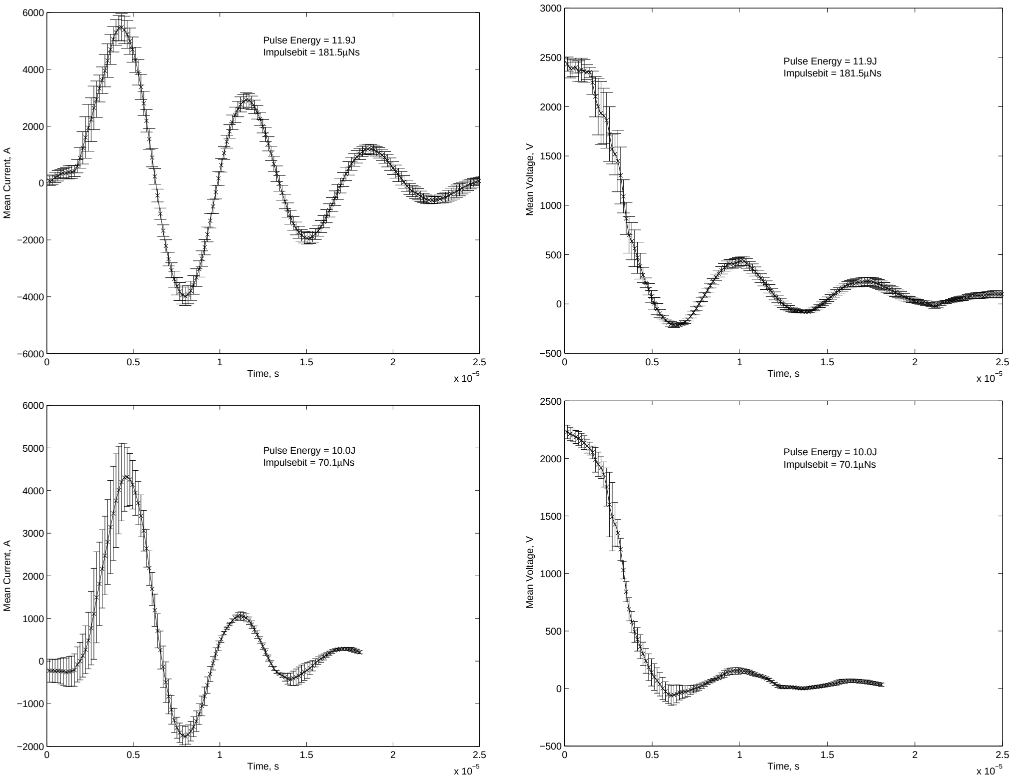

Figure B.28: Profiles 1-2: Electrode separation = 50mm, no Teflon^{TM}

B.5.4 70mm Electrode Separation

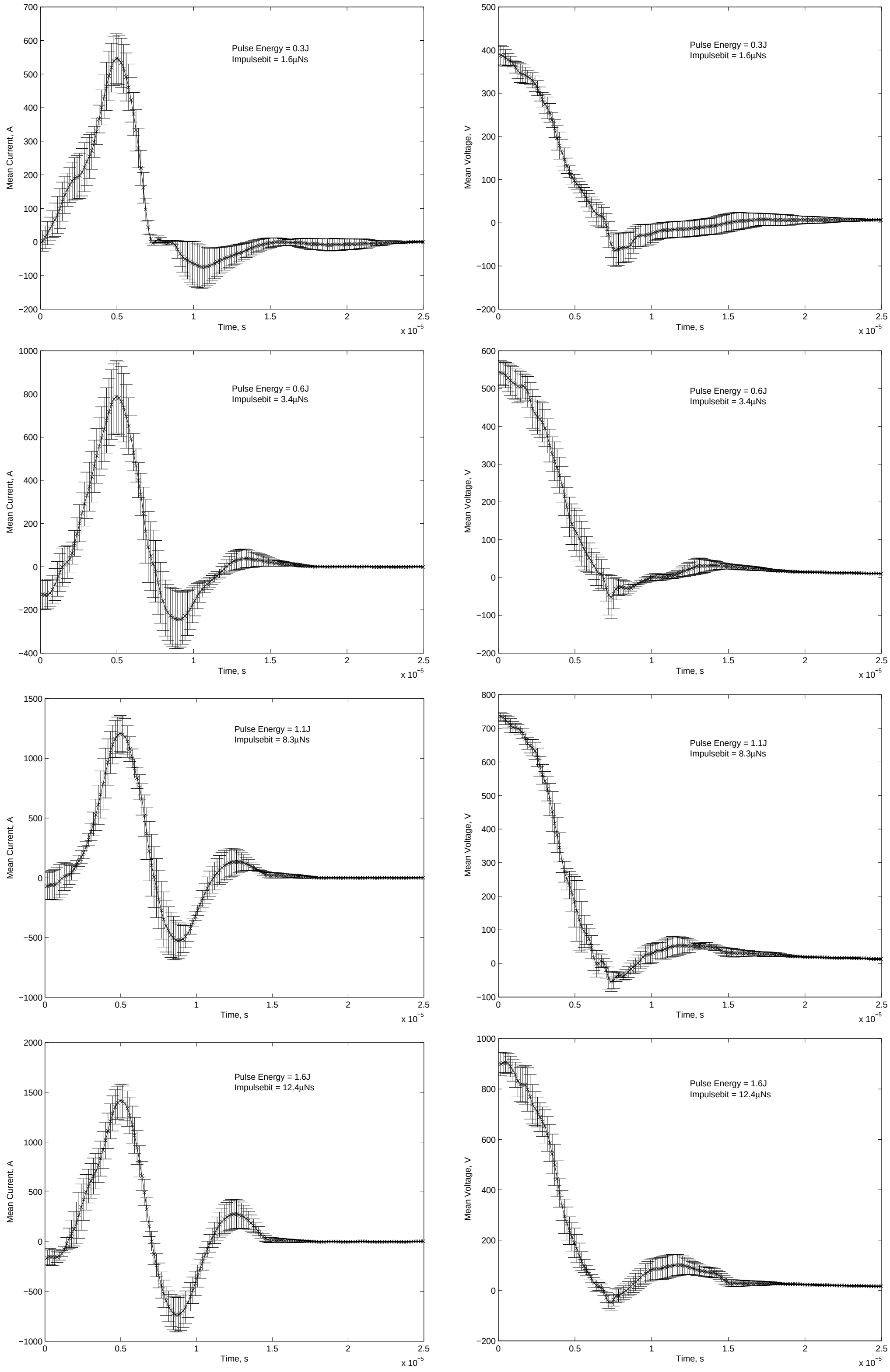

Figure B.29: Profiles 1-4: Electrode separation = 70mm, no Teflon^{TM}

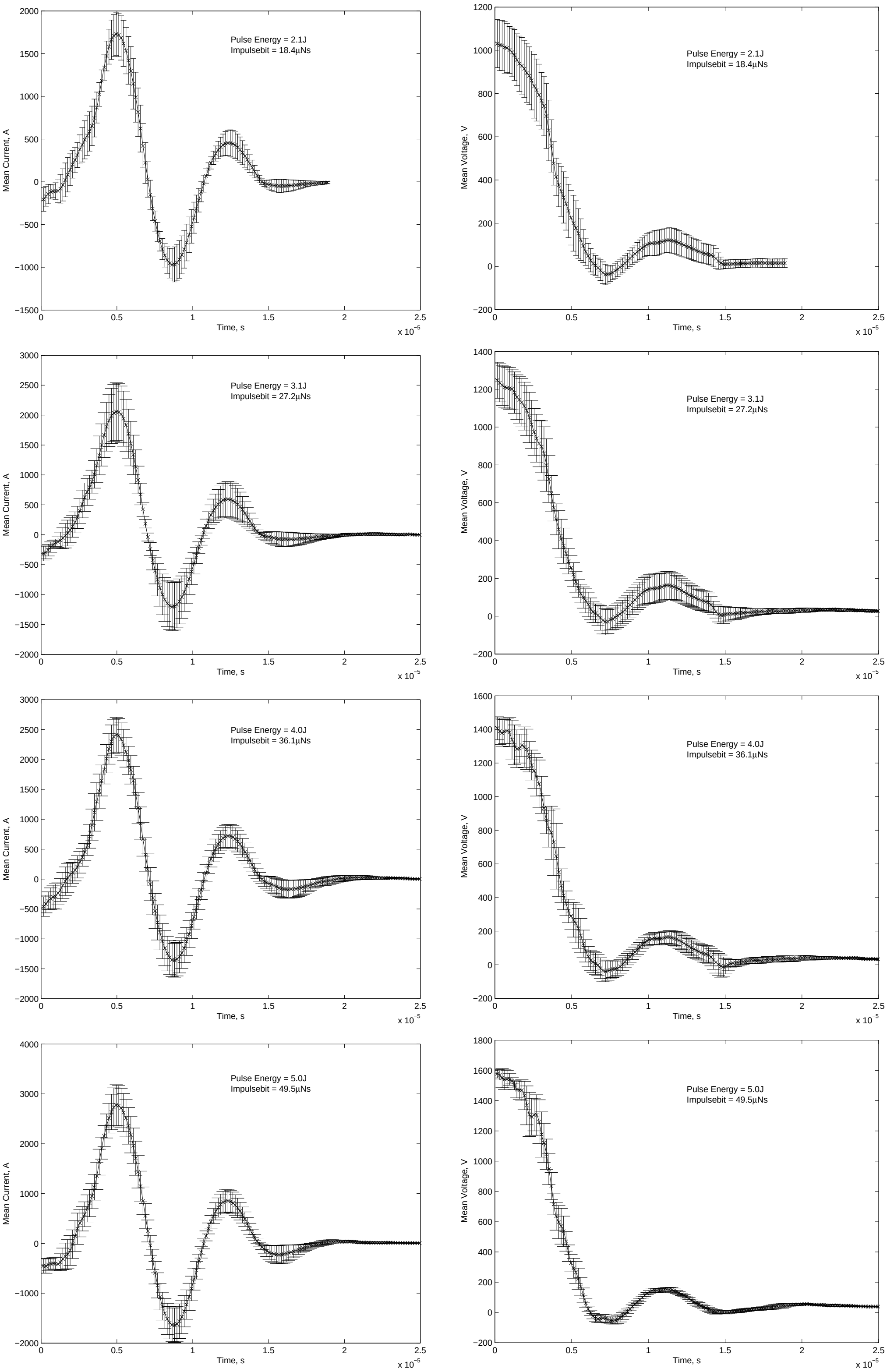

Figure B.30: Profiles 1-4: Electrode separation = 70mm, no Teflon^{TM}

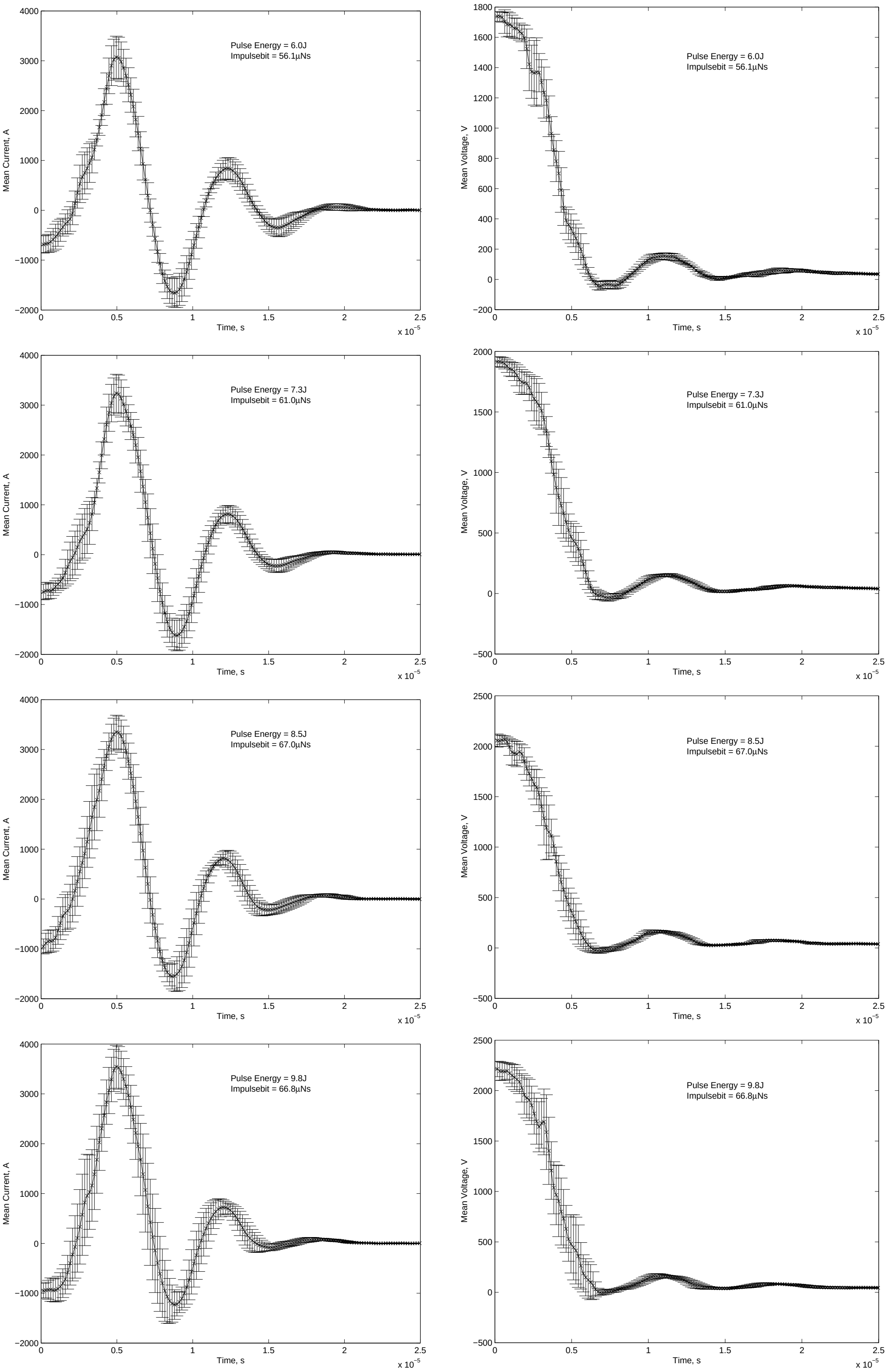

Figure B.31: Profiles 1-4: Electrode separation = 70mm, no Teflon^{TM}

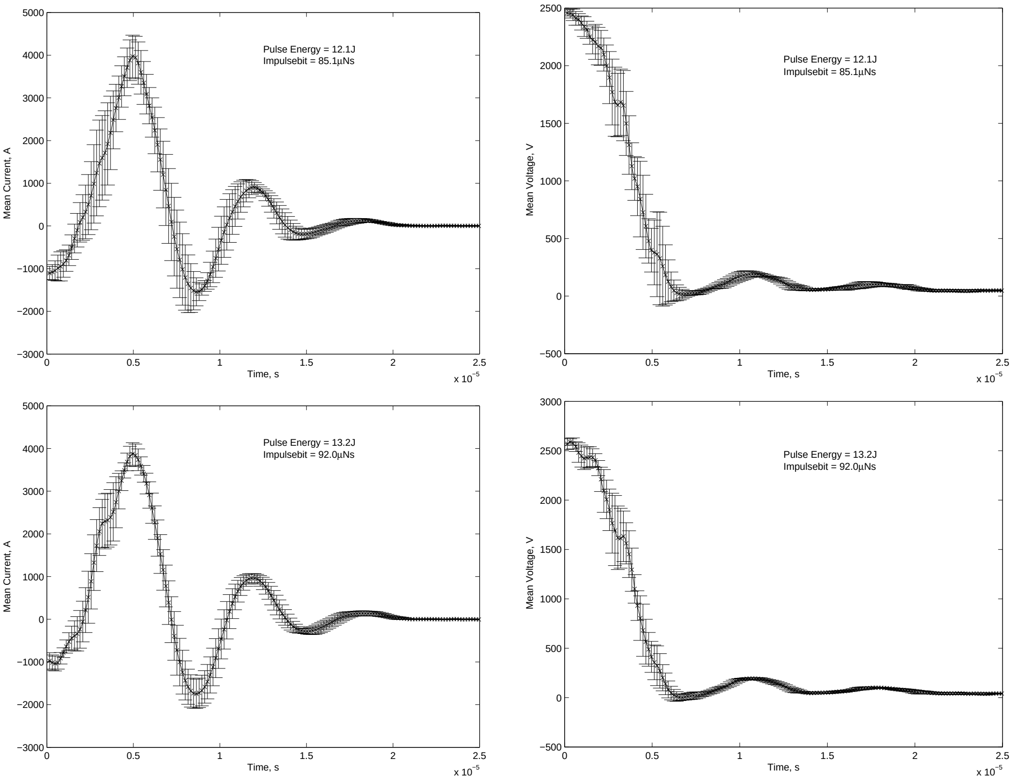

Figure B.32: Profiles 1-2: Electrode separation = 70mm, no Teflon^{TM}

B.5.5 80mm Electrode Separation

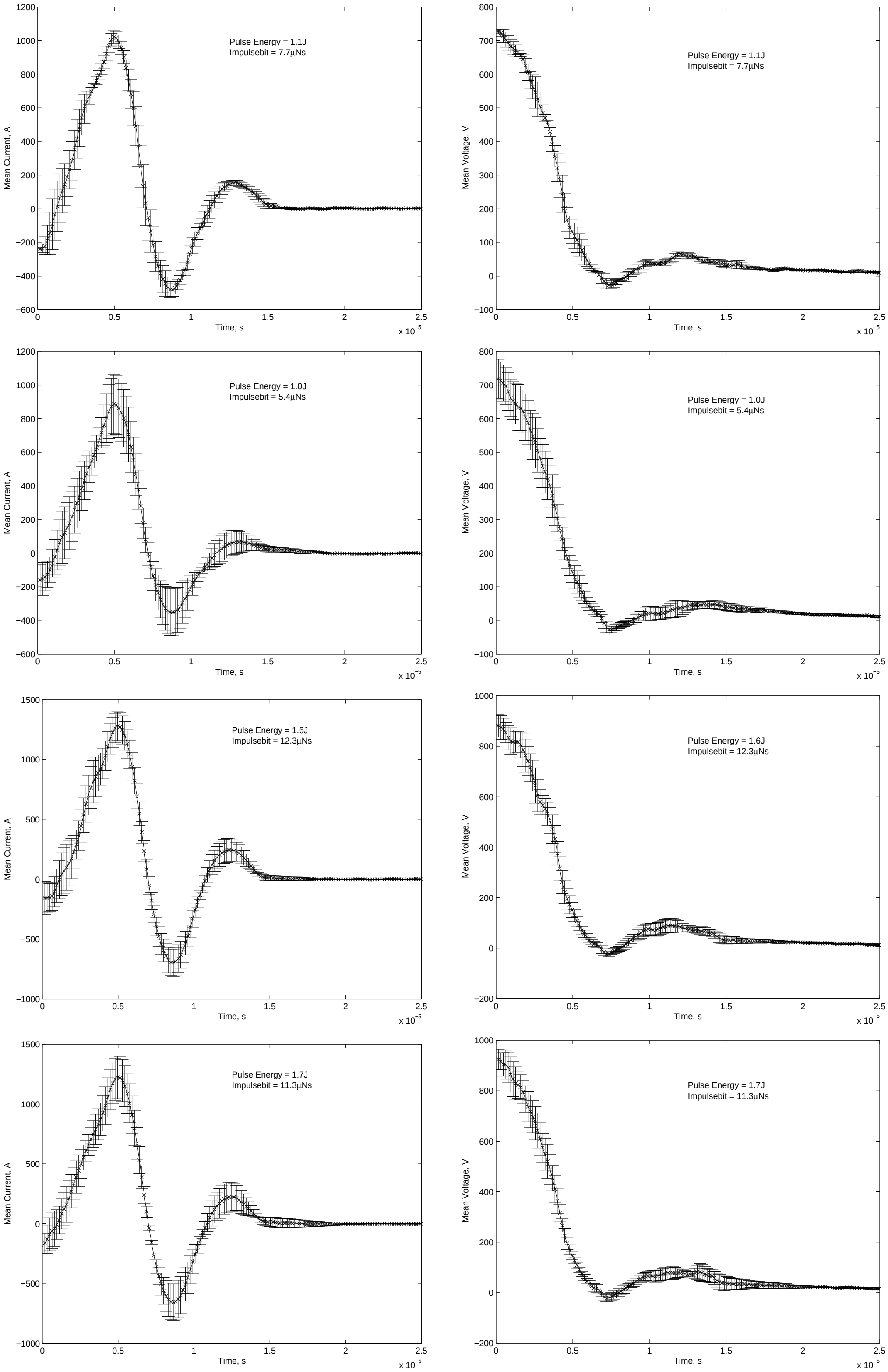

Figure B.33: Profiles 1-4: Electrode separation = 80mm, no Teflon^{TM}

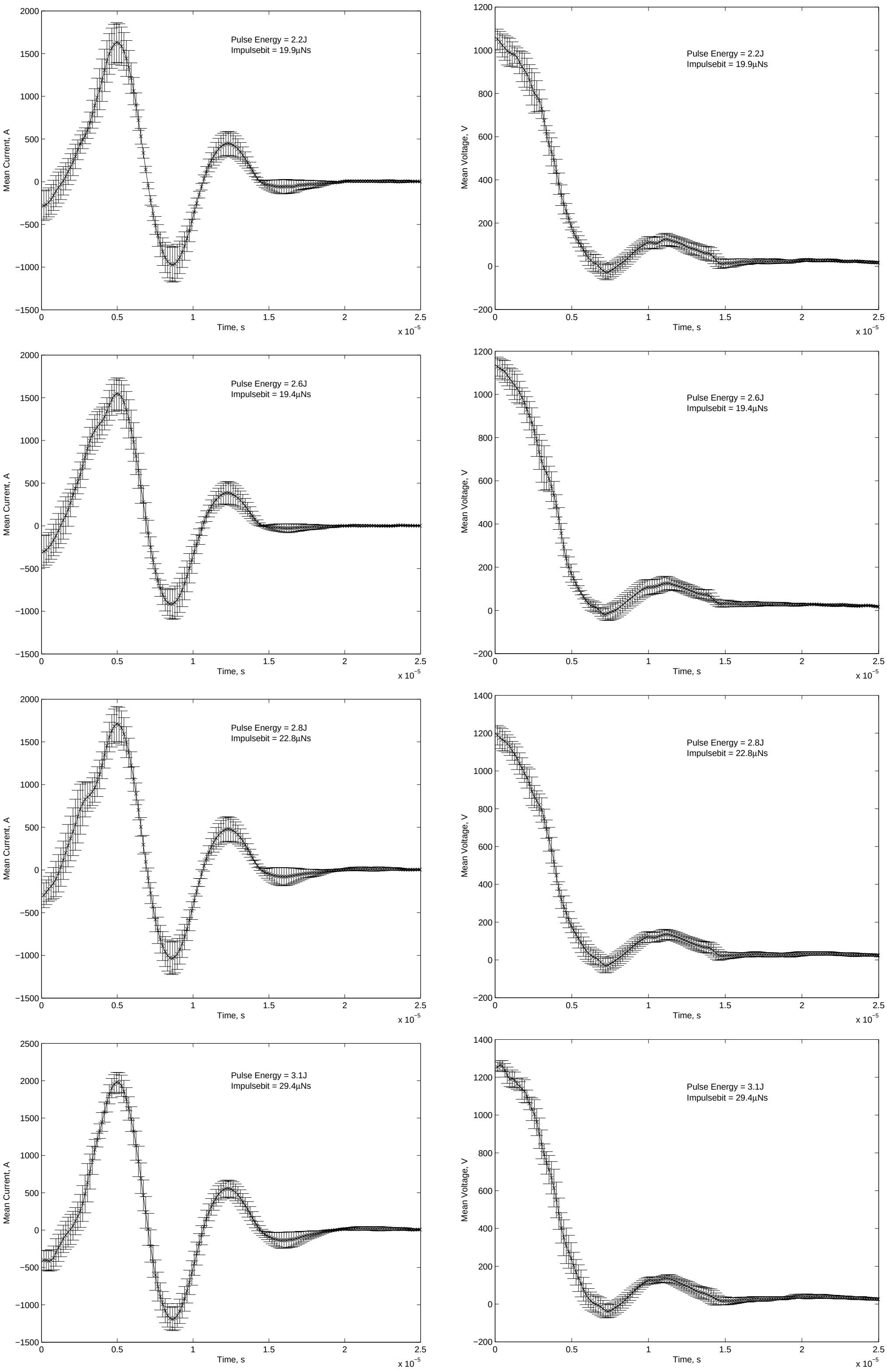

Figure B.34: Profiles 1-4: Electrode separation = 80mm, no Teflon^{TM}

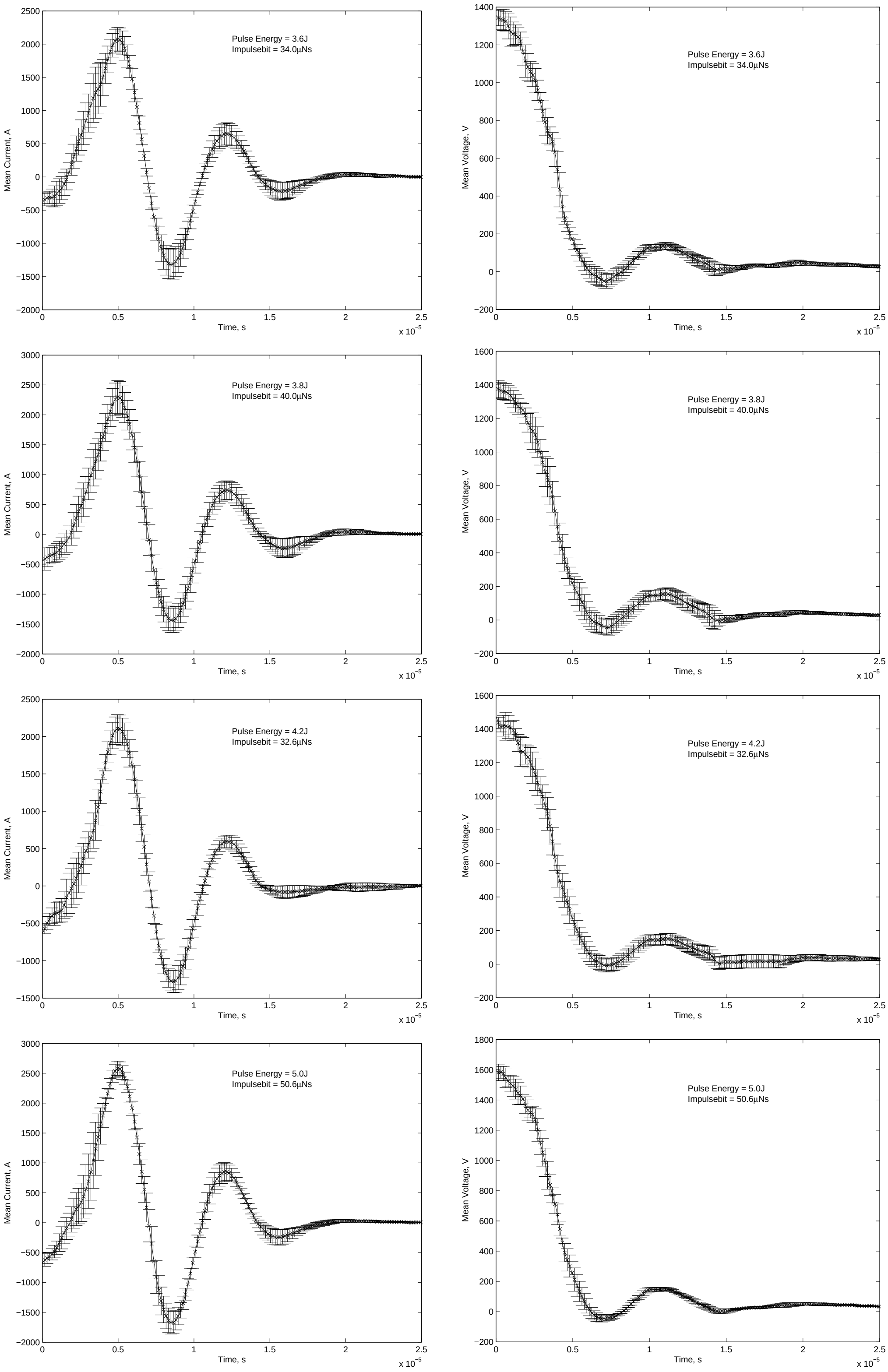

Figure B.35: Profiles 1-4: Electrode separation = 80mm, no Teflon^{TM}

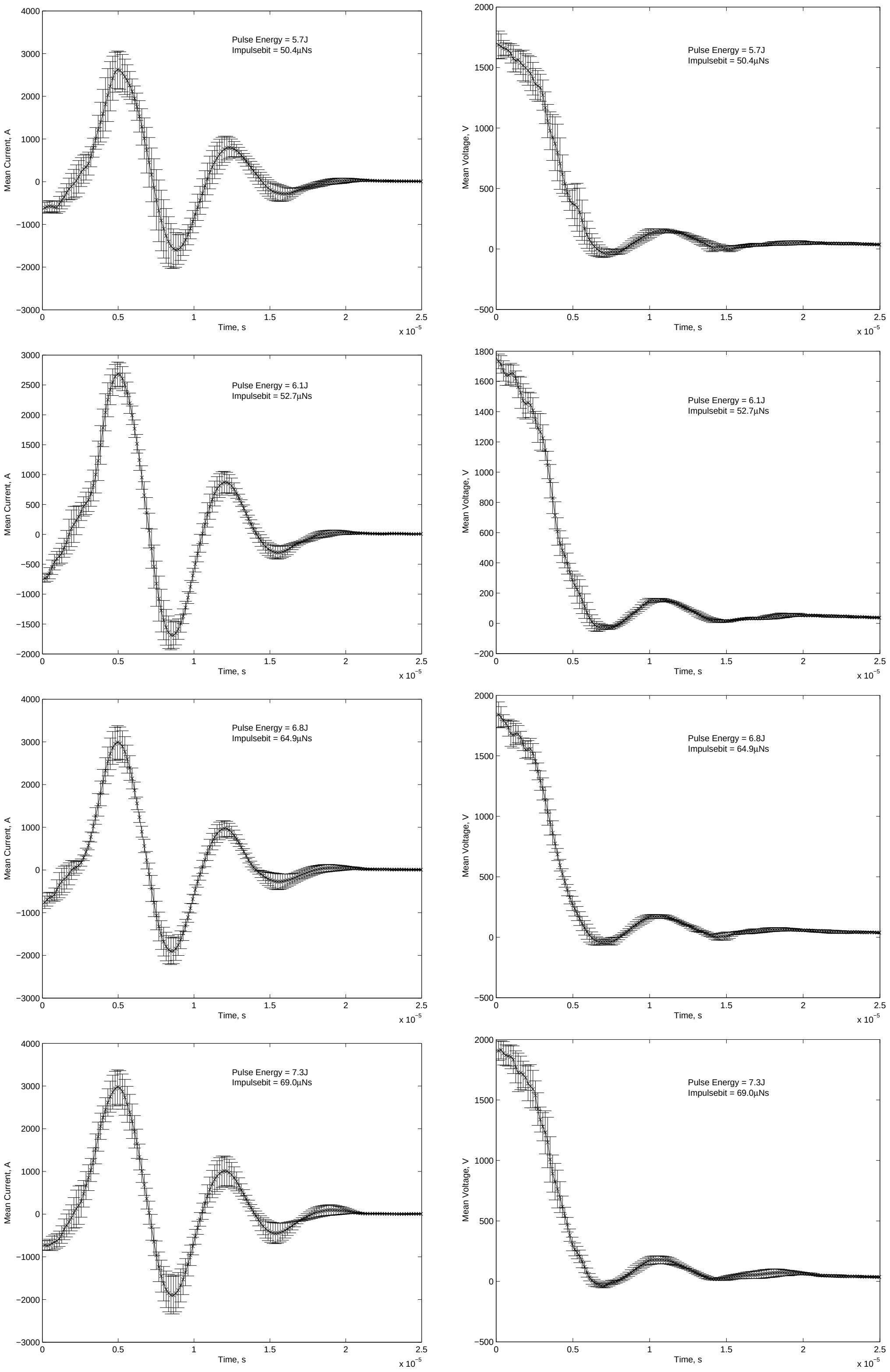

Figure B.36: Profiles 1-4: Electrode separation = 80mm, no Teflon^{TM}

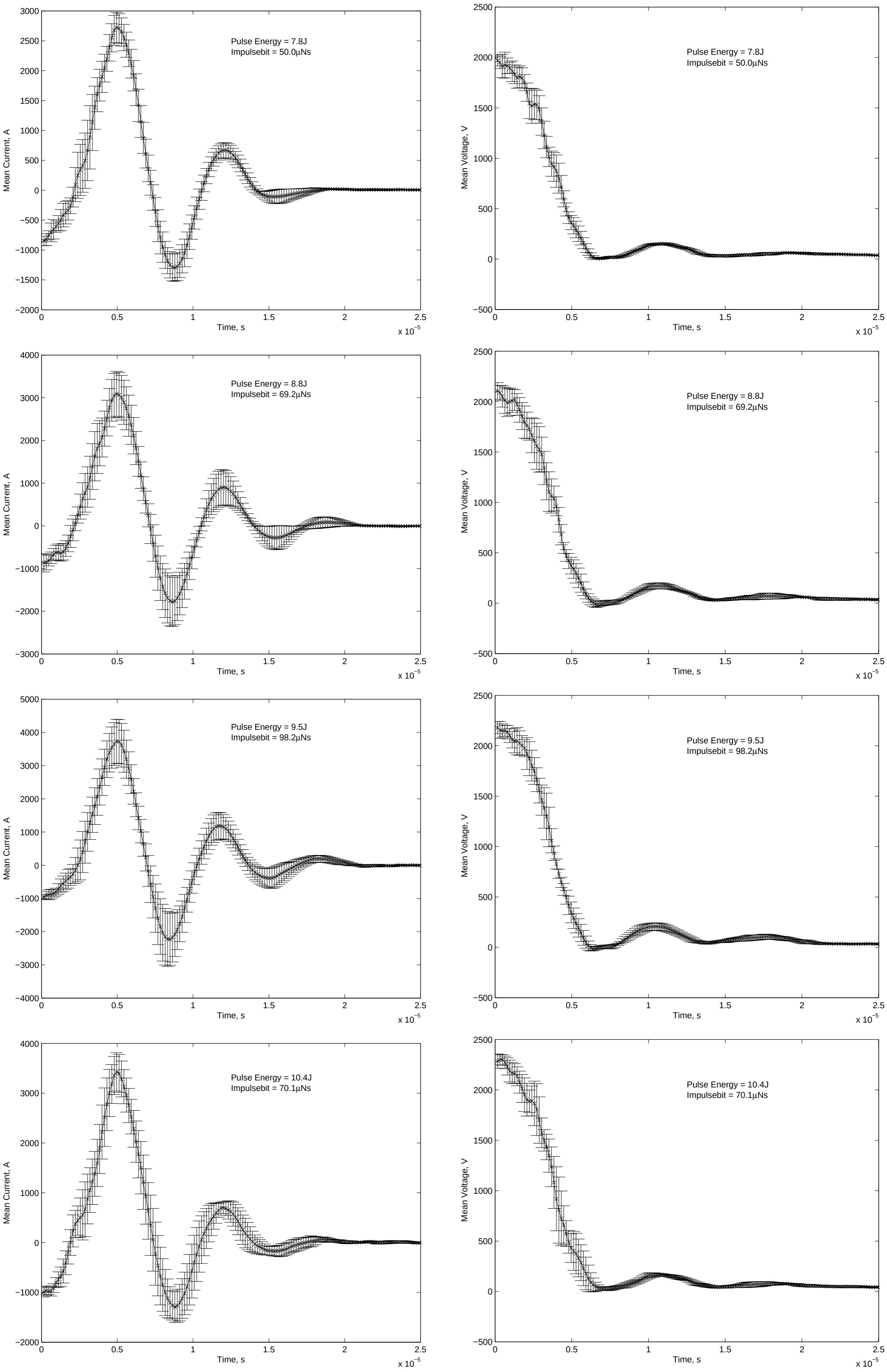

Figure B.37: Profiles 1-4: Electrode separation = 80mm, no Teflon^{TM}

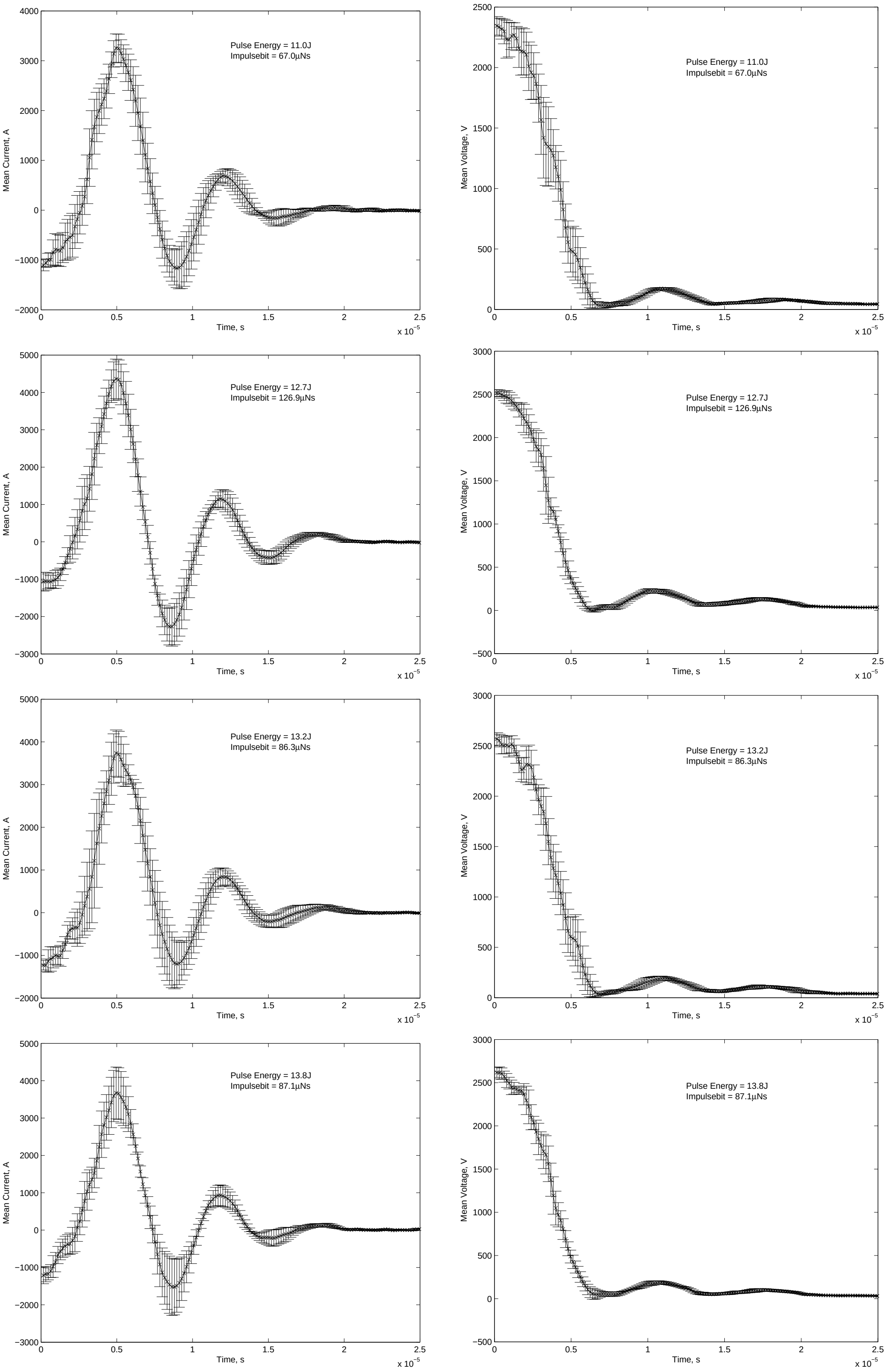

Figure B.38: Profiles 1-4: Electrode separation = 80mm, no Teflon^{TM}

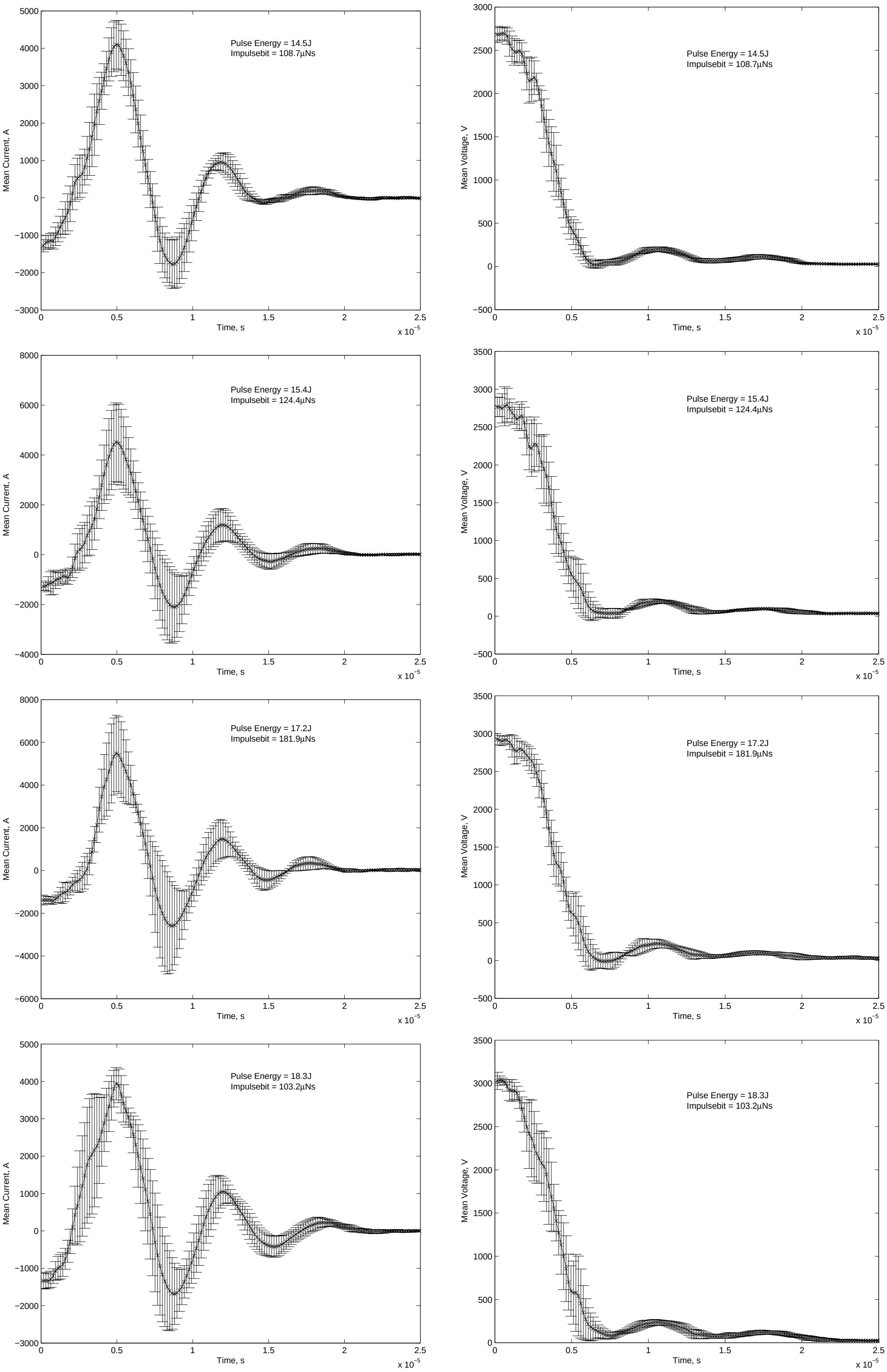

Figure B.39: Profiles 1-4: Electrode separation = 80mm, no Teflon^{TM}

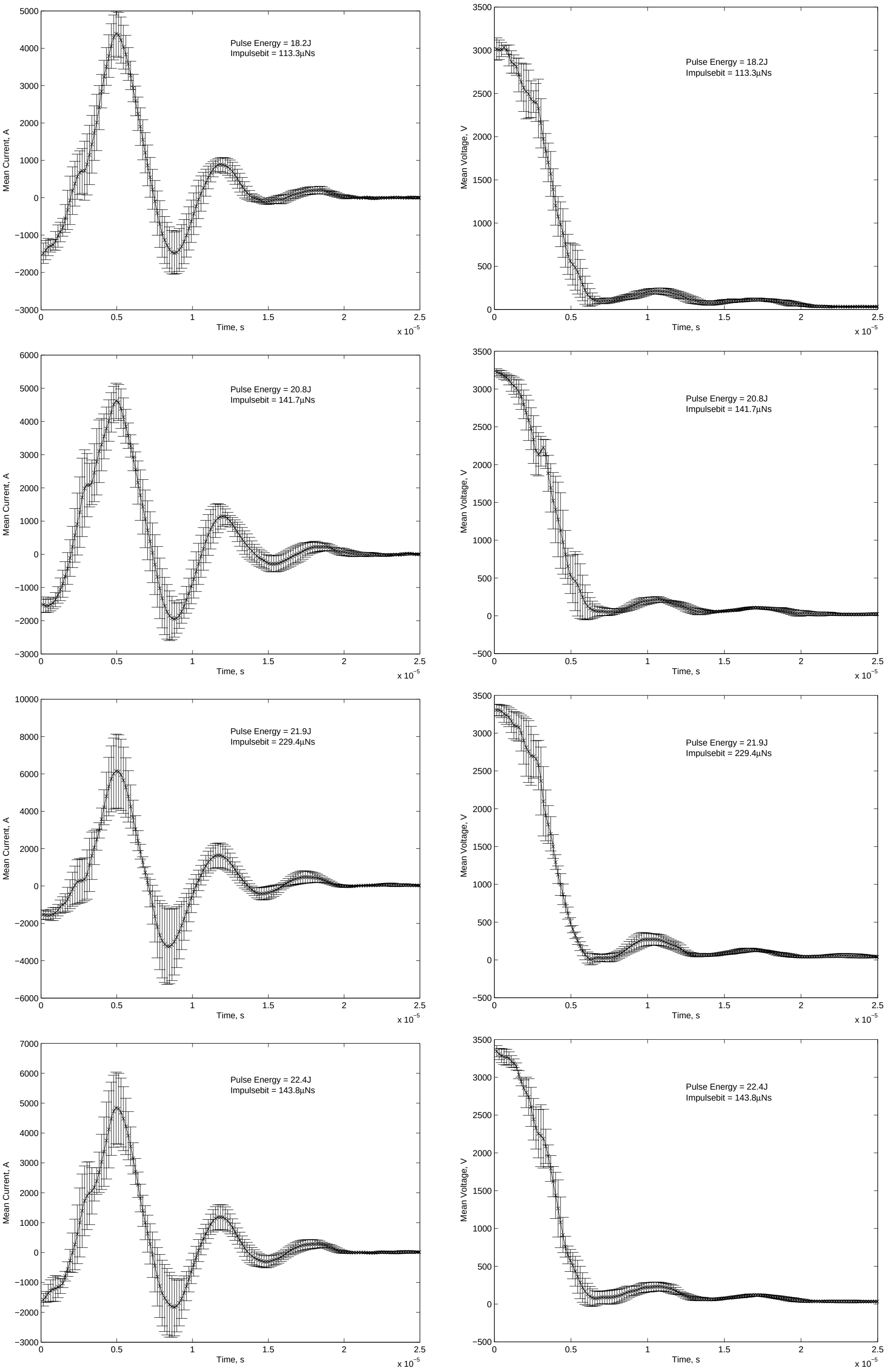

Figure B.40: Profiles 1-4: Electrode separation = 80mm, no Teflon^{TM}

B.5.6 90mm Electrode Separation

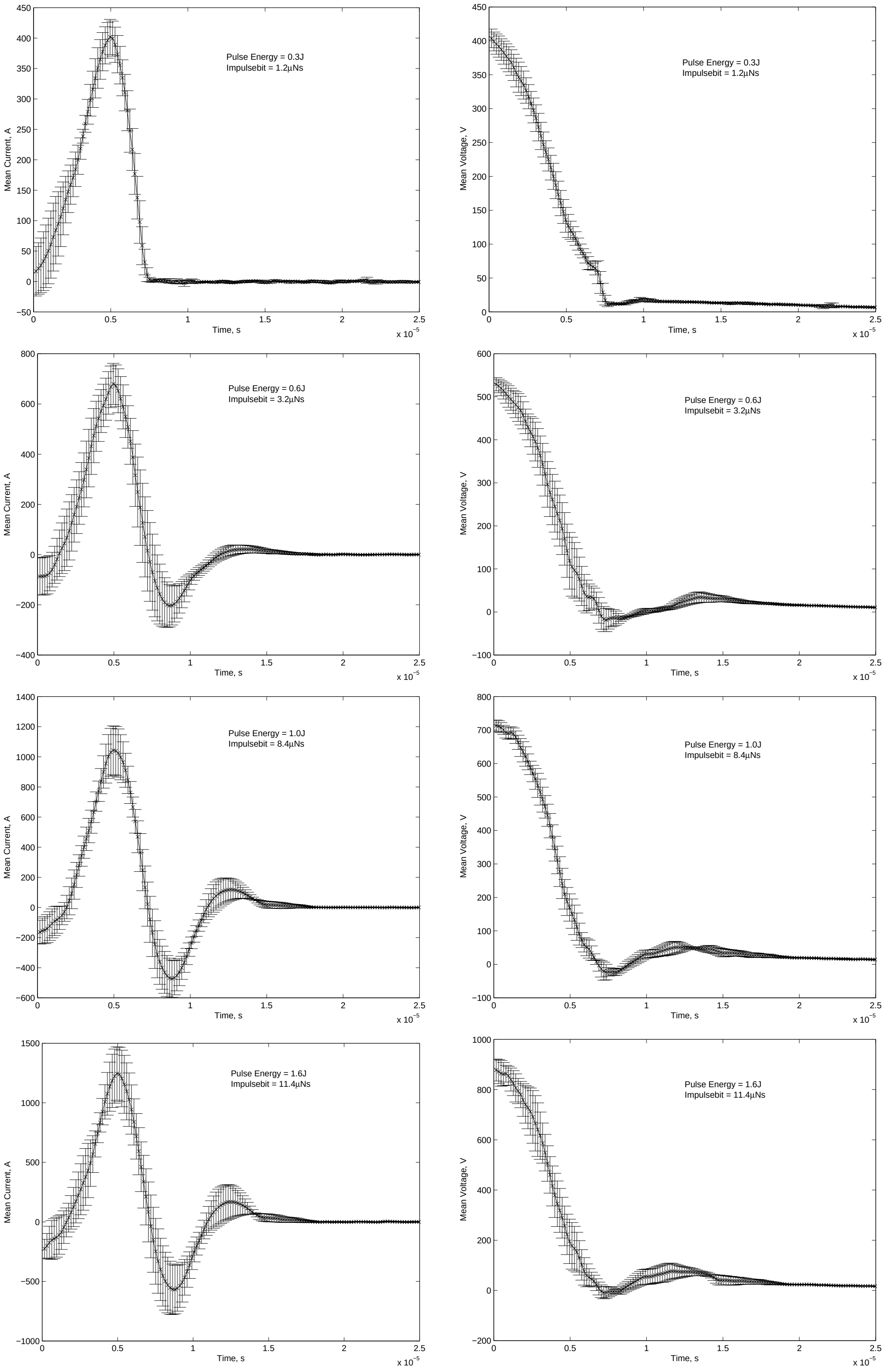

Figure B.41: Profiles 1-4: Electrode separation = 90mm, no Teflon^{TM}

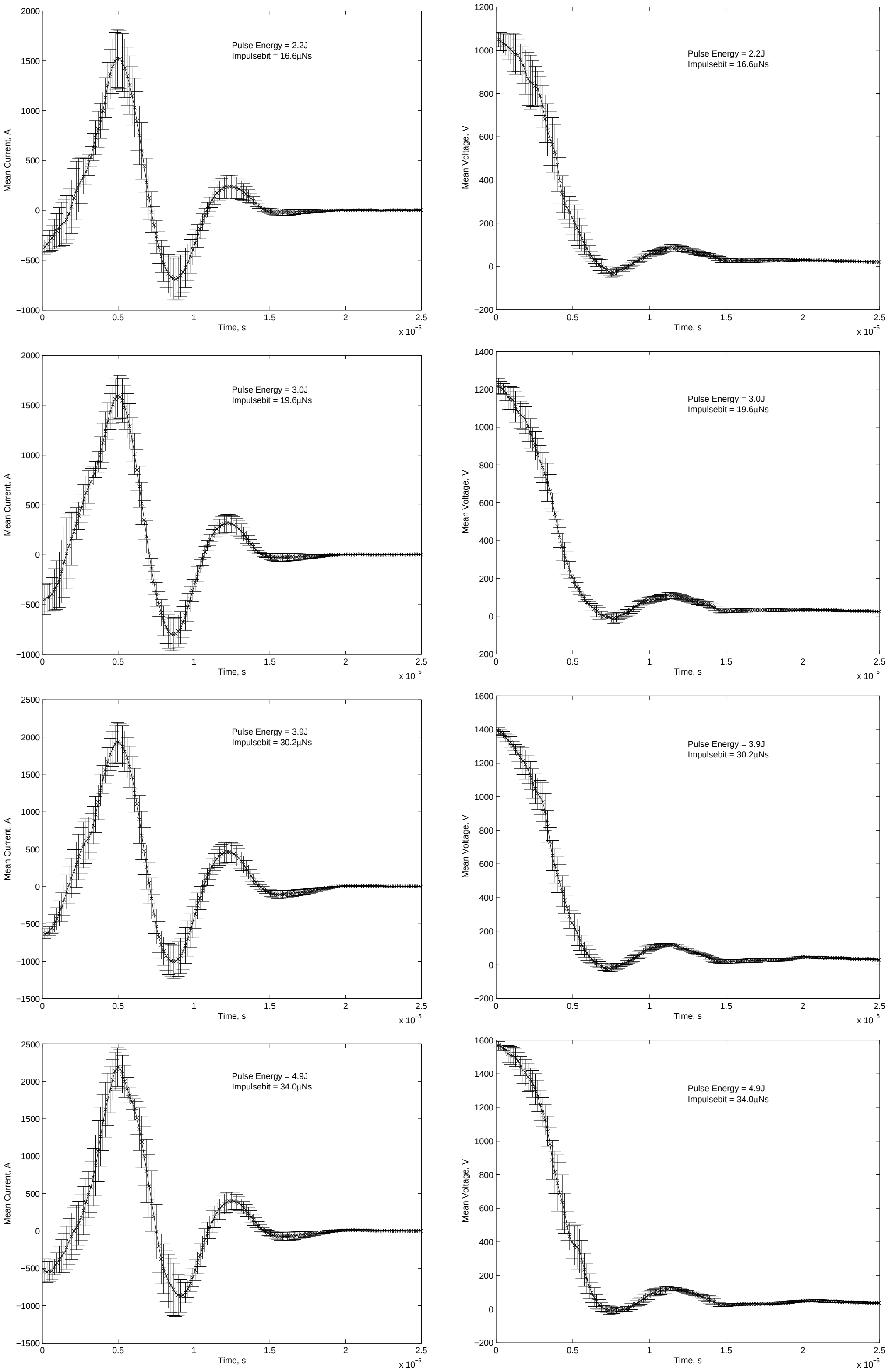

Figure B.42: Profiles 1-4: Electrode separation = 90mm, no Teflon^{TM}

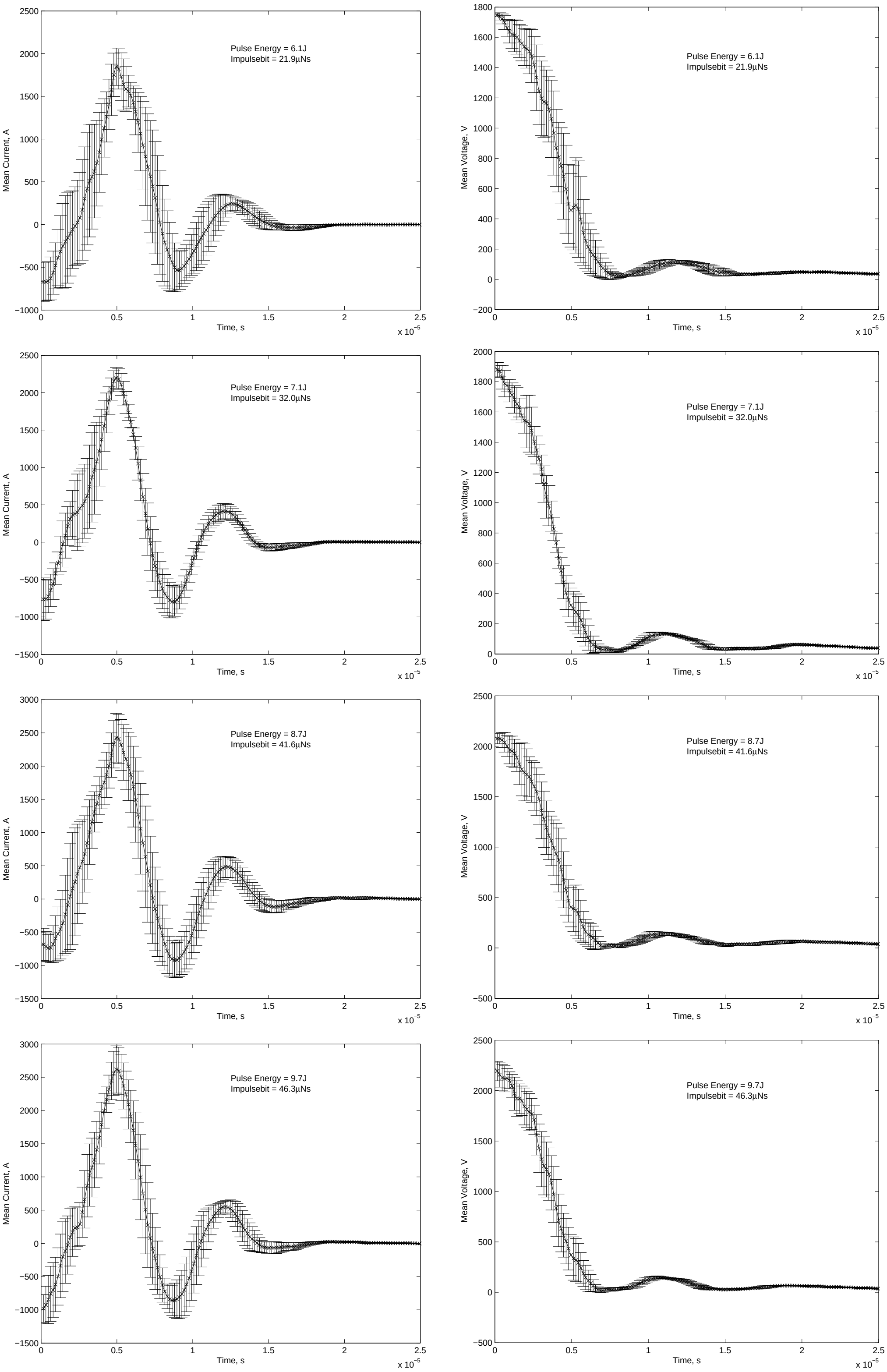

Figure B.43: Profiles 1-4: Electrode separation = 90mm, no Teflon^{TM}

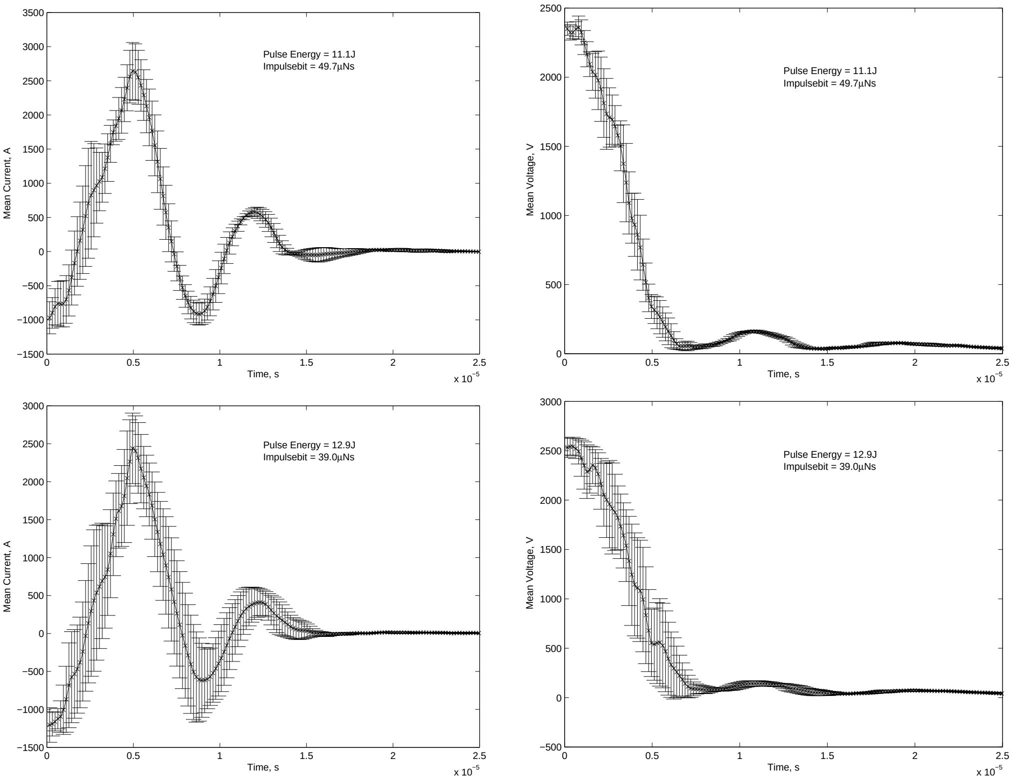

Figure B.44: Profiles 1-2: Electrode separation = 90mm, no Teflon^{TM}

B.6 Performance Comparison with and without Teflon^{TM}

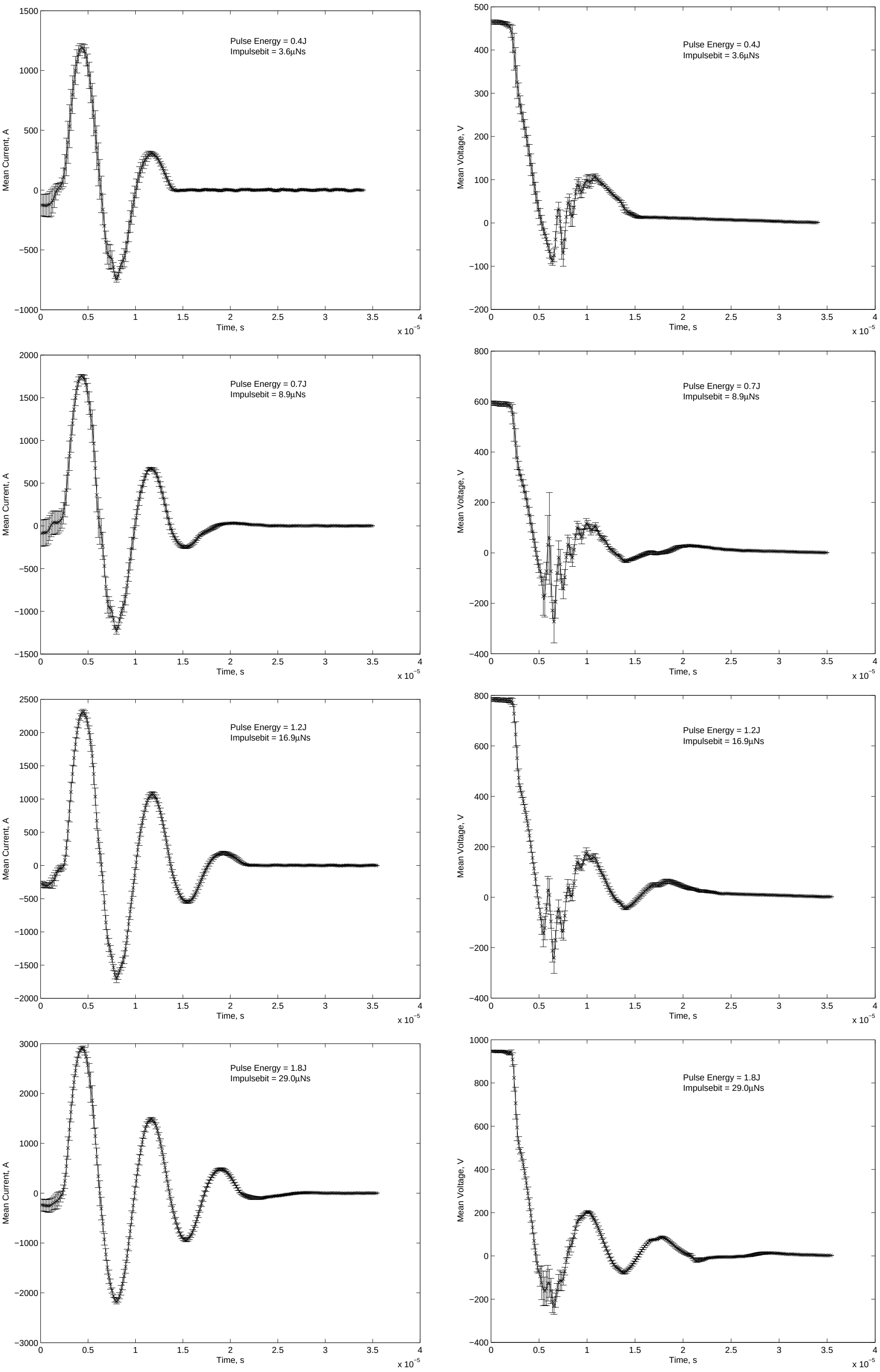

Figure B.45: Profiles 1-4: Electrode separation = 30mm, Teflon^{TM} width = 6.00mm

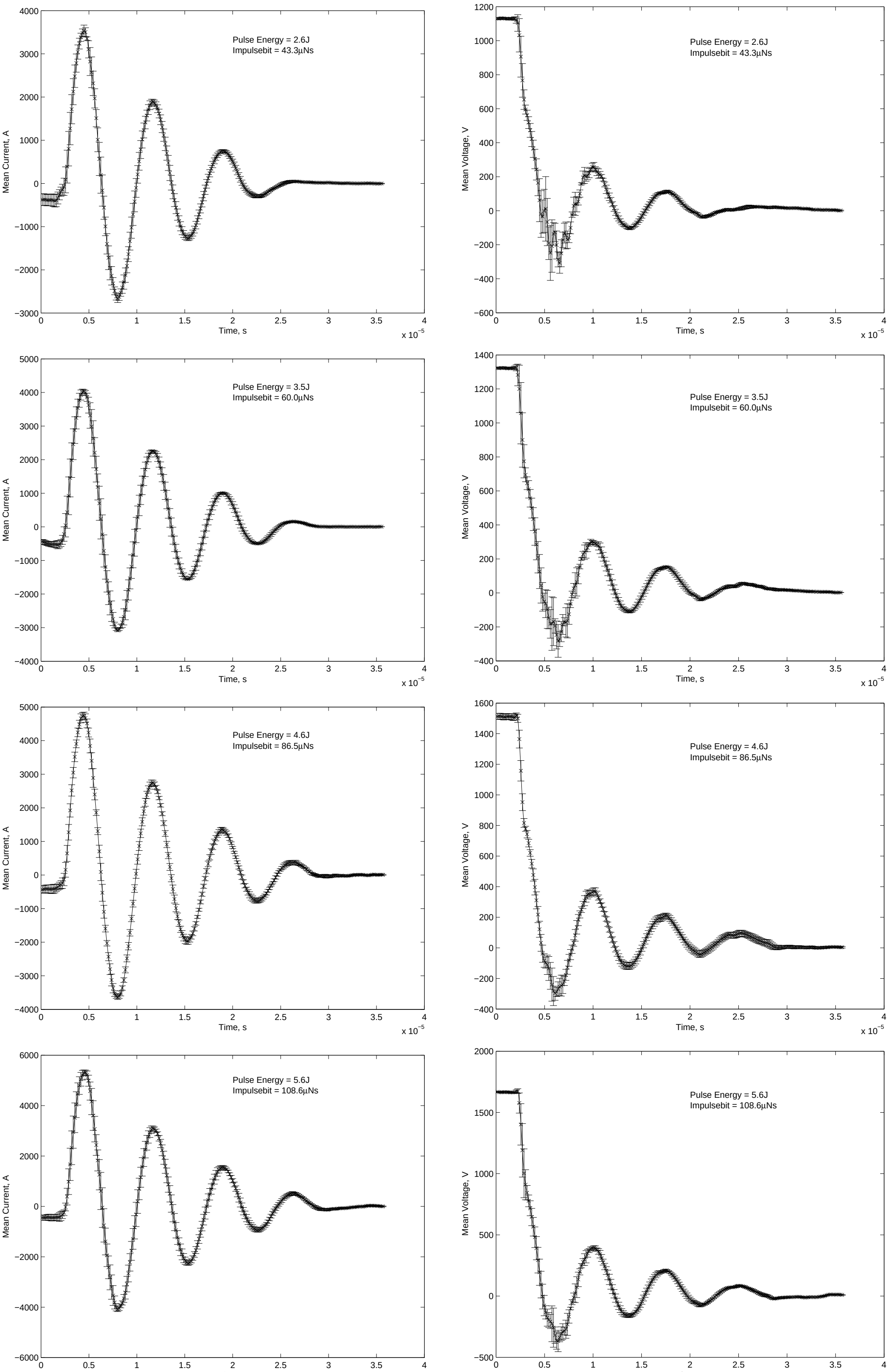

Figure B.46: Profiles 1-4: Electrode separation = 30mm, Teflon^{TM} width = 6.00mm

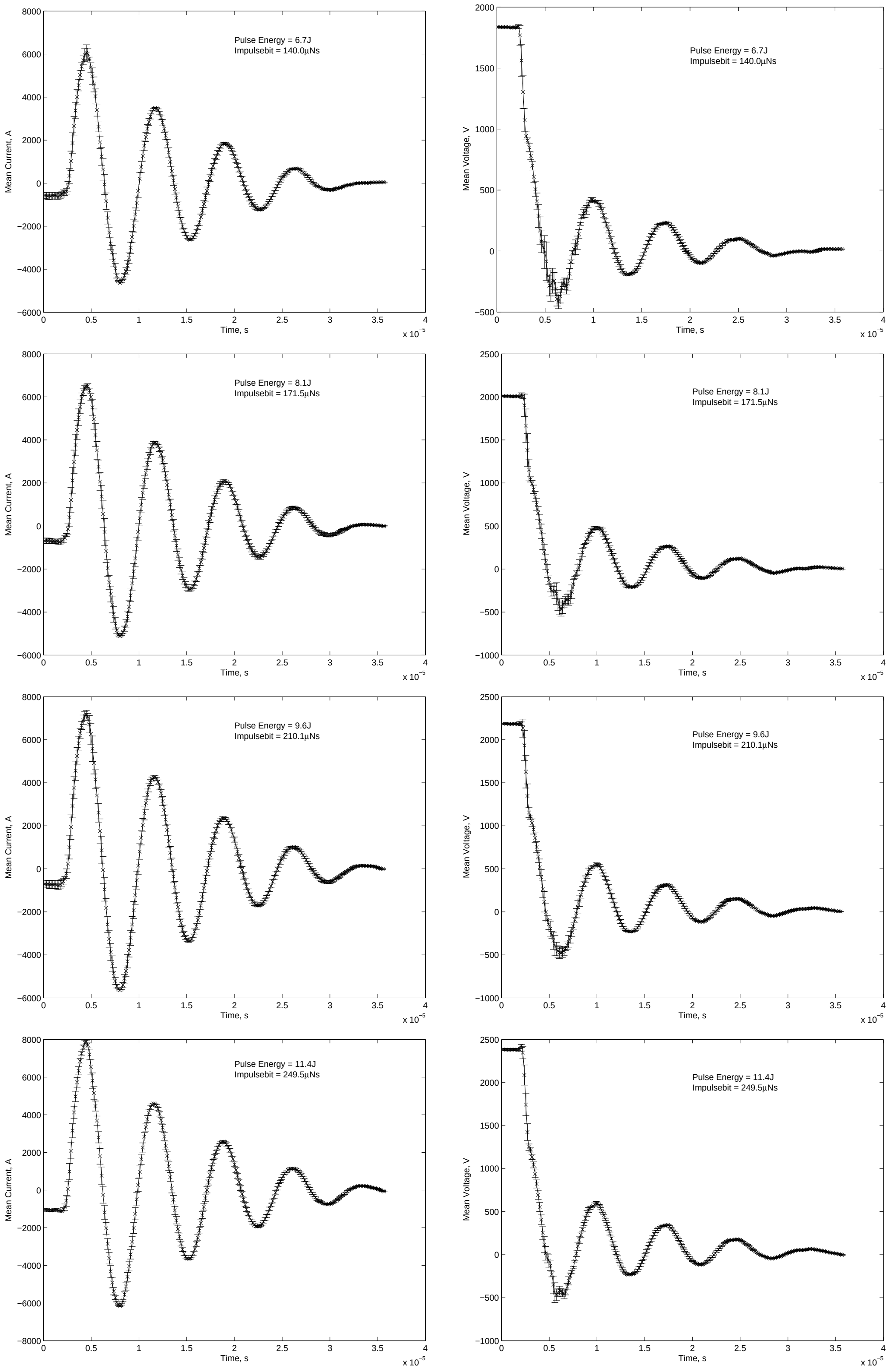

Figure B.47: Profiles 1-4: Electrode separation = 30mm, Teflon^{TM} width = 6.00mm

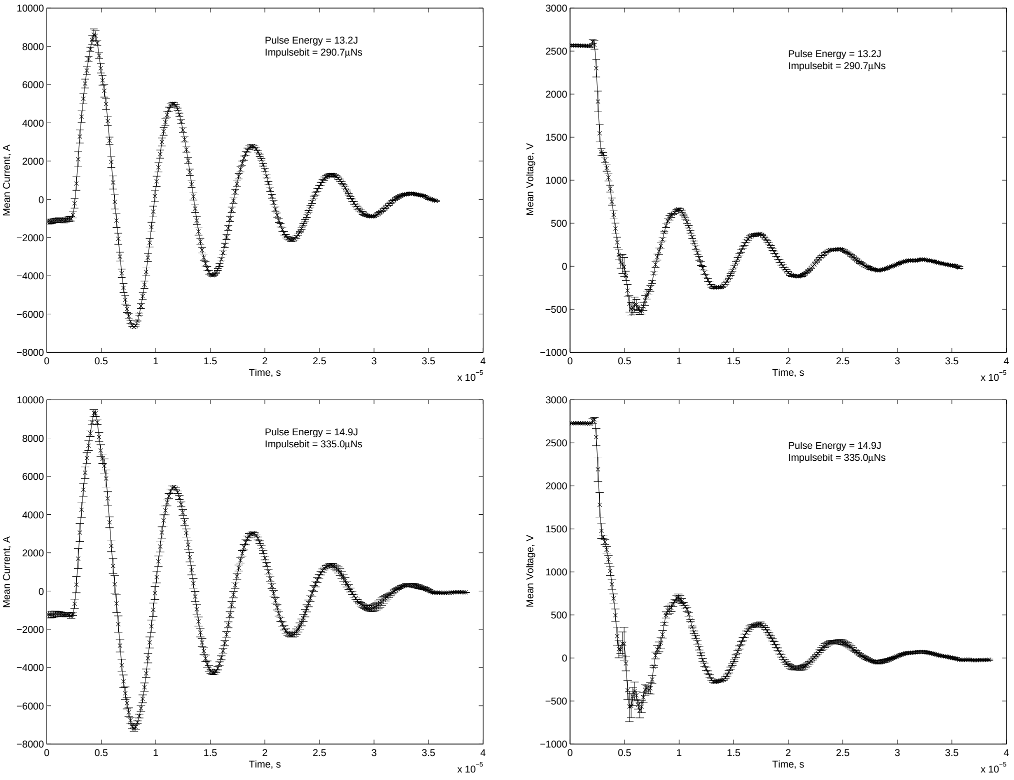

Figure B.48: Profiles 1-2: Electrode separation = 30mm, Teflon^{TM} width = 6.00mm